Modelling Settling-Driven Gravitational Instabilities at the base of volcanic clouds

Lemus, Jonathan

Université de Genève
Département des Sciences de la Terre

Faculté des sciences
Professeure Costanza Bonadonna

Modelling Settling-Driven Gravitational Instabilities at the base of volcanic clouds

THÈSE

présentée à la Faculté des sciences de l'Université de Genève
pour obtenir le grade de Docteur ès sciences, mention Sciences de la Terre

par

Jonathan LEMUS

de Le Robert (Martinique - FRANCE)

Thèse N^o 5669

Genève
Atelier de reprographie ReproMail
2022

UNIVERSITÉ
DE GENÈVE
FACULTÉ DES SCIENCES

DOCTORAT ÈS SCIENCES, MENTION SCIENCES DE LA TERRE

Thèse de Monsieur Jonathan LEMUS

intitulée :

«Modelling Settling-Driven Gravitational Instabilities at the Base of Volcanic Clouds»

La Faculté des sciences, sur le préavis de Madame C. BONADONNA, professeure ordinaire et directrice de thèse (Département des sciences de la Terre), Monsieur B. CHOPARD, professeur ordinaire (Département d'informatique), Monsieur J. LATT, professeur associé (Département d'informatique), Monsieur T. SHELDRAKE, professeur assistant (Département des sciences de la Terre), Monsieur P. JARVIS, docteur (GNS Science, Wellington, Nouvelle Zélande), Madame A. CLARKE, professeure (School of Earth and Space Exploration, Arizona State University, United States of America) et Monsieur M. DE'MICHIELLI VITTURI, professeur (Instituto Nazionale di Geofisica e Vulcanologia, Pisa, Italie) autorise l'impression de la présente thèse, sans exprimer d'opinion sur les propositions qui y sont énoncées.

Genève, le 2 août 2022

Thèse - 5669 -

Le Doyen

N.B. - La thèse doit porter la déclaration précédente et remplir les conditions énumérées dans les "Informations relatives aux thèses de doctorat à l'Université de Genève".

Acknowledgements

First of all, I would like to thank prof. Costanza Bonadonna, my PhD director. I will be always grateful to her as, by giving me the opportunity to work in her group, she saved my soul when I was selling it to the Petroleum industry. I appreciated the confidence she had in me to carry out this PhD project, allowing me to improve my vision of academic research and science in general.

Second, working on this project would not have been the same without my team mates Allan Fries and Paul Jarvis. Thanks Paul for your rigour, the long scientific discussions and for the time spent to improve my writing skills. Allan, I remember when we realised one week before starting our PhDs: "Wait, you are also from Martinique ?!". It was a real pleasure to learn the basics of volcanology with you. It is a honour to count you as a friend now and I am happy to continue the adventure in the group with you. And as I always say in creole; "ou ké rivé lwen" !

Third, a special "thank you" to prof. Jonas Lätt for his (great!) patience and support when I was struggling with *Palabos*. Thank you as well as to prof. Bastien Chopard who always had a wise vision on the project; I really appreciated our scientific discussions.

Then, the life in the "Maraîchers" office would not be such a pleasure without meeting nice people like Valentin Freret-Lorgeril (aka "mafia"), Lucia Dominguez (aka "Speedy Dominguez"), Eduardo Rossi, Maria-Paz Reyes Hardy, Luigia Di Maio, Sebastien Biasse, Stefano Pollastri, Corine Frischknecht, Stefano Mannini, Christine Lovis, Valerie Baumann, Matthew John Edwards, Laura Pioli, Bocar Sy. Impossible to forget the life in the "Battelle" office with Christophe Coreixas, Anthony Boulmier, Francesco Marson, Christos Kotsalos, Orestis Malaspinas (My merge request is ready !), Rémy Petkanchin, Raphaël Conradin, Franck Raynaud, Yann Thorimbert, Joël Beny, Karthik Thyagarajan, Pedro José De Santana Neto, Pierre Kuenzli, Jean-Luc Falcone, Christophe Charpilloz.

Last bust not least, I would like to warmly thank my parents and my sisters.

I would not be able to achieve my goals without their unfailing support and I am more than proud to be the man I am today thanks to them.

This work was supported by the Swiss National Science Foundation (project N. 200021_169463)

Contents

List of Figures

List of Tables

Summary

Explosive volcanic eruptions inject large quantities of magma fragments (tephra) into the atmosphere. Dispersion and sedimentation of tephra particles can cause significant impact such as damage to infrastructure, pollution of the ecosystem and paralysis of economic and transport sectors. Recent eruptions (e.g., 2010 Eyjafjallajökull, Iceland; 2021 Cumbre Vieja, Spain) have shown that even moderate events can significantly impact our society. Also, significant effort has been involved to improve Volcanic Ash Transport and Dispersal Models (VATDMs) used for the forecasting necessary to emergency management during volcanic crises.

Field observations and laboratory experiments have shown that tephra sedimentation can be significantly affected by collective settling mechanisms that promote premature ash deposition (i.e., deposition of particles < 2 mm). This has important implications for dispersal and associated impacts. Indeed, the amount of ash in the atmosphere may be overestimated by VATDMs that do not take in account the processes that promote premature sedimentation. These mechanisms include particle aggregation and settling-driven gravitational instabilities (SDGIs) taking the form of downward moving ash fingers. Volcanic ash aggregation has been documented over the past decades while SDGIs remain poorly described as well as the combination of both processes. The main objectives of this thesis include to: i) develop an accurate numerical model able to simulate the dynamics of SDGIs; ii) use this model alongside field and experimental studies in order to constrain the parameters controlling the formation of SDGIs; and iii) combine the modelling of both ash aggregation and SDGIs to better interpret their associated roles in premature ash sedimentation.

First, a single-phase model has been developed using a novel approach involving a Lattice Boltzmann model in order to solve the fluid motion, while a Weighted Essentially Non Oscillatory (WENO) finite difference scheme is employed to solve the particle transport. The model is then validated thanks to comparison with ex-

periments and theoretical works. Second, the model is applied to experimental and natural configurations in order to study the effect of controlling parameters such as the particle concentration and size. I found that increasing the particle concentration enhances the development of SDGIs while increasing the particle size beyond a threshold prohibits the formation of fingers. The study also revealed that the critical Grashof number usually used to characterise such instabilities is about ten times larger than the value suggested by previous studies. The addition of shear has also confirmed that SDGIs are able to produce similar ground signature as ash aggregation. Third, a numerical scheme has been integrated in order to include the aggregation process, the goal being the study of possible effects of aggregation on SDGIs. Simulations showed that aggregation enhances all the sedimentation modes including individual settling and SDGIs. Conversely, the turbulence generated within SDGIs can also promote ash aggregation. Finally, a two-phase model has also been developed. This model solves the motion of individual particles but, given the numerical cost, the use of this model is limited to the study of small scale processes involving only a reasonable number of particles.

My numerical investigations have demonstrated that the triggering of SDGIs at the base of volcanic clouds is controlled by several parameters such as the particle concentration, the particle size and the shear induced by the wind. Volcanic ash aggregation and SDGIs present the same ground signature and the two processes enhance each other. However, further work is needed regarding the effect of turbulence, the analytical scaling of the fingers vertical velocity and the development of a comprehensive parametrisation of SDGIs to model the loss of fine ash in the cloud due to SDGIs.

Résumé en Français

Les éruptions volcaniques explosives injectent de grandes quantités de fragments de magma (téphra) dans l'atmosphère. La dispersion et la sédimentation de ces particules de téphra peuvent avoir des impacts significatifs tels que les dégâts d'infrastructures, la pollution de l'écosystème et la paralysie de secteurs économiques et liés aux transports. Des éruptions récentes (par exemple 2010 Eyjafjallajökull, Islande; 2021 Cumbre Vieja, Espagne) ont montré que même des événements d'intensité modérée peuvent affecter notre société de façon significative. De nombreux moyens ont été mis en oeuvre dans le but d'améliorer les modèles de transport et dispersion de cendres volcaniques (Volcanic Ash Transport and Dispersal Models (VATDMs)) utilisés pour la prévision nécessaire à la gestion de crises liées aux éruptions volcaniques.

Des observations de terrain ainsi que des expériences en laboratoire ont montré que la sédimentation de téphras peut être significaivement affectée par les mécanismes de sédimentation de groupe provoquant le dépot prématuré de cendre (c'est-à-dire le dépôt de particules < 2 mm). Ceci comporte d'importantes implications pour la dispersion et les impacts associés. En effet, la quantité de cendres dans l'atmosphère peut être surestimée par les VATDMs ne prenant pas en compte les processus provoquant la sédimentation prématurée. Ces mécanismes incluent l'agrégation de particules mais aussi les instabilités gravitationelles générées par sédimentation (settling-driven gravitational instabilities (SDGIs)) ayant la forme de colonnes de cendres verticales. L'agrégation de cendres volcaniques a été documentée durant les dernières décennies alors que les SDGIs restent très peu décrites, au même titre que la combination des deux phénomènes. Les objectifs principaux de ce mémoire de thèse sont: i) le développement d'un modèle numérique précis capable de simuler la dynamique des SDGIs; ii) l'utilisation du modèle parallèlement aux études expérimentales et de terrain, dans le but d'étudier les paramètres contrôlant la formation de SDGIs; et iii) combiner la modelisation à la fois de l'agrégation et des SDGIs afin de mieux interpréter leur rôle sur la sédimentation prématurée.

Premièrement, un modèle monophasique a été developpé au moyen d'une nouvelle approche mettant en oeuvre un modèle Lattice Boltzmann resolvant l'écoulement fluide, et un schéma en différences finies de type Weighted Essentially Non Oscillatory (WENO) pour résoudre l'équation de transport des particules. Le modèle est ensuite validé grâce à des comparaisons avec des travaux théoriques et expérimentaux. Deuxièmement, le modèle est appliqué à des configurations expérimentales et naturelles dans le but d'étudier l'effet de paramètres tels que la concentration en particules mais aussi leur taille. J'ai découvert qu'augmenter la concentration en particules accroît le développement de SDGIs alors qu'augmenter la taille des particules au delà d'une valeur seuil à tendance à annihiler le phénomène. L'étude a aussi révélé que le nombre de Grashof, habituellement utilisé pour caractériser ce type d'instabilité, est dix fois plus grand que la valeur suggérée par l'analogie au cas thermique. L'ajout du cisaillement a également confirmé que les SDGIs sont capables de produire une signature au sol similaire à celle donnée par l'agrégation de cendres. Troisièmement, un schéma numérique décrivant l'agrégation a été intégré au modèle, le but étant l'étude de possibles effets de l'agrégation sur les SDGIs. Des simulations ont montré que l'agrégation renforcait tous les modes de sédimentation incluant la sédimentation individuelle ainsi que les SDGIs. A l'inverse, la turbulence générée dans les SDGIs peut aussi favoriser l'agrégation de cendres. Enfin, un modèle diphasique a également été développé en parallel. Ce modèle résout le mouvement de particules individuellement et étant donné le coût numérique associé, l'utilisation de ce modèle est limité à l'étude de processus à petite échelle mettant en jeu un nombre raisonnable de particules.

Mes investigations numériques ont démontré que la formation de SDGIs à la base de nuages volcaniques est contrôlée par plusieurs paramètres tels que la concentration en particules, leurs tailles mais aussi le cisaillement induit par le vent. L'agrégation de cendres volcaniques ainsi que les SDGIs présentent la même signature au sol et les deux procédés se renforcent mutuellement. Cependant, des futurs travaux sont nécessaires concernant les effets de la turbulence, les études analytiques sur la vitesse verticale des fingers ainsi que le développement d'un paramétrage pour modéliser la perte en cendres fines liée aux SDGIs dans les nuages volcaniques.

Chapter 1

Introduction

Volcanic eruptions are among the most drammatic natural events, not only on Earth but also on other rocky extraterrestrial bodies and are associated with the expulsion of material (magma) coming from the depth. In the case of explosive volcanic eruptions, large quantities of magma fragments (tephra) are ejected in the atmosphere and dispersed over wide areas, depending on their sizes [Bonadonna et al., 2015a]. Ultimately, the dispersal and sedimentation of tephra may cause a wide range of hazards at both local and global scales. Recent events have demonstrated the extent of the impacts associated with tephra dispersal and sedimentation. Evidently, we can mention the different disruptions (especially to air traffic) subsequent to the 2010 eruption of Eyjafjallajökull (Iceland) which affected many countries worldwide and caused a financial loss of more than a billion euros [Lund and Benediktsson, 2011; Sammonds et al., 2010]. Another event, more recent, is the eruption of the Cumbre Vieja volcano in the Canary islands in 2021, which was associated with damage to buildings and infrastructure. Those examples clearly highlight the potential of the tephra to impact a variety of public and economic sectors at multiple temporal and spatial scales. Tephra particles can be divided in categories depending on their size and thus the associated residence time in the atmosphere. The first class of tephra concerns ejected material of size $\geq$ 64 mm (*Bombs and Blocks*). Given their size, the area of influence is a few kilometers around the volcano. *Lapilli* range from 2 to 64 mm and affect an area of few tens of kilometers. Finally, *coarse ash* of size 63 μm to 2 mm and *fine ash* of size $\leq$ 63 μm can be transported for hundreds to thousands kilometers from the volcanic source. Considering the wide range of distances of influence (from few km to thousands km) and the wide spectrum of potential threat

(e.g. air traffic, infrastructures, building, human health, agriculture) [Guffanti et al., 2008; Prata and Rose, 2015; Spence et al., 2005; Jenkins et al., 2015; Gudmundsson, 2011; Wilson et al., 2011], having a complete understanding of the dispersal and sedimentation of tephra in the atmosphere is crucial.

Given that lapilli and ash are transported at long distance, a fundamental question concerns how they sediment to the ground. The terminal velocity of such particles is a relevant parameter describing the sedimentation that can be affected by many processes. When lapilli or volcanic ash settle individually, their terminal velocities are determined according to physical parameters such as the shape and drag coefficient (which quantifies the resistance of an object immersed in a fluid flow). Several studies have investigated on the shape of lapilli and volcanic ash in order to characterise how they influence their terminal velocities [Bagheri et al., 2016; Liu et al., 2015; Riley et al., 2003; Saxby et al., 2018]. In parallel, other studies have focused on the accurate determination of the drag coefficient [Bagheri et al., 2015; Dioguardi et al., 2018; Ganser, 1993; James et al., 2003]. Nevertheless, specific sedimentation processes can also affect the terminal velocity. These sedimentation processes, that can be described as collective settling, can increase the terminal velocity by clustering particles in bigger structures (particle aggregates) [Gilbert and Lane, 1994; James et al., 2002, 2003; Durant et al., 2009; Rose and Durant, 2011; Brown et al., 2012; Van Eaton et al., 2012; Van Eaton and Wilson, 2013; Burns et al., 2017; Vogel et al., 2019; Rossi et al., 2021; Del Bello et al., 2017] or through settling-driven gravitational instabilities (SDGIs). SDGIs contribute to the early deposition of fine ash with similar outcomes as aggregation (e.g., grain-size bimodality, premature sedimentation of fine ash). These instabilities generate downward-moving ash columns (fingers) which grow from the base of the ash cloud [Carazzo and Jellinek, 2012; Manzella et al., 2015; Scollo et al., 2017]. Neglecting collective sedimentation of fine ash (i.e. the premature removal of fine ash from the cloud) causes the underestimation of the associated concentration in the volcanic cloud [Scollo et al., 2008]. A detailed understanding and physical description of the dynamics of collective settling is crucial to improve the atmospheric dispersal models used for forecasting and risk management [Jones et al., 2007; Bonadonna et al.,

2012; Folch, 2012; Folch et al., 2020; Prata et al., 2021; Del Bello et al., 2017]. In this thesis we will specifically treat the description and dynamics of SDGIs including their interaction with particle aggregation.

1.1 Field and experimental characterisation of settling-driven gravitational instabilities

By increasing their terminal velocity, SDGIs can explain the depletion of fine ash observed in large volcanic clouds far from the source [Hoyal et al., 1999; Carazzo and Jellinek, 2013; Durant, 2015; Gouhier et al., 2019]. Despite the various efforts dedicated to volcanic ash aggregation [Gilbert and Lane, 1994; James et al., 2002, 2003; Durant et al., 2009; Rose and Durant, 2011; Brown et al., 2012; Van Eaton et al., 2012; Van Eaton and Wilson, 2013; Burns et al., 2017; Vogel et al., 2019; Rossi et al., 2021; de'Michieli Vitturi and Pardini, 2021], the attention regarding SDGIs remains relatively poor.

SDGIs affect the sedimentation of particles in various fields such as river plumes [Hoyal et al., 1999; Davarpanah Jazi and Wells, 2016; Henniger and Kleiser, 2012], sedimentation of tephra in oceans [Carey, 1997; Manville and Wilson, 2004; Jacobs et al., 2013] and volcanic clouds [Carazzo and Jellinek, 2012; Manzella et al., 2015; Scollo et al., 2017]. SDGIs during volcanic events are poorly documented and one of the first mentions is given in Bonadonna et al. [2002] where they observed "finger-like protrusions" in the sedimentation of volcanic ash during the September 1997 eruption of Soufrière Hills (Montserrat) volcano. Later, some "instability structures" have been described in Bonadonna et al. [2005] and characterised as processes that potentially enhance the deposition of fine volcanic ash below a weak volcanic plume from Ruapehu (New-Zealand). Additionally and more recently, the development of ash fingers has been observed during the 23 November 2013 lava fountain of Etna volcano (Italy) [Andronico et al., 2015; Scollo et al., 2017]. However, SDGIs have been quantitatively studied for the first time during the 2010 eruption of Eyjafjallajökull (Iceland) using both video acquisitions and field observations of the tephra deposit [Manzella et al., 2015]. Manzella et al. [2015] observed the formation of ash

fingers at the base of the volcanic cloud $\sim$ 1.4 km from the vent before reaching the ground approximately 10 km downwind. This distance between initiation and deposition obviously depends on the fingers vertical velocity, which itself depends on parameters such as the particle concentration, the wind velocity, etc... Then, in order to constrain the dynamics underlying SDGIs, several characteristics related to fingers have been measured:

- the average finger width : 168 $\pm$ 26 m,
- the average finger spacing : 180 $\pm$ 60 m,
- the downward finger velocity is 1 $\pm$ 0.5 m.s^{-1} while the horizontal velocity is about 8.5 $\pm$ 0.8 m.s^{-1},

Additionally, the ground signature of premature sedimentation has been observed in the resulting deposits [Bonadonna et al., 2011]. Indeed, quantitative studies of the deposit at different distances (i.e. at $\sim$ 2, 10 and 20 km from the vent) have been performed and the one at $\sim$ 10 km revealed the presence of structures such as aggregates, as well as bimodal deposits with coarse (d $\approx$ 500 μm) and fine (d $\approx$ 150 μm) modes. As 10 km also corresponds to the distance where fingers have been observed to reach the ground, the mode associated with the fine fraction in the bimodal deposits can be attributed to both processes enhancing premature sedimentation: aggregates breaking upon impact and fine ash transported within SDGIs. The fact that aggregates have been observed at the same location where SDGIs have supposedly reached the ground highlights a fundamental question about a possible relation between the two phenomena, especially if particle aggregation could happen both in the volcanic plume and in ash fingers.

Some experimental investigations have also been performed in the laboratory in order to constrain the parameters describing SDGIs [Cardoso and Zarrebini, 2001; Hoyal et al., 1999; Carazzo and Jellinek, 2012; Scollo et al., 2017; Manzella et al., 2015]. Using the results of experiments involving a layer of particle suspension placed above a denser fluid layer, Hoyal et al. [1999] derived a critical criterion based on the ratio between gravitational and viscous forces that needs to be satisfied in order to trigger SDGIs. Alongside this criterion, a strong coupling between particles and the

carrier fluid is required, which is the case in numerous volcanic clouds as suggested by Carazzo and Jellinek [2012]. Scollo et al. [2017] performed dedicated experiments using glass beads and also samples of volcanic ash. Those experiments in a static configuration also involved a two-layer system where a particle suspension is placed above a denser sugar solution. The main goal was to focus on the influence of the initial particle concentration and size. More recently, Fries et al. [2021] used the same experimental conditions to extend the range of concentrations, making use of sophisticated techniques to provide interesting insights about fingers dynamics. They particularly showed that the initial particle concentration has a significant influence on the number and also the velocity of fingers. Also, the particle concentration in the cloud depends on parameters such as the initial amount of particles ejected out of the vent and on the ambient fluid entrained. As these time-dependent parameters are complex to assess, this shows the difficulty in identifying specific volcanoes and/or types of eruption likely to trigger fingers. However, Fries et al. [2021] also derived a dimensionless number that depends on the measurable cloud mass-loading and thickness, which can be used to assess the potential for SDGIs to form at the base of volcanic clouds.

1.2 Theoretical studies on settling-driven gravitational instabilities

Carazzo and Jellinek [2012] mentioned SDGIs as "Rayleigh-Taylor-type" instabilities that can strongly modify the dynamics of umbrella clouds. Indeed, the mechanisms involved during the development of SDGIs resemble the classical Rayleigh-Taylor instabilities (RTIs). RTIs are fingering instabilities that grow when a perturbation is applied at the unstable interface between a dense fluid placed above a lighter one [Sharp, 1984; Chandrasekhar, 1961]. However, in the case of SDGIs, the mechanism is different as the settling of particles play an important role, especially in our cases where the configurations are initially density-stable . Typically, considering a particle-laden layer placed above a denser fluid layer, the settling of particles across the density interface creates a Particle Boundary Layer (PBL), unstable if

the bulk density is greater than the lower layer density [Hoyal et al., 1999; Carazzo and Jellinek, 2012]. Thus, a quantitative condition to trigger SDGIs can be based on the dimensionless Grashof number Gr which describes the ratio between the gravitational and viscous forces

$$Gr = \frac{g'\delta^3}{\nu^2}, \tag{1.1}$$

where ν is the effective kinematic viscosity of the PBL, δ a characteristic length scale and g' the reduced gravity of the PBL $g' = g(\rho_{PBL} - \rho_f)/\rho_f$, $g = 9.81$ m.s^{-1} being the gravitational acceleration and ρ_{PBL} and ρ_f the density of the PBL and the ambient, respectively. Hoyal et al. [1999] made an analogy with the thermal case (i.e. Rayleigh-Bénard convection) [Turner, 1973] and suggested that the growth of instabilities occurs whenever the Grashof number becomes greater than a critical value Gr_c=10^3. Carazzo and Jellinek [2012] suggested to consider the PBL thickness as characteristic length scale which ultimately gives the critical PBL thickness for the development of SDGIs

$$\delta_{PBL} = 10\left(\frac{\nu^2}{g'}\right)^{\frac{1}{3}}. \tag{1.2}$$

In addition, dimensional analyses have been used to predict that the downward propagation velocity of the generated fingers is function of δ and is given by

$$V_f = g'^{\frac{2}{5}}\left[\frac{\pi V_s \delta_{PBL}^2}{4}\right]^{\frac{1}{5}}, \tag{1.3}$$

where V_s is the particle individual settling velocity [Hoyal et al., 1999; Carazzo and Jellinek, 2012].

Whilst the critical Grashof number provides a criterion for the formation of fingers, there is also another simple criterion. In fact, fingers form when the growth rate of the instability at the particle interface is greater than the settling velocity of individual particles [Carazzo and Jellinek, 2012]. Furthermore, other theoretical studies have been conducted in order to estimate the instability growth rate related to SDGIs. They involve linear stability analyses (LSA) of the governing equations of the problem, focusing on the early linear stage of the instability. LSA consist of defining a field equation-satisfying base state for each of the unknown fields in a problem and then applying an infinitesimally small perturbation to each

of these fields. The equations are then expanded to linear order in the perturbation, with higher order terms assumed to be negligible. By assigning the perturbation to have the form of a complex waveform, the system of equations reduces to an eigenvalue problem, which can be solved to determine which wavelengths will grow or decay [Burns and Meiburg, 2012; Yu et al., 2013; Chandrasekhar, 1961; Farenzena and Silvestrini, 2017]. Interestingly, such analyses have especially revealed that the instability growth rate strongly depends on the particle individual velocity and consequently, on the PBL thickness. Some have also highlighted the limits between instabilities generated by particle settling and by double-diffusive effects [Burns and Meiburg, 2012].

1.3 Numerical modelling settling-driven gravitational instabilities

In addition to the field, experimental and theoretical investigations on SDGIs, numerical studies have also provided a significant contribution. Whilst no numerical studies have been specifically dedicated to SDGIs from volcanic clouds, numerical investigations on the particle-induced Rayleigh-Taylor instability have been performed [Burns and Meiburg, 2014; Yu et al., 2014; Jacobs et al., 2013; Chou and Shao, 2016; Yamamoto et al., 2015]. Indeed, several strategies have been developed in order to simulate the process, including fully Eulerian (grid-based) and Euler-Lagrange (EL) models (discrete Lagrangian particles coupled with fluid). In the Eulerian models, the particle suspension is modelled as a continuum-phase for which the transport is described by an advection-diffusion law.

In order to accurately resolve sharp gradients, Burns and Meiburg [2014] performed direct numerical simulations using high-order finite difference schemes (up to tenth order) for the spatial discretisation and Runge-Kutta/Crank-Nicolson for the time stepping. They showed that the effective settling velocity of particles within fingers is several order of magnitude greater than the individual settling velocity.

Yu et al. [2014] used a completely different strategy. They applied a pseudo-spectral method involving Fourier expansions for the variables in the two horizontal

directions while a rational collocation method (with the associated Chebyshev grid transformation) is used for the vertical direction [Cortese and Balachandar, 1995]. Here again, a Runge-Kutta/Crank-Nicolson scheme has been used for the time stepping. Even though their investigations include also double-diffusive effects, the crucial outcomes are that the dynamics of the generated instabilities are controlled by the individual settling velocity of particles, the initial particle concentration in the upper layer and the ratio between the species diffusivities.

Furthermore, Jacobs et al. [2013] developed a multiphase model in order to simulate the sedimentation of volcanic ash in water as described in Carey [1997]. An interesting aspect is that the multiphase system is solved with a finite element method coupled with an adaptive mesh refinement which allows to dynamically resolve the grid in specific region of interest.

Finally, the works of Yamamoto et al. [2015] and Chou and Shao [2016] bridge the gap between the fully Eulerian and EL solvers. Indeed, Yamamoto et al. [2015] performed both Eulerian and EL simulations in order to constrain a dimensionless number derived by Harada et al. [2013] which illustrates the transition between particle-like and fluid-like behaviour for particle-induced Rayleigh-Taylor instabilities. This number has been derived using a narrow configuration (Hele-Shaw cell). It is function of the particle diameter, the particle volume fraction and the instability wavelength in order to provide a transition between the fluid-like and particle-like behaviour. On the one hand, they also made use of finite-difference/Crank-Nicolson schemes to solve the Navier-Stokes equations as well as the advection-diffusion, applying the interface tracking method which involves binary markers in order to differentiate the pure fluid from the particle suspension. On the other hand, the lagrangian method solves explicitly the particle motion equation using the point-force model [Bosse et al., 2005] while the fluid motion is treated in the same way as for the eulerian model. Regarding the work of Chou and Shao [2016], the goal was to compare the dynamics of RTIs using both fully eulerian and EL. The fluid solver for both eulerian and EL is defined by a finite-volume method while the tracking of particles for the EL model is performed using a cell-waise particle transport algorithm [Chou et al., 2015]. Then, the use of the EL model allowed to highlight

that the shape of the vortex ring upstream a finger (and ultimately its dynamic) is strongly affected by the non-uniformity in the particle distribution caused by fluid entrainment.

1.4 Parametrisations of SDGIs for VATDMs

There is a strong need to build a comprehensive parametrisation of SDGIs, that prematurely remove fine ash from the cloud, in order to improve the calculations of ash dispersal in the atmosphere. Having a good understanding about the dynamics of SDGIs with the contribution of numerical, theoretical and experimental investigations is crucial for the improvement of Volcanic Ash Transport and Dispersal Models (VATDMs) [Folch, 2012]. Indeed, once tephra is present in the atmosphere, subsequent dispersion can be modelled using VATDMs such as PUFF [Searcy et al., 1998], NAME [Jones et al., 2007], VOL-CALPUFF [Barsotti and Neri, 2008], HYSPLIT [Stein et al., 2015] and FALL3D [Folch et al., 2020] (see [Bonadonna and Costa, 2013; Bonadonna et al., 2015a; Folch, 2012] for reviews). While ash aggregation are included in some dispersal models such as FALL3D [Folch et al., 2020], very recently in NAME [Beckett et al., 2022] or even TephraProb used for long-term hazard assessment [Biass et al., 2016], there is no effect of SDGIs included. For instance, in the two former models that are respectively eulerian and lagrangian, aggregation is treated by solving a Population Balance equation (PBE) [Kumar and Ramkrishna, 1996; Kumar et al., 2006; Pesmazoglou et al., 2016; Rossi, 2018]. TephraProb allows to estimate the ground deposit of ash by applying an analytical solution of the transport equation and the consideration of aggregation is given by an empirical parameter which represents a weight fraction of particles that forms aggregates [Bonadonna et al., 2002; Cornell et al., 1983].

1.5 Objectives of this work

The previous sections highlighted the fact that SDGIs and the associated effects on volcanic ash sedimentation remain poorly documented. The contribution of numerical investigations, alongside field and experimental works, helps to address funda-

mental questions regarding the dynamics of SDGIs. This thesis therefore seeks to answer the following questions:

1. How to build a numerical model in order to accurately study the dynamics of SDGIs?
2. What are the conditions to trigger the formation of SDGIs?
3. What are the parameters that control the process?
4. How do SDGIs affect the sedimentation of fine ash and the associated accumulation on the ground?
5. What are the effects of external parameters such as the ambient wind?
6. How is the volcanic cloud dynamics affected by the presence of SDGIs?
7. Is there any relation between ash aggregation and SDGIs and is it possible to somehow distinguish their effects?
8. Finally, how to gather various insights into a general and comprehensive parametrisation of SDGIs?

This thesis consists of four main chapters. **Chapter 2** presents the paper published in the special issue of Frontiers in Earth Science, for the special research topic: "High-Performance Computing in Solid Earth Geohazards: Progresses, Achievements and Challenges for a Safer World". This paper describes the 3D hybrid numerical model developed to investigate the dynamics of SDGIs. Indeed, this work presents a novel approach by coupling the Lattice Boltzmann Method with a low-diffusive finite difference scheme. The model is validated thanks to comparisons with experimental data and theoretical studies. The model confirmed the experimental observations that suggested a critical Grashof number for the triggering of SDGIs an order of magnitude greater than previous studies. The model also provides some insights into the ground signature of SDGIs, especially in relation to the particle accumulation rate.

Chapter 3 extends the application of the 3D model in order to study the effect of shear on the development of SDGIs. The shear can be generated by both gravitational spreading (gravity currents) and wind advection (air flow arround the volcanic cloud). A quick validation is performed by comparisons of simulations with experimental and theoretical results for the simple spreading of particle-free gravity currents. Then the sedimentation is studied with particle bearing simulations for different spreading velocities and the effect on the cloud geometry is highlighted. Finally, a case study related to a recent volcanic event (i.e. the 2010 eruption of Eyjafjallajökull (Iceland)) has been set up in order to investigate on the effect of wind shear and also on the characteristic ground signature of SDGIs. The main outcome being that SDGIs can produce a bimodal grainsize in the deposit, without aggregation.

In **Chapter 4**, we describe how the Smoluchowski coagulation equation is implemented with the 3D numerical model. The main goal is to study the possible relation between particle aggregation and SDGIs. Some validations are performed comparing with an analytical solution of the Smoluchowski equation for a specific case. Then, we performed a full simulation in order to combine SDGIs and aggregation and we investigate their mutual effects. Specifically, by observing the particle accumulation rate on the ground, we show that aggregation enhances both sedimentation modes (i.e. individual and collective settling). I also demonstrate that the turbulence inside fingers has the potential to cause aggregation.

Finally, the last **Chapter 5** is a methods chapter which describes the two-phase model developed in parallel of the single-phase model presented in the Chapter 2. This model combines the use of the Lattice Boltzmann Method (in order to solve the fluid motion) with lagrangian point particles. Indeed, the model solves the motion equation for each individual particles using the Verlet integration method, allowing accuracy and performance. Additionally, this model includes drag effects which allows a full description of the coupling between fluid and particles. The main outcome is that, given the numerical cost underlying the simulation of a large

number of particles, the use of this model is limited to the study of the dynamics of small structures.

Chapter 2

Modelling settling-driven gravitational instabilities at the base of volcanic clouds using the lattice boltzmann method[1]

2.1 Introduction

Explosive volcanic eruptions can inject large quantities of ash into the atmosphere, generating multiple hazards at various spatial and temporal scales [Blong, 2000; Bonadonna et al., 2021]. Subsequent volcanic ash dispersal and sedimentation can strongly disrupt air traffic [Guffanti et al., 2008; Prata and Rose, 2015], affect inhabited areas [Jenkins et al., 2015; Spence et al., 2005], and impact ecosystems and public health [Gudmundsson, 2011; Wilson et al., 2011]. A good understanding of ash dispersal is critical for effective forecasting and management of the response to these hazards. Modern volcanic ash transport and dispersal models have now reached high levels of sophistication [Bonadonna et al., 2012; Folch, 2012; Folch et al., 2020; Jones et al., 2007; Prata et al., 2021] but do not include all of the physical processes affecting ash transport, such as particle aggregation and settling-driven gravitational instabilities [e.g. Durant, 2015]. Various studies have highlighted the need to take these processes into account by revealing discrepancies between field measurements and numerical models [Scollo et al., 2008], premature sedimentation

[1] Published as: Lemus, J., Fries, A., Jarvis, P. A., Bonadonna, C., Chopard, B., and Lätt, J. (2021). Modelling Settling-Driven Gravitational Instabilities at the Base of Volcanic Clouds Using the Lattice Boltzmann Method. *Front. Earth Sci.* 9. doi:10.3389/feart.2021.713175.

of fine ash leading to bimodal grainsize distributions not only related to particle aggregation [Bonadonna et al., 2011; Manzella et al., 2015; Watt et al., 2015] and significant depletion of airborne fine ash close to the source [Gouhier et al., 2019].

Alongside particle aggregation, settling-driven gravitational instabilities contribute to the early deposition of fine ash with similar outcomes (e.g. grainsize bimodality, premature sedimentation of fine ash). These instabilities generate downward-moving ash columns (fingers) which grow from the base of the ash cloud (Figure 2.1) [Carazzo and Jellinek, 2012; Manzella et al., 2015; Scollo et al., 2017]. This phe-

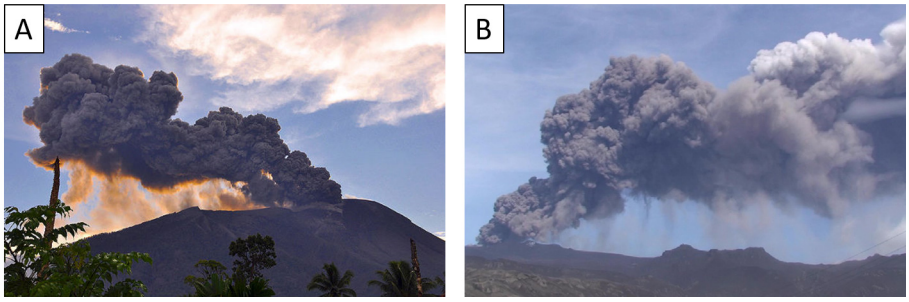

Figure 2.1: Gravitational instabilities observed at the base of a volcanic plume during (A) the 2011 Gamalama eruption. (Credit: AP) and (B) the 2010 eruption of Eyjafjallajökull [Manzella et al., 2015]

nomenon has the potential to enhance the sedimentation rate of fine ash beyond the terminal fall velocity of individual particles, reducing the residence time of fine ash in the atmosphere. Thus, a rigorous understanding of these processes is important in order to build a comprehensive parametrisation that can be included in dispersal models [Bonadonna et al., 2012; Durant, 2015; Folch, 2012; Scollo et al., 2010].

Settling-driven gravitational instabilities should be fully characterized as they also have the potential to impact other ash-related processes. First, the high particle concentration and the turbulence induced by fingers (i.e., the intrinsic turbulence within fingers as well as the shear generated during the downward motion) may enhance particle aggregation by increasing the collision rate of particles [Costa et al., 2010; Scollo et al., 2017]. This process could happen regardless of plume height and atmospheric conditions contrary to ice nucleation for example, which requires specific conditions [Maters et al., 2020]. Second, as settling-driven gravitational instabilities trigger premature deposition of fine ash, this may affect the residence time of other elements in the plume. Indeed, fine ash is involved in some geochemical processes

such as the adsorption of volatiles (e.g., sulphur or halogens) [Bagnato et al., 2013; Zhu et al., 2020]. Considering that the sedimentation rate of volatiles depends on the sedimentation rate of fine ash, the possible premature deposition of volatiles can be explained by the presence of both settling-driven gravitational instabilities and particle aggregation. Finally, fine ash has been shown to play an important role in the volcanic cloud heating through radiative processes that may affect the dynamics [Niemeier et al., 2009; Stenchikov et al., 2021]. Thus, in order to model the large-scale transport of volcanic clouds, there is a need to estimate accurately the amount of fine ash within the cloud, and, therefore, to constrain all size-selective sedimentation processes such as settling-driven gravitational instabilities.

Settling-driven gravitational instabilities occur at the interface between an upper, buoyant particle suspension, e.g., a volcanic ash cloud, and a lower, denser fluid, e.g., the underlying atmosphere [Burns and Meiburg, 2012; Davarpanah Jazi and Wells, 2016; Hoyal et al., 1999; Manzella et al., 2015]. Whilst the initial density configuration is stable, particle settling across the density interface creates a narrow unstable region called the particle boundary layer (PBL) [Carazzo and Jellinek, 2012]. Once this attains a critical thickness [Hoyal et al., 1999], a Rayleigh-Taylor-like instability [Chandrasekhar, 1961; Sharp, 1984] can form at the interface between the PBL and the lower layer, generating finger-like structures which propagate downwards. A further critical condition for instability is that the particle settling velocity V_s must be smaller than the growth rate of gravitational instabilities V_f [Carazzo and Jellinek, 2012]. Thus, the occurrence of the instability enhances the sedimentation rate [Manzella et al., 2015; Scollo et al., 2017]. Alternatively, if V_s is greater than the propagation velocity of fingers V_f, then particles settle individually before a PBL can form and no instability occurs.

Settling-driven gravitational instabilities have been widely studied in laboratory experiments that simulate various natural settings. Many experiments have considered an initial two-layer system, where the particle suspension is initially separated from the underlying denser layer by a removable horizontal barrier [Davarpanah Jazi and Wells, 2016; Fries et al., 2021; Harada et al., 2013; Hoyal et al., 1999; Manzella et al., 2015; Scollo et al., 2017] whilst other experiments have involved injection of

the suspension into a density-stratified fluid at its neutral buoyancy level [Carazzo and Jellinek, 2012; Cardoso and Zarrebini, 2001]. Similar instabilities can also be studied by allowing fine particles to sediment through the free surface between water and air [Carey, 1997; Manville and Wilson, 2004]. Additionally, dimensional analysis has been used to predict that the downward propagation velocity of the generated fingers is given by [Carazzo and Jellinek, 2012; Hoyal et al., 1999]

$$V_f = \left[g \left(\frac{\rho_{PBL} - \rho_f}{\rho_f} \right) \right]^{\frac{2}{5}} \left[\frac{\pi V_s \delta_{PBL}^2}{4} \right]^{\frac{1}{5}}, \tag{2.1}$$

where ρ_{PBL} is the PBL bulk density, ρ_f the underlying fluid density, $g = 9.81$ m.s^{-2} the gravitational acceleration and δ_{PBL} the PBL thickness, which by analogy with thermal convection [Turner, 1973] is taken to be [Hoyal et al., 1999]

$$\delta_{PBL} = \left(\frac{Gr_c \nu^2}{g'} \right)^{\frac{1}{3}}, \tag{2.2}$$

where $g' = g\left(\rho_{PBL} - \rho_f\right)/\rho_f$, ν the kinematic viscosity and Gr_c a critical Grashof number (see Table 2E.1 in 2.E for all acronyms and symbols used in this paper). The reduced gravity g' describes the change in the gravitational acceleration due to buoyancy forces. Continuing the analogy with thermal convection, it has been proposed that $Gr_c = 10^3$ [Hoyal et al., 1999], although recent experimental observations suggests $Gr_c \approx 10^4$ may be more accurate [Fries et al., 2021]. Therefore, for known particle and fluid properties, it is possible to predict whether collective settling will occur and fingers subsequently form using the condition $V_f > V_s$ [Hoyal et al., 1999]. According to this relation, the limit between collective and individual settling occurs when $V_f = V_s$. However, the transition is likely to be smooth, with a transitionary regime where both fluid-like and particle-like settling occur at the same time, as suggested by Harada et al. [2013].

For the initial two-layer configuration, Hoyal et al. [1999] also developed a series of analytical mass-balance models predicting the average particle concentration in the lower layer depending on whether the upper and lower layers were convecting or not. In the case of a quiescent upper layer and a convective lower layer (convection initiated by finger propagation), the evolution of the mass of particles in the lower

layer M_2 depends on the balance between the mass flux of particles arriving from the upper layer $\dot{M}_{in}$ and the mass flux of particle leaving by sedimentation $\dot{M}_{out}$

$$\frac{dM_2}{dt} = \dot{M}_{in} - \dot{M}_{out}, \tag{2.3}$$

where t is time. Assuming that $M_2(t) = Ah_2C_2(t)$, where $C_2(t)$ is the average particle concentration in the lower layer, h_2 the lower layer thickness and A the horizontal cross section of the tank, Hoyal et al. [1999] solved this equation using $\dot{M}_{in} = AV_sC_1(0)$, $\dot{M}_{out} = AV_sC_2(t)$ and the initial condition $C_2(0) = 0$. Thus

$$C_2(t) = C_1(0)\left[1 - e^{-\frac{V_s}{h_2}t}\right], \tag{2.4}$$

where $C_1(0)$ is the initial particle concentration in the upper layer.

Further studies of settling-driven gravitational instabilities have taken theoretical approaches, such as using linear stability analyses to predict the growth rate and characteristic wavelengths of the instability at very early stages [Alsinan et al., 2017; Burns and Meiburg, 2012; Yu et al., 2013]. Moreover, various numerical models simulating settling-driven gravitational instability have also been developed [Burns and Meiburg, 2014; Chou and Shao, 2016; Jacobs et al., 2013; Keck et al., 2021; Yamamoto et al., 2015]. Most numerical approaches to this problem have used continuum-phase models, where the coupling between particles and fluid is strong enough to describe them as a single-phase [Burns and Meiburg, 2014; Chou and Shao, 2016; Yu et al., 2014]. This Eulerian description is valid under the assumptions of sufficiently small particles and a large enough number of particles such that they remain fully coupled with the fluid (i.e. the drag force is in equilibrium with the gravitational force). The condition on the particle size can be quantified through the Stokes number [Burgisser et al., 2005; Roche and Carazzo, 2019], one possible definition of which is

$$St = \frac{\rho_p D_p^2 U}{18\mu L}, \tag{2.5}$$

where ρ_p is the particle density, D_p the particle diameter, μ the dynamic viscosity and U and L characteristic velocity and length scales of the flow. For $St < 1$, the particles and fluid can be considered coupled and, providing there are enough

particles, the continuum approach is valid.

The Eulerian description can be extended to multiple phases in order to simulate their interaction (e.g., gas-liquid interaction) using adaptive mesh refinements to resolve the phase interfaces [Jacobs et al., 2013]. However, for large particle diameters and small particle volume fractions, collective behaviour no longer occurs and the continuum-phase method cannot be applied. In this case, there is a need to explicitly model particle motion, taking the drag force into consideration [Chou and Shao, 2016; Yamamoto et al., 2015].

This paper presents an innovative method to implement a continuum model by coupling the Lattice Boltzmann Method (LBM) with a low-diffusivity finite difference (FD) scheme. This model takes advantage of the LBM capabilities to simulate complex flows through uniform grids and thus, the ease of coupling with finite difference methods. This hybrid model has been validated by comparing the results with those from linear stability analysis and laboratory experiments [Fries et al., 2021]. The validated model then allows us to gain new insights into the fundamental processes by exploring experimentally-inaccessible regions of the parameter space. We first describe the general framework and governing equations that describe settling-driven gravitational instabilities, then the configuration of the validatory experiments to which we apply the model. Next, we propose a numerical strategy involving a hybrid model in order to solve the system of equations. We then go on to present the linear stability analysis before finally describing and discussing the results of our simulations.

2.2 Methods

2.2.1 Problem formulation

The model consists of a two-way coupling between fluid momentum, fluid density, and particle volume fraction, based on the assumption that the particle suspension can be represented by a continuum concentration field. Moreover, particles have no inertia (drag force in equilibrium with the gravitational force) such that the forcing term in the fluid momentum equation is equivalent to a buoyant force term

(Boussinesq approximation), which depends on the particle volume fraction $\phi(\vec{x},t)$ [Burns and Meiburg, 2014; Chou and Shao, 2016; Yu et al., 2014]. $\phi(\vec{x},t)$ satisfies the advection-diffusion-settling equation

$$\frac{\partial\phi}{\partial t}+\vec{\nabla}.[\phi(\vec{u}_f-V_s\vec{e}_z)]=D_c\nabla^2\phi, \tag{2.6}$$

where $\vec{u}_f(\vec{x},t)$ is the fluid velocity, D_c the particle diffusion coefficient, $\vec{e_z}$ the vertical unit vector and $\vec{x}=(x,y,z)$ the position coordinate. The particle settling velocity V_s can be fixed or allowed to be a function of other parameters. Its formulation will be set later according to the assumptions of the flow configuration. The fluid is considered incompressible meaning $\vec{\nabla}.\vec{u}_f=0$. Thus, equation 2.6 becomes

$$\frac{\partial\phi}{\partial t}+(\vec{u}_f-V_s\vec{e}_z).\vec{\nabla}\phi-\phi\vec{\nabla}.(V_s\vec{e}_z)=D_c\nabla^2\phi. \tag{2.7}$$

The particle settling velocity depends on the ambient fluid density ρ, which in turn depends on any transported density-altering properties, such as temperature or the concentration of a chemical species, e.g., the sugar in our validatory experiments [Fries et al., 2021]. We incorporate the effect of a single density-altering property on the fluid density through a classical advection-diffusion equation

$$\frac{\partial\rho(\rho_0,S)}{\partial t}+\vec{u}_f.\vec{\nabla}\rho(\rho_0,S)=D_s\nabla^2\rho(\rho_0,S), \tag{2.8}$$

where ρ_0 is a reference density of the carrier fluid, S the density-altering quantity (temperature or concentration), and D the associated diffusion coefficient. Additionally, under the Boussinesq approximation, we assume that the density depends linearly on S. The fluid momentum is modelled with the incompressible Navier-Stokes momentum equation

$$\frac{\partial\vec{u}_f}{\partial t}+(\vec{u}_f.\vec{\nabla})\vec{u}_f=-\frac{1}{\rho_0}\vec{\nabla}p+\nu\nabla^2\vec{u}_f+\vec{F}, \tag{2.9}$$

where p is the pressure and $\vec{F}$ the buoyant body force term. We complete the system of equations by taking this force term to be a function of ϕ and ρ

$$\vec{F} = \left[\left(\frac{\rho_p - \rho_0}{\rho_0} \right) \phi + \left(\frac{\rho}{\rho_0} - 1 \right) (1 - \phi) \right] \vec{g}. \tag{2.10}$$

The system of equations presented so far assumes that all particles are of uniform size. In order to generalise to systems with polydisperse particle size distributions, we consider N different particle concentration fields ϕ_i, where each one is associated with a different size class and individually satisfies equation 2.7. Furthermore, the body force term becomes

$$\vec{F} = \left[\left(\frac{\rho_p - \rho_0}{\rho_0} \right) \phi_{tot} + \left(\frac{\rho}{\rho_0} - 1 \right) (1 - \phi_{tot}) \right] \vec{g} \tag{2.11}$$

where

$$\phi_{tot} = \sum_{i=1}^{N} \phi_i. \tag{2.12}$$

2.2.2 Flow configuration and experiment description

Full details of the validatory laboratory experiments can be found in Fries et al. [2021] but we summarise the essential details here. The experiments are performed in a configuration identical to that of Manzella et al. [2015] and Scollo et al. [2017] (Figure 2.2) and consist of a water tank divided into two horizontal layers, initially separated by a removable barrier. The upper layer is an initially mixed particle suspension, which represents the ash cloud, and the lower layer is a denser sugar solution, analogue to the underlying atmosphere. The particles are spherical glass beads with a median diameter of 41.5 $\pm$ 0.5 μm (measured using laser diffraction with a Bettersizer S3 Plus) and a density ρ_p of 2519.4 $\pm$ 0.09 kg/m^3 (measured using helium pycnometry UltraPyc 1200e), and are sufficiently small to be well-coupled with the fluid, whilst the initial particle concentration $C_1(0)$ of the upper layer is varied from 1 to 10 g/l i.e. for volume fractions from 3.97×10^{-4} to 3.97×10^{-3} (see Table 2.1 for the conversion to particle volume fraction ϕ_0). The lower layer density is kept constant at $\rho_f = 1008.4$ kg/m^3 (corresponding to a sugar concentration of $S_0 = 35$ g/l), always ensuring an initially stable density configuration.

Before starting an experiment, the upper layer is manually and carefully stirred

using a brush. Then the barrier separating the two layers is immediately removed, allowing particle settling through the interface. A PBL subsequently forms and finger formation is initiated. Experiments are illuminated from the side of the water tank with a planar laser and recorded with a high-contrast camera. We measure the vertical finger velocity by tracking the progression of the finger front with time. Additionally, Planar Laser Induced Fluorescence (PLIF) [Crimaldi, 2008; Koochesfahani, 1984] and particle imaging are used to quantify the spatial distribution of the fluid phase density and particle concentration.

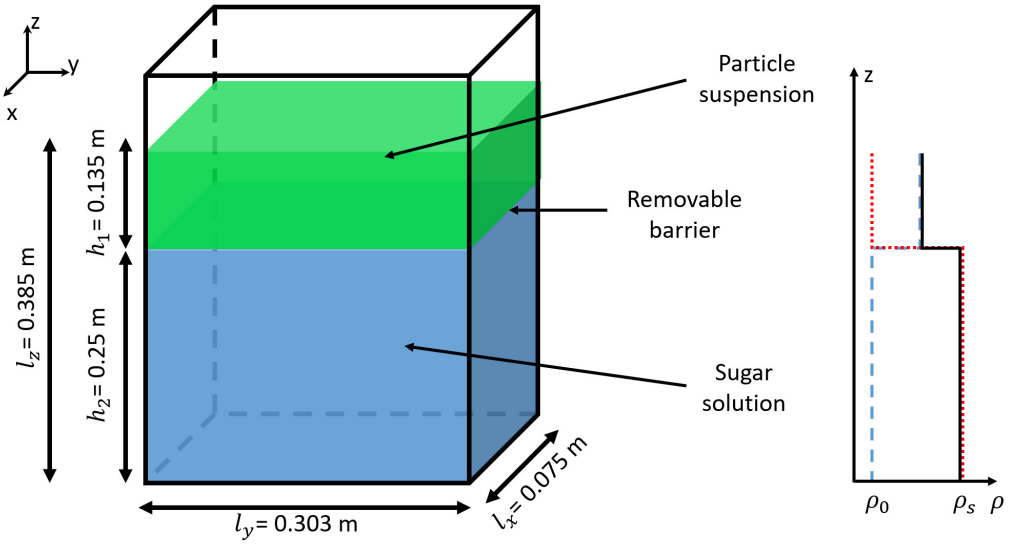

Figure 2.2: Experimental setup used by Fries et al. [2021] and the initial density profiles associated with the contributions from particles (blue dashed) and sugar (red dotted), as well as the bulk density (black solid). The density of fresh water is given by ρ_0

Application to flow configuration

We apply the general system of equations presented in section 2.2.1 to the configuration of the validatory experiments. The particles are spherical and sufficiently small that their terminal settling velocity in water is given by the Stokes velocity [Stokes, 1851]

$$V_s = \frac{D_p^2 g \left[\rho_p - \rho\left(S\right)\right]}{18\mu}, \tag{2.13}$$

where S is the sugar concentration and $\rho = \rho_0 \left(1 + \alpha S\right)$, with α the sugar expansion coefficient.

Initial particle concentration (g/l)	Volume fraction	Particle diameter (μm)	z_H (mm)	z_ϕ (mm)	z_s (mm)
1	3.97×10^{-4}	40	12.11	2.59	0.67
2	7.94×10^{-4}	40	7.37	2.20	0.63
3	1.19×10^{-3}	40	5.47	1.99	0.61
4	1.59×10^{-3}	40	5.01	1.99	0.61
5	1.98×10^{-3}	40	4.20	1.84	0.60
6	2.38×10^{-3}	40	3.45	1.72	0.59
7	2.78×10^{-3}	40	3.25	1.70	0.60
8	3.18×10^{-3}	40	3.17	1.72	0.61
9	3.57×10^{-3}	40	3.01	1.71	0.62
10	3.97×10^{-3}	40	2.54	1.58	0.61
3	1.19×10^{-3}	25	-	-	-
3	1.19×10^{-3}	55	-	-	-
3	1.19×10^{-3}	70	-	-	-
3	1.19×10^{-3}	85	-	-	-
3	1.19×10^{-3}	100	-	-	-
3	1.19×10^{-3}	115	-	-	-
3	1.19×10^{-3}	130	-	-	-
9	3.57×10^{-3}	25	-	-	-
9	3.57×10^{-3}	55	-	-	-
9	3.57×10^{-3}	70	-	-	-
9	3.57×10^{-3}	85	-	-	-
9	3.57×10^{-3}	100	-	-	-
9	3.57×10^{-3}	115	-	-	-
9	3.57×10^{-3}	130	-	-	-
9	3.57×10^{-3}	145	-	-	-
9	3.57×10^{-3}	160	-	-	-

Table 2.1: List of simulations performed. All the simulations have been performed using an initial lower layer fluid density of 1008.4 kg/m^3. z_H, z_ϕ and z_s are parameters used in the linear stability analysis (LSA) in order to describe the different base states associated with the particle and sugar profiles in equations 2.39 and 2.40. The LSA has been performed only for a constant particle size of 40 μm in order to study the effect of the particle volume fraction.

The diluted system ensures the Boussinesq assumption is valid as the ratio $\Delta\rho/\rho_0$ is much less than 1 (about 6×10^{-3} for the highest initial particle volume fraction). We simulate the solid walls of the tank around our domain with a no-slip boundary condition for the fluid velocity. No-flux boundary conditions are employed for ϕ and ρ to avoid any flux of particles or sugar across the walls. Thus we impose

$$\frac{\partial \phi}{\partial x} = 0, \tag{2.14}$$

and

$$\frac{\partial \rho}{\partial x} = 0, \tag{2.15}$$

on the walls. Furthermore, we define the following initial states for ϕ and S

$$\phi\left(\vec{x}, t=0\right) = \begin{cases} 0 & \text{for} \quad z < H_0 \\ \phi_0 & \text{for} \quad z > H_0 \end{cases} \tag{2.16}$$

and

$$S\left(\vec{x}, t=0\right) = \begin{cases} S_0 & \text{for} \quad z < H_0 \\ 0 & \text{for} \quad z > H_0 \end{cases} \tag{2.17}$$

where ϕ_0 and S_0 are the initial particle volume fraction in the upper layer and initial sugar concentration in the lower layer, respectively, and H_0=0.25 m the initial height of the interface ($z = 0$ corresponds to the base of the tank). We also add a small perturbation to the particle volume fraction field in order to initiate the instability. Without this numerical perturbation, even though the PBL is unstable, the numerical system would remain at its equilibrium state and the perturbation is needed to slightly move the system away from the equilibrium and initiate the instability. Applying the perturbation at each numerical node ensures we can reproduce the shortest-possible wavelength modes of the instability. Finally, the system is initially stationary so $\vec{u_f}\left(\vec{x}, t=0\right) = \vec{0}$.

2.2.3 Numerical methods

The 3D numerical model is implemented using a hybrid strategy where a LBM solves the fluid motion and is coupled with finite difference schemes that solve the advection-diffusion equations for ϕ and S.

Fluid motion

The LBM is an efficient alternative to conventional Computational Fluid Dynamics (CFD) methods that explicitly solve the Navier-Stokes equations at each node of a discretised domain [Chen and Doolen, 2010; He and Luo, 1997]. It is a well-established approach for simulating complex flows, including multiphase fluids [Leclaire et al., 2017] and thermal and buoyancy effects [Noriega et al., 2013; Parmigiani et al., 2009]. The LBM originates from the kinetic theory of gases and provides a description of gas dynamics at the mesoscopic scale. This scale exists between the microscopic, which describes molecular dynamics, and the macroscopic, which gives a continuum description of the system with variables such as density and velocity. Thereby, the mesoscopic scale considers a probability distribution function of molecules described by the Lattice Boltzmann equation. This model reduces the process to two main steps: streaming (i.e., displacement of populations between consecutive calculation nodes), and collision (i.e., interaction of populations on a node). The Bhatnagar-Gross-Krook (BGK) model [Bhatnagar et al., 1954] provides a simple collision process based on a fundamental property given by kinetic theory which describes gas motion as a perturbation around the equilibrium state. Then, the LBM-BGK model solves, for the particle population f_i, which are a discrete representation of the probability distribution function, the equation

$$f_i\left(\vec{x}+\vec{c_i}\delta t, t+\delta t\right) = -\frac{\delta t}{\tau}\left(f_i\left(\vec{x},t\right) - f_i^{eq}\right), \tag{2.18}$$

where δt is the time step, $f_i^{eq}\left(\rho, \vec{u_f}\right)$ the equilibrium distribution function, τ the relaxation time associated with the flow viscosity and $\vec{c_i}$ the local particle velocity. The LBM is applied to specific types of lattices that describe how the populations move through the calculation nodes [Kruger et al., 2017]. These types of lattice are commonly summarized in the form $DrQm$ where r denotes the dimension of the system and m the number of directions in which populations can propagate.

Figure 2.3 shows the scheme D3Q19 used for our 3D simulations and the associated set of local velocities.

The macroscopic fluid state is described through the usual macroscopic variables such as density, velocity and kinematic viscosity. These variables are related to the

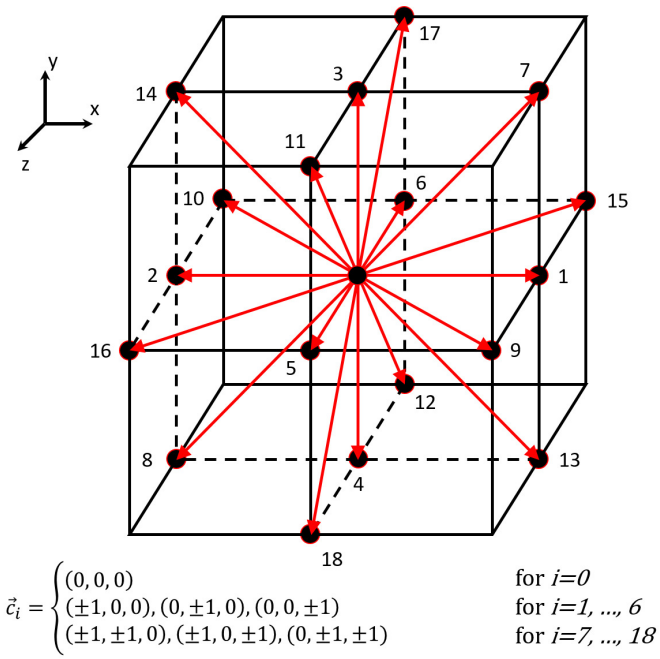

Figure 2.3: Depiction of the D3Q19 lattice. The red arrows show the different possible directions of propagation. The associated local velocities are summarised in the velocity set $\vec{c_i}$.

moments of the populations f_i through

$$\rho = \sum_i f_i, \tag{2.19}$$

and

$$\rho \vec{u_f} = \sum_i f_i \vec{c_i}, \tag{2.20}$$

whilst the kinematic viscosity controls the relaxation to equilibrium through the relaxation time

$$\tau = \frac{\nu}{c_s^2} + \frac{\delta t}{2}, \tag{2.21}$$

The variable c_s^2 is commonly called the speed of sound and is equal to $(1/\sqrt{3})(\delta x/\delta t)$ where δx is the spatial step. However, the classical LBM-BGK model described above does not take into account any forcing term. One way to include forcing is to rewrite equation 2.18 as

$$f_i\left(\vec{x}+\vec{c_i}\delta t, t+\delta t\right) = -\frac{\delta t}{\tau}\left(f_i\left(\vec{x},t\right) - f_i^{eq}\right) + F_i\delta t, \tag{2.22}$$

where F_i is the forcing term, which can be expressed by a power series in the local particle velocities, and the equilibrium distribution is now given by $f_i^{eq} = f_i^{eq}\left(\rho, \vec{u_f^*}\right)$, where $\rho\vec{u_f^*} = \sum_i f_i\vec{c_i} + b\vec{F}\delta t$. The determination of the coefficient b, as well as the power series expansion of F_i, are described by Guo et al. [2002]. Finally, no-slip boundary conditions in the LBM, to simulate walls for example, can be implemented using the classical $bounce-back$ boundary condition [Kruger et al., 2017] where the populations arriving on a wall node during the streaming step are simply reflected back to their previous nodes.

Transport of particles and other density-altering quantities

The particles and other density-altering quantities are described by continuum fields that follow an advection-diffusion law coupled with the fluid motion as simulated with the LBM. The numerical solution of the advection equation is particularly challenging for methods which, like ours, are Eulerian (i.e., mesh-based). Indeed, such methods exhibit numerical diffusion which may strongly reduce model accuracy and, in some cases, even exceed the amplitude of the actual, physical diffusion term. The lack of physical diffusion in our problem and the presence of sharp interfaces restrict our ability to solve the advection equations with the LBM. In fact, the advection-diffusion equation can be solved by the LBM with a BGK approach in analogous fashion to the fluid motion by modifying the equilibrium distribution and the relaxation time to depend on the diffusion coefficient D rather than ν

$$\tau = \frac{D}{c_s^2} + \frac{\delta t}{2}. \tag{2.23}$$

However, a stability condition for a LBM-BGK algorithm is $\tau/\delta t = 1/2$. Thus, since the problem is convection dominated, the low diffusion coefficient ($D \ll 1$) drives the model towards the stability limit, introducing strong numerical errors near sharp concentration gradients [Hosseini et al., 2017]. For this reason, we solve the advection term using two finite-difference schemes which are selected depending

on the required accuracy: the classical first-order upwind finite difference and the third-order Weighted Essentially Non Oscillatory (WENO) finite difference scheme [Jiang and Shu, 1996; Liu et al., 1994].

Coupling the LBM with an upwind finite difference scheme allows us to avoid the stability problem. First-order FD schemes however, still suffer from the problem of numerical diffusion due to the truncation error associated with terminating the Taylor expansion after the first spatial derivative. The induced numerical error NE for the convective term in the advection-diffusion equation is given by

$$NE \sim u\frac{\delta x}{2}\frac{\partial^2 \phi}{\partial x^2}, \tag{2.24}$$

where u is the transport velocity. NE acts like an additional diffusion term because of the presence of the second-order derivative (a quantitative estimate of the numerical diffusion for both first order and WENO procedure is available in Appendix 2.B). The numerical diffusion associated with the solution of S is negligible due to the low fluid velocity and consequently the use of the first order FD scheme does not significantly affect the accuracy. However, in the solution of ϕ, which includes an additional velocity contribution due to the settling, the truncation error associated with the first-order scheme becomes non-negligible. Whilst decreasing δx would reduce numerical diffusion, we would require an unpractically small value in order to get a sufficiently accurate solution. Additionally, simply increasing the order of the scheme introduces dispersion (spurious oscillations) near regions of high gradient, according to the Godunov theorem [Godunov, 1954, 1959]. Therefore, we choose here to implement the low diffusive WENO procedure for the solution of ϕ, thus achieving a stable and high-resolution scheme without dispersion.

Further information on how we discretise the convective term in the advection-diffusion equation using the first order upwind and the third order WENO finite difference schemes is detailed in Appendix 2.A.

Numerical implementation

Our model is implemented using *Palabos* (Parallel Lattice Boltzmann Solver), a Computational Fluid Dynamics (CFD) solver based on the Lattice Boltzmann Method

and developed by the Scientific Parallel Computing group of the Computer Science Department, University of Geneva [Latt et al., 2020]. *Palabos* is designed to perform calculations on massively parallel computers, thus allowing very high spatial resolutions in order to accurately simulate the finger dynamics.

2.3 Linear stability analysis

In order to validate our model, we compare the early-time simulated behaviour against predictions from linear stability analysis (LSA). LSA is applied to the onset of the physical instability at the interface between layers of different particle concentration. It involves defining a field equation-satisfying base state for each of the unknown fields in a problem and then applying an infinitesimally small perturbation to each of these fields. The equations are then expanded to linear order in the perturbation, with higher order terms assumed to be negligible. By assigning the perturbation to have the form of a complex waveform, the system of equations reduces to an eigenvalue problem, which can be solved to determine which wavelengths will grow or decay [Chandrasekhar, 1961]. In this section, we assume that the system is invariant under translation in the x-y plane, thus reducing the analysis to a 2D problem. We strongly follow the procedure described by [Burns and Meiburg, 2012] in order to solve our problem.

2.3.1 Nondimensionalisation

We nondimensionalise our system of equations by defining

$$l^c = \left(\frac{\nu^2}{g}\right)^{\frac{1}{3}}, \tag{2.25}$$

$$t^c = \left(\frac{\nu}{g^2}\right)^{\frac{1}{3}}, \tag{2.26}$$

and

$$p^c = \rho_0 \left(\nu g\right)^{\frac{2}{3}}, \tag{2.27}$$

where l^c, t^c and p^c are characteristic quantities. We also define the dimensionless parameters

$$S^* = \alpha S_0, \tag{2.28}$$

$$\phi^* = \phi_0, \tag{2.29}$$

$$Fr = \frac{1}{t^c}\sqrt{\frac{l^c}{g}}, \tag{2.30}$$

and

$$Sc_i = \frac{\nu}{D_i}, \tag{2.31}$$

noting that Fr is a Froude number and Sc_i are Schmidt numbers. Furthermore, the stream function ψ is defined such that $\vec{u_f} = (\partial\psi/\partial z, -\partial\psi/\partial x)$ and the vorticity as $\vec{\omega} = \vec{\nabla}\times\vec{u_f}$. Then, applying the characteristic quantities to the vorticity formulation and equations (2.7-2.9), we obtain the dimensionless system (for the rest of the analysis, all the symbols used represent dimensionless quantities)

$$\omega = -\nabla^2\psi, \tag{2.32}$$

$$\frac{\partial\omega}{\partial t} + \left(\vec{u_f}.\vec{\nabla}\right)\omega = \nabla^2\omega + \frac{\partial\phi}{\partial y}\frac{\phi^*}{Fr^2}\left[SS^* - \left(\frac{\rho_p - \rho_0}{\rho_0}\right)\right] - \frac{\partial S}{\partial y}\frac{S^*}{Fr^2}\left(1 - \phi\phi^*\right), \tag{2.33}$$

$$\frac{\partial S}{\partial t} + \vec{u_f}.\vec{\nabla}S = \frac{1}{Sc_s}\nabla^2 S, \tag{2.34}$$

and

$$\frac{\partial\phi}{\partial t} + \left(\vec{u_f} - V_s\vec{e_z}\right).\vec{\nabla}\phi = \frac{1}{Sc_c}\nabla^2\phi. \tag{2.35}$$

Note that here we have neglected the term $-\phi\vec{\nabla}.\left(V_s\vec{e_z}\right)$ in equation 2.7 assuming

that the fluid density variation across the interface is sufficiently small that it does not affect the particle settling velocity.

2.3.2 Variable expansion and eigenvalue problem

We linearise the system of equations by expanding each variable in terms of a base state and a perturbation

$$\varphi\left(y,z,t\right)=\bar{\varphi}\left(z\right)+\varphi'\left(y,z,t\right), \tag{2.36}$$

where $\varphi\left(y,z,t\right)=\{\psi,\omega,\phi,S\}$, $\bar{\varphi}\left(z\right)=\{\bar{\psi},\bar{\omega},\bar{\phi},\bar{S}\}$ the associated base state and $\varphi'\left(y,z,t\right)=\{\psi',\omega',\phi',S'\}$ the perturbation. We choose the following base states

$$\bar{\psi}=0, \tag{2.37}$$

$$\bar{\omega}=0, \tag{2.38}$$

$$\bar{\phi}\left(z,t\right)=\frac{1}{2}\left[1+\mathrm{erf}\left(\frac{z}{z_{\phi}}\right)\right], \tag{2.39}$$

$$\bar{S}\left(z,t\right)=\frac{1}{2}\left[1-\mathrm{erf}\left(\frac{z-V_{s}t}{z_{S}}\right)\right], \tag{2.40}$$

where $z_{\phi}\left(T\right)$ and $z_{S}\left(T\right)$ are coefficients fitted in order to have similar base states to the profiles observed in the simulations prior to the onset of the instability which starts growing at the time T. We choose these base states to represent the initial conditions of the validatory experiments; equations 2.37, 2.38 ensure an initially-zero velocity field whilst the error functions in equations 2.39, 2.40 ensure sigmoidal distributions for S and ϕ.

Solutions for the perturbation are assumed to have the form of normal modes

$$\varphi'\left(y,z,t\right)=\hat{\varphi}\left(z\right)\exp\left(iky+\sigma t\right), \tag{2.41}$$

where $\hat{\varphi}\left(z\right)$ is the perturbation amplitude, k the wavenumber and σ the instability

growth rate. The linearised system of equations is then formulated in matrix form so that the problem is reduced to the eigenvalue problem $K\vec{x} = \sigma W\vec{x}$ where

$$\vec{x} = \begin{pmatrix} \hat{\psi}(z) \\ \hat{\omega}(z) \\ \hat{S}(z) \\ \hat{\phi}(z) \end{pmatrix}, \tag{2.42}$$

and, in a reference frame moving downward at V_s, the matrices K and W are given by

$$K = \begin{pmatrix} M & I & 0 & 0 \\ 0 & M - V_s D_z & -ik\frac{S^*}{Fr^2}\left(1 - \bar{\phi}\phi^*\right) I & ik\frac{\phi^*}{Fr^2}\left[SS^* - \left(\frac{\rho_p - \rho_0}{\rho_0}\right)\right] I \\ ik\frac{d\bar{S}}{dz} I & 0 & \frac{1}{Sc_S} M - V_s D_z & 0 \\ ik\frac{d\bar{\phi}}{dz} I & 0 & 0 & \frac{1}{Sc_c} M \end{pmatrix}, \tag{2.43}$$

and

$$W = \begin{pmatrix} 0 & 0 & 0 & 0 \\ 0 & I & 0 & 0 \\ 0 & 0 & I & 0 \\ 0 & 0 & 0 & I \end{pmatrix}, \tag{2.44}$$

where $D_z = \partial/\partial z$, $M = -k^2 + D_z^2$ and I is the identity operator.

The eigenvalues σ determine the stability of the system:

- If all the eigenvalues have negative real parts, the system remains stable
- If at least one eigenvalue has a positive real part, the system is unstable.

In order to solve the eigenvalue problem, the spatial derivatives are discretised using the linear rational collocation method with a grid transformation allowing a fine resolution around narrow interfacial regions [Baltensperger and Berrut, 2001; Berrut and Mittelmann, 2004].

The key result of the LSA is the dispersion relation between σ and k. Figure 2.4 presents the growth rate as a function of the wavenumber, for different initial particle volume fractions. The parameters for the different base states used to produce these curves are summarised in the Table 2.1. We use this result in Section 2.4.1 in order to compare the predictions of the LSA with the results of our numerical model.

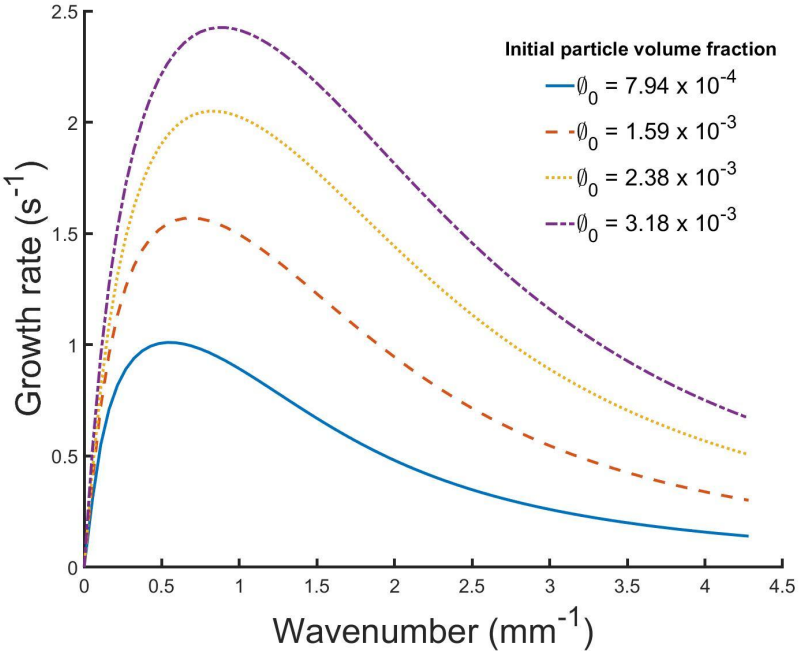

Figure 2.4: Dispersion relation obtained from LSA for several initial particle concentrations.

2.4 Results

We validate our numerical model by comparing the results with predictions from LSA and experimental observations. The LSA predicts the growth rates of different perturbation wavenumbers during the very early stage of the instability, which can be compared with the spectrum of wavenumbers present in the particle concentration interface in the numerical model. Additionally, the experiments of Fries et al. [2021] employ imaging techniques to measure quantities, such as the particle concentration field and finger velocity, at times beyond the linear regime. Finally, our results are compared with some results of previous analyses on settling-driven gravitational instabilities [Carazzo and Jellinek, 2012; Hoyal et al., 1999].

2.4.1 Comparison of model results with predictions from linear stability analysis

In order to compare our 3D simulations with the 2D linear stability analysis, we consider just the central plane of the simulation domain, i.e., a slice in the (y, z) plane located at $x = l_x/2$ (l_x being the tank depth) (Figure 2.2). We define the front of the particle field to be the lowest position where $\phi = \phi_0/2$ and also define $H(y)$ to be the separation between $z = 0$ and this front. Our study has shown that the front position is only weakly affected when using other possible thresholds, i.e., $\phi_0/10$ or $\phi_0/5$ (relative change $\lesssim 3\%$). Figure 2.5A shows an example of a space-time diagram showing the evolution of $H(y)$ through time. Furthermore, by calculating the Fourier transform $\tilde{H}(k, t)$ of $H(y)$ at different times, we can identify different dominant wavenumbers and their associated amplitudes as shown in the space diagram of the power spectral density (PSD) $\Gamma_H(k, t) = (1/(k_S L_S))\,|\tilde{H}(k, t)|^2$ (Figure 2.5B), where k_S is the sampling wavenumber and L_S the number of samples. We extract the dominant mode and its associated growth rate from $\Gamma_H(k, t)$ and compare the results with the predicted growth rates from LSA. We apply this analysis during a period when the amplitude $|\tilde{H}(k, t)|$ of any given mode does not exceed 40% of its wavelength, thus ensuring we are still in the linear regime [Lewis, 1950].

During the linear regime, we can assume that the growth of the spectral amplitude can be described as [Völtz et al., 2001]

$$|\tilde{H}(k, t)| = |\tilde{H}_i(k)|\exp(\sigma_{sim}(k)\, t), \tag{2.45}$$

with $|\tilde{H}_i(k)|$ the initial amplitude and $\sigma_{sim}(k)$ the instability growth rate as determined from the simulations. Thus, the PSD can be expressed as

$$\Gamma_H(k, t) = \Gamma_{H_i}\exp(2\sigma_{sim}(k)\, t), \tag{2.46}$$

where Γ_{H_i} is the initial spectral density.

At each time step, we extract the PSD and the wavenumber k_{sim} associated with the dominant mode as shown in Figure 2.6. However, we observe that the dominant mode remains at the same wavenumber during instability growth except for three

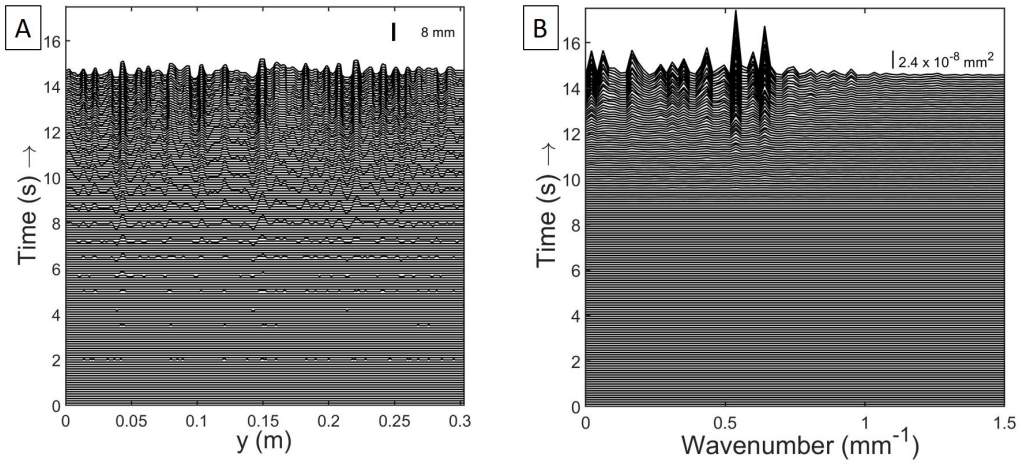

Figure 2.5: (A) Space-time diagram of the particle front height $H(y,t)$. (B) Evolution of the power spectral density of the particle interface over time. Initial particle volume fraction: $\phi_0 = 3.97 \times 10^{-4}$.

cases ($\phi_0 = 1.59 \times 10^{-3}$, 2.38×10^{-3} and 3.97×10^{-3}) where we observed that the dominant mode changed its position in the spectral space. For these simulations only, we have a set of several wavenumbers $k_{sim,i}$, $(i = 1, 2, 3)$ associated with the dominant mode. With the computed PSD of the dominant mode as a function of time $\Gamma_H(k_{sim}, t)$, we apply our exponential fitting (equation 2.46) to determine the growth rate $\sigma_{sim,i}$ (Figure 2.6B). For the simulations which resulted in several values of $k_{sim,i}$ for the dominant mode, we measured the growth rates of each mode $\sigma_{sim,i}$ and found identical values, up to a precision of 5%. Additionally, for each simulation, we find the time T when the instability starts growing, easily identified as the time at which the modal wavenumber becomes non-zero (e.g., in Figure 2.6A this is at approximately 6 s). At this time, we extract the associated vertical profiles of particle and sugar concentration which are used to find the coefficients $z_\phi(T)$ and $z_S(T)$ (equations 2.39-2.40) and thus determine the base states of $\bar{\phi}(z,T)$ and $\bar{S}(z,T)$ (Figure 2.7). We then perform the LSA for each ϕ_0, using the appropriate base states, and obtain a dispersion relation $\sigma = f(k)$. Using this relation, we predict the different growth rates $\sigma = \sigma_{LSA,i}$ associated with $k = k_{sim,i}$ and we compare with $\sigma(k_{sim,i})$ as measured in our simulations. Figure 2.8 shows the comparison between σ_{sim} (black dots) and $\sigma_{LSA,i}$ (red triangles), as predicted from the LSA, for the dominant wave mode. The error bars associated with the simulation data show the uncertainty on the fitted results of σ_{sim} (given by the 95% confidence interval). For

the cases including a moving dominant mode, we plotted the growth rates associated with the different measured wavenumbers. We see that the dependence of the largest value of $\sigma_{LSA,i}$ on the initial particle concentration is in good agreement with the simulated growth rate.

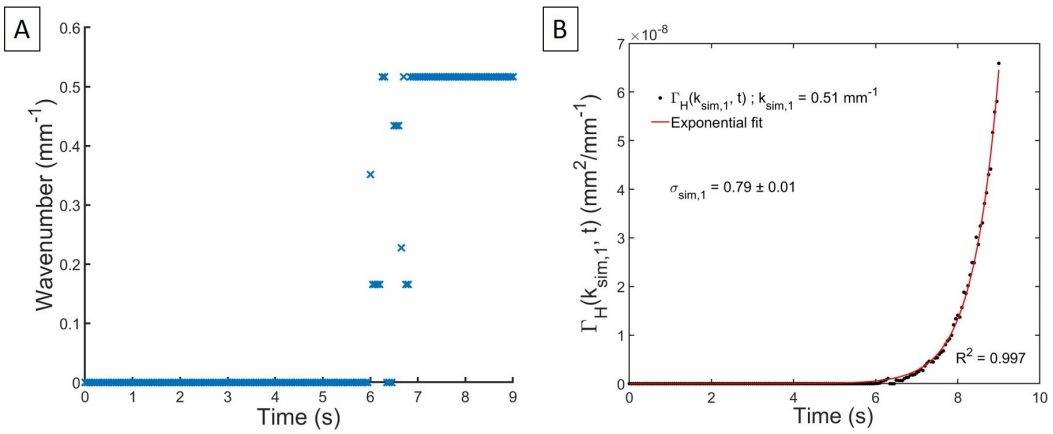

Figure 2.6: (A) Example of dominant wavenumbers extracted from the maximum of the PSD. Initial particle volume fraction $\phi_0 = 7.94 \times 10^{-4}$. (B) Exponential fitting to the temporal evolution of the PSD for the first maximum in (A), $k_{sim,1} = 0.517\, mm^{-1}$.

2.4.2 Comparison with experimental investigations

Figures 2.9A and 2.9B show a qualitative comparison between snapshots taken from experiments [Fries et al., 2021] and simulations (slice in the numerical domain). First, we note that our model is able to qualitatively reproduce the shape and size of fingers, especially their fronts where we observe the formation of lobes and eddies due to the Kelvin-Helmholtz instability [Chou and Shao, 2016]. Second, we provide a quantitative validation of the non-linear regime by comparing our model with experiments, through measurements of the PBL thickness and the vertical finger velocity as functions of the particle volume fraction and size.

Characterisation of the PBL and effect of the initial particle volume fraction on the finger velocity

The bulk density profile ρ_{blk}, derived from the contributions of the particle concentration and sugar profiles, is given everywhere by the relation

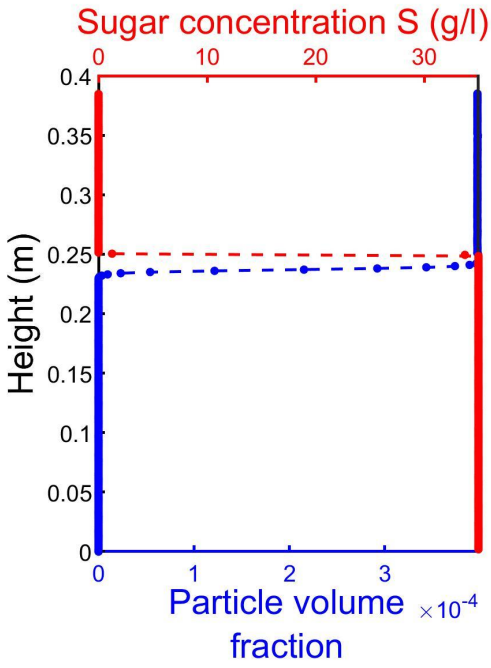

Figure 2.7: Example of LSA base states extracted from the simulations for $\phi_0 = 3.97 \times 10^{-4}$. Dots: profiles extracted from the simulations at $T = 9.55s$ (start of the instability growth). Dotted lines: Fit with equations 2.39 and 2.40. i.e., base states used for the LSA. Blue: particle volume fraction. Red: Sugar concentration.

$$\rho_{blk} = \phi\rho_p + (1-\phi)\,\rho_f. \tag{2.47}$$

Figure 2.10 shows the profiles of ϕ, ρ_f and ρ_{blk} in the numerical simulations as well as in the experiments 8 seconds after the barrier removal for the same initial conditions ($\phi_0 = 3.18 \times 10^{-3}$). Despite some differences associated with limitations in achieving idealised initial conditions in the experiments, as well as the experimental data collection method, it can be seen that, in both the model and the experiments, there is an increase of the bulk density below the initial interface, owing to the particle front moving downwards. This zone of excess density corresponds to the unstable PBL from which instabilities occur, generating fingers. To calculate the finger velocity using the same method as in experiments, we extract slices from the 3D numerical domain and manually track the fronts of several fingers (6 to 15 fingers) from when they become fully developed until just before they become too diluted. For each simulation with different volume fraction, we then average the velocity of all tracked fingers and the uncertainty is the standard deviation associated

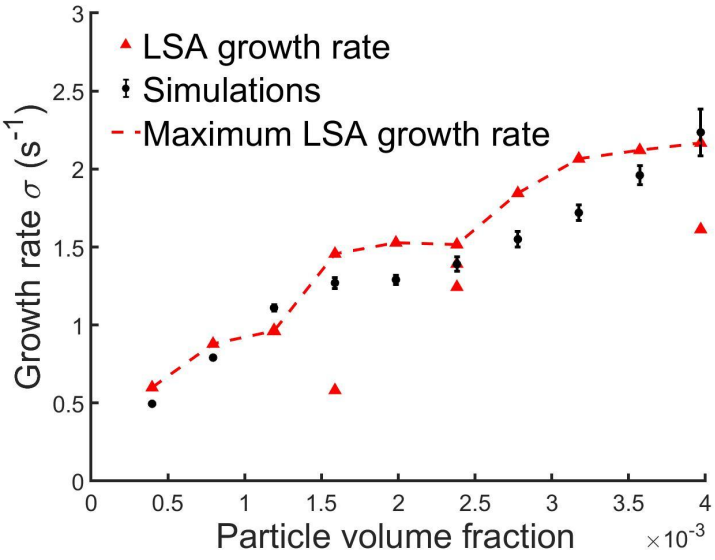

Figure 2.8: Comparison of the instability growth rate measured in the simulations (black circles) and that predicted by the linear stability analysis (red triangles).

with each set of fingers used for the measurements. Figure 2.11A shows the average finger velocity V_f as a function of ϕ_0, for both experiments [Fries et al., 2021] and simulations. Our simulation results are in good agreement with the experimental measurements and highlight that the increase of V_f with ϕ_0 is non-linear.

By analogy with thermal convection, it has previously been assumed that $Gr_c = 10^3$ [Hoyal et al., 1999], but this is only an order of magnitude estimate and its application to settling-driven gravitational instabilities remains uncertain [Fries et al., 2021]. Figure 2.11A shows good agreement between the simulations and equation 2.1 for a fitted Gr_c of $1.2 \pm 0.4 \times 10^4$ ($R^2 = 0.92$), which is an order of magnitude higher than the value previously assumed [Carazzo and Jellinek, 2012; Hoyal et al., 1999]. This agrees reasonably with the experiments, where the best fit is obtained for $Gr_c = 1.9 \pm 0.7 \times 10^4$ ($R^2 = 0.75$), but the experimental results show more scatter. However, neither of these fits have completely satisfactory values of R^2. We therefore further investigate the applicability of equation 2.1 by examining the dependence of V_f on ϕ_0, assuming a more general power law of the form $V_f \propto \phi_0^q$. According to equation 2.1, $q = 4/15 \approx 0.27$. However, from the experiments, we obtain $q = 0.50 \pm 0.16$ (with $R^2 = 0.95$) while for our simulations $q = 0.37 \pm 0.08$ (with $R^2 = 0.98$). Here Gr_c, q and their associated uncertainties have been calcu-

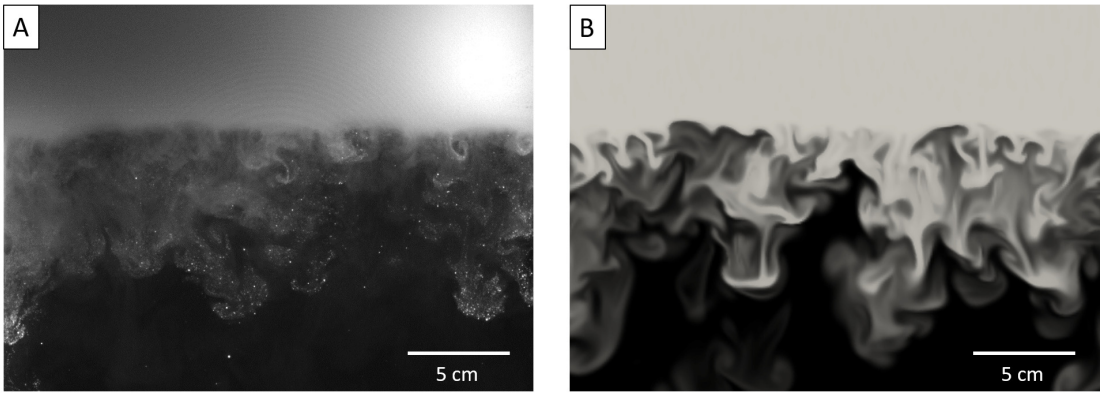

Figure 2.9: Settling-driven gravitational instabilities observed 19.5 s after the barrier removal (A) in the laboratory [Fries et al., 2021] and (B) in numerical simulations. Particle size: 40 μm and initial volume fraction : $\phi_0 = 2.78 \times 10^{-3}$.

lated accounting for the uncertainty on V_f with the SciPy (Python-based ecosystem) procedure *scipy.optimize.curve_fit*.

Effect of particle size on the finger vertical velocity

Since gravitational instabilities cause particles to sediment faster than their settling velocity, it is of interest to explore the transition from collective to individual settling, since this has implications for which grain sizes may prematurely sediment from a volcanic cloud [Scollo et al., 2017]. Figure 2.11B shows the effect of particle size on the finger velocity as measured from the model, for two different initial volume fractions, in the experiments configuration (i.e. in the tank filled with water). We clearly observe two regimes:

- For particle sizes less than or equal to 115 μm (for $\phi_0 = 1.19 \times 10^{-3}$) and 145 μm (for $\phi_0 = 3.57 \times 10^{-3}$), we observe fingers, with the finger velocity increasing with particle size.
- For greater particle sizes, no fingers are observed to form.

From our simulations, we constrain the transition between the two regimes to occur at a critical particle diameters around 115 μm and 145 μm respectively for $\phi_0 = 1.19 \times 10^{-3}$ and $\phi_0 = 3.57 \times 10^{-3}$. We also note that this size range corresponds to the particle size at which the Stokes velocity exceeds the predicted finger velocity. This result agrees with the experimental observations of Scollo et al. [2017], who

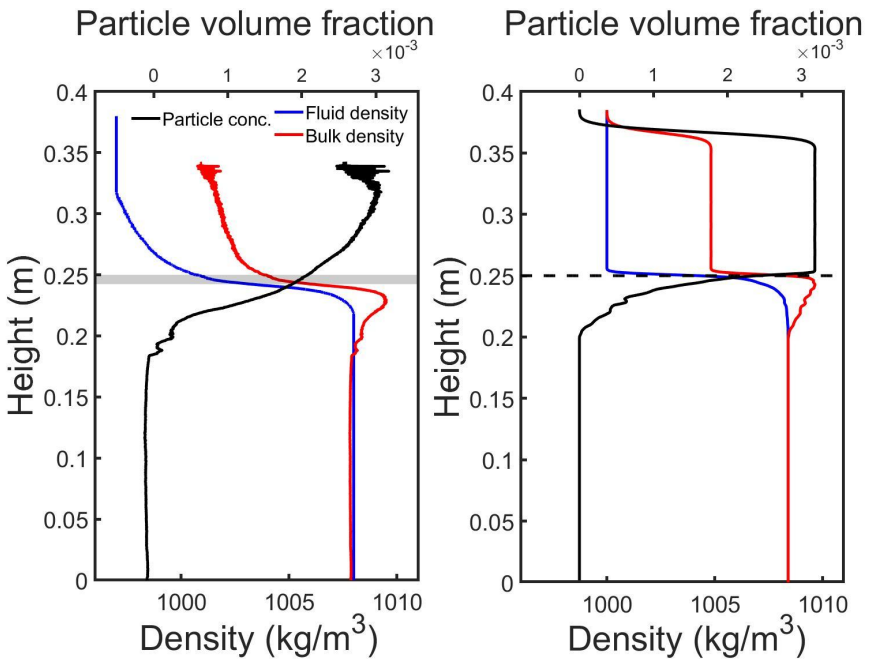

Figure 2.10: Density profile after 8 seconds for experiments (left) [Fries et al., 2021] and simulations (right) with $\phi_0 = 3.18 \times 10^{-3}$ and a particle size of 40 μm.

observed that no fingers form for particles with diameter larger than $\sim$ 125 μm with in initial particle volume fraction of $\phi_0 = 1.19^{-3}$. We also compare the dependence of V_f on the particle diameter with that predicted by equation 2.1 and find a best fit for $Gr_c = 7.6 \pm 3.6 \times 10^3$ (with $R^2 = 0.91$) and $Gr_c = 2.7 \pm 0.8 \times 10^4$ (with $R^2 = 0.87$) respectively for the two initial volume fractions (Figure 2.11B). We observe again that the values for the fitted Gr_c are greater than the one proposed by Hoyal et al. [1999] by analogy with thermal convection, whilst they also substantially differ from one another. We therefore also fit the results to a power law $V_f \propto D_p^{\eta}$ finding $\eta = 0.38 \pm 0.13$ ($R^2 = 0.94$) and $\eta = 0.42 \pm 0.10$ ($R^2 = 0.88$) respectively to the two volume fractions which is in very good agreement with the analytical formulation (equation 2.1) that suggests $\eta = 0.4$.

Particle mass flux, particle concentration in the lower layer and accumulation rate

Given the excellent agreement between the proposed model and both LSA analysis and analogue experiments described above, we take advantage of having 3D data from the numerical simulations in order to extract other parameters which are

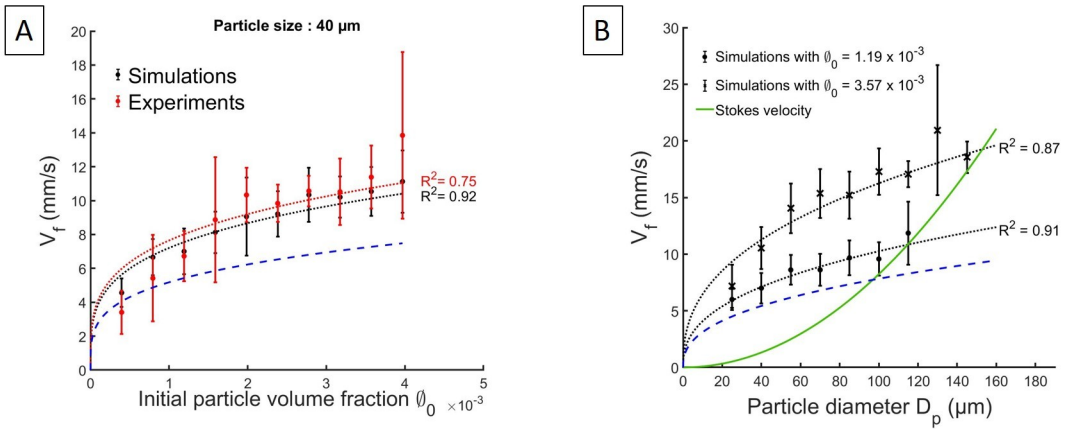

Figure 2.11: (A) Average finger speed (V_f) as a function of the initial volume fraction (ϕ_0) for a particle diameter of 40 μm. Red and black dotted lines show the best fits to the experiments [Fries et al., 2021] and simulations, respectively, using equation 2.1 with Gr_c as the fit parameter. For the simulations, we find $Gr_c = 1.2 \pm 0.4 \times 10^4$ whilst for the experiments $Gr_c = 1.9 \pm 0.7 \times 10^4$. (B) Average finger speed (V_f) as a function of the initial particle diameter (D_p), for two different particle volume fractions. The green line is the Stokes velocity for individual particles. The black dotted lines show the best fits to the simulations using equation 2.1 with Gr_c as the fit parameter. For $\phi_0 = 1.19 \times 10^{-3}$, the best fit gives $Gr_c = 7.6 \times 10^3$ and no fingers are observed to form for particle sizes higher than 115 μm. For $\phi_0 = 3.57 \times 10^{-3}$, the best fit gives $Gr_c = 2.7 \times 10^4$ and no fingers are observed to form for particle sizes higher than 145 μm. In the two plots, the blue dashed line shows equation 2.1 using $Gr_c = 10^3$ from the analogy with thermal convection [Hoyal et al., 1999].

difficult to obtain otherwise [Fries et al., 2021]. Three interesting parameters are the particle mass flux across a plane, the particle concentration in the lower layer and the amount of particles accumulated at the bottom of the tank, which can be related to the accumulation rate. The latter is especially interesting as, when the model is applied to volcanic clouds, it could eventually be compared with field data [Bonadonna et al., 2011].

We calculate the mass flux across a horizontal plane (actually a thin box of thickness δx) as shown in Figure 2.12A with

$$J = \frac{\Delta m}{A \Delta t}, \tag{2.48}$$

where Δm is the mass crossing the yellow plane of area A in time Δt, and is given by the mass difference in the volume below the plane between t and $t - \Delta t$. The mass below at each time is calculated by summing the mass of particles in each cell i of volume ΔV, which is individually given by $m_i = \Delta V \phi_i \rho_p$. Figure 2.12B shows

the temporal evolution of the particle mass flux settling through the yellow plane (located at 0.15 m below the barrier), for several initial particle volume fractions. The vertical black dashed line indicates the theoretical time T_i when particles would be expected to reach the plane if they were settling individually at their Stokes velocity. For the different simulations, we clearly observe that the moments when the flux starts initially increasing (i.e. the arrival of the fastest finger) are much earlier than T_i and this shows the extent to which the collective settling enhances the premature sedimentation. After the initial increase, the fluxes exhibit strong oscillations around a high plateau. These oscillations are associated with the intermittent nature of PBL detachment and convection in the lower layer. Finally, the particle mass flux reaches a plateau after some time which shows the end of convection and a transition to individual settling. Throughout, the average mass flux, as well as the amplitude of the oscillations increases with the initial volume fraction.

Another way to highlight the enhancement of the sedimentation rate by collective settling is to study the spatial distribution of particles beneath the interface. Assuming a quiescent upper layer and a convective lower layer, akin to our simulations, Hoyal et al. [1999] derived equation 2.4 for the evolution of the particle concentration in the lower layer. The derivation of this formulation assumes that $\dot{M}_{out} \neq 0$ since $t = 0$ but in fact, $\dot{M}_{out} = 0$ for $t < t_a$ where t_a is the time when the first particles reach the bottom of the tank. Also, equation 2.4 only remains valid for $t < t_{lim}$, where $t_{lim} = h_1/V_s$, h_1 being the thickness of the upper layer. After this time, there are no longer any particles remaining in the upper layer and $\dot{M}_{in} = 0$. We therefore propose an extension for the solution of the problem (see Appendix 2.C) which becomes

$$C_2(t) = \frac{V_s}{h_2} C_1(0)\, t, \quad \text{for} \quad t < t_a, \tag{2.49}$$

$$C_2(t) = C_1(0)\left[1 + \left(\frac{V_s}{h_2} t_a - 1\right) e^{-\frac{V_s}{h_2}(t - t_a)}\right], \quad \text{for} \quad t_a \leq t < t_{lim}, \tag{2.50}$$

$$C_2(t) = C_1(0)\left[1 + \left(\frac{V_s}{h_2}t_a - 1\right)e^{-\frac{V_s}{h_2}(t_{lim}-t_a)}\right]\left(1 + \frac{h_1}{h_2} - \frac{V_s}{h_2}t\right), \quad \text{for} \quad t \geq t_{lim}, \tag{2.51}$$

where h_2 is the thickness of the lower layer. Equation 2.51 assumes that the convection stops at t_{lim}, which suggests a quiescent settling in the lower layer after that time with a constant flux $\dot{M}_{out} = AV_sC_2(t_{lim})$.

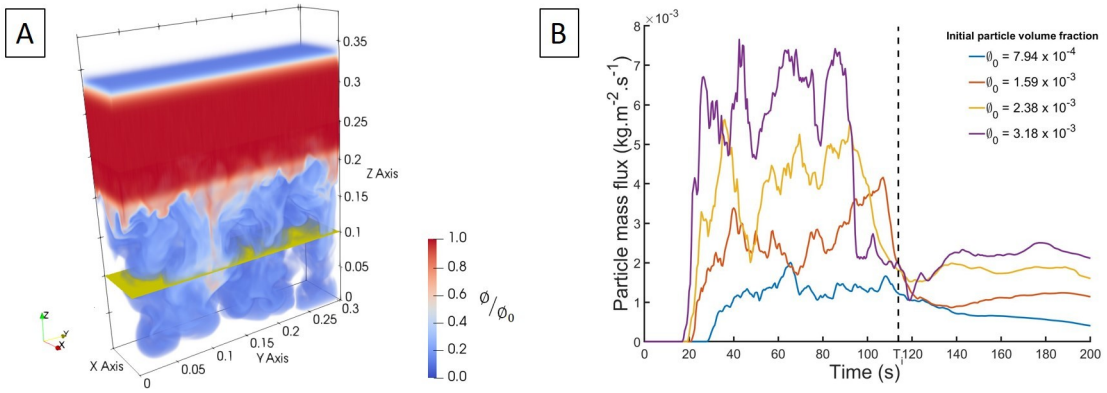

Figure 2.12: (A) Horizontal planar surface (yellow slice) located 0.15 m below the barrier, across which the particle mass is computed in the simulation domain. (B) Temporal evolution for the mass of particles crossing the plane. Black dashed line: theoretical time for the particles to reach the plane at their individual Stokes velocity.

An interesting result coming out of the previous analytical study is the mass of particles accumulating at the bottom of the tank and the associated accumulation rate. We can derive an analytical prediction for the mass of particles m_b accumulated at the bottom of the tank for the different regimes highlighted above. Thus, by integration of the flux (see Appendix 2.C) we have

$$m_b = 0, \quad \text{for} \quad t < t_a, \tag{2.52}$$

$$m_b = m_0\frac{V_s}{h_1}\left[t + \left(\frac{h_2}{V_s} - t_a\right)e^{-\frac{V_s}{h_2}(t-t_a)} - \frac{h_2}{V_s}\right], \quad \text{for} \quad t_a \leq t < t_{lim}, \tag{2.53}$$

$$m_b = m_0 \frac{V_s}{h_1}\{t_{lim} - \frac{h_2}{V_s}\left[1 + \left(\frac{V_s}{h_2}t_a - 1\right)e^{-\frac{V_s}{h_2}(t_{lim}-t_a)}\right]\left(1 + \frac{h_1}{h_2} - \frac{V_s}{h_2}t\right)\}, \quad \text{for} \quad t \geq t_{lim}, \tag{2.54}$$

where m_0 is the initial mass of particles injected in the upper layer. Finally, at the time $t_{lim} + h_2/V_s$, all the particle have settled through the lower layer, thus $m_b = m_0$. Figure 2.13A shows the simulated particle accumulation at the bottom of the tank through time, for different particle sizes as well as the analytical prediction (equations 2.52-2.54). We compare as well with the analytical formulation of the mass which assumes that the lower layer is still turbulently convective even after the time t_{lim} (equation 2C.20 in Appendix 2.C, dashed lines in Figure 2.13A). In order to compare between this prediction and the model results, t_a is fitted in order to have the best agreement between the numerical data and equations 2.52-2.54. The results show clearly that the quiescent model of the lower layer for $t \geq t_{lim}$ agrees very well with the simulations and suggest that the entirely convective model underestimates the accumulation rate. Additionally, the fitted parameter t_a is coherent with the time for the first fingers to reach the bottom of the tank in the simulations. Figure 2.13B shows the instantaneous accumulation rate computed from the numerical data for several initial volume fractions, as estimated by

$$\frac{1}{A}\frac{dm_b}{dt}. \tag{2.55}$$

We observe, for each initial particle volume fraction, an initial increase of the accumulation rate with time which reflects the enhancement of the sedimentation process due to convection. Interestingly, the accumulation rate then reaches a plateau at around $t = t_{lim}$, indicating that the system switches to a steady settling regime once all particles have left the upper layer. We compare also with the analytical relations which again have very good agreement with our simulations.

Finally, using the determined t_a, we can also calculate the concentration $C_2(t)$, as calculated with the analytical expressions in equations 2.49-2.51. Figure 2.14 shows a comparison with the average $C_2(t)$ as measured in simulations for a particle size of 40 μm and three different initial upper layer concentrations, finding very good

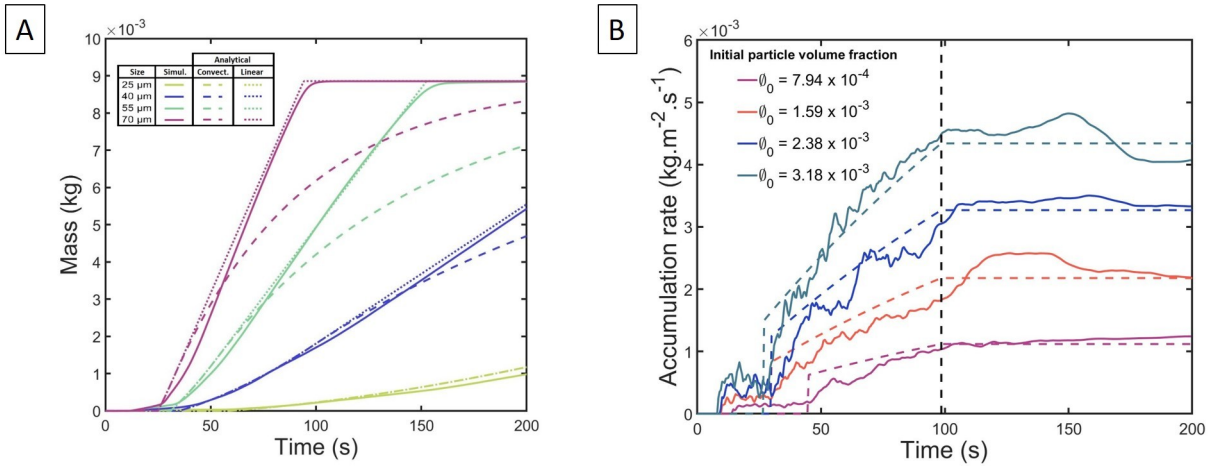

Figure 2.13: (A) Temporal evolution of the mass of particles accumulating at the bottom of the tank for several particle sizes. The dashed and dotted lines represent the extended analytical model of Hoyal et al. [1999]. Particle volume fraction $\phi_0 = 1.19 \times 10^{-3}$. (B) Accumulation rate calculated at the bottom of the tank for several particle volume fractions and a particle size of 40 μm. The coloured dashed lines are the rate derived from the analytical model. The black dashed line is the theoretical time at which all particles have settled across the interface.

agreement.

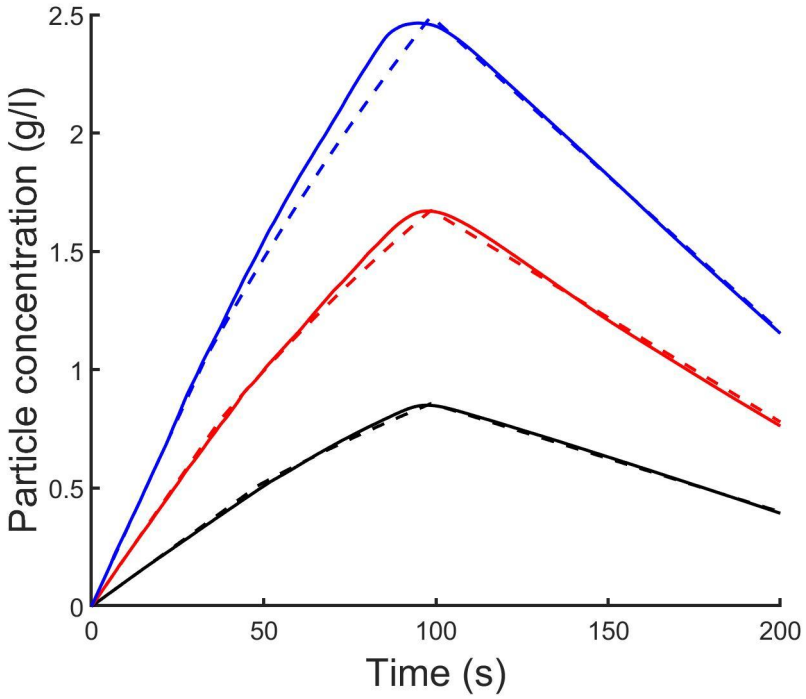

Figure 2.14: Evolution of the average particle volume fraction in the lower layer for particle of size 40 μm. Black: $C_0 = 2g/l$ ($\phi_0 = 7.94 \times 10^{-4}$), Red: $C_0 = 4g/l$ ($\phi_0 = 1.59 \times 10^{-3}$) and Blue: $C_0 = 6g/l$ ($\phi_0 = 2.38 \times 10^{-3}$). Solid lines: numerical model. Dashed lines: modified Hoyal et al. [1999] model (equations 2.4 and 2.49-2.51).

2.5 Discussion

2.5.1 Model caveats

Our numerical model has been validated by comparing various outputs with results from linear stability analysis, lab experiments [Fries et al., 2021] and theoretical predictions from previous studies [Carazzo and Jellinek, 2012; Hoyal et al., 1999]. Even though these comparisons are good (Figures 2.9-2.14), the results provided by the model inherits the caveats of the experiments. Indeed, the static and confined configuration, as well as the fact that we performed the simulations in water, mean that we cannot fully extend the results to the volcanic case yet. Thus, further investigations are necessary to better simulate the volcanic environment (e.g., in air, with wind, etc.). Additionally, it is necessary to consider the limits of validity of the different assumptions. In our study, particles are small enough that they have no inertia and thus the fluid-particle interaction force is governed by the buoyant

force term in the fluid momentum equation. However, as soon as the particle size increases, we need to consider some other dynamics. Indeed, a rigid particle moving in a fluid produces locally a disturbance flow which generates other contributions to the fluid-particle force terms. The assumption that particles settle at their Stokes velocity will then no longer be valid as the created local flow affects V_s [Maxey and Riley, 1983; Cartwright et al., 2010; Patočka et al., 2020].

Whilst the condition on the particle coupling is given by the Stokes number ($St < 1$), there is also a condition on the particle volume fraction to take in account. Harada et al. [2013] and Yamamoto et al. [2015] derived a dimensionless number in order to characterise the transition between fluid-like and particle-like settling. Although this number is only valid for narrow channel configurations, which are considerably different from ours, it highlights the fact that the particle size, volume fraction and characteristic length scale of the flow are critical parameters to define the validity of the continuum assumption. Thus, the transition from fluid-like to particle-like behaviour is achieved by decreasing the volume fraction and characteristic length scale and increasing the particle size. Near this transition, the use of a single-phase model, such as that presented here, should be treated with caution and this reveals the need for a comparison with future models which explicitly account for the drag contribution of individual particles. In multiphase models this contribution has been commonly represented through a force term involving the ratio between the phases differential velocities and the relaxation time (drag timescale) [Laibe and Price, 2014; Chou and Shao, 2016].

Another related caveat concerns the numerical diffusion underlying the use of an Eulerian approach to describe the transport of particles. Compared to classical first order finite difference methods, the use of the third order WENO procedure has drastically reduced the numerical diffusion. It is also possible to further reduce the induced numerical diffusion by increasing the order of the WENO scheme (i.e. increase also the computational cost). However, for problems purely related to advection, where the presence of any diffusion is critical, another strategy, such as two-phase models (using a Lagrangian approach where individual particles are explicitly modelled), has to be considered.

2.5.2 Vertical finger velocity

We have compared the simulated vertical velocity of fingers with experimental observations [Fries et al., 2021] and a theoretical prediction (equation 2.1) from [Carazzo and Jellinek, 2012; Hoyal et al., 1999] (Figure 2.11). This expression depends on a critical Grashof number which, by analogy with thermal convection [Turner, 1973], has previously been assumed to be 10^3 [Hoyal et al., 1999]. This value effectively corresponds to a dimensionless critical PBL thickness at which point the PBL can detach and form fingers. However, both the model results and experimental observations summarised in Figure 2.11 suggest that $Gr_c > 10^3$ for our configuration. Furthermore, as seen in Figure 2.11B, the curve for V_f using $Gr_c = 10^3$ (blue dotted line) crosses the Stokes velocity curve around 95 μm for instance with an initial particle volume fraction of $\phi_0 = 1.19 \times 10^{-3}$, suggesting this value should be the upper particle size limit for finger formation. However, in agreement with experiments [Fries et al., 2021; Scollo et al., 2017], we observe a larger threshold for the finger formation to be in the size range $[115-125]$ μm, for $\phi_0 = 1.19 \times 10^{-3}$, and in the range $[145-160]$ μm for $\phi_0 = 3.57 \times 10^{-3}$, in this particular configuration. We also showed that equation 2.1 poorly predicts the observed dependence of the finger velocity on the initial particle volume fraction. Indeed, our studies suggests an alternative power law that better describes the dependence of V_f on ϕ_0 (i.e. $V_f \propto \phi_0^{0.37\pm0.08}$). Equation 2.1 has been derived by a scaling theory that considers δ_{PBL} as characteristic length of the problem [Carazzo and Jellinek, 2012; Hoyal et al., 1999]. The discrepancies highlighted in this paper (Figure 2.11) may suggest that δ_{PBL} actually has a slightly different dependence on the initial particle volume fraction. Future theoretical works on a different scaling of δ_{PBL}, especially concerning its dependence on ϕ_0, but also V_s, would certainly confirm our results. Moreover, the use of the Grashof number as an appropriate scaling for the PBL thickness remains uncertain. On the one hand, our results suggest that if instability does occur once a critical Grashof number is reached, the critical value taken from the thermal convection analogy is not valid. On the other hand, the Grashof number may simply not be the correct dimensionless form of the PBL thickness, and different flow configurations will produce different critical values. The fact that both the experiments and simulations agree very well

shows that the "true" value for Gr_c, if it exists, is an order of magnitude higher than in the thermal case. However, Figure 2.11B shows that we find a ratio of ~ 3.5 between the two fitted Gr_c which is interestingly close to the ratio of three between the two associated particle volume fractions. Whilst the variability of Gr_c might come from the measurement itself (fitting of the numerical and experimental data), this behaviour is coherent considering the definition of Gr_c (ratio between buoyancy and viscous forces) and the fact that the buoyancy force is a function of the particle volume fraction. Obviously, this is only the case so long as the particle concentration does not affect the bulk viscosity, which is the case in our study. Therefore, we highlight here that the order of magnitude found for Gr_c is valid for the flow configuration presented in this study and also that there is a dependence on the initial particle volume fraction. Further analyses with different flow configurations (i.e., different buoyancy and viscous conditions) are required to constrain the variability of Gr_c and confirm that it may not be a rigorous scaling for the PBL thickness. A study involving settling-driven gravitational instabilities in air and in the presence of shear is currently being performed and will certainly provide some insights on the dependence of Gr_c on the flow configuration. The predicted dependence of the finger velocity on the particle diameter by equation 2.1 shows a very good agreement with our simulated results, as confirmed by a power-law fitting between V_f and D_p. Thus, whilst we have demonstrated the need for a better scaling of δ_{PBL}, equation 2.1 can still provide a good estimate for the particle size threshold to form fingers. Consequently, if the size threshold to form fingers is given when equation 2.1 equals the Stokes velocity (equation 2.5) we can derive a formulation for the threshold

$$D_p^* = \left[\frac{(18\mu)^2 \, \phi \delta_{PBL}}{g \left(\rho_p - \rho_f\right) \rho_f} \sqrt{\left(\frac{\pi}{4}\right)} \right]^{\frac{1}{4}}. \tag{2.56}$$

The main caveats for this formulation are that it strongly depends on having a correct scaling for δ_{PBL} and obviously, this estimation is valid under the assumption that particles settle at their Stokes velocity, which is reasonable for our study but might be uncertain in nature where the ambient fluid is air and for non-spherical particles.

2.5.3 Particle concentration in the lower layer and mass accumulation rate

We have proposed a modified analytical formulation for the particle concentration in the lower layer $C_2(t)$ and consequently for the mass of particles accumulated at the bottom of the tank $m_b(t)$. Despite some numerical artefacts that can be seen in Figure 2.13B where the computed accumulation rate seems to be non-zero before t_a, there is very good agreement between the simulations and the analytical model. The artefacts themselves are due to fluctuating numerical errors that do not affect the final results.

The analytical predictions for $C_2(t)$ and $m_b(t)$ are step-wise functions depending on t_a, the time it takes for the first particles to reach the bottom. For $t < t_a$, the analytical model predicts that $C_2(t)$ increases linearly with time since the formulation assumes that, during this period, particles are settling individually. In fact, our numerical results show that convective settling does occur for $t < t_a$ but, since this time period is short, the linear law seems to be a satisfactory approximation for the early-time average lower layer particle concentration. However, in order to compare our simulated results with the analytical prediction, we fitted the parameter t_a in this study. Although we are able to obtain excellent agreement between model and theory, it would be better to develop a fully independent formulation. To achieve this, it is necessary to also provide an analytical estimation for t_a. One possible approach would be to assume the decomposition $t_a = t_a^{'} + t_a^{''}$ where $t_a^{'}$ is the time during which the PBL initially grows beneath the interface at the individual particle settling velocity, i.e., $t_a^{'} = \delta_{PBL}/V_s$, and $t_a^{''}$ is the time between the PBL detachment and the first arrival of particles at the base of the domain. If, during this stage, we assume that the particles are advected at the finger velocity then $t_a^{''} = (h_2 - \delta_{PBL})/V_f$. We therefore see that t_a strongly depends on δ_{PBL}, which highlights once again the need for a correct scaling of the PBL thickness, as discussed in the previous section. Another interesting result concerns the accumulation rate of particles at the base of the domain in the presence of fingers. Figure 2.13B shows the accumulation rate increases with time for $t_a < t < t_{lim}$, in agreement with the analytical prediction (i.e. combination of equations 2.53 and 2.55 which provides an exponential increase

of m_b). Conversely, if the particles had settled individually, the accumulation rate would be temporally constant. This shows that temporally resolved measurements of the accumulation rate of particles from volcanic clouds may record temporal signatures of sedimentation via settling-driven gravitational instabilities. Whilst there is already a spatial deposit signature of settling-driven gravitational instabilities (i.e. bimodal grainsize distribution) [Bonadonna et al., 2011; Manzella et al., 2015], this is not unique and can be generated by other mechanisms such as particle aggregation [Brown et al., 2012]. Accumulation rate data from the field may therefore provide a powerful tool for distinguishing the efficiency of convective sedimentation beneath volcanic clouds.

2.6 Conclusions

We have presented an innovative hybrid Lattice Boltzmann Finite Difference 3D model in order to simulate settling-driven gravitational instabilities at the base of volcanic ash clouds. Such instabilities occur when particles settle through a density interface at the base of a suspension, leading to the formation of an unstable particle boundary layer [Carazzo and Jellinek, 2012; Hoyal et al., 1999; Manzella et al., 2015], and also occur in other natural settings, such as river plumes [Davarpanah Jazi and Wells, 2016]. Our numerical model makes use of a low-diffusive WENO procedure to solve the advection-diffusion-settling equation for the particle volume fraction. The use of such a routine allows us to minimise errors associated with numerical diffusion and has the advantage of being applied to simple uniform meshes, which makes the coupling with the LBM easier. This innovative use of the WENO scheme, therefore, represents an effective tool for the solving of advection-dominated problems. Our implementation of the third order WENO finite difference scheme will be integrated in a future release of the open-source *Palabos* code. Our model has been successfully validated by comparing the results with i) predictions from linear stability analysis where we show that the model is able to simulate settling-driven gravitational instabilities from the initial disturbance through the linearly-unstable regime, ii) analogue experiments [Fries et al., 2021] and iii) theoretical

models [Carazzo and Jellinek, 2012; Hoyal et al., 1999] in order to reproduce the non-linear regime which describes the downward propagation of fingers. We also confirmed the premature sedimentation process through collective settling compared to individual settling.

Our model provides new insights into:

- the value of the critical Grashof number. From measurements of the vertical finger speed, we have found $Gr_c \sim 10^4$ in our configuration. This value differs from the one suggested by analogy with thermal convection ($Gr_c \sim 10^3$) [Hoyal et al., 1999]. Our results suggest that either the critical Grashof number for settling-driven gravitational instabilities is greater than in the thermal convection case or that the Grashof number may not be the correct dimensionless form of the PBL thickness. In any case, this highlights the need for further investigation of the scaling of the PBL thickness δ_{PBL}.

- the presence of a particle size threshold for the finger formation. Using our results, we have proposed an analytical formulation for this threshold depending on the density of particles, the viscosity of the medium and also the bulk density difference between the two fluid layers.

- the signature of settling-driven gravitational instabilities (i.e. accumulation rate). We show that the accumulation rate of particles at the tank base initially increases with time before reaching a plateau. This contrasts with the constant accumulation rate associated with individual particle settling. This suggests that accumulation rate data could be used during tephra fallout to distinguish between sedimentation through settling-driven gravitational instabilities and individual-particle sedimentation.

We have also demonstrated how our numerical model can be used to expand the initial conditions and configuration settings that can be explored through experimental investigations. The results presented so far in an aqueous media permitted model validation but have also opened fundamental questions that will be addressed in future works involving configurations more similar to the natural system. Indeed,

thanks to the strengths of the LBM, the model can easily be applied to more complex systems and provide a robust tool for the transition from the laboratory studies to volcanic systems, as well as other environmental flows.

Author Contributions

Jonathan Lemus integrated the WENO procedure in the Palabos framework, conducted the simulations and data analysis under the supervision of Paul Jarvis, Jonas Lätt, Costanza Bonadonna and Bastien Chopard. Jonathan Lemus drafted the manuscript. Jonas Lätt and Bastien Chopard were involved in the development of the Palabos code. All authors have contributed to data interpretation as well as the editing and finalising of the paper.

Acknowledgments

All the simulations presented in this paper have been performed using the High Performance Computing (HPC) facilities *Baobab* and *Yggdrasil* of the University of Geneva. We would like to thank Amanda B. Clarke and Jeremy C. Phillips for constructive discussions about the problem.

Appendix

2.A Description of the finite difference schemes

2.A.1 First-order upwind finite difference scheme

In the following description, we describe only the one-dimensional scheme as the method is easily generalised to higher dimensions by simply applying the procedure separately to each dimension [Ferziger and Peric, 2002]. The finite difference method is based on the approximation of the derivatives at the node locations of a discretised domain and can be applied to both uniform and non-uniform meshes. However, we describe here the case where the numerical domain is uniformly discretised with the spatial step δx, such that the domain is divided in a set of equally-spaced points $\{x_0, x_1, ..., x_i..., x_n\}$. We also consider the one-dimensional conservation equation

$$\frac{\partial a}{\partial t} + u\frac{\partial a}{\partial x} = 0, \tag{2A.1}$$

where a is the transported information and u the advection velocity. In our discrete domain, we use the notation $a_i^n = a\,(x = x_i, t = t_n)$,with n denoting the time coordinate and i the spatial coordinate.

Among the numerous methods used to approximate the derivative $\partial a/\partial x$ at location x_i, the Taylor expansion is the most common. Following this procedure, there are two ways to estimate the derivative with a first order accuracy:

- Using the Taylor expansion at the location $x_{i+1} = x_i + \delta x$, we get the forward difference

$$\left(\frac{\partial a}{\partial x}\right)_F \approx \frac{a_{i+1}^n - a_i^n}{\delta x}. \tag{2A.2}$$

- Using the Taylor expansion at the location $x_{i-1} = x_i - \delta x$ we get the backward difference

$$\left(\frac{\partial a}{\partial x}\right)_B \approx \frac{a_i^n - a_{i-1}^n}{\delta x}. \tag{2A.3}$$

The central finite difference approximation can be determined by combining the forward and backward differences. Thus, we have the second order accurate discretisation

$$\left(\frac{\partial a}{\partial x}\right)_C \approx \frac{a_{i+1}^n - a_{i-1}^n}{2\delta x}. \tag{2A.4}$$

The upwind finite difference method scheme is an adaptive procedure to discretise the problem based on the direction of propagation of the information. The estimation of the quantity a_i^{n+1} depends on the sign of u:

- If $u > 0$, the backward difference is used

$$a_i^{n+1} = a_i^n - \frac{\delta t}{\delta x} u \left[a_i^n - a_{i-1}^n\right]. \tag{2A.5}$$

- If $u < 0$, the forward difference is used

$$a_i^{n+1} = a_i^n - \frac{\delta t}{\delta x} u \left[a_{i+1}^n - a_i^n\right]. \tag{2A.6}$$

All these properties of the first order upwind scheme guarantee a strong stability of the solution providing the Courant–Friedrichs–Lewy (CFL) condition is satisfied [Courant et al., 1928]

$$\frac{\delta t}{\delta x} u \leq 1. \tag{2A.7}$$

2.A.2 Third-order Weighted Essentially Non-Oscillatory (WENO) finite-difference scheme

In the following description, the numerical domain is discretized using the same set of points as presented in the previous section. The low-diffusive WENO scheme belongs to a family of high-resolution methods and was developed in order to solve hyperbolic partial differential equations of the form

$$\frac{\partial a}{\partial t} + \frac{\partial h}{\partial x} = 0, \tag{2A.8}$$

where, in our case, the flux takes the form $h(a) = ua(x)$ [Jiang and Shu, 1996; Liu et al., 1994]. The WENO scheme provides a third order accurate method in smooth regions, i.e., where the spatial gradient is small. On the other hand, the scheme adapts where the gradient is high. In these cases, the accuracy tends toward second-order. This adaptive aspect of the WENO procedure ensures the suppression of spurious oscillations, predicted by the Godunov theorem [Godunov, 1954, 1959], around shocks (regions of high gradient). The principle is to build a convex combination of interpolants for the flux at given points of the domain, using different stencils. The third-order WENO procedure uses two adjacent stencils of two points each (Figure 2A.1).

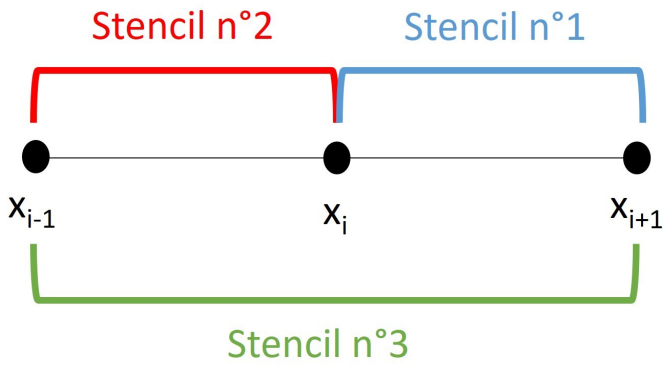

Figure 2A.1: Numerical stencil used for the 3rd order WENO procedure

It is possible to approximate the spatial derivative with the commonly used half-node flux:

$$\frac{\partial h}{\partial x} \approx \frac{h_{i+\frac{1}{2}} - h_{i-\frac{1}{2}}}{\delta x}, \tag{2A.9}$$

where $h_{i+\frac{1}{2}} = h\left(a\left(x_{i+\frac{1}{2}}\right)\right)$ is the numerical flux at the half-node location $x_{i+\frac{1}{2}}$ (i.e., the central position between the points x_i and x_{i+1}). There are three ways to construct the half node flux $h_{i+\frac{1}{2}}$. Firstly, we can use polynomial interpolants of degree 1 $p_1(x)$ and $p_2(x)$, respectively, in the two-point stencils 1 and 2. Then, the flux at the location $x_{i+\frac{1}{2}}$ is given either by $h^{(1)}_{i+\frac{1}{2}} \equiv p_1\left(x_{i+\frac{1}{2}}\right)$ or $h^{(2)}_{i+\frac{1}{2}} \equiv p_2\left(x_{i+\frac{1}{2}}\right)$

and for $u > 0$ we have

$$h^{(1)}_{i+\frac{1}{2}} = \frac{1}{2}\left(h_i + h_{i+1}\right), \tag{2A.10}$$

and

$$h^{(2)}_{i+\frac{1}{2}} = -\frac{1}{2}\left(h_{i-1} - 3h_i\right). \tag{2A.11}$$

Note that the flux approximations for each stencil in this case have an accuracy of second order. The last way to determine the flux $h_{i+\frac{1}{2}}$ is with an interpolating polynomial $p_3(x)$ of degree 2 inside the three-point stencil 3 (i.e., the union of stencils 1 and 2 in Figure 2A.1). Then, the third-order flux at the location $x_{i+\frac{1}{2}}$ is given by

$$h^{(3)}_{i+\frac{1}{2}} = \frac{3}{4}h_i - \frac{1}{8}h_{i-1} + \frac{3}{8}h_{i+1}. \tag{2A.12}$$

The three interpolations of the half-node flux presented above are efficient assuming that the function h is smooth through the associated stencil and it is even possible to write the third-order flux $h^{(3)}_{i+\frac{1}{2}}$ as a linear combination of $h^{(1)}_{i+\frac{1}{2}}$ and $h^{(2)}_{i+\frac{1}{2}}$

$$h^{(3)}_{i+\frac{1}{2}} = \gamma_1 h^{(1)}_{i+\frac{1}{2}} + \gamma_2 h^{(2)}_{i+\frac{1}{2}}, \tag{2A.13}$$

where $\gamma_1 = 3/4$ and $\gamma_2 = 1/4$. However, the presence of any discontinuity would break the stability of the procedure, introducing spurious oscillations in the calculated solution. The treatment of this aspect constitutes the essence of the WENO method which retains the property of relating the total flux $h_{i+\frac{1}{2}}$ to a convex combination $h^{(1)}_{i+\frac{1}{2}}$ and $h^{(2)}_{i+\frac{1}{2}}$, similarly to equation 2A.13, but including non-linear weights

$$h^{(3)}_{i+\frac{1}{2}} = \omega_1 h^{(1)}_{i+\frac{1}{2}} + \omega_2 h^{(2)}_{i+\frac{1}{2}}, \tag{2A.14}$$

where ω_1 and ω_2 are functions of the smoothness of h and must satisfy $\omega_1 + \omega_2 = 1$. If h is smooth in all the stencils, $\omega_i \to \gamma_i$ and ensures a third-order accuracy. Conversely, the presence of any discontinuity in the i^{th} stencil means $\omega_i \to 0$, decreasing the accuracy to second-order. This property is guaranteed by determining ω_i

$$\omega_i = \frac{\tilde{\omega}_i}{\sum_j \tilde{\omega}_j}, \tag{2A.15}$$

where

$$\tilde{\omega_j} = \frac{\alpha_j}{(\epsilon + \beta_j)^2}, \tag{2A.16}$$

and, in the third-order WENO case, $\alpha_1 = 2/3$, $\alpha_2 = 1/3$, $\beta_1 = (h_{i+1} - h_i)^2$ and $\beta_2 = (h_i - h_{i-1})^2$ (β_j are referred to as smoothness indicators). A positive mathematical coefficient ϵ is introduced in order to avoid any division by zero for the calculation of $\tilde{\omega}_j$.

The WENO reconstruction presented above is valid for $u > 0$. In order to include potential changes of the flow direction, we use an upwind splitting of the flux. Thus, as a mirror image of the procedure described above, we have for $u < 0$

$$h^{(1)}_{i+\frac{1}{2}} = -\frac{1}{2}\left(h_{i+2} - 3h_{i+1}\right), \tag{2A.17}$$

and

$$h^{(2)}_{i+\frac{1}{2}} = \frac{1}{2}\left(h_{i+1} + h_i\right). \tag{2A.18}$$

$$\beta_1 = \left(h_{i+1} - h_{i+2}\right)^2, \tag{2A.19}$$

and

$$\beta_2 = \left(h_i - h_{i+1}\right)^2. \tag{2A.20}$$

With an appropriate time discretisation, the third-order WENO procedure remains a Total Variation Diminishing (TVD) scheme, i.e., $\sum_i |a^{n+1}_{i+1} - a^{n+1}_i| \leq \sum_i |a^n_{i+1} - a^n_i|$ [Harten, 1983]. This property avoids the introduction of new local extrema in the solution. Therefore, a TVD third-order WENO scheme is given using an iterative third-order Runge-Kutta method for the time discretisation:

$$a^{(1)} = a^n + \delta t W\left(a^n\right), \tag{2A.21}$$

$$a^{(2)} = \frac{3}{4}a^n + \frac{1}{4}a^{(1)} + \frac{1}{4}\delta t W\left(a^{(1)}\right), \tag{2A.22}$$

and

$$a^{n+1} = \frac{1}{3}a^n + \frac{2}{3}a^{(2)} + \frac{2}{3}\delta t W\left(a^{(2)}\right), \tag{2A.23}$$

with $W(a)$ is the spatial derivative given by the WENO algorithm described above.

2.B Numerical diffusion

In this subsection, we demonstrate the reduced numerical diffusivity of the WENO procedure compared to the first order upwind scheme. We performed some simulations involving a rectangular signal moving at a velocity equivalent to the settling velocity of 40 micron particles in water. We used both the WENO and first order upwind schemes and compared with the expected analytical solution. The spatial and temporal discretisation are the same as used for the different simulations in the main manuscript. Figure 2B.1 shows the simulations results after 60 s and we clearly observe the reduced numerical diffusion provided by the WENO procedure as well as the lack of dispersion. Moreover, we also computed the mean absolute difference (error) of each method with the analytical solution and find that, for this case study, the error associated with the first order upwind scheme is $\sim$3 times greater than the WENO error.

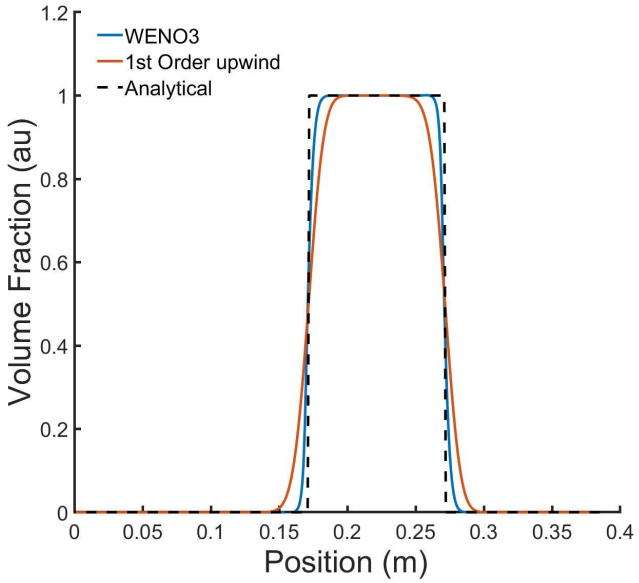

Figure 2B.1: Advection of a rectangular signal. Comparison between the analytical solution (dashed black line), the first order upwind (red solid line) and the WENO scheme (blue solid line).

2.C Extension of analytical model of Hoyal et al. [1999]

2.C.1 Particle concentration

For a particle suspension placed above a denser fluid, an estimate for the evolution of the particle concentration in the lower layer has been derived by Hoyal et al. [1999]. We provide here an extension of this formulation.

Upper layer

First, let's consider a quiescent upper layer of thickness h_1 with an initial particle concentration $C_1(0)$. For a quiescent settling at the velocity V_s, the constant flux of particles leaving the upper layer is given by $-AV_sC_1(0)$. Thus, the evolution for the mass of particles is described by the equation

$$\frac{dM_1}{dt} = -AV_sC_1(0)\,. \tag{2C.1}$$

Assuming that the mass of particles depends on the concentration as

$$M_i(t) = Ah_iC_i(t), \tag{2C.2}$$

A being the horizontal cross section of the tank (where $i = 1$ for the upper layer and $i = 2$ for the lower layer), the temporal evolution of the particle concentration in the upper layer is the solution of

$$\frac{dC_1}{dt} = -\frac{V_s}{h_1}C_1(0). \tag{2C.3}$$

Then

$$C_1(t) = C_1(0)\left[1 - \frac{V_s}{h_1}t\right]. \tag{2C.4}$$

Lower layer

Now, let's define $\dot{M}_{in}$ as the flux of particle entering the lower layer (i.e. the particles arriving from the upper layer) and $\dot{M}_{out}$ the flux of particles leaving (i.e. particles that deposit at the bottom of the tank). Thus, the mass of particle in the lower layer $M_2(t)$ is governed by the equation

$$\frac{dM_2}{dt} = \dot{M}_{in} - \dot{M}_{out}, \tag{2C.5}$$

- There is a time t_a before which particles have not yet reached the bottom of the tank and evidently $\dot{M}_{out} = 0$. Still assuming a quiescent upper layer, we have also

  $$\dot{M}_{in} = AV_sC_1(0). \tag{2C.6}$$

  So, combining 2C.2, 2C.5 and 2C.6 the particle concentration in the lower layer for $t < t_a$ is the solution of

  $$\frac{dC_2}{dt} = \frac{V_s}{h_2}C_1(0). \tag{2C.7}$$

  that is to say (assuming $C_2(0) = 0$)

$$C_2(t) = \frac{V_s}{h_2} C_1(0)\, t. \tag{2C.8}$$

- Once the first particles have reached the bottom of the tank (i.e. $t \geq t_a$), the flux of particles leaving the lower layer becomes

$$\dot{M}_{out} = A V_s C_2(t). \tag{2C.9}$$

Similarly to the previous point, combining equations 2C.2 (which assumes that the lower layer is turbulently convecting and is homogeneous), 2C.5, 2C.6 and 2C.8 we obtain

$$\frac{dC_2}{dt} + \frac{V_s}{h_2} C_2 = \frac{V_s}{h_2} C_1(0). \tag{2C.10}$$

Using the initial condition $C_2(t_a) = (V_s/h_2) C_1(0)\, t_a$ (continuity with 2C.8), the solution of this equation is

$$C_2(t) = C_1(0) \left[1 + \left(\frac{V_s}{h_2} t_a - 1 \right) e^{-\frac{V_s}{h_2}(t - t_a)} \right]. \tag{2C.11}$$

It is evident that when $t_a = 0$, 2C.11 is equivalent to the original formulation of Hoyal et al. [1999] (equation 4 in the Introduction).

- However, 2C.11 is only valid for the condition that particles keep settling across the interface, i.e., for a time $t < t_{lim}$ (where $t_{lim} = h_1/V_s$). We have extended the formulation to later times once all particles from the upper layer have settled across the interface i.e. for a time $t \geq t_{lim}$. As there are no longer particles in the upper layer, the flux $\dot{M}_{in}$ drops to zero. Two possibilities are now available. On one hand, if we consider that the lower layer is still turbulently convecting after t_{lim}, equation 2C.10 becomes:

$$\frac{dC_2}{dt} + \frac{V_s}{h_2} C_2 = 0. \tag{2C.12}$$

Assuming that all particles have crossed the interface by the time t_{lim}, we

substitute t_{lim} into 2C.11 in order to find the initial condition for equation 2C.12. Thus the initial condition is now

$$C_2\left(t_{lim}\right) = C_1\left(0\right)\left[1 + \left(\frac{V_s}{h_2}t_a - 1\right)e^{-\frac{V_s}{h_2}\left(t_{lim} - t_a\right)}\right]. \tag{2C.13}$$

which allows to solve equation 2C.12 and to find the solution of $C_2\left(t\right)$ for a convective lower layer at $t > t_{lim}$

$$C_2\left(t\right) = C_1\left(0\right)e^{\frac{h_1}{h_2}}\left[1 + \left(\frac{V_s}{h_2}t_a - 1\right)e^{-\frac{V_s}{h_2}\left(t_{lim} - t_a\right)}\right]e^{-\frac{V_s}{h_2}t}. \tag{2C.14}$$

On the other hand, if we assume that the convection stops at t_{lim}, then we have to consider a quiescent settling in the lower layer. Thus the associated constant flux becomes

$$\dot{M}_{out} = AV_sC_2\left(t_{lim}\right), \tag{2C.15}$$

and 2C.12 becomes

$$\frac{dC_2}{dt} + \frac{V_s}{h_2}C_2\left(t_{lim}\right) = 0. \tag{2C.16}$$

Then, keeping the initial condition 2C.13 to solve 2C.12, the solution of $C_2\left(t\right)$ for a quiescent lower layer at $t > t_{lim}$ is

$$C_2\left(t\right) = C_1\left(0\right)\left[1 + \left(\frac{V_s}{h_2}t_a - 1\right)e^{-\frac{V_s}{h_2}\left(t_{lim} - t_a\right)}\right]\left(1 + \frac{h_1}{h_2} - \frac{V_s}{h_2}t\right). \tag{2C.17}$$

2.C.2 Mass of particles accumulating at the bottom

From the mass balance models, Hoyal et al. [1999] derived an estimate for the mass of particle which accumulate at the bottom of the domain. Here we detail the calculation of the mass and extend it by including the solution of $C_2\left(t\right)$ for $t > t_{lim}$ (presented above). Particles start to accumulate as soon as they reach the bottom of the tank (i.e. after a time t_a). Then for $t < t_a$, we have

$$m_b = 0. \tag{2C.18}$$

where m_b is the mass at the base of the tank. Furthermore, for $t_a \leq t < t_{lim}$ we integrate the flux $AV_sC_2(t)$ between t_a and t, using equation 2C.11 for $C_2(t)$. Thus we have

$$m_b = m_0 \frac{V_s}{h_1} \left[t + \left(\frac{h_2}{V_s} - t_a \right) e^{-\frac{V_s}{h_2}(t-t_a)} - \frac{h_2}{V_s} \right], \tag{2C.19}$$

where m_0 is the initial mass of particles introduced in the upper layer. We observe that this relation is equivalent to equation 24 derived in Hoyal et al. [1999], but delayed by t_a. Finally, for $t > t_{lim}$ we integrate the flux between t_{lim} and t, taking into account that some particles have already accumulated between t_a and t_{lim} according to 2C.19. As we have presented two different cases for the lower layer after t_{lim} (convective and quiescent), there are also two possibilities for the mass of particles. Then, for a convective lower layer we have

$$m_b = m_0 \frac{V_s}{h_1} \left\{ t_{lim} - \frac{h_2}{V_s} e^{\frac{h_1}{h_2}} \left[1 + \left(\frac{V_s}{h_2} t_a - 1 \right) e^{-\frac{V_s}{h_2}(t_{lim}-t_a)} \right] e^{-\frac{V_s}{h_2}t} \right\}, \tag{2C.20}$$

and for a quiescent lower layer

$$m_b = m_0 \frac{V_s}{h_1} \left\{ t_{lim} - \frac{h_2}{V_s} \left[1 + \left(\frac{V_s}{h_2} t_a - 1 \right) e^{-\frac{V_s}{h_2}(t_{lim}-t_a)} \right] \left(1 + \frac{h_1}{h_2} - \frac{V_s}{h_2} t \right) \right\}, \tag{2C.21}$$

2.D 2D Fourier analysis of the interface

We performed a 2D Fourier analysis of the interface for one initial particle volume fraction ($\phi_0 = 1.98 \times 10^{-3}$) in order to compare with the results given by the Fourier analysis in the central section of the domain. At different time steps, we extract the particle field interface with the same threshold as in section 4.1 (Figure 2D.1). Then we can compute a 2D map of the interface height which allows to perform the 2D Fourier analysis. The result is a map in the spectral space (k_x, k_y) as shown in

Figure 2D.2 and as usual, at different time steps we extract the main peak which correspond to the main mode and the associated coordinates (k_x, k_y) in the spectral space. We observe that the norm $k = \sqrt{k_x^2 + k_y^2}$ very well with the previous results provided in our study for this initial particle volume fraction (Figure 2D.3).

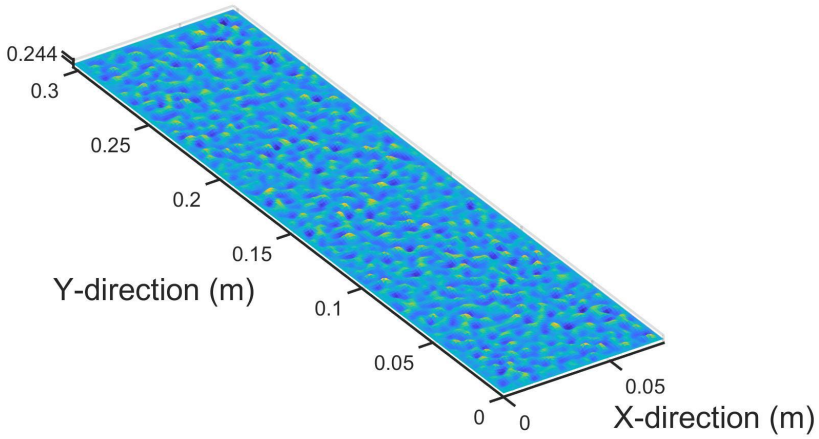

Figure 2D.1: Particle field interface for an initial particle volume fraction $\phi_0 = 1.98 \times 10^{-3}$ at time T=4s.

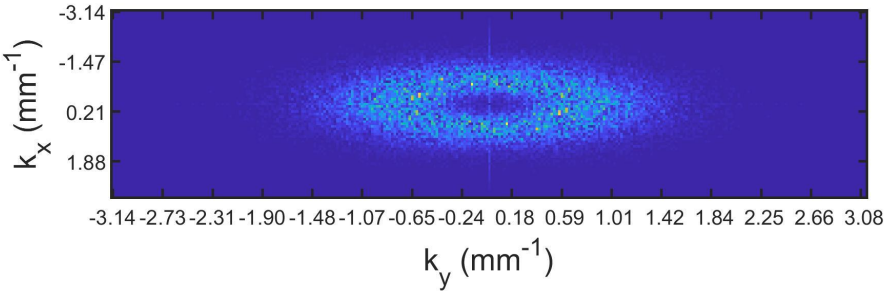

Figure 2D.2: Map of the power spectral density associated with the particle field interface shown in Figure 2D.1

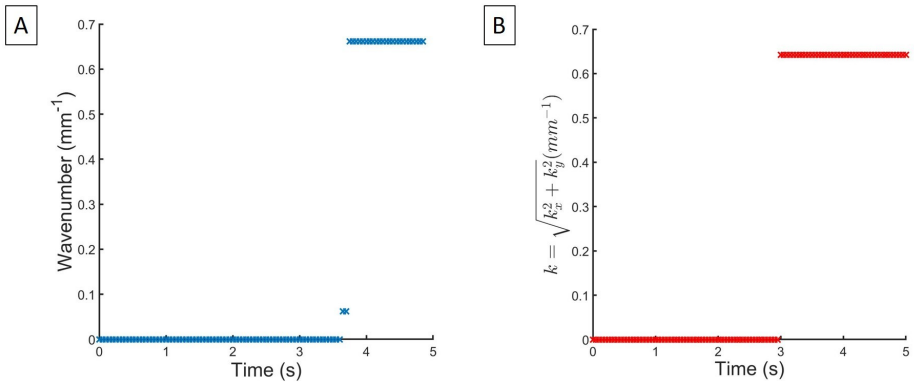

Figure 2D.3: Wavelength of the dominant mode extracted from (A) the Fourier analysis in the central plane of the domain and (B) from the 2D Fourier analysis of the particle interface. (initial particle volume fraction $\phi_0 = 1.98 \times 10^{-3}$

2.E Acronyms and symbols

A	Area of the plane through which the particle mass flux is computed
b	Coefficient used to compute the force term in the Guo et al. [2002] formulation
c_i	Local particle velocity associated to a given lattice type in the LBM
c_s	Speed of sound used in the LBM
C_1	Particle concentration in the upper layer
C_2	Particle concentration in the lower layer
D, D_c, D_S	Diffusion coefficients respectively for the density-altering quantity, the particle field and the sugar
D_p	Particle diameter
D_z	Differential operator
$\vec{e_z}$	Vertical unit vector
f_i, f_i^{eq}	Particle population and equilibrium distribution function
$\vec{F}$	Body force term

F_i	Power series expansion in the Guo et al. [2002] formulation
Fr	Froude number
g, g'	Gravitational acceleration and reduced gravity
Gr_c	Critical Grashof number
h_1, h_2	Thicknesses of the upper and lower layer respectively
H, H_o	Heights of the particle interface at any time and at time $t = 0$
$\tilde{H}, \lvert\tilde{H}_i\rvert$	Fourier transform of H and the associated initial amplitude
I	Identity operator
J	Particle mass flux
k, k_{sim}	Wavenumber associated with the instability and the value computed from the simulations
k_S	Sampling wavenumber
K	Left term in the matrix form of the eigenvalue problem in the LSA
l^c	Characteristic length used in the viscous scaling
l_x, l_y, l_z	Domain extent respectively in the x,y and z directions
L	Characteristic length of the flow
L_S	Number of samples in the instability Fourier analysis
m_b	Mass of particles accumulated at the bottom of the domain
M	Compacted form of the second order differential operator ($M = -k^2 + D_z^2$)
M_2	Mass of particles in the lower layer
$\dot{M}_{in}, \dot{M}_{out}$	Particle mass flux entering and leaving the lower layer respectively
NE	Numerical diffusion error in the first order finite-difference scheme

p, p^c	Fluid pressure and characteristic pressure in the viscous scaling
q	Power used in the law defining V_f as a function of ϕ
$S, S_0, S^*, \bar{S}, \hat{S}$	Sugar concentration, sugar concentration at time $t = 0$ and $S^*(= S_0)$ is used in the nondimensionalisation, base state and perturbation amplitude for the sugar concentration
Sc_i	Schmidt number
St	Stokes number
t, t_a, t^c, t_{lim}	Time, time for the particle first arrival at the bottom of the tank, characteristic time in the viscous scaling and time at which all particle have settle across the initial interface.
T	Time at which the instability starts growing
$u, \vec{u_f}$	Transport velocity and fluid velocity
U	Characteristic velocity
V_f, V_s	Respectively the fingers velocity and individual particle settling velocity
W	Right term in the matrix form of the eigenvalue problem in the LSA
$\vec{x} = (x, y, z)$	Position vector and associated 3D components
z_ϕ, z_s	Error function parameters used for the base states of volmue fraction and sugar respectively
α	Sugar expansion coefficient
Γ_H, Γ_{H_i}	Power spectral density (PSD). The i index stands for the initial PSD
$\delta t, \delta x$	Temporal and spatial steps
δ_{PBL}	PBL thickness
Δt	Integration time for the particle mass flux
η	Power used in the law defining V_f as a function of D_p

μ	Fluid dynamic viscosity
ν	Fluid kinematic viscosity
$\rho, \rho_0, \rho_f, \rho_p, \rho_{PBL}, \rho_{blk}$	Density, fresh water density, fluid density (including sugar), particle density, PBL density, bulk density (including sugar and particles)
$\sigma, \sigma_{sim}, \sigma_{LSA,i}$	Growth rate of the instability, growth rate computed from simulations and growth rate predicted by LSA
τ	Relaxation coefficient in the LBM
$\varphi, \bar{\varphi}, \varphi', \hat{\varphi}$	Arbitrary variable, associated base state, perturbation and perturbation amplitude
$\phi, \phi_{tot}, \phi_i, \phi_0, \phi^*, \bar{\phi}, \hat{\phi}$	Particle volume fraction, total particle volume fraction (polydisperse case), volume fraction of the $i-th$ size class, initial particle volume fraction, ϕ^* $(= \phi_0)$ is used in the nondimensionalisation, volume fraction base state, perturbation amplitude
$\psi, \bar{\psi}, \hat{\psi}$	Stream function, associated base state, perturbation amplitude
$\omega, \bar{\omega}, \hat{\omega}$	Vorticity, associated base state, perturbation amplitude s

Table 2E.1: List of symbols used in the main manuscript

Chapter 3

Effect of gravitational spreading and wind shear on settling-driven gravitational instabilities within volcanic ash clouds

3.1 Introduction

In the previous chapter (i.e., published as [Lemus et al., 2021]), we presented a newly-developed numerical model which extended previous investigations studying settling-driven gravitational instabilities (SDGIs) at the base of volcanic clouds. This model has been validated against theoretical studies (linear stability analysis), laboratory experiments and analytical predictions for the vertical mass transfer of volcanic ash [Lemus et al., 2021]. Furthermore, we confirmed that the instability growth rate during the early linear stage, as well as the finger vertical velocity during the later nonlinear regime, increase with the particle volume fraction. Finally, we have demonstrated that characteristic signatures of SDGIs may be preserved in measurable parameters such as the sedimentation mass flux or the accumulation rate on the ground. These results complement the fundamental insights into finger dynamics obtained based on analogue laboratory experiments [Manzella et al., 2015; Scollo et al., 2017; Fries et al., 2021]. However, these studies, as well as our prior work [Lemus et al., 2021], consider a static configuration and do not take into account the possible effect of shearing at the base of the cloud, which can be due to either gravitational spreading, wind advection or both. In fact, the first experimental studies on settling-driven gravitational instabilities mostly focused on the

conditions for the formation of fingers in relation to the development of a boundary layer [Manzella et al., 2015; Scollo et al., 2017; Fries et al., 2021]. Nonetheless, gravitational and/or wind spreading is almost ubiquitous in natural volcanic ash plumes and clouds; as a result, accurate modelling of settling-driven gravitational instabilities needs to also describe the effect of shear.

Evidence for shear at the base of volcanic plumes and clouds comes from both direct observations and analysis of deposits. Strong plumes form laterally-spreading umbrella clouds at their neutral-buoyancy level [Constantinescu et al., 2021; Webster et al., 2020; Costa et al., 2013; Bonadonna and Phillips, 2003], which can be modelled as intrusive gravity currents (GCs) [Bursik et al., 1992; Johnson et al., 2015]. Meanwhile, weak-plumes exhibit bent centre-line trajectories leading to elongated ash deposits [Bonadonna et al., 2005, 2015b; Ernst et al., 1994; Carey and Sparks, 1986]. In both cases, a vertical gradient in the horizontal flow profiles exists, i.e., a shear flow. Such shear flows, which occur in density-stratified fluid, are susceptible to a range of shear instabilities, including the Kelvin-Helmholtz instability (KHI) [Kelvin, 1871; von Helmholtz, 1886]. This wave-like instability appears at the interface between two fluids placed on top of each other and moving at different velocities and can be related both to gravitational spreading and wind advection. It grows from initial perturbations at the density interface to form billows that finally collapse, inducing turbulent mixing [Thorpe, 1973]. Indeed, KHI billows have been observed at the base of bent volcanic plumes due to the velocity gradient between the plume and the surrounding atmosphere [Bursik et al., 2021]. Specific conditions are required to trigger instabilities such as KHIs. Indeed, we saw in the previous chapter that a stratified configuration involving a fluid layer placed above a denser one provides a stable configuration [Chandrasekhar, 1961; Sharp, 1984]. Nonetheless, the addition of velocity shear (whether this is related to gravitational spreading, to wind or to both) tends to destabilise the system and linear stability analysis provides a condition on the gradient Richardson number Ri_g [Drazin, 1958; Goldstein, 1931; Miles, 1961]. Assuming an inviscid and incompressible flow under the action of gravity, the instability occurs for $Ri_g < 1/4$ where

$$Ri_g = \frac{\frac{g}{\rho(z)}\frac{d\rho(z)}{dz}}{\left(\frac{du(z)}{dz}\right)^2}, \tag{3.1}$$

with $g = 9.81$ m s^{-2} the gravitational acceleration, z the vertical position coordinate, $\rho(z)$ the vertical density profile and $u(z)$ the horizontal velocity.

KHIs have been widely studied in numerous fields such as meteorology [Chapman and Browning, 1997; Reiss and Corona, 1977], oceanography [van Haren and Gostiaux, 2010; Smyth and Moum, 2012] and even astronomy [Ray, 1981; Cavus and Kazkapan, 2013]. KHIs represent an important mechanism for mixing density-stratified fluids [Ellison and Turner, 1959; Christodoulou, 1985; Strang and Fernando, 2001] and, consequently, an analysis of the effect of shear on SDGIs needs to consider interactions between the two types of instability (i.e. SDGIs and KHIs). Some theoretical studies involving linear stability analyses have been carried out, with results showing that the instability growth rate and wavelength depend on the Richardson number and the particle settling velocity [Farenzena and Silvestri, 2017; Konopliv et al., 2018]. In particular, it has been found that the presence of shear tends to dampen the growth of SDGIs, as it also does for double-diffusive instabilities (DDIs) [Linden, 1974; Smyth and Kimura, 2007; Kimura and Smyth, 2007]. These have also been proposed as mechanism for fingering processes in volcanic ash clouds [Linden, 1974; Smyth and Kimura, 2007; Kimura and Smyth, 2007; Carazzo and Jellinek, 2013].

Whilst the interaction between KHIs and SDGIs is understudied, the interaction between Rayleigh Taylor instabilities (RTIs) and KHIs is more documented. Linear stability analyses of combined RTI-KHI have shown that the presence of shear between two unstable layers tends to increase the instability growth rate during the early linear stage (compared to non-sheared RTIs) [Chandrasekhar, 1961; Guzdar et al., 1982; Zhang et al., 2005]. Interestingly, numerical studies focused on the later nonlinear regime have highlighted some conditions for which the opposite situation occurs, i.e., the shear stabilises the Rayleigh-Taylor process (decreases the RTI growth rate) until a point where KHIs dominate [Olson et al., 2011; Shumlak and Roderick, 1998]. Furthermore, it appears that the addition of shear tends to

suppress the RTI isotropy property [Olson et al., 2011]. Indeed, our 2D Fourier analysis of the particle interface in non-sheared experiments showed that SDGIs are isotropic within the plane perpendicular to the settling direction (cf. Appendix chapter 2). Given the lack of study on KHI-SDGI interactions, these results on KHI-RHI interactions provide a crucial starting point for interpreting the effect of shear on SDGIs.

In this chapter, we use the previously-developed numerical model [Lemus et al., 2021] to investigate the interaction between shear and SDGIs, as well as the associated implications for volcanic ash settling. First, we perform simulations of laboratory-scale, lock-release particle bearing gravity currents that propagate over a denser ambient [Jarvis et al., in prep]. These experiments allow us to investigate the fundamental physics of SDGIs in a sheared environment, as well as validate our model against experimental results. Second, we expand our model to the natural setting by simulating ash sedimentation during the 2010 eruption of Eyjafjallajökull volcano, Iceland, where the plume was largely affected by wind [Bonadonna et al., 2011].

3.1.1 Shear associated with gravitational spreading

Gravity currents (GCs) are flows where horizontal motion follows a pressure gradient due to a horizontal density difference [Benjamin, 1968; Simpson, 1997]. They are frequently used to model the dynamics of many processes associated with geological settings, especially volcanic eruptions [Hallworth et al., 1993; Gladstone et al., 2004; Castruccio et al., 2010; Sparks et al., 1991; Johnson et al., 2015]. Dedicated laboratory experiments have been scaled to be representative of gravitationally-spreading volcanic clouds [Jarvis et al., in prep]. The experiments involve lock-release configurations and allow the creation of constant-volume GCs. Numerous theoretical, experimental and numerical studies have been performed in order to characterise the fundamental properties of such currents [Thomas et al., 2003; Lowe et al., 2002; Marino et al., 2005; Hallworth et al., 1993; Balasubramanian and Zhong, 2018; Ottolenghi et al., 2018; Mukherjee and Balasubramanian, 2020; Shin et al., 2004]. An interesting outcome is that, during the propagation of gravity currents, three phases

can be distinguished. There is first a slumping regime where the current propagates at a constant velocity. Then, there is a second inertial regime where the current motion is governed by the balance between buoyancy and inertial forces. Finally, a viscous regime occurs where the current spreading is dominated by viscous effects [Huppert and Simpson, 1980; Cantero et al., 2007]. In order to characterise the current front velocity throughout these phases, and for Boussinesq currents (i.e., where the density difference between the current and the ambient is very small), the front velocity is usually expressed as a dimensionless Froude number given by [Benjamin, 1968]

$$Fr_H = \frac{U}{\sqrt{g'H}}, \tag{3.2}$$

where the reduced gravity $g' = g|\rho_f - \rho_s|/\rho_s$, where ρ_f the current density, ρ_s the ambient density and H the total fluid depth. Moreover, for an ideal flow configuration, i.e., energy conserving, buoyancy-driven and full-depth release, Benjamin [1968] derived a value of 1/2 for Fr_H which ultimately gives the front velocity as

$$U = \frac{\sqrt{g'H}}{2}. \tag{3.3}$$

This ideal energy-conserving case is, however, difficult to achieve in reality due to internal dissipative processes and mixing [Benjamin, 1968]. In Benjamin's model, the imposition of energy conservation produces a current which occupies a depth of $h = 0.5H$ (for a full-depth lock-release experiment). More recently, a newer analytical model has been derived relating the energy loss flux $\Delta\dot{E}$ (in practice the dimensionless energy loss $\Delta\hat{\dot{E}}$) to H and h through the relation [Shin et al., 2004]

$$\Delta\hat{\dot{E}} = \frac{\Delta\dot{E}}{\rho_1 g'^{3/2} H^{5/2}} = \frac{h^{5/2}\,(H-2h)\,(2H-h)^{1/2}}{2H\,(H+h)^{3/2}\,(H-h)^{1/2}}. \tag{3.4}$$

where ρ_1 is the light fluid density in the stratified configuration. Figure 3.1.1 shows the dimensionless loss of energy as a function of the dimensionless current depth. Whilst the energy-conserving case, i.e., $\Delta\hat{\dot{E}}(0.5) = 0$, can be seen for $h = 0.5H$, the non-conserving regime is given for $h < 0.5H$ with a maximum loss at $h = 0.347H$, which also corresponds to the depth for which the current is at its maximum speed

[Shin et al., 2004]. This region corresponds with lock release experiments that generate GCs with finite volumes. However, the case $h > 0.5H$, i.e., when $\Delta\hat{\dot{E}} < 0$ is *a priori* impossible, unless an external source of energy is supplied to the current.

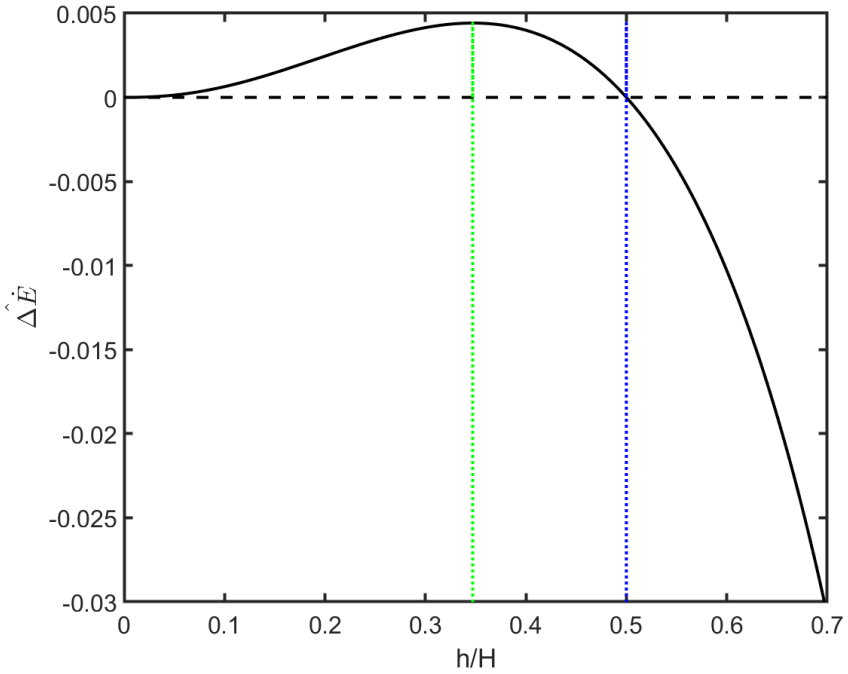

Figure 3.1.1: Dimensionless energy loss $\Delta\hat{\dot{E}}$ as a function of h/H (h being the current thickness and H the domain depth) [Shin et al., 2004]. The dotted blue line corresponds to the energy-conserving case [Benjamin, 1968] while the dotted green line denotes the current thickness associated with maximum energy loss. The black dashed line represents the energy-conserving case.

The relevance of GCs to this study is that they are a class of stratified shear flow within which both SDGIs and KHIs, as well as their interaction, can be studied. Indeed, because of the gravitational spreading, the induced shear at the interface between the current and the ambient may trigger shear instabilities such as KHIs [Thorpe, 1973; Patterson et al., 2006]. Those shear instabilities then tend to cause mixing between the current and the ambient by entrainment [Ellison and Turner, 1959; Christodoulou, 1985; Strang and Fernando, 2001]. This results in local changes in the density gradient and ultimately affects the buoyancy properties of the current. Furthermore, in the presence of particles, this mixing process also affects the sedimentation of particles. Indeed, among the various studies on GCs, some experimental ones have focused on the effect of sedimentation during the spreading

of currents through stratified environments [Maxworthy, 1999; Sutherland et al., 2018, 2021]. These particle-bearing GC experiments are generally scaled in order to investigate the deposition of sediments from turbulent plumes in riverine, lacustrine or coastal environments [McCool and Parsons, 2004; Parsons et al., 2001; Davarpanah Jazi and Wells, 2020]. Interestingly, similarly to our static experiments (cf. Chapter 2), McCool and Parsons [2004] highlighted that the sedimentation from highly concentrated plumes is dominated by convective settling, with the resulting convective plumes, that can be associated with SDGIs, having a settling velocity twice the expected Stokes velocity for individual particles. This is an important outcome as SDGIs are a process with significant implications for sediment removal from particle-rich plumes such as volcanic clouds [Scollo et al., 2017; Carazzo and Jellinek, 2012; Manzella et al., 2015].

3.1.2 Shear associated with wind advection: the case of the 2010 eruption of Eyjafjallajökull

In the second part of this chapter, we go beyond the previous laboratory-scale simulations to consider the more complex configuration of a volcanic ash cloud at the natural scale. We focus on the 2010 Eyjafjallajökull eruption, for which the second phase lasted from the 14^{th} of April to the 24^{th} of May. During this event, SDGIs have been observed and further measurements such as the deposit grainsize distribution have been performed. A wide range of eruption source parameters (ESPs) exist that include the volume fraction of ash in the cloud, total grain-size distribution (TGSD), erupted mass, plume height, mass eruption rate and ash texture [Cioni et al., 2014; Bonadonna et al., 2011; Kaminski et al., 2011; Taddeucci et al., 2011; Bagnato et al., 2013; Borisova et al., 2012; Dellino et al., 2012; Gislason et al., 2011; Gudmundsson et al., 2012; Degruyter and Bonadonna, 2012; Marzano et al., 2016; Mereu et al., 2015]. Furthermore, the observed SDGIs have been characterised for the first time using both video acquisitions and field observations of the tephra deposit [Manzella et al., 2015].

The input parameters used in our model come from the work of Bonadonna et al. [2011] (for the TGSD and particle density) and Manzella et al. [2015] (for the total

particle volume fraction, the wind velocity and the cloud spreading velocity) who performed quantitative observations on the 4th of May. Although satellite measurements could be used to estimate the ash concentration at large scales [Gudmundsson et al., 2012; Prata and Prata, 2012], there is strong uncertainty on local variations that could be relevant to SDGI triggering [Manzella et al., 2015]. We therefore use the observed vertical propagation velocity of fingers [Manzella et al., 2015] and the analytical formulation of Carazzo and Jellinek [2012] to calculate the approximate range for the particle volume fraction [Manzella et al., 2015]. Indeed, we recall that, for a given particle size, the analytical estimation for the vertical velocity of fingers proposed by Carazzo and Jellinek [2012] is given by

$$V_f = g'^{\frac{2}{5}} \left(\frac{V_s \pi \delta_{PBL}^2}{4} \right)^{\frac{1}{5}}, \tag{3.5}$$

where V_s is the individual particle settling velocity, δ_{PBL} the thickness of the particle boundary layer (PBL) and $g' = g(\rho_{PBL} - \rho_a)/\rho_a$, $\rho_a = 1.3$ kg.m^{-3} being the density of the atmosphere and ρ_{PBL} the bulk density within the PBL. Then, assuming a vertical velocity of fingers measured at $V_f = 1.0 \pm 0.5$ m.s^{-1}, a δ_{PBL} measured at approximately 90 m and $V_s = 1$ m.s^{-1}, the PBL bulk density can be estimated as $\rho_{PBL} = 1.30 - 1.31$ kg.m^{-3}. Ultimately, also assuming the density of volcanic ash in the interval [1400-1700] kg.m^{-3}, the particle volume fraction is estimated in the range $[1 \times 10^{-6}; 4 \times 10^{-6}]$ [Manzella et al., 2015].

Regarding the initial particle size distribution in the cloud, we can assume that it can be approximated with the TGSD determined by Bonadonna et al. [2011] for the time period between the 4^{th} and 8^{th} of May. In their study, Bonadonna et al. [2011] combined the size distribution of the ground deposit with satellite measurements to characterise the TGSD within a distance range of [2-1000] km from the vent (Figure 3A.1a). Additionally, the associated pumice densities have been computed as a function of the grain size (Figure 3A.1b) . We clearly observe that the TGSD is mostly unimodal and centred around $Phi = 1$ ($Phi = -log_2(D/D_0)$, D being the particle diameter in mm and D_0 a reference diameter equal to 1 mm). However, grainsize distributions at individual locations are often bimodal, suggesting premature deposition of fine ash [Manzella et al., 2015; Cioni et al., 2014].

Finally, it was observed that there was a difference between the volcanic cloud spreading velocity and the ambient wind speed during the 2010 Eyjafjallajökull eruption. This discrepancy in velocity suggests that the volcanic cloud holds some inertia and, therefore, the induced shear may have a significant effect on the development and dynamics of SDGIs. The volcanic cloud velocity $U_{cloud} = 7.9 \pm 1.3$ m/s has been measured by Manzella et al. [2015] using records of High-Definition videos captured during the event on the 4^{th} of May (12:49:21 GMT). The associated wind velocity $U_{wind} = 11 \pm 0.5$ m/s has been extracted from meteorological models which interpolate the conditions at the desired location (European Centre for Medium-Range Weather Forecasts ERA-40 reanalysis interpolated at 0.25° resolution above the volcano) [Manzella et al., 2015].

3.1.3 Aims and objectives

In order to investigate the effect of shear on SDGIs, we use the hybrid 3D single-phase model developed in the previous chapter. This model uses the Lattice Boltzmann method (LBM) to solve for the fluid motion, a 3^{rd} order WENO (weighted essentially non-oscillatory) scheme to solve for the transport of particles and a 1^{st} order upwind finite-difference scheme to solve the transport of any density-altering quantity. We consider two configurations which represent different scales and address shear associated with gravitational spreading and wind advection, respectively:

- First, we reproduce aqueous laboratory experiments where lock-release GCs that have been generated with the aim of studying the lateral spreading of volcanic clouds. A first part involving particle-free gravity currents aims at the validation of the 3D hybrid model regarding the addition of lateral motion. This validation involves comparison of the simulation results with experimental and theoretical results including the current front velocity and thickness. We then consider particle-bearing currents to examine the effect of sedimentation on current properties.

- Second, we investigate the shear associated with wind advection as a comparison with the case study of the 2010 eruption of Eyjafjallajökull where

SDGIs have been observed and key ESPs have been characterised based on multidisciplinary strategies. The first goal is to constrain the ranges of input parameters that enable triggering of SDGIs. Then, we examine the ground deposits produced during the simulations to identify the specific ground signature of SDGIs.

3.2 Methods

3.2.1 Gravitational spreading of particle-free clouds and particle-bearing experiments

The configuration is designed to reproduce laboratory experiments reported in Jarvis et al. [in prep]. By reproducing these experiments, we can first further validate the numerical model and, secondly, identify the fundamental physics underpinning the relationship between gravitational spreading and SDGIs. As an extension of previous static laboratory experiments [Manzella et al., 2015; Scollo et al., 2017; Fries et al., 2021], the apparatus involves a flume of dimensions 12.2 × 329 × 50 cm, with a removable gate 29 cm from one end separating the flume into short and long sections. Initially, the short part of the flume is filled with the light fluid (freshwater and dye or freshwater particle suspension) whilst on the other side of the gate is a denser sugar solution. The height of fluid both sides of the gate is 40 cm. Upon gate removal, buoyancy-driven lateral motion of the lighter layer initiates, creating a gravity current that propagates along the free-surface. Using a numerical domain of size 12.2 × 329 × 40 cm (see Figure 3.2.1), we have performed two sets of simulations (see Table 3.2.1 for the list of simulations performed).

Particle-free clouds: comparison between laboratory experiments and numerical model

The first set of simulations involves the lateral spreading of particle-free gravity currents and allows us to validate the numerical model as well as investigate the effect of varying the reduced gravity $g' = (\rho_1 - \rho_c)/\rho_1$, where ρ_1 is the density of the sugar solution and ρ_c is the bulk density of the current, on the lateral spreading. We

tested two different boundary conditions (no-slip and free-slip) for the top boundary (corresponding to the free-surface). The no-slip boundary condition, implemented with the bounce-back method, imposes zero velocity relative to the boundary while the free-slip imposes zero-gradient for the tangential velocity components. In order to visualise the spreading current, a red dye was added to the experiments in Jarvis et al. [in prep]. In these simulations, we track the evolution of this dye by defining a scalar field $a(\mathbf{x}, t)$, initialised as shown in Figure 3.2.1, and relate it to the fluid density $\rho(\mathbf{x}, t)$ through

$$\rho(\mathbf{x}, t) = \rho_2 a(\mathbf{x}, t) + (1 - a(\mathbf{x}, t))\, \rho_1. \tag{3.6}$$

As described previously, we maintain the three-way coupling model using the LBM to solve for the fluid motion coupled with finite difference schemes for the fluid density and the dye concentration.

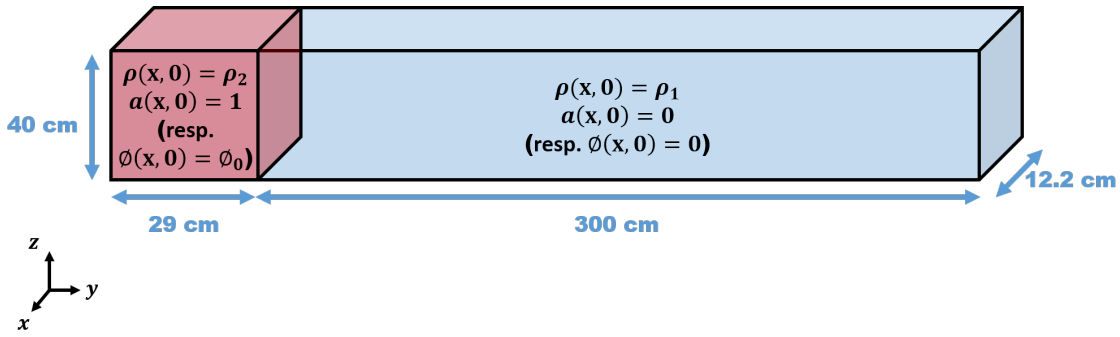

Figure 3.2.1: Numerical domain used to simulate the lock-release experiments (modified from [Jarvis et al., in prep]).

Gravitational spreading of particle bearing clouds

The second set of simulations involves particle-bearing gravity currents to investigate the effect of lateral spreading on settling and especially on SDGIs. As shown on Figure 3.2.1, the particle-suspension is initially set up with Φ_0 (with the additional perturbation to trigger instabilities). In the previous chapter, we showed that SDGIs are sensitive to the initial particle volume fraction Φ_0. Therefore, in order to avoid the influence of the particle volume fraction and to isolate the effect of the lateral spreading on the sedimentation process, we keep Φ_0 constant and only vary the sugar

Simulation	g' (m s^{-2})	Fresh water density (kg/m^3)	Sugar solution density (kg/m^3)
A1	0.00451	1003.04	1003.5
A2	0.00940	1003.04	1004
A3	0.01912	1003.04	1005
A4	0.0289	1003.04	1006
A5	0.0386	1003.04	1007
A6	0.0483	1003.04	1008
A7	0.0580	1003.04	1009
A8	0.0676	1003.04	1010
A9	0.0773	1003.04	1011
A10	0.0869	1003.04	1012
B1	0.00451	1000	1003.5
B2	0.00550	1000	1003.6
B3	0.00647	1000	1003.7
B4	0.00744	1000	1003.8
B5	0.00842	1000	1003.9
B6	0.00940	1000	1004
B7	0.0192	1000	1005
B8	0.0289	1000	1006
B9	0.0386	1000	1007
B10	0.0483	1000	1008
B11	0.05780	1000	1009
B12	0.0676	1000	1010
B13	0.0773	1000	1011
B14	0.0869	1000	1012

Table 3.2.1: List of performed simulations. Gray shaded part: particle-bearing gravity currents. For those simulations the particle size is 40 μ m and the initial volume fraction is $\Phi_0 = 2 \times 10^{-3}$.

solution density. As usual, the transport of particles is described by an advection-diffusion-settling equation for the volume fraction and solved using the WENO finite difference procedure.

We use some post-processing procedures in order to compute parameters such as the current front velocity, the current average thickness and the ground accumulation rate. Similarly to the static case-study (Chapter 2), we extract a slice in the (y, z) plane located at the middle of the tank depth for each simulation. Then, we measure the front head displacement at several time steps in order to compute the spreading velocity.

In order to compare with the particle-free experiments, we measure the front position with the same method used in [Jarvis et al., in prep]. Along a horizontal line located 2 cm under the free-surface, we evaluate the position at which $a(\mathbf{x}, t) = a(\mathbf{x}, 0)/2$ (see Figure 3.2.2 for an example of the front detection). For particle-bearing experiments, this method is no long valid because the head of the current can settle below this transect. In this case, the front head is defined as the maximum position along the y-axis where $\Phi = \Phi_0/2$.

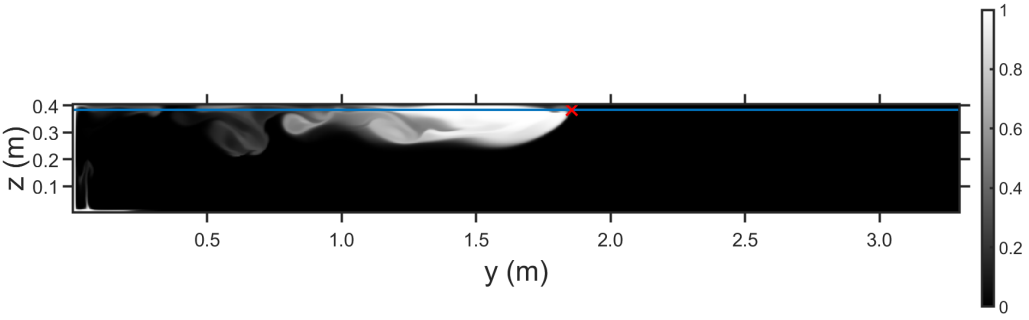

Figure 3.2.2: Detection of the front position for a simulation with $g' = 9.40 \times 10^{-3}$ m s^{-2} at the time $t = 55$ s. The solid blue line is the detection line located 2 cm under the water free-surface. The red cross is the detected position of the current front. The colorbar is associated with the value of $a(\mathbf{x}, t)$.

In order to measure the average variation of the current thickness we consider a measurement window between positions $x = y_i = 1$ m and $x = y_f = 2$ m. Whilst the head of the current is propagating through this window, we measure the current thickness between the points at 10 and 20 cm upstream of the current front. To do so, we first compute the profile of a (for the particle-free currents) or Φ (for the settling currents) along a vertical line. Then, the thickness is defined by the distance between two points on that line where a and Φ reach half of their initial values (see Figure 3.2.3). This thickness is then averaged across the distance between 10 and 20 cm upstream of the current front. Finally, we define the thinning rate of the current head by dividing the absolute change in average thickness divided by the time taken by the current to cross the measurement window.

Finally, the accumulation rate of sediment on the domain floor Θ is computed in the same way as in chapter 2 with

$$\Theta = \frac{1}{A}\frac{dm_b}{dt}, \tag{3.7}$$

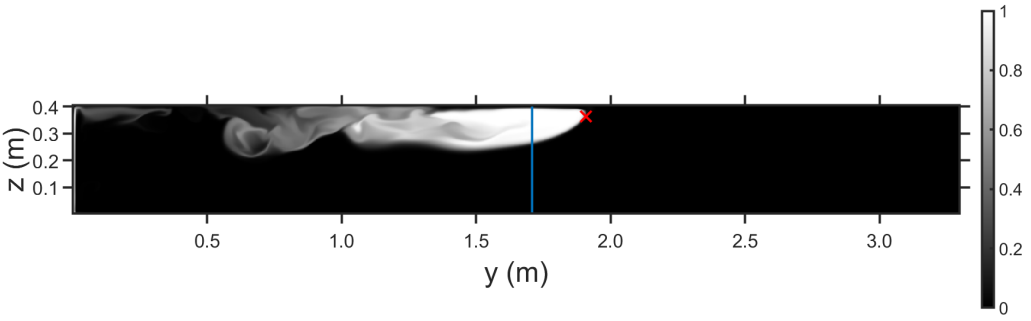

Figure 3.2.3: Example of measurement for the current thickness 20cm before the front

where A is the area of the collection surface, t time since start of the simulation and m_b the mass of particles accumulated on the ground.

3.2.2 Case study: the 2010 Eyjafjallajökull eruption

A key difference between these simulations and those presented in Section 3.2.1 is that the carrier fluid is now air instead of water. We, therefore, take an air density of 1.3 kg.m^{-3} and a kinematic viscosity of 1.4×10^{-5} m^2 s^{-1} (see Table 3A.1 in Appendix 3.A). Furthermore, the domain is a box of dimensions 3 $\times$ 20 $\times$ 3 km in order to simulate a volcanic cloud. The longest dimension is aligned with the spreading direction of the plume. Within this domain, simulations are initiated with two superposed layers which represent the volcanic ash cloud and the underlying atmosphere, respectively. Regarding the spatial discretisation, each grid cell represents a distance of 30 m. As seen in Figure 3.2.4, the velocity field U is initially imposed with a step change corresponding to the situation where the cloud spreading velocity is lower than the wind velocity [Manzella et al., 2015]. Thus, the different boundary conditions used for the fluid field are (Figure 3.2.4):

- inlet at $(x, 0, z)$
- outlet at $(x, 20, z)$
- no-slip (i.e. zero value for U on the ground) at $(x, y, 0)$
- Dirichlet conditions for the others (i.e., cloud spreading and wind velocity respectively)

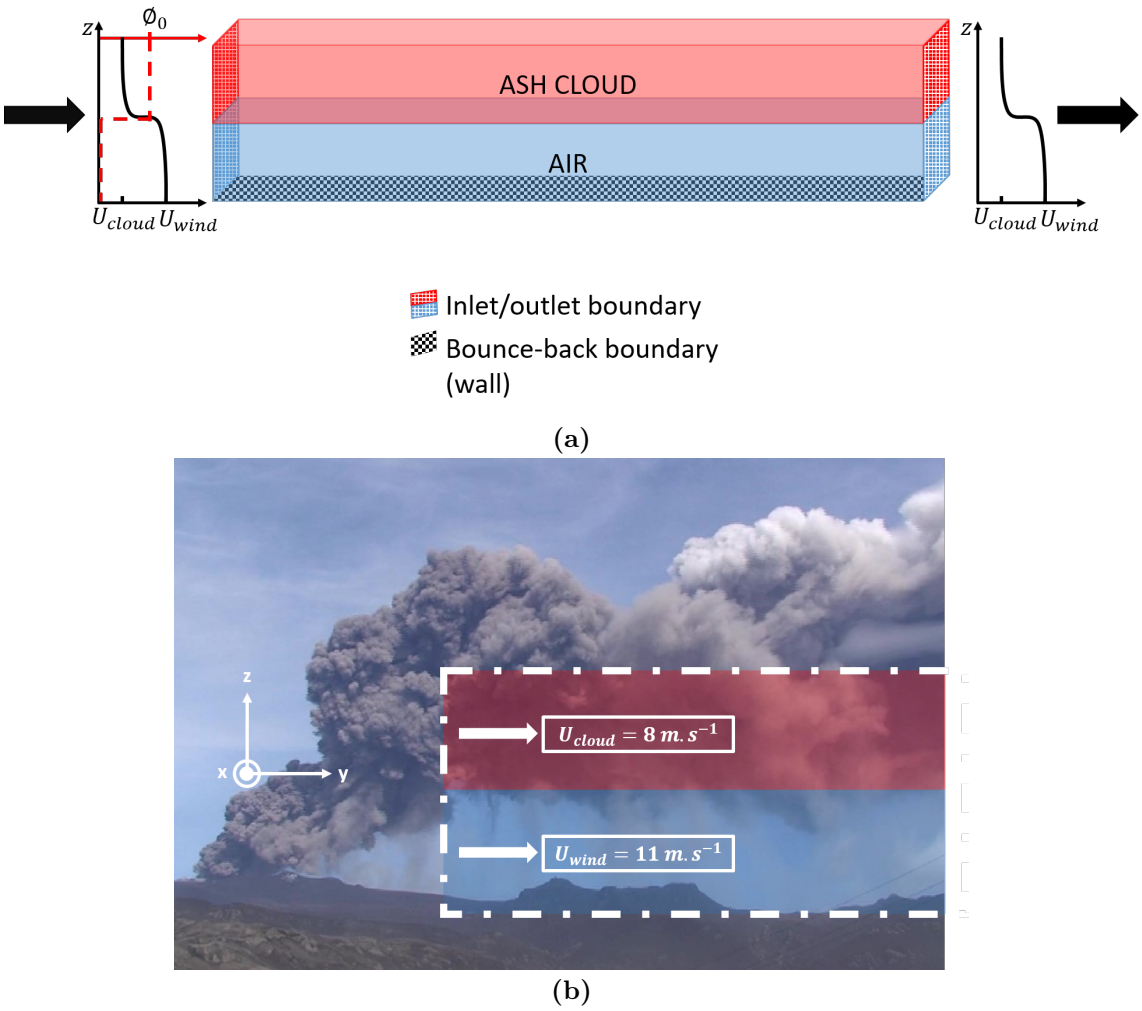

Figure 3.2.4: (a) Sketch of the numerical domain used in the simulations inspired from (b) the natural case of the 2010 Eyjafjallajökull eruption. Data from Manzella et al. [2015].

For this case study, we use a polydisperse particle size distribution, and we solve simultaneous advection-diffusion-settling equations (cf equation 2.7 Chapter 2) for each class. Indeed, in order to reproduce the settling dynamics of a volcanic cloud and the associated deposit as accurately as possible, it is necessary to utilise the total grain size distribution (TGSD) as an input. We initialise 12 particle size classes, where the volume fraction of each is represented as a single scalar fields, from -2 to 9 *Phi* ($Phi = -\log_2(D/D_0)$ (D being the particle diameter in mm) and D_0 a reference diameter equal to 1 mm) in order to represent the TGSD (cf. Figure 3A.1a). Thus, each particle volume fraction field is initiated uniformly within the upper layer with the value $\Phi_i = f\,(\Phi + \xi)$, where f is the fraction of material contained within size class i, ξ a small perturbation in order to trigger the instability

and Φ is the total volume fraction. Throughout the simulation, this volume fraction for each size fraction is maintained at the inlet, representing particle supply from the plume. The model is then iterated in time to allow a steady flow to establish before starting post-processing analysis. Given the significant uncertainty related to the total particle volume fraction Φ_{tot} in the volcanic cloud, especially around the zone where SDGIs are triggered, we performed several simulations using four different values, $\Phi_{tot} = [4 \times 10^{-6}; 1 \times 10^{-5}; 2 \times 10^{-5}; 3 \times 10^{-5}])$ in order to constrain the critical value that trigger SDGIs. Note that the first value is the one suggested by Manzella et al. [2015] in order to be consistent with the collapsing PBL theory [Carazzo and Jellinek, 2012].

3.3 Results

3.3.1 Particle-free gravity currents

The set of particle-free simulations allows us to validate the numerical model by reproducing the lateral spreading of the current. A qualitative comparison with the lock release experimental results shows that the numerical model accurately reproduces the behaviour of gravity currents generated in the laboratory. Indeed, Figure 3.3.1 shows snapshots of both experiments and numerical simulations at different times for the same reduced gravity. Despite some slight differences in the spreading velocity, the simulations show similar shapes of the current and, in both cases, billows appear at the base of the cloud from the beginning of the lateral motion. Also, we observe that upstream of the current head, some current fluid is left behind and takes the form of a tail.

For a more quantitative validation, the current front velocity was measured and compared with the experimental results and with the aforementioned analytical formulation (equation 3.3). To calculate the simulated current velocity, we consider the front position of each current as a function of time (Figure 3.3.2a). The current velocity is approximately constant along the domain, suggesting that the current remains in the slumping phase throughout [Huppert and Simpson, 1980; Simpson, 1997]. We, therefore, perform the current front velocity measurement from the

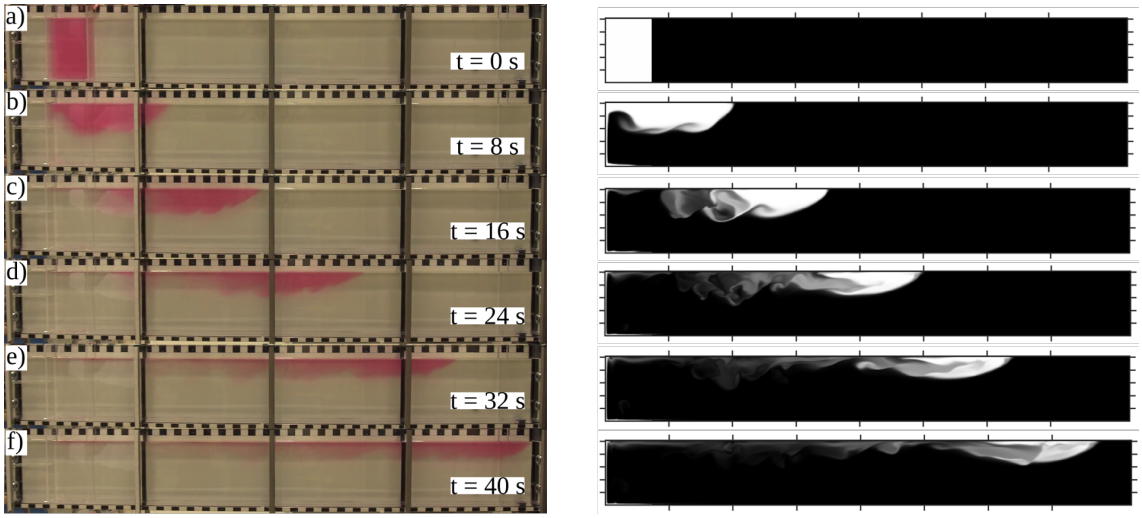

Figure 3.3.1: Qualitative comparison between flume experiments (left) [Jarvis et al., in prep] and analogue numerical simulations using the top free-slip boundary condition (right) at different times. g'=0.057 m s^{-2}

positions $y = y_i = 1$ m and $y = y_f = 2$ m. Figure 3.3.3a shows the measured current front velocity as a function of g' for both no-slip and free-slip upper boundary conditions. The error bars are given by the standard deviation of the set of front velocities computed between different time steps. We observe a good agreement between the experimental results and the numerical simulations using the free-slip top boundary. There is also a very good agreement with Benjamin's analytical model using a value of 1/2 for the Froude number. In addition, we show that the current front velocity using free-slip boundary conditions is greater than the value obtained using no-slip conditions, suggesting a lower value of Fr_H. As shown on Figure 3.3.3b and considering the equation 3.2, the best fit of the Froude number for the no-slip results seems to be $Fr_H = 0.42$. This agrees with the results of Härtel et al. [2000] who used numerical simulations to show that $Fr_H^{free-slip} > Fr_H^{no-slip}$ (i.e., $U^{free-slip} > U^{no-slip}$).

Another interesting aspect is related to the evolution of gravity current depth as it provides indications about the energy balance during the spreading. As mentioned before, we observe that some fluid is left behind and also that the current occupies less than half of the flume depth. These facts suggest that energy is not conserved. Figure 3.3.4 shows an example of a particle free gravity current with $g' = 0.004511$ m s^{-2}. We observe that, despite some perturbations to the current interface at

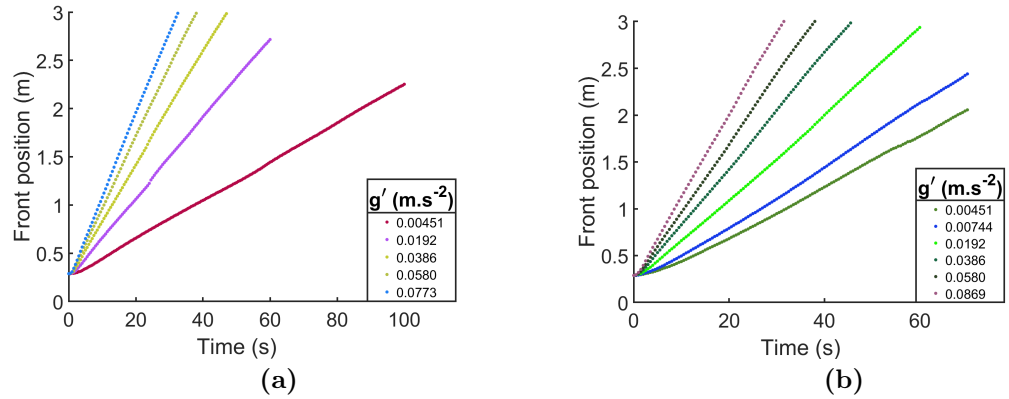

Figure 3.3.2: Current front absolute position as a function of time for (a) the particle-free simulations and (b) the particle-bearing simulations.

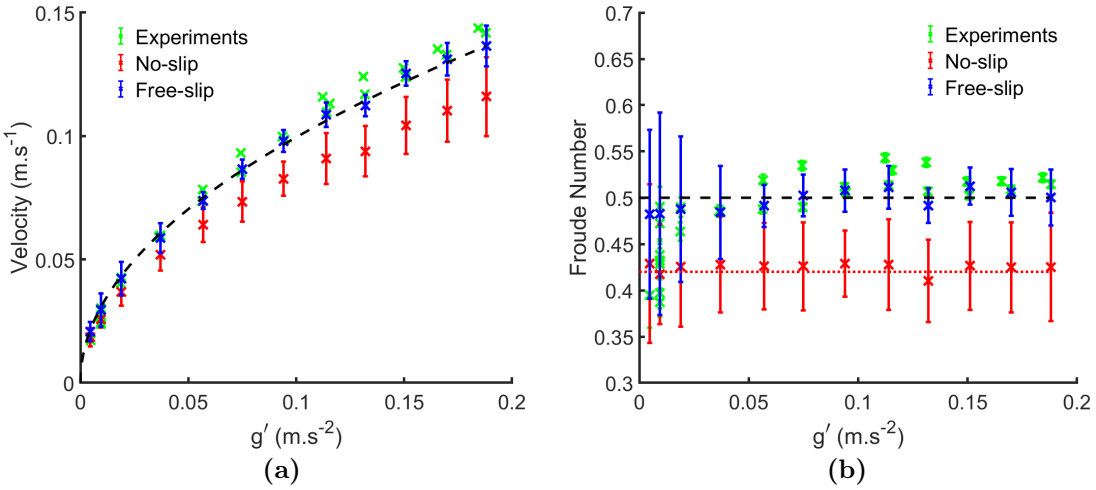

Figure 3.3.3: (a) Particle-free gravity current front velocity as a function of the reduced gravity for the experiments and the numerical simulations (no-slip and free-slip). The black dashed line refers to equation 3.3. (b) Associated Froude number. The black dashed line and the red dotted line denote $Fr_H = 1/2$ and $Fr_H = 0.42$, respectively.

the start of the spreading, the current occupies less than half of the flume depth. Moreover, the current depth seems to stabilise at the maximum energy loss level, i.e., when the current depth is $h = 0.347H$ as shown in Figure 3.3.5.

3.3.2 Particle-bearing gravity currents

The second set of simulations now involves particle-bearing currents and the associated settling process. In Figures 3.3.2b and 3.3.6a we observe that the presence of particles does not seem to affect the current front spreading velocity as the results still fit Benjamin's analytical model (using $Fr_H = 1/2$). However, when computing

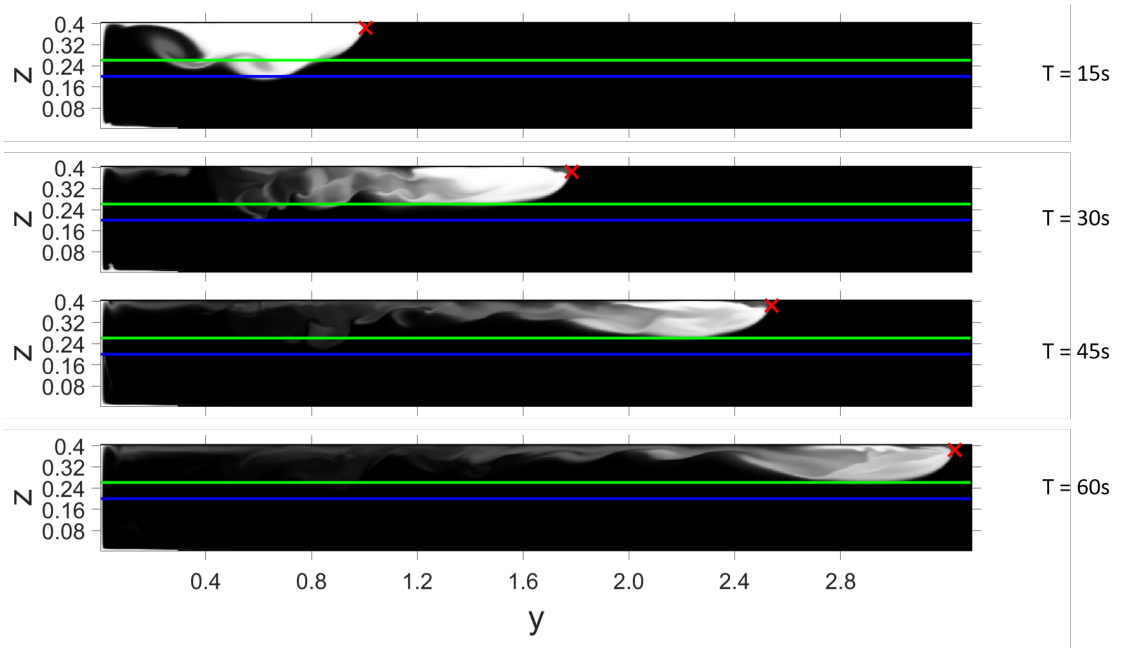

Figure 3.3.4: Snapshots of simulations without particles for $g' = 0.004511 m.s^{-2}$ at different times. The solid blue line corresponds to $h = 0.5H$ while the solid green line is for $h = 0.347H$.

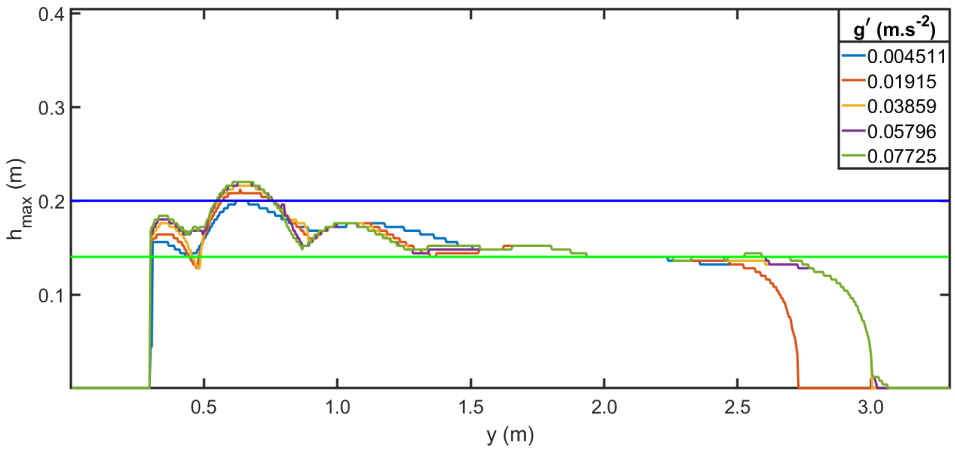

Figure 3.3.5: Evolution of the maximum current thickness h_{max} as a function of its associated position while the current front is located between $y = 1$ m and $y = 3$ m. The solid blue line corresponds to $h = 0.5H$ while the solid green line is for $h = 0.347H$.

the Froude number as shown in Figure 3.3.6b, we clearly observe that although the results agree with the energy-conserving value of 1/2, as g' decreases towards zero the Froude number appears to rapidly increase, as does the calculated uncertainty on the Froude number.

Additionally, we quantify the evolution of the current thickness in order to characterise the contribution of settling to the current shape evolution. Figure 3.3.7

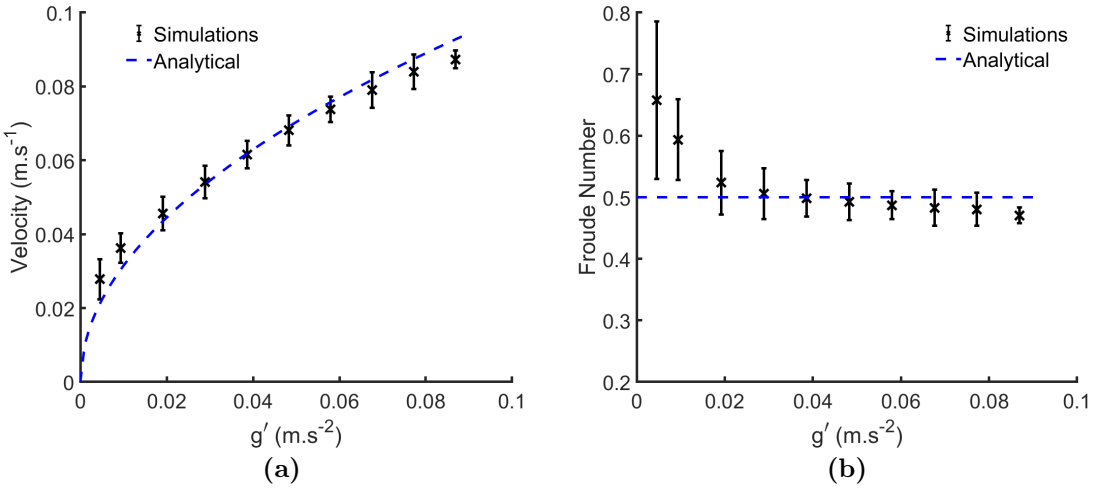

Figure 3.3.6: (a) Current front velocity (with particles) as a function of the reduced gravity for the numerical simulations (using free-slip upper boundary). (b) Associated Froude number. The dashed line denotes $Fr_H = 1/2$.

shows snapshots of simulations for different g' at time steps corresponding to when the current front has propagated approximately 2 m. The pictures on the left-hand side represent the particle volume fraction of the current while the right hand side shows the fluid density. First, we observe that for small values of reduced gravity, the settling process is important to the point that most of particles have settled before the current fully develops. Then, as g' increases, the current has enough inertia to overcome the sedimentation of particles. We also observe an effect of the presence of settling particles on the current shape. Indeed, we can see that for higher values of g', the current shape seems to be similar to that observed in the particle-free simulations. However, there is a difference around the current tail which stays below the $0.5H$ line. Moreover, there is a situation when the settling process is comparable with the lateral spreading (i.e. for smaller g'). We can quantify this by computing the ratio between the different characteristic velocities U/V_s with V_s the Stokes velocity of particles. Figure 3.3.8 shows this ratio as a function of g' and we observe that this ratio decreases monotonically with g'. However, for the smallest values of g' it appears that the ratio remains low suggesting that the lateral spreading is still the dominant process. Given the strong sedimentation observed in our simulations, this result implies that the Stokes velocity is not a relevant characteristic parameter and that particles settle faster by collective sedimentation. Additionally, we clearly

observe that the current head becomes thinner as we decrease the value of g'. The same behaviour is seen in the fluid density field, suggesting the particles seems to enhance the removal of fluid from the current and ultimately confirms the current head thinning.

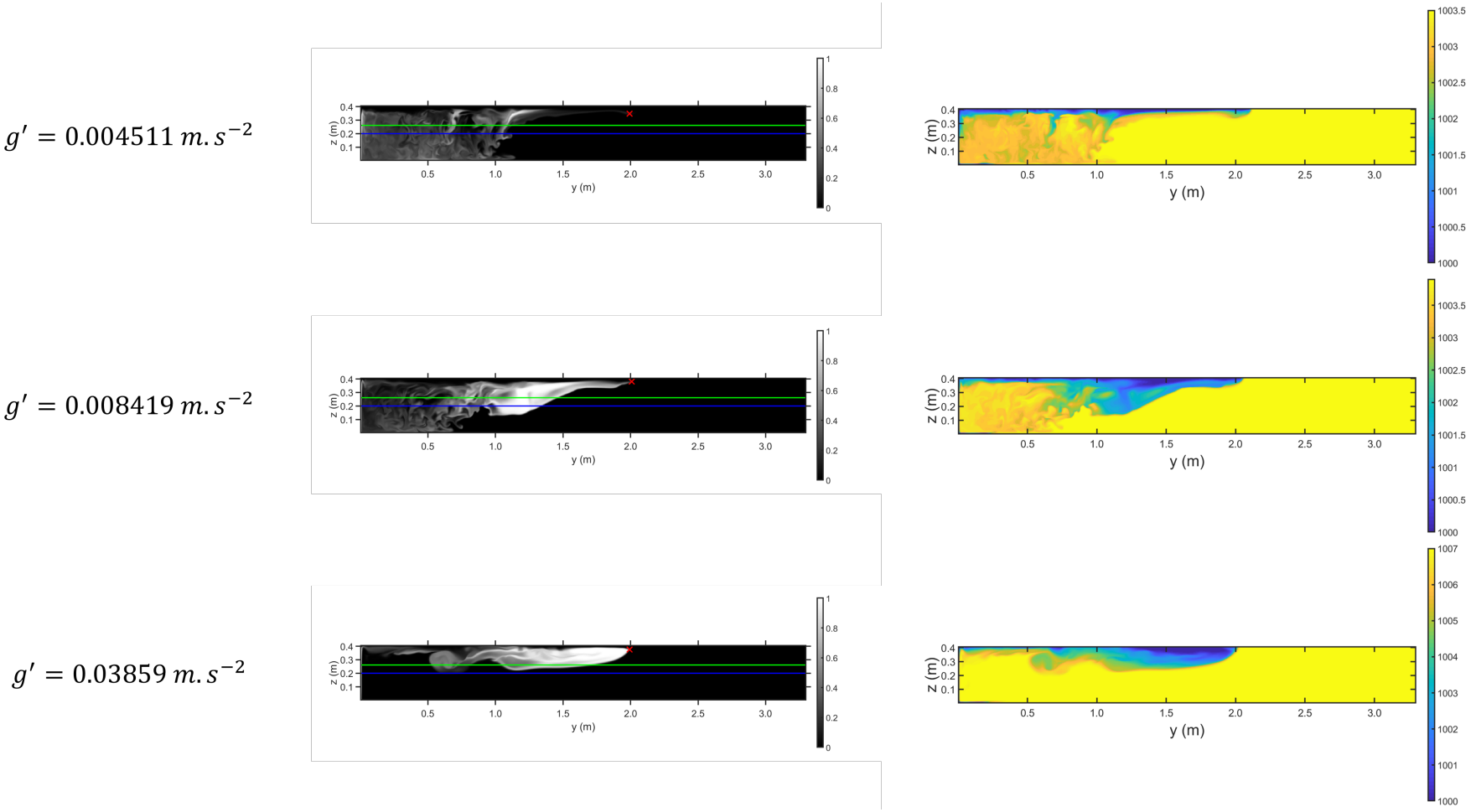

Figure 3.3.7: Snapshots of simulations for different values of g' at times when the current fronts is at ~ 2 m. Left: snapshots of the particle field. Right: snapshot of the fluid density field.

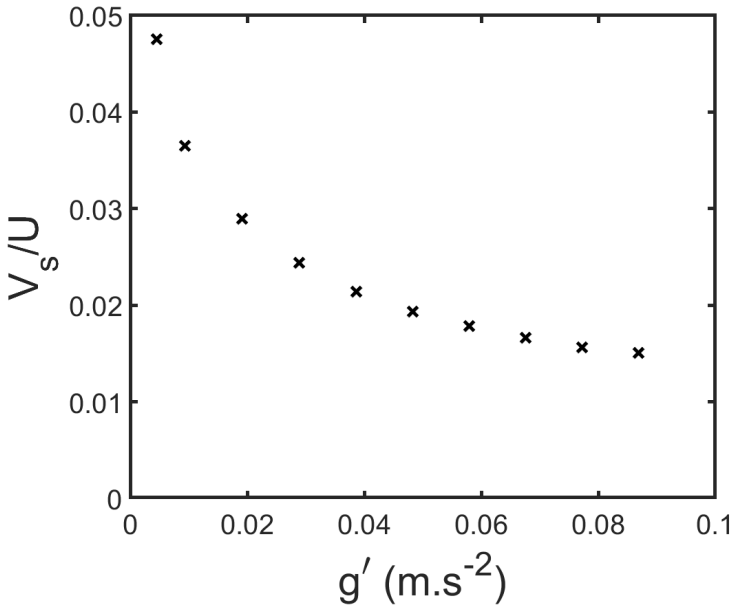

Figure 3.3.8: Ratio of theoretical characteristic velocities V_s/U (V_s the Stokes velocity of particles, and U the current front velocity) as a function of the reduced gravity g'.

Whilst the mechanisms causing the current thinning are different between the particle-free and the particle-bearing currents, we also quantify the evolution of the current thickness during its lateral spreading. As shown in Figure 3.3.9, the current thickness seems to decrease almost linearly along the measurement window (1 - 2 m), allowing calculation of an average thinning rate. Figure 3.3.10 shows the thinning rate (averaged over 10 and 20 cm upstream of the current front) as a function of the reduced gravity. First, we observe that the thinning rate increases strongly as g' decreases towards zero. Second, as g' increases beyond approximately 0.02 m s^{-2}, the current thinning rate appears to converge to a fixed value which corresponds to approximately the individual particle settling velocity. All those results suggest the presence of two different regimes where the sedimentation process seems to influence strongly the current geometry (i.e. for small values of g') and where the effect is moderate.

We also look for evidence of the effect of SDGIs on sedimentation through quantification of the particle accumulation rate at the bottom of the domain. It has been previously noted in the static case that collective settling through fingers causes an increasing accumulation rate (compared to a constant value for individual settling). Figure 3.3.11 shows the accumulation rate computed at the bottom of the domain

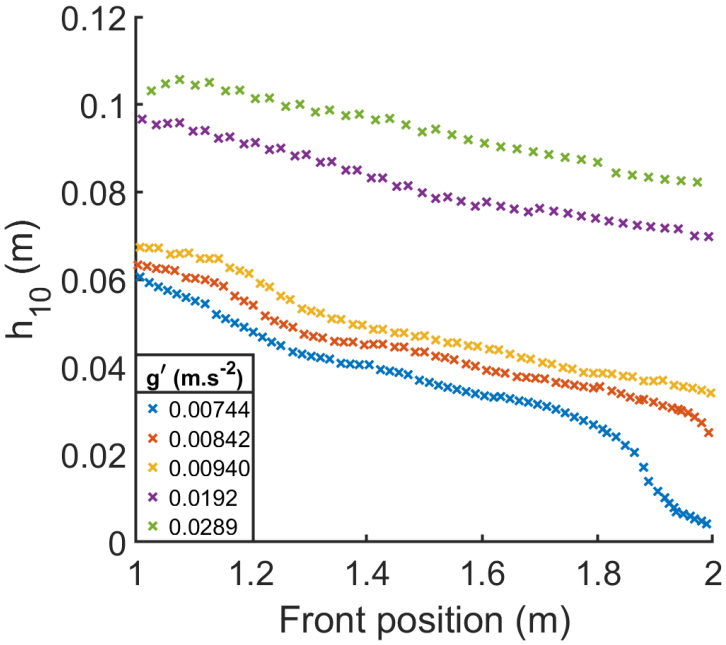

Figure 3.3.9: Current thickness h_{10} measured 10cm upstream from the front, along the measurement window.

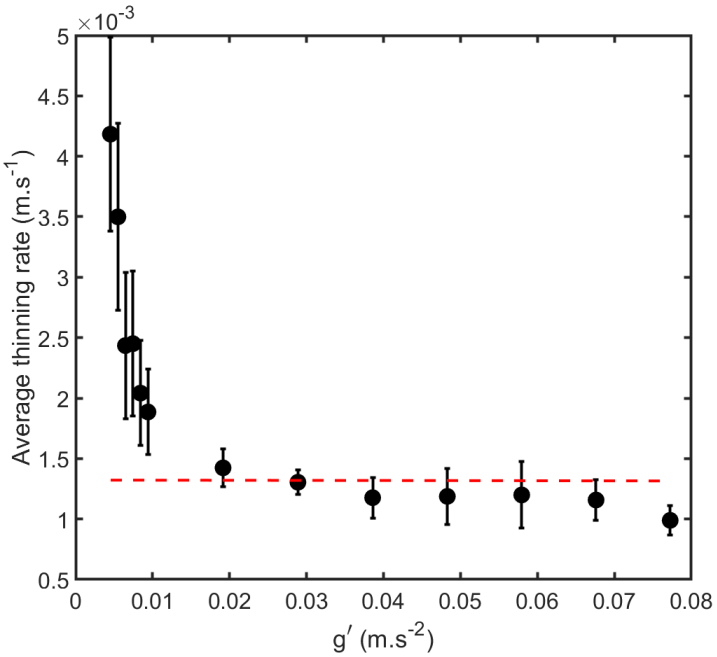

Figure 3.3.10: Average thinning rate as a function of g'. The red dashed line is the particle Stokes velocity.

between the positions $x = 0.29$ m and $x = 3.29$ m. Because the domain located between $x = 0$ m and $x = 0.29$ m is affected by the initial deposition of particles (by individual settling) before the current spreading, we do not take it in account.

First, we observe that increasing the value of g' delays the onset of particles reaching the floor by sedimentation. Second, the trend is similar to the static case as we note an increasing phase which is terminated by a constant phase. However, here the increasing phase may not be easily related to collective settling. Indeed, the accumulation rate for the static configuration was computed using vertical flux through a fixed surface which is no longer the case for the spreading configuration. Finally, for greater values of g', the current appears to have enough inertia to avoid any sedimentation during the spreading phase. It is the case for the curves related to $g' = 0.02888$ m.s^{-2} and $g' = 0.03859$ m.s^{-2} where all the sedimentation occurs after the spreading phase i.e. after the current has reached the end of the domain.

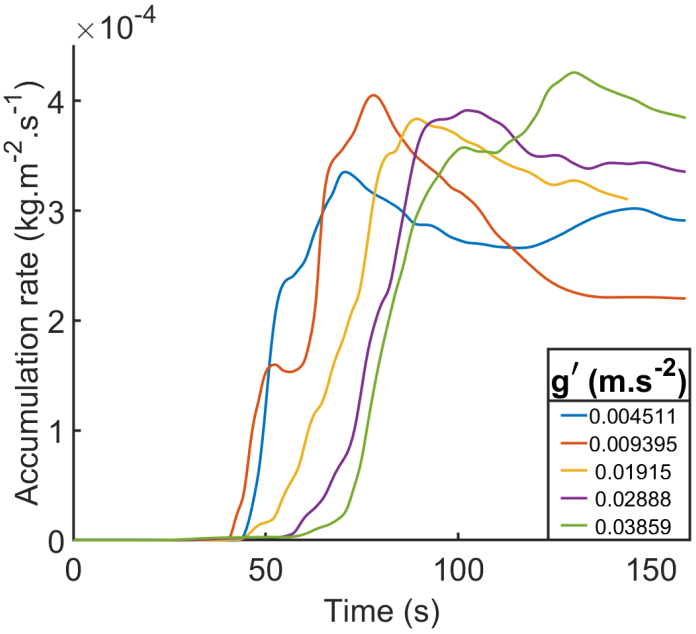

Figure 3.3.11: Accumulation rate computed at the bottom boundary of the domain for different values of g'.

Finally, we also analyse the spatial distribution of the deposit. Figure 3.3.12 shows the accumulation rate computed at the bottom of the domain at the moment when the current head is around the position $y = 2$ m. First, we observe that the area of the deposit increases as g' decreases. Second, the accumulation rates are heterogeneously distributed, contrary to what would be expected in the case of individual settling.

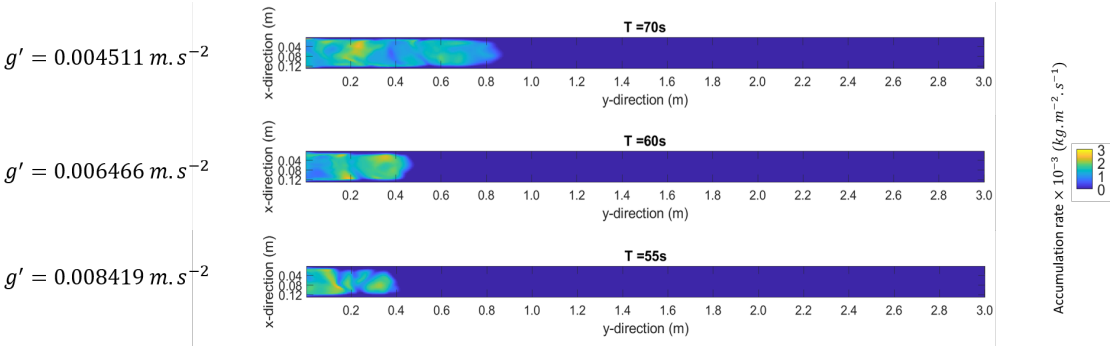

Figure 3.3.12: Accumulation rate at the domain bottom for different values of g'. The situation corresponds to the one showed on Figure 3.3.7

3.3.3 The 2010 eruption of Eyjafjallajökull

A qualitative overview of the different simulations performed shows that Φ_{tot} is a critical and sensitive parameter. Using the value suggested by Manzella et al. [2015] ($\Phi_{tot} = 4 \times 10^{-6}$), we observed that no fingers were triggered within the domain as shown in Figure 3.3.13a. However, increasing the initial total volume fraction causes the formation of fingers at the base of the cloud. Indeed, we highlighted in the previous chapter that increasing the initial volume fraction enhances the development of instabilities at the density interface. So, we verify this aspect here as fingers are finally triggered with a greater value of Φ_{tot}. Figures 3.3.13b, 3.3.13c and 3.3.13d show simulation snapshots for $\Phi_{tot} = 1 \times 10^{-5}$, $\Phi_{tot} = 2 \times 10^{-5}$ and $\Phi_{tot} = 3 \times 10^{-5}$, respectively. We clearly observe that fingers start forming at the density interface. Interestingly, we note that for $\Phi_{tot} = 1 \times 10^{-5}$, fingers are forming but reach the ground quite far from the inlet (i.e., beyond 20 km). On the contrary, for $\Phi_{tot} = 3 \times 10^{-5}$, the cloud seems to destabilise around 6km from the inlet before completely collapsing around 10 km. Fingers on Figure 3.3.13c start forming around 6km and reach the ground in a range of [10-12] km from the inlet. As a comparison, according to the observations of Manzella et al. [2015] on the 4^{th} of May, fingers started to form around 1.4 km from the vent before reaching the ground approximately at 10 km from the vent. Another interesting observation is that coarse particles (with size ≥ 250 μm) fallout closer to the inlet than fine particles. This can be seen by following the lines corresponding to the trajectory of a coarse fraction, for example, between the inlet and the ground at $y = 2.5$ km.

Obviously, this fallout has an impact on the total tephra volume fraction in the cloud. Indeed, we measured the local volume fraction within the destabilising cloud layer, which can be associated with the PBL, in the blue boxes highlighted in Figure 3.3.13. As expected, this local total volume fraction is smaller than that at the inlet.

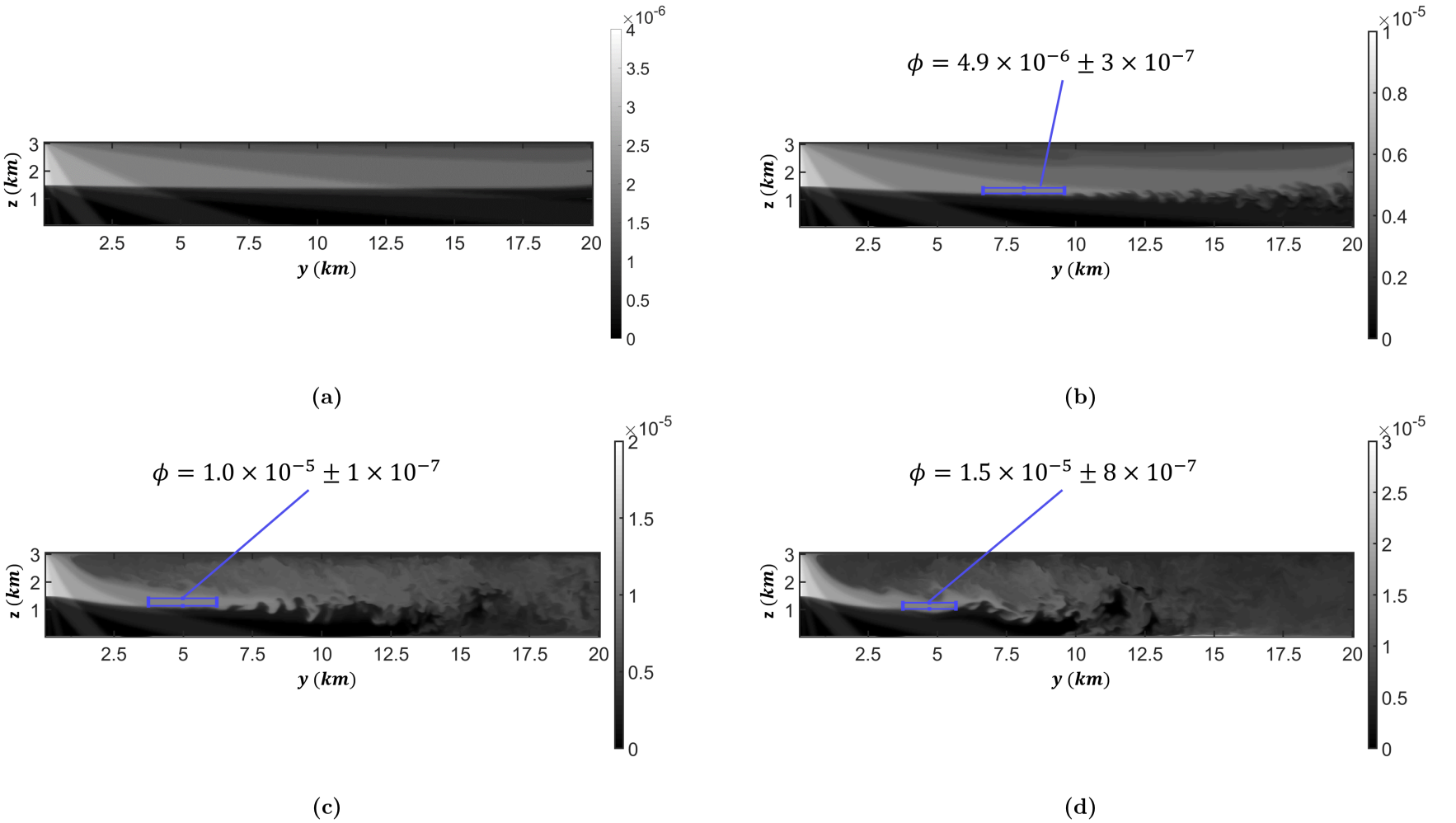

Figure 3.3.13: Simulations of a volcanic cloud using the 2010 Eyjafjallajökull eruption configuration for (a) $\Phi_{tot} = 4 \times 10^{-6}$, (b) $\Phi_{tot} = 1 \times 10^{-5}$, (c) $\Phi_{tot} = 2 \times 10^{-5}$ and (d) $\Phi_{tot} = 3 \times 10^{-5}$. The blue boxes are regions of interest in order to probe the local volume fraction in the destabilising cloud layer.

More quantitatively, we also investigate the ground deposit at specific downwind locations in order to determine the local size distribution of deposited particles. We calculate the particle size fraction X_i (in wt%) using the relation

$$X_i = 100 \times \frac{\phi_i}{\sum_i \phi_i}, \tag{3.8}$$

where ϕ_i is the volume fraction of each size class. Figure 3.3.14 presents the particle size distribution inside the ground deposit computed from simulations with different values of Φ_{tot} and we compare with the results found on the field [Manzella et al., 2015]. The collection durations for the different samples are 10 min for the sample EJ14, 96 min for the sample EJ15 and 50 min for the sample EJ17. In our simulations, the collection duration is fixed at 130 min. Globally, the Φ value associated with the distribution mode increases with the distance from the vent for all the cases as illustrated in appendix 3.B. However, in Figure 3.3.14a, the field sample at 10 km reveals a bimodal distribution. This aspect has been explained by the presence of processes that enhance the premature sedimentation of fine ash such as aggregation and SDGIs. The simulation using $\Phi_{tot} = 4 \times 10^{-6}$ does not present any bimodal distribution, which is consistent with the fact that no fingers were formed in this simulation. However, the size distribution for $\Phi_{tot} = 2 \times 10^{-5}$ is in reasonable agreement with the field observations, especially at 10 km where the distribution is also bimodal with equivalent modes. Finally, the bimodality at 10 km disappears for $\Phi_{tot} = 3 \times 10^{-5}$.

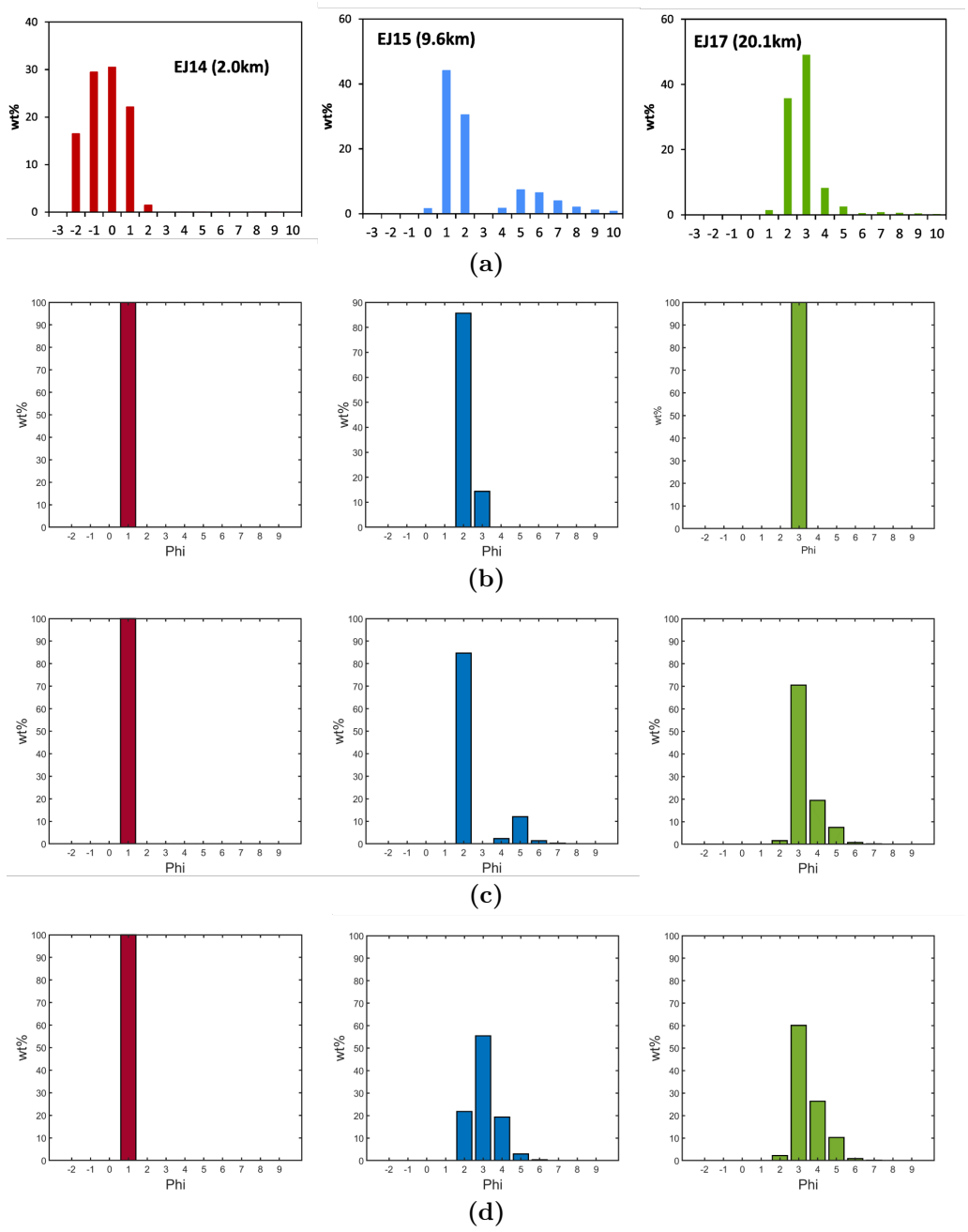

Figure 3.3.14: Size distribution in the deposit at 2 km (red), 10 km (blue) and 20 km (green) from (a) the field observations, (b) the simulations using $\Phi_{tot} = 4 \times 10^{-6}$, (c) $\Phi_{tot} = 2 \times 10^{-5}$ and (d) $\Phi_{tot} = 3 \times 10^{-5}$.

3.4 Discussion

3.4.1 Gravitational spreading

Using the model presented in the previous chapter, we have simulated the spreading of laboratory scale, buoyant gravity currents, propagating at a free surface. Our re-

sults allow us to validate the capabilities of the 3D hybrid model to produce lateral spreading of currents by buoyancy effects. The simulations have successfully reproduced both theoretically-predicted [Benjamin, 1968] and experimentally-measured current velocities and Froude numbers. However, we noticed some slight differences between the current spreading velocity measured in both the experiments and the simulations (cf. Figure 3.3.1). As the current spreading velocity in the simulations has been validated with theoretical predictions, the experiments/simulations discrepancy might come from uncertainties surrounding the start time of the experiments (i.e., the manual removal of the gate separating the two layers). Furthermore, we show that the equilibrium current depth is given by $h = 0.347H$. This is equal to the current depth theoretically predicted by a maximally-dissipating current [Shin et al., 2004] and thus, confirms the fact that the flow is not energy-conserving. Additionally in our simulations, as the maximum energy loss is associated with the maximum current speed, the current front speed remains at this maximum value, which is coherent with the constant value observed along the domain. This suggest finally that our configuration restricts the current spreading to the slumping phase [Huppert and Simpson, 1980; Simpson, 1997].

We have also gone beyond these validatory simulations by modelling buoyant gravity currents which carry a sedimenting particulate phase. These results have shown that there are some significant differences caused by the addition of particles to the behaviour of the current. Indeed, we showed that the presence of particles tends to increase the Froude number for small values of g' and, as illustrated by Figure 3.3.7, the sedimentation process becomes stronger as g' decreases. In fact, the apparent value of g' is calculated using the initial particle volume fraction. However, there is some delay between the lock-release time and the moment when the current becomes fully developed. For smaller values of g' this time is relatively long. Thus, during this time, there is some initial sedimentation of particles which causes the decrease of the volume fraction and thus, the current bulk density which ultimately increases the reduced gravity. Therefore, the effective g' of particle-bearing current with initially-small values of g' becomes greater than the initial value, leading to a higher Froude number.

Furthermore, our simulations have also shown that particles deposit on the ground as fast as g' decreases. However, the ratio of the characteristic velocities V_s/U (Figure 3.3.8) shows that V_s remains an order of magnitude lower than the spreading velocity. Since we observe considerable sedimentation in the simulations, this suggests that the particles' Stokes velocity is not relevant. Indeed, for smaller g', individual settling does not seem to be the preferred sedimentation mode, but rather collective settling. Therefore, if we consider, for example, the finger vertical velocity V_f proposed by Carazzo and Jellinek [2012] (cf. equation 2.1 in chapter 2) as a characteristic velocity, we note that both settling and spreading processes become comparable (Figure 3.4.1). Finally, this ratio decreases as soon as we increase g', implying that the lateral spreading is the dominant process. In fact, no collective settling was observed at the base of the current during spreading for high values of g'. This interesting observation suggests that the presence of shear and thus the associated inertial effects, tend to inhibit the development of instabilities at the density interface. Olson et al. [2011] and Shumlak and Roderick [1998] observed in their numerical investigations that the presence of shear between two moving, and also gravitationally unstable, layers, tends to stabilise the RTI process. Our results suggest that the same effect occurs in the case of settling-driven instabilities.

Additionally, the strong sedimentation during spreading affects the current geometry. Indeed, whilst the current thickness variation in the particle-free case is controlled by internal dissipative effects, the behaviour is significantly different in the case of particle-bearing currents. We observed in our simulations that the sedimentation of particles causes the thinning of the current head. According to Figure 3.3.10, we can identify two regimes separated by a critical value for the reduced gravity g'_c which seems to be around 0.02 m.s^{-2}. For $g' > g'_c$, the thinning rate converges to the rate of individual particle settling whilst, for $g' < g'_c$, the thinning rate strongly increases (i.e., with values much higher than the individual settling rate) as g' decreases, which suggests collective settling is taking place and enhancing the sedimentation of particles. Also, we note that the settling particles entrain some carrier fluid (cf Figure 3.3.7) which also causes the thinning of the current as seen in the fluid density field. Even though a volcanic cloud would deform because of

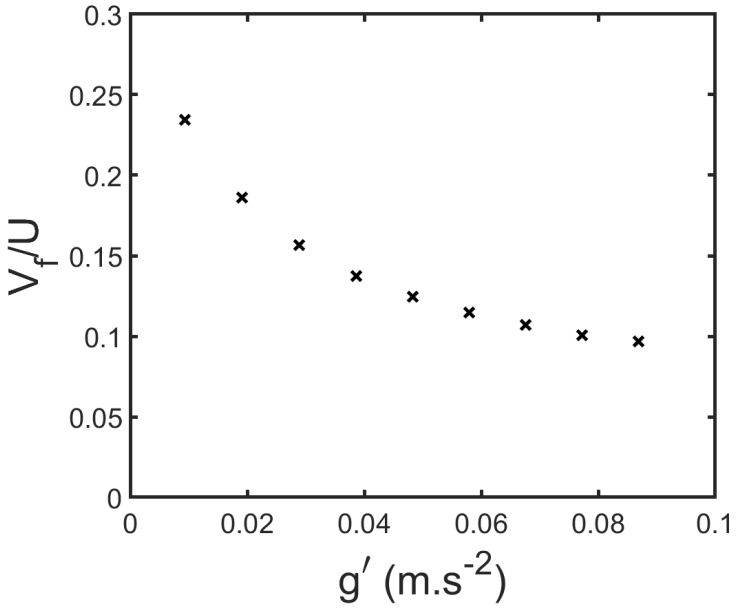

Figure 3.4.1: Ratio of theoretical characteristic velocities V_f/U (V_f being the finger vertical velocity calculated using the relation proposed by Carazzo and Jellinek [2012] and U the current front velocity) as a function of the reduced gravity g'

atmospheric diffusion or density stratification, these results suggest that measuring the volcanic cloud thickness variation could provide an indirect means of providing information on the ash sedimentation regime (i.e., individual or collective). Finally, similarities in the ground signature of SDGIs in sedimenting gravity currents have been found with the static case. In both cases, the computed accumulation rates at the bottom of the domain show an increasing phase. However, unlike in the static case, this phase in the spreading configuration cannot be easily attributable to collective settling. Nonetheless, the heterogeneous nature of the accumulation, as shown on Figure 3.3.12, remains a useful indicator for the presence of collective settling. Indeed in the case of individual settling, we should expect accumulating particles on a surface to grow at the same speed as the current front spreading, with no transverse variation. However, we clearly see in Figure 3.3.12 that the basal accumulation rate contains clear transverse heterogeneities.

3.4.2 Case study of the 2010 eruption of Eyjafjallajökull

Conditions for SDGIs

We selected the eruption of Eyjafjallajökull as a case study as this well-studied eruption allowed us to gather multiple data sources derived from field observations in order to set up a numerical configuration similar to the volcanic cloud. Our results have shown that the total volume fraction is a critical and sensitive parameter that controls the triggering of ash fingers. Our simulations suggest that Φ_{tot} is 5 times greater than the value proposed in the previous work of Manzella et al. [2015]. However, the value of Φ_{tot} includes the contributions of coarse particles that are too big to be entrained within fingers (i.e. they individually settled close to the vent). The volume fraction proposed by Manzella et al. [2015] is coherent with the theory of the PBL destabilisation [Carazzo and Jellinek, 2012] and is only valid for the fine portion of volcanic ash likely to be entrained within fingers. Indeed, in the static configuration, we also confirmed this theory as we start with a stable situation (upper layer lighter than the lower layer) which becomes unstable because of the PBL formation by settling. Instabilities then occur at the base of the PBL when the ratio between the buoyancy forces and the viscous forces reaches a critical value. Previous studies all show that, in the absence of shear, the value of $\Phi_{tot} = 4 \times 10^{-6}$ would trigger fingers with the same mechanism of PBL destabilisation as shown in appendix 3.C. In order to accurately characterise the conditions required to trigger SDGIs, we have to consider the fraction of fine ash that can be entrained within fingers i.e. not the initial Φ_{tot} but the local volume fraction within the destabilising layer in the cloud. Figure 3.3.13c actually shows that, for the case where the initial $\Phi_{tot} = 2 \times 10^{-5}$, the local concentration in the destabilising layer (which can be considered as a PBL) is about $\Phi_{loc} = 1 \times 10^{-5}$. This local value is estimated once coarse particles have settled on the ground. Then, the remaining particles are related with the resulting instabilities and can be defined as sufficiently fine to be entrained through fingers. Furthermore, the calculated value is more than two times greater than the suggested value of 4×10^{-6}. There are several explanations for this discrepancy. The value of 4×10^{-6} was obtained considering a single fine particle size while the value measured in our simulations takes in account a range of particle

size classes (i.e. for particle sizes $\leq$ 125 μm). Additionally, the presence of shear (induced by the wind) certainly introduces new dynamics as now the buoyancy forces have to overcome not only the viscous forces but also the inertial forces which come into play. Finally, an interesting remark is the confirmation that the size threshold to trigger fingers is directly related to the particle volume fraction, as it is shown by the equation 2.56 derived in Chapter 2.

Ground signature of SDGIs

We observed a bimodal distribution in the ground deposit for $\Phi_{tot} = 2 \times 10^{-5}$ (i.e. $\Phi_{loc} = 1 \times 10^{-5}$. This bimodality suggests the presence of mechanisms that enhance the premature deposition of fine ash such as aggregation and SDGIs. The very interesting outcome from our simulations is that the SDGI process alone is able to produce this specific ground signature. Indeed, no aggregation process takes place in our simulations. However, despite good agreement with the field observations, the numerical results still suffer some caveats. For example, we observed in the results presented Figure 3.3.14 that the distributions are narrower than the field measurements. Several reasons might explain this aspect. First, atmospheric diffusion, which is not described in our model, produces poly-dispersed ground deposits. Second, in our simulations, the inlet fluid velocity profile as well as the Φ_{tot} profile are kept constant. On the contrary, both wind and volcanic activity vary through time. Third, aggregation in the natural cloud, as suggested by field evidence [Bonadonna et al., 2011] can have further effects on the deposit grain size distribution. Fourth, the TGSD in the model needs to be discretised and, in this study, consists of 12 size classes. Using a finer discretisation could lead to smoother deposit size distributions. Additional caveats have to be taken in account for this study. Here, we modelled a portion of the cloud which might restrict some geometrical effects of the cloud on the particle transport (such as the x-direction or also the deformation of the cloud due to the intrinsic turbulence). Furthermore, the use of our continuum model to simulate the transport of coarse ash does not consider the drag effects on these particles, as has already been discussed in the previous chapter. These aspects can be taken into account in further developments of the model.

3.4.3 Comparison between gravitational spreading and wind advection

The GCs simulations have highlighted that for a fixed particle volume fraction, the reduced gravity g' is a critical parameter to trigger SDGIs. In terms of forces, this means that as g' increases the current spreads faster until a point where the inertial forces dampen the growth of SDGIs. However, the Eyjafjallajökull case study showed that the particle volume fraction is also a critical parameter to trigger fingers in the presence of fixed wind. Then, the particle volume fraction and the horizontal motion (which is caused by gravitational spreading in one case and wind advection in the other case), need to be combined in order to trigger the SDGIs. Furthermore, whilst the cloud thinning may be a useful parameter to estimate the sedimentation from the cloud, it is difficult to measure. Indeed, some very fine fraction of ash might remain in the cloud (i.e. not entrained within fingers) which would hide any geometry variation due to settling (at least in the visible range).

There is also a fundamental difference between the two cases. In the case of gravitational spreading, the current spreads at a given velocity which is higher than the ambient velocity. In the case of wind advection, the cloud has enough inertia to spread at a lower velocity than the ambient (i.e. lower than the wind speed). In the presence of KHIs, this plays an important role for the direction of rotation of the generated billows and ultimately the resulting fingers.

3.5 Conclusions

In this chapter, we have applied the 3D numerical model developed in the previous chapter to sheared environments. We have simulated both laboratory-scale gravity current experiments and the cloud associated with the 2010 eruption of Eyjafjallajökull. Our laboratory-scale simulations have provided further validation of the model as well as presented insights into the fundamental physics of the interaction between shear and SDGIs including:

- in the absence of particles the geometry of the spreading cloud is controlled by the loss of energy due to internal processes.

- the addition of particles to the current also affects the cloud geometry, depending on the value of the reduced gravity g'. Indeed, we find two regimes: a regime at low g' where the cloud thins at a high rate because of collective settling and a regime for greater values of g' where the cloud thins at a much slower rate due to individual settling.

- the accumulation rate (AR) behaves similarly to the static case, but not necessarily due to collective settling. However, the heterogeneous deposit in the presence of collective settling remains an indicative ground signature.

Our key insights from the simulations of the Eyjafjallajökull ash cloud include:

- fingers are triggered for a local particle volume fraction of $\Phi_{loc} = 1 \times 10^{-5}$ in the PBL (for particle sizes ≤ 125 μm). This value is more than twice the value proposed in the literature (i.e. $\Phi = 4 \times 10^{-6}$) [Manzella et al., 2015]. This aspect highlights the fact that, in the presence of wind, the inertial forces may play an important role.

- SDGIs can produce bimodal size distributions in the deposit even in the absence of aggregation.

Finally, the caveats associated with our numerical modelling confirm the necessity to develop a more complete volcanic plume-cloud model taking in account further physical processes, for example, the turbulence advected into the cloud from the plume. Our results also demonstrate that further investigation is needed on the relation between SDGIs and aggregation. This aspect will be treated in the next chapter.

Author Contributions

Jonathan Lemus conducted the simulations, data analysis and drafted the manuscript. Paul Jarvis performed the experiments used for validation. Jonas Lätt and Bastien Chopard supervised the use of the Palabos code. Jonathan Lemus, Costanza Bonadonna and Paul Jarvis have contributed to data interpretation as well as the editing and finalising of the paper.

Acknowledgments

All the simulations presented in this paper have been performed using the High Performance Computing (HPC) facilities *Baobab* and *Yggdrasil* of the University of Geneva.

Appendix

3.A Input parameters for the 2010 eruption Eyjafjallajökull

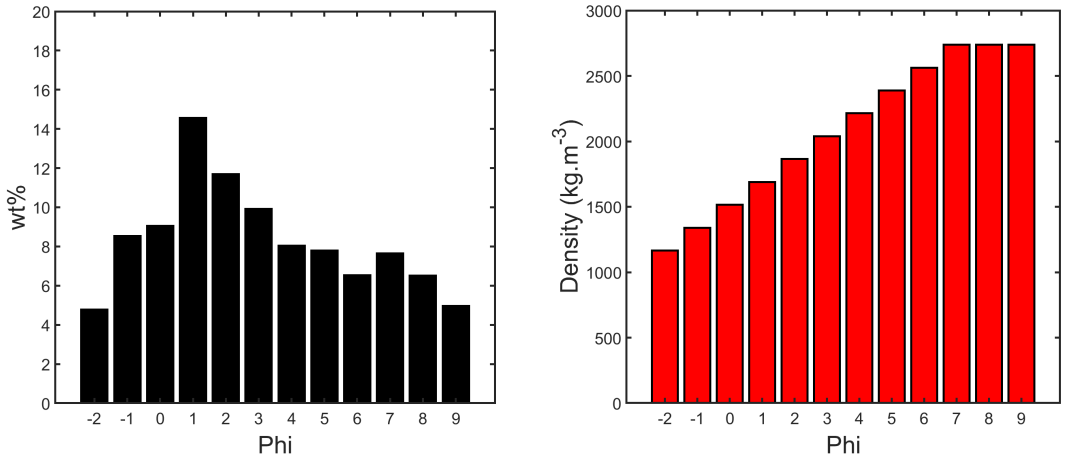

(a) (b)

Figure 3A.1: (a) TGSD obtained by Bonadonna et al. [2011] for the 4-8 of May and 2-1000 km from the vent. (b) Associated pumice density for each size class.

Parameter	Value
Wind velocity ($m.s^{-1}$)	11
Cloud spreading velocity ($m.s^{-1}$)	8
Air density ($kg.m^{-3}$)	1.3
Air kinematic viscosity ($m^2.s^{-1}$)	1.4×10^{-5}

Table 3A.1: List of input parameters taken from [Manzella et al., 2015]

3.B Particle grain-size within the ground deposit

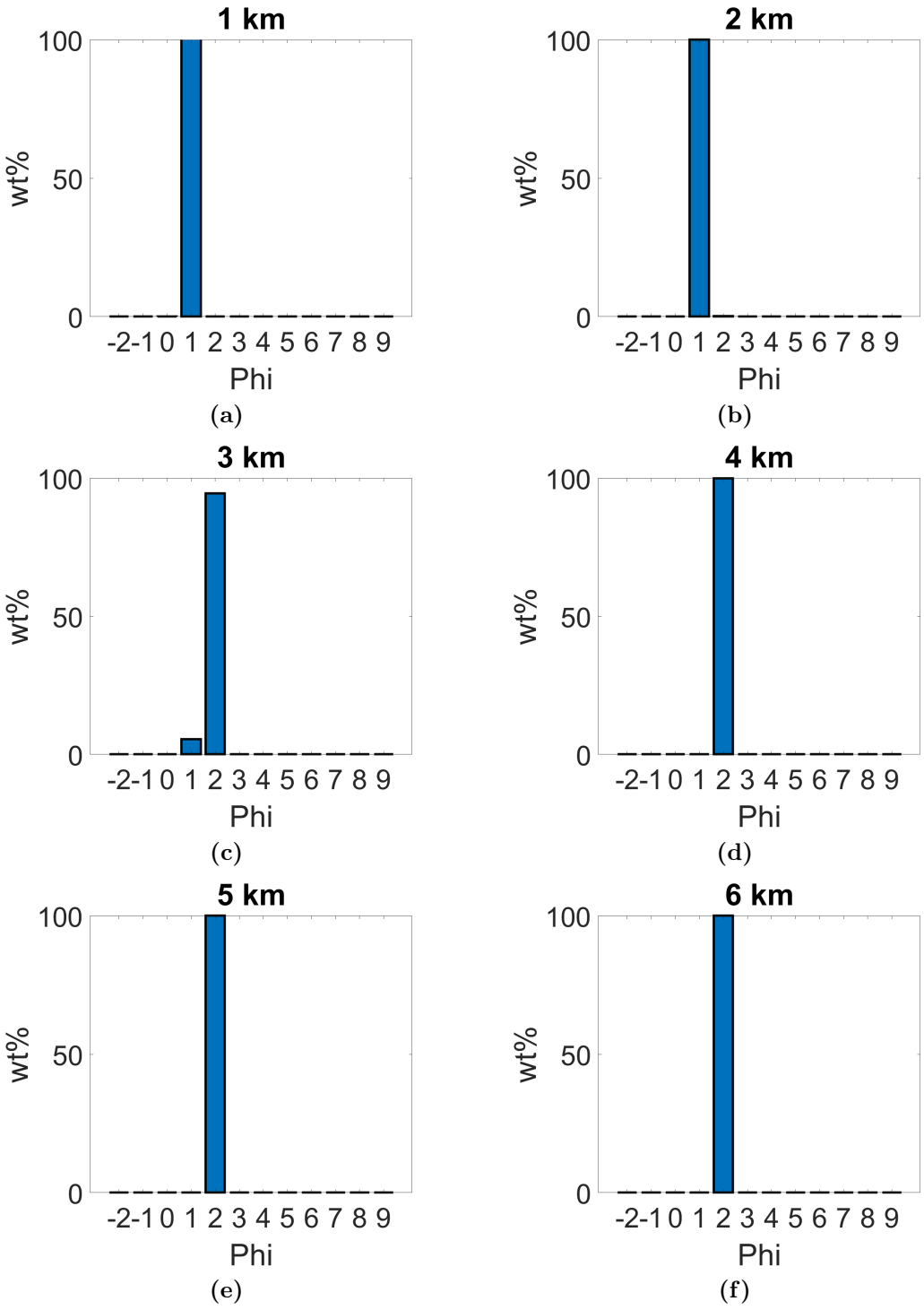

(a) (b) (c) (d) (e) (f)

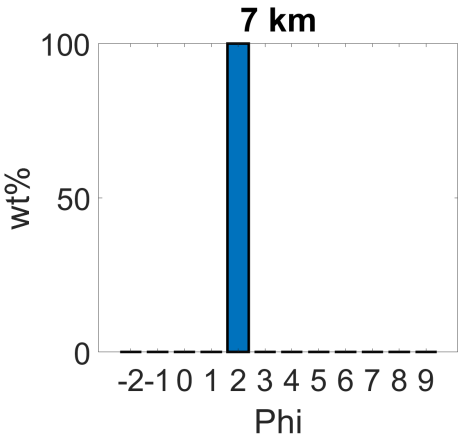
7 km
100
50
0
wt%
-2-1 0 1 2 3 4 5 6 7 8 9
Phi

(g)

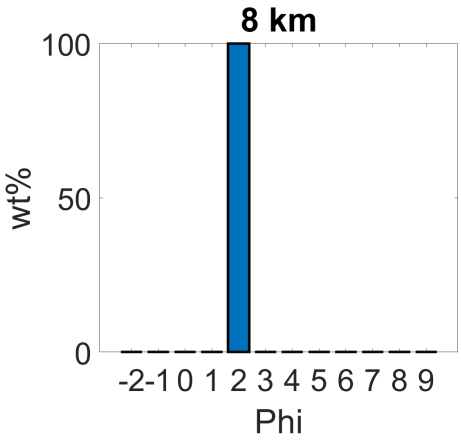
8 km
100
50
0
wt%
-2-1 0 1 2 3 4 5 6 7 8 9
Phi

(h)

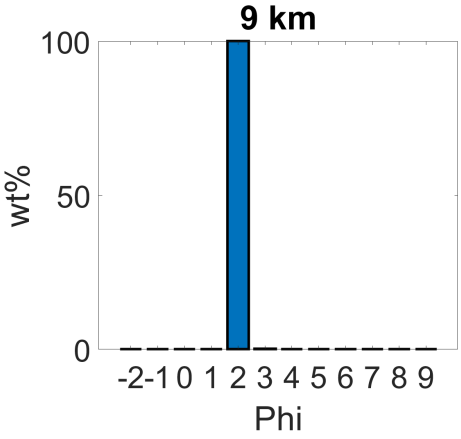
9 km
100
50
0
wt%
-2-1 0 1 2 3 4 5 6 7 8 9
Phi

(i)

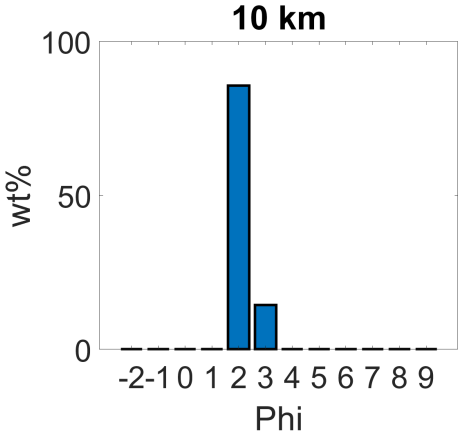
10 km
100
50
0
wt%
-2-1 0 1 2 3 4 5 6 7 8 9
Phi

(j)

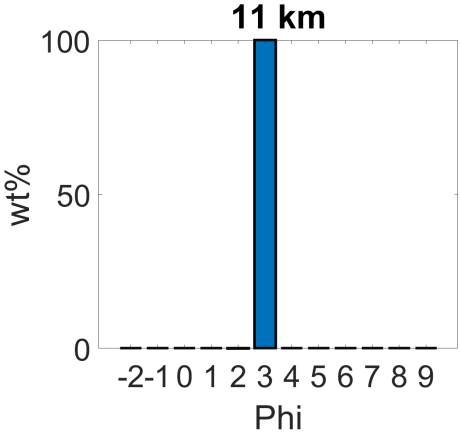
11 km
100
50
0
wt%
-2-1 0 1 2 3 4 5 6 7 8 9
Phi

(k)

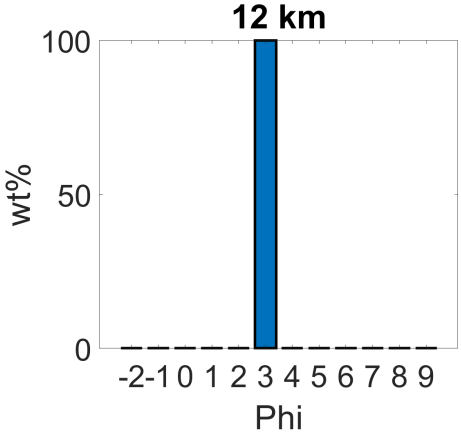
12 km
100
50
0
wt%
-2-1 0 1 2 3 4 5 6 7 8 9
Phi

(l)

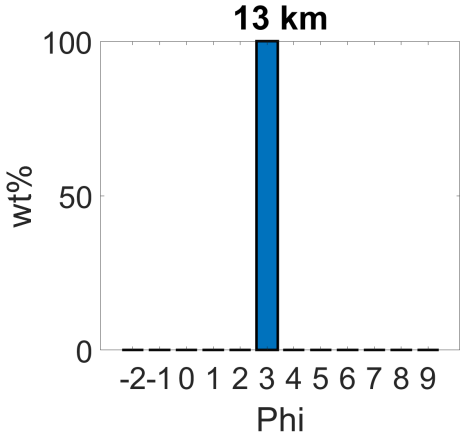
13 km
100
50
0
wt%
-2-1 0 1 2 3 4 5 6 7 8 9
Phi

(m)

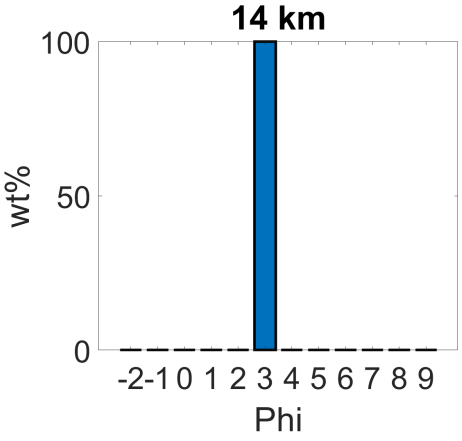
14 km
100
50
0
wt%
-2-1 0 1 2 3 4 5 6 7 8 9
Phi

(n)

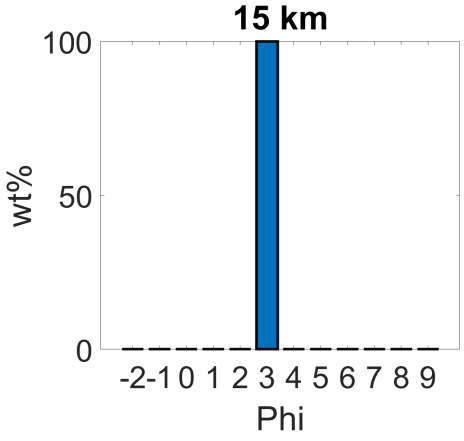
15 km
100
50
0
wt%
-2-1 0 1 2 3 4 5 6 7 8 9
Phi

(o)

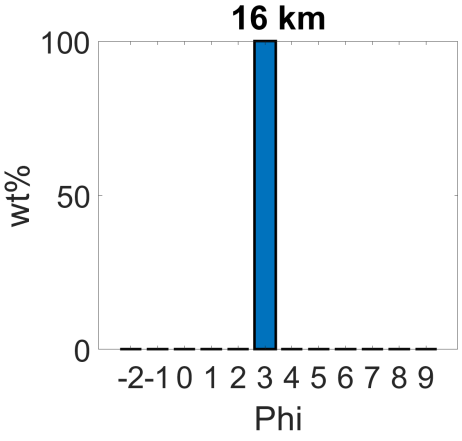
16 km
100
50
0
wt%
-2-1 0 1 2 3 4 5 6 7 8 9
Phi

(p)

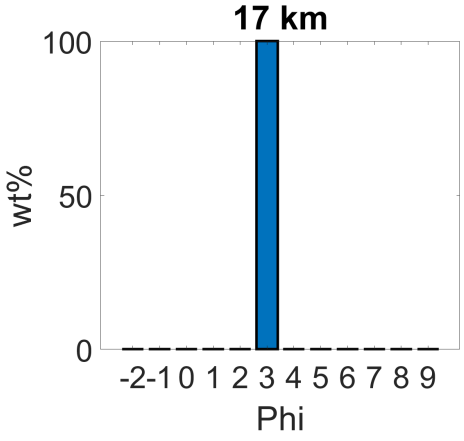
17 km
100
50
0
wt%
-2-1 0 1 2 3 4 5 6 7 8 9
Phi

(q)

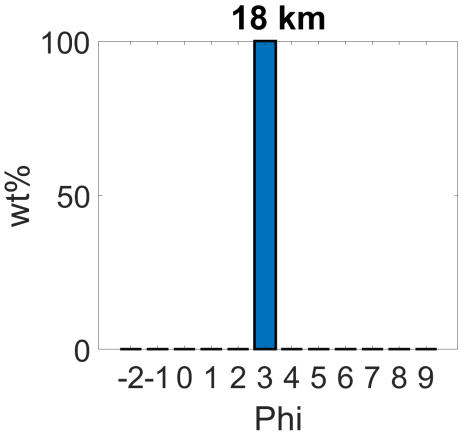
18 km
100
50
0
wt%
-2-1 0 1 2 3 4 5 6 7 8 9
Phi

(r)

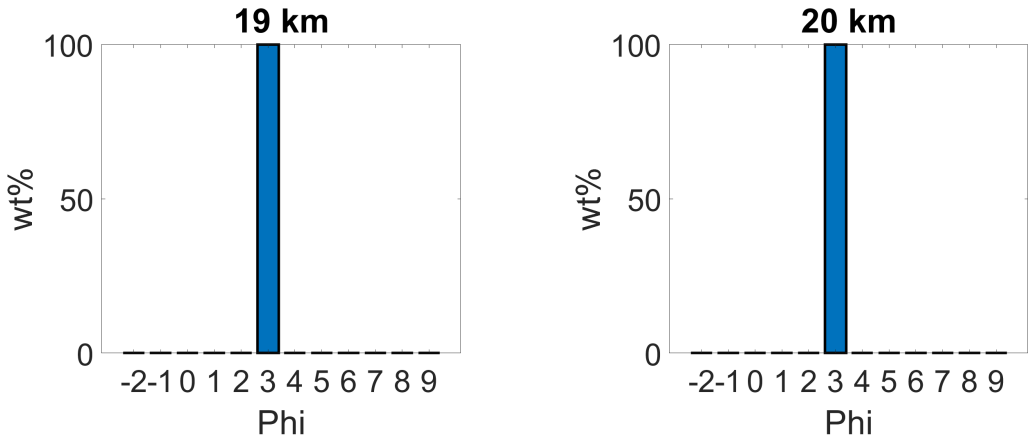

(s) **(t)**

Figure 3B.1: Size distribution in the deposit from 1 to 20 km in the simulations using $\Phi_{tot} = 4 \times 10^{-6}$.

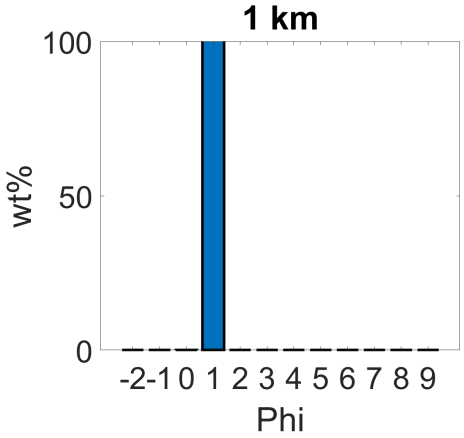
1 km
100
50
0
wt%
-2-1 0 1 2 3 4 5 6 7 8 9
Phi

(a)

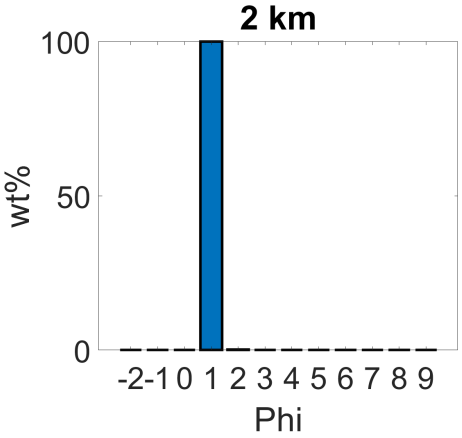
2 km
100
50
0
wt%
-2-1 0 1 2 3 4 5 6 7 8 9
Phi

(b)

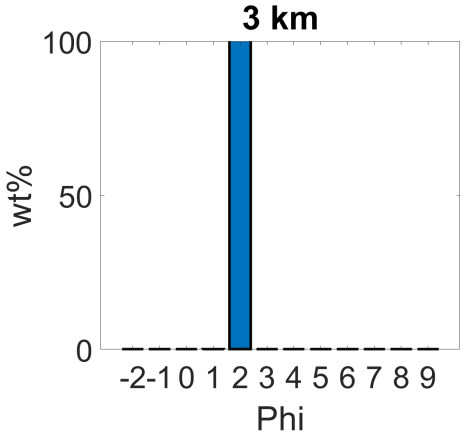
3 km
100
50
0
wt%
-2-1 0 1 2 3 4 5 6 7 8 9
Phi

(c)

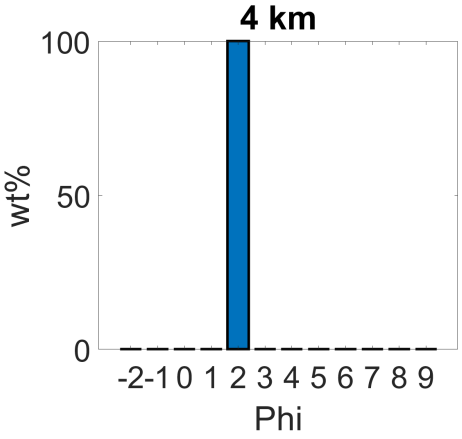
4 km
100
50
0
wt%
-2-1 0 1 2 3 4 5 6 7 8 9
Phi

(d)

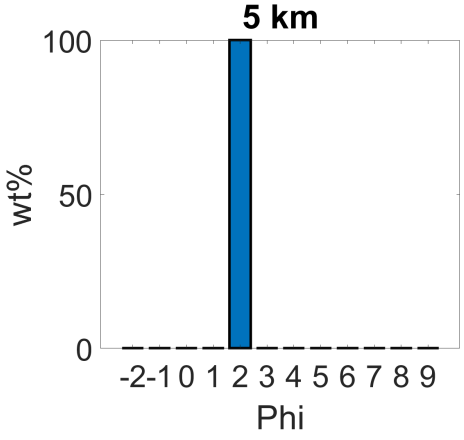
5 km
100
50
0
wt%
-2-1 0 1 2 3 4 5 6 7 8 9
Phi

(e)

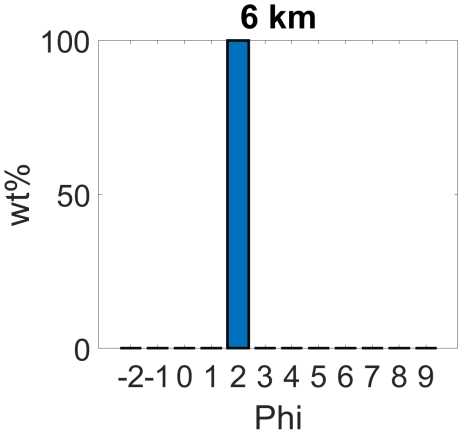
6 km
100
50
0
wt%
-2-1 0 1 2 3 4 5 6 7 8 9
Phi

(f)

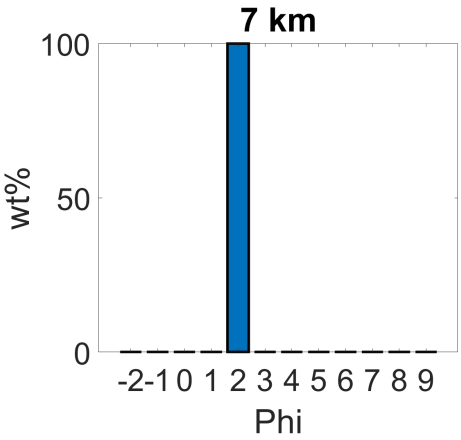
7 km
100
50
0
wt%
-2-1 0 1 2 3 4 5 6 7 8 9
Phi

(g)

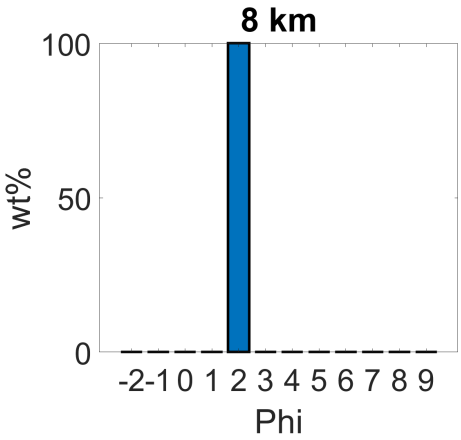
8 km
100
50
0
wt%
-2-1 0 1 2 3 4 5 6 7 8 9
Phi

(h)

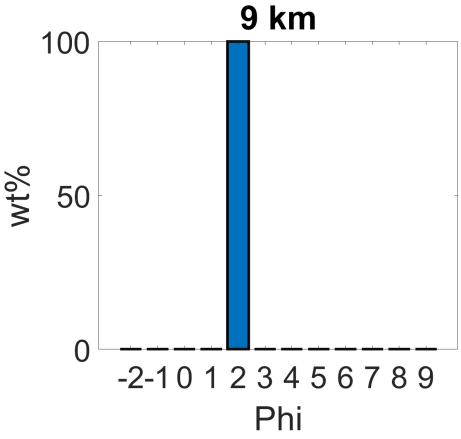
9 km
100
50
0
wt%
-2-1 0 1 2 3 4 5 6 7 8 9
Phi

(i)

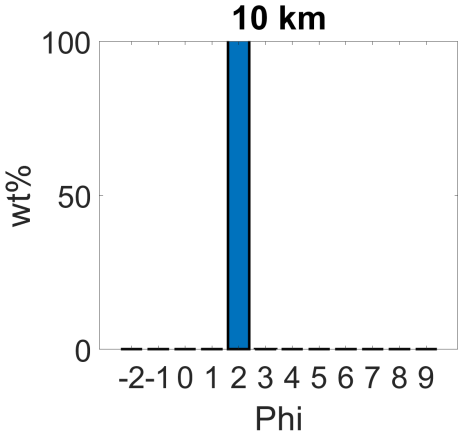
10 km
100
50
0
wt%
-2-1 0 1 2 3 4 5 6 7 8 9
Phi

(j)

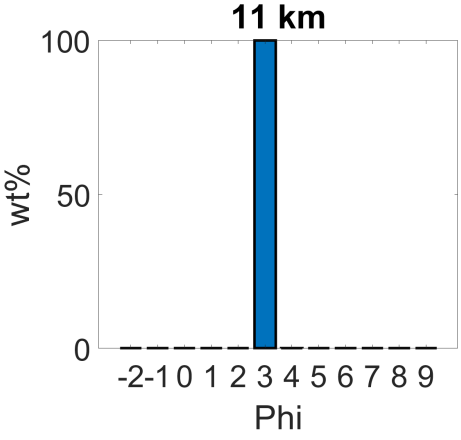
11 km
100
50
0
wt%
-2-1 0 1 2 3 4 5 6 7 8 9
Phi

(k)

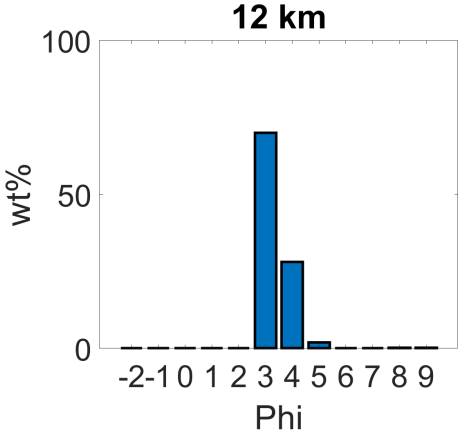
12 km
100
50
0
wt%
-2-1 0 1 2 3 4 5 6 7 8 9
Phi

(l)

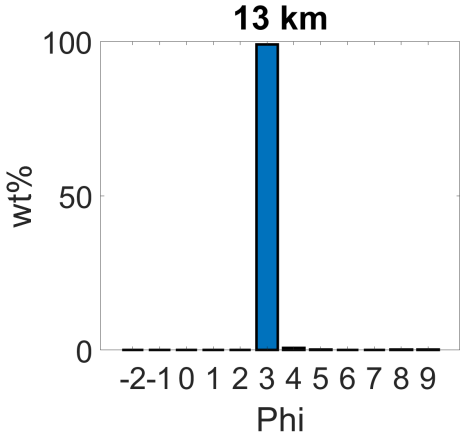
13 km
100
50
0
wt%
-2-1 0 1 2 3 4 5 6 7 8 9
Phi

(m)

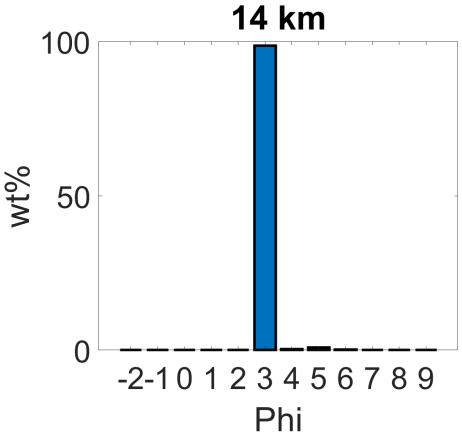
14 km
100
50
0
wt%
-2-1 0 1 2 3 4 5 6 7 8 9
Phi

(n)

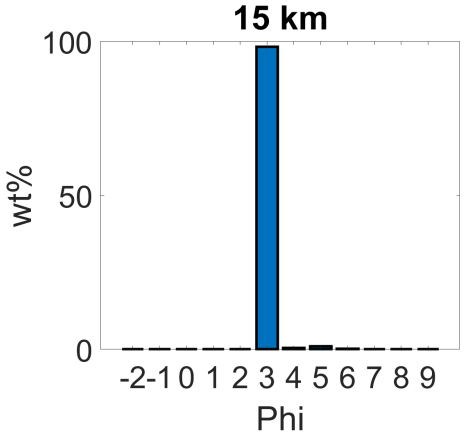
15 km
100
50
0
wt%
-2-1 0 1 2 3 4 5 6 7 8 9
Phi

(o)

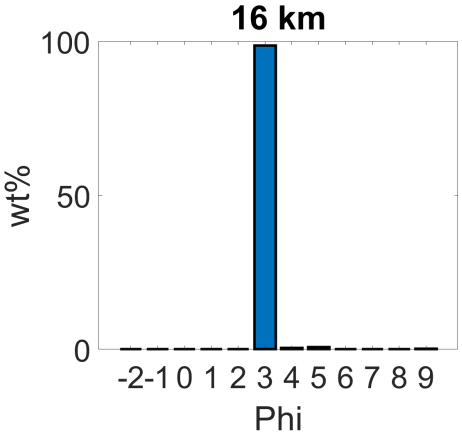
16 km
100
50
0
wt%
-2-1 0 1 2 3 4 5 6 7 8 9
Phi

(p)

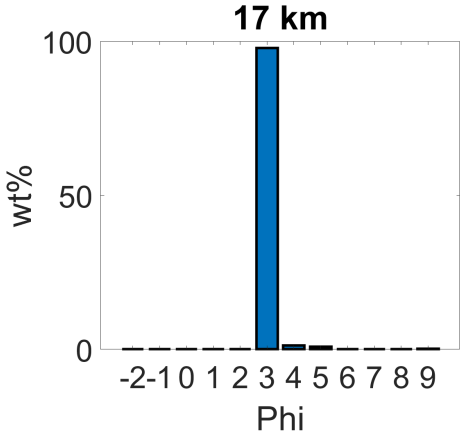
17 km
100
50
0
wt%
-2-1 0 1 2 3 4 5 6 7 8 9
Phi

(q)

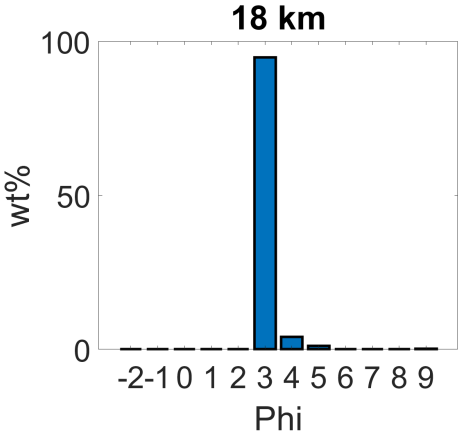
18 km
100
50
0
wt%
-2-1 0 1 2 3 4 5 6 7 8 9
Phi

(r)

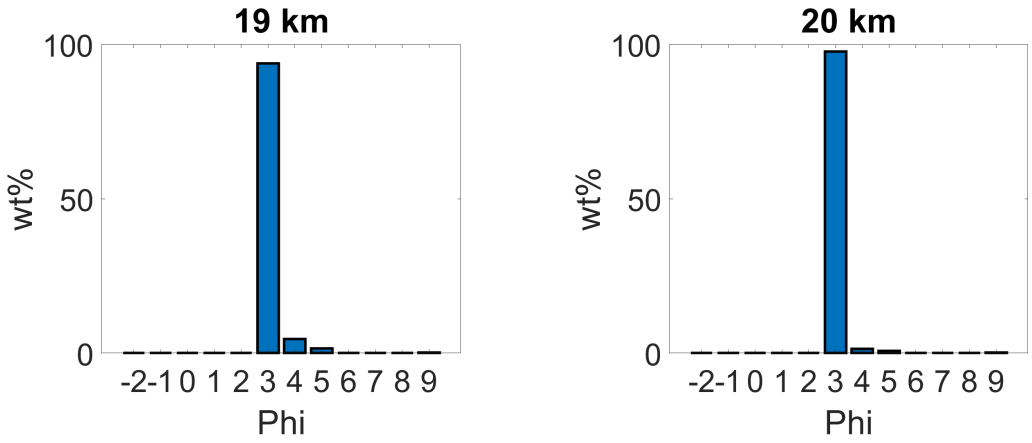

(s) **(t)**

Figure 3B.2: Size distribution in the deposit from 1 to 20 km in the simulations using $\Phi_{tot} = 1 \times 10^{-5}$.

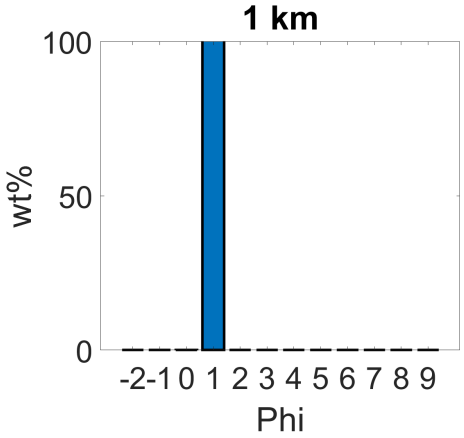
1 km
100
50
0
wt%
-2-1 0 1 2 3 4 5 6 7 8 9
Phi

(a)

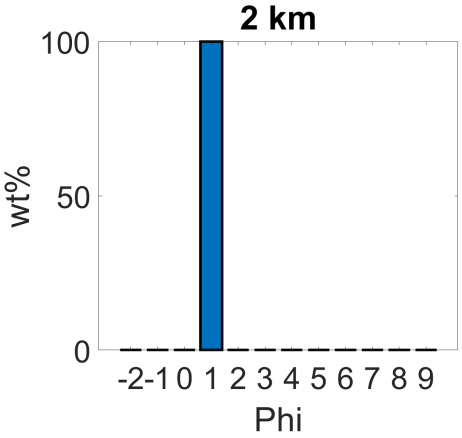
2 km
100
50
0
wt%
-2-1 0 1 2 3 4 5 6 7 8 9
Phi

(b)

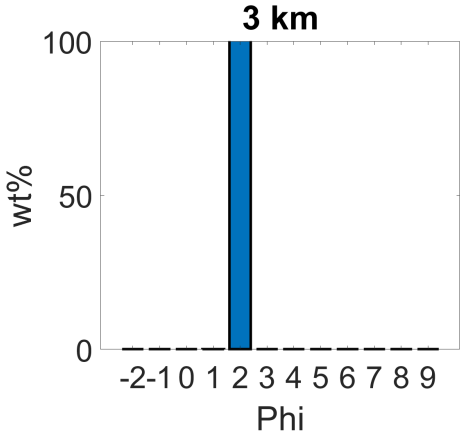
3 km
100
50
0
wt%
-2-1 0 1 2 3 4 5 6 7 8 9
Phi

(c)

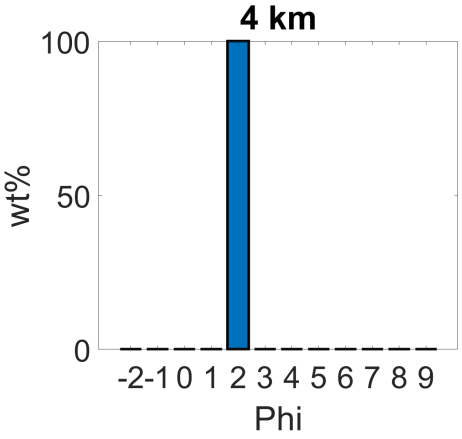
4 km
100
50
0
wt%
-2-1 0 1 2 3 4 5 6 7 8 9
Phi

(d)

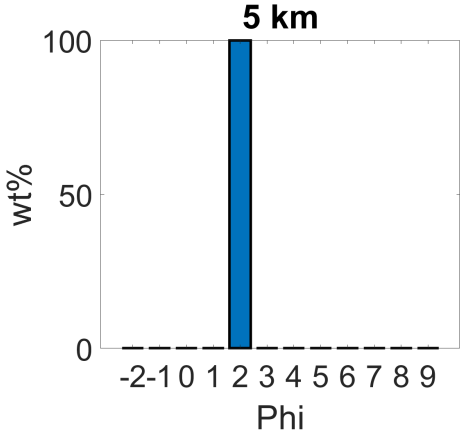
5 km
100
50
0
wt%
-2-1 0 1 2 3 4 5 6 7 8 9
Phi

(e)

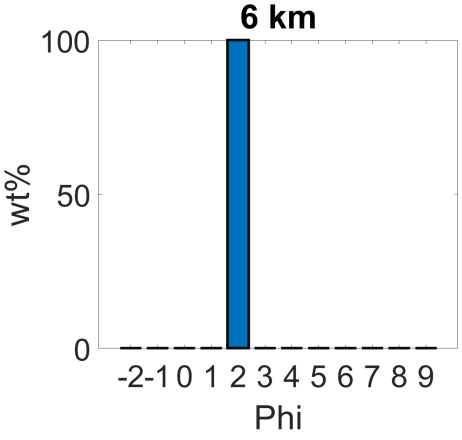
6 km
100
50
0
wt%
-2-1 0 1 2 3 4 5 6 7 8 9
Phi

(f)

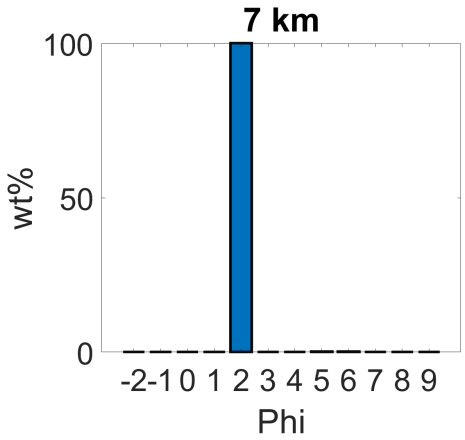
7 km
100
50
0
wt%
-2-1 0 1 2 3 4 5 6 7 8 9
Phi

(g)

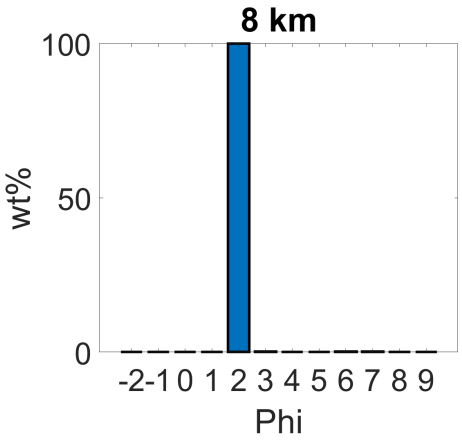
8 km
100
50
0
wt%
-2-1 0 1 2 3 4 5 6 7 8 9
Phi

(h)

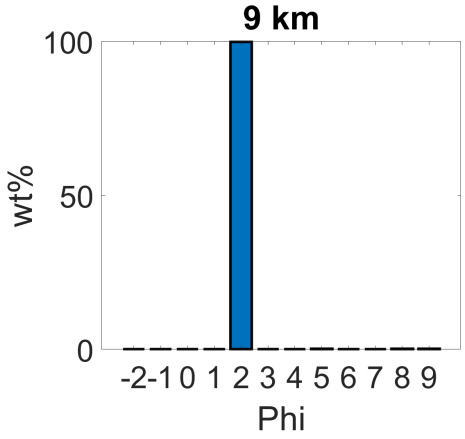
9 km
100
50
0
wt%
-2-1 0 1 2 3 4 5 6 7 8 9
Phi

(i)

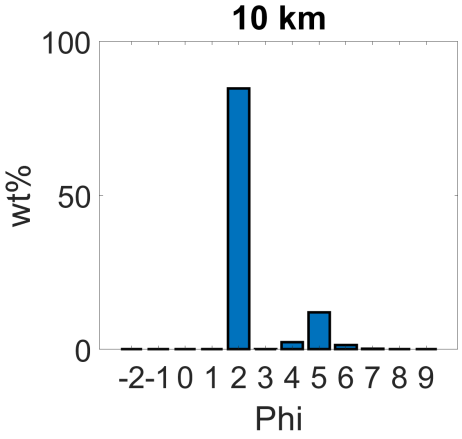
10 km
100
50
0
wt%
-2-1 0 1 2 3 4 5 6 7 8 9
Phi

(j)

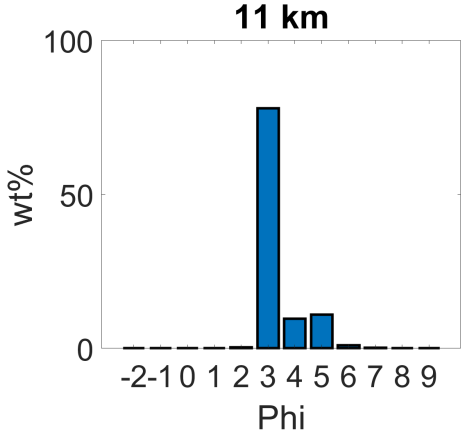
11 km
100
50
0
wt%
-2-1 0 1 2 3 4 5 6 7 8 9
Phi

(k)

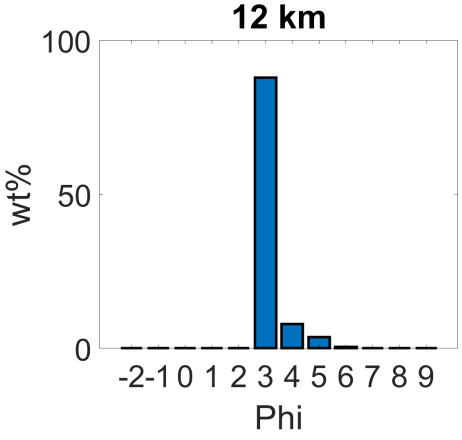
12 km
100
50
0
wt%
-2-1 0 1 2 3 4 5 6 7 8 9
Phi

(l)

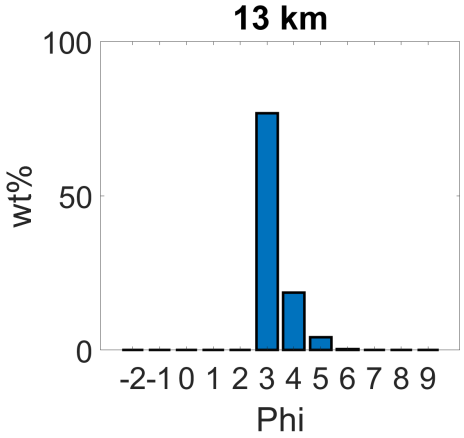
13 km
100
50
0
wt%
-2-1 0 1 2 3 4 5 6 7 8 9
Phi

(m)

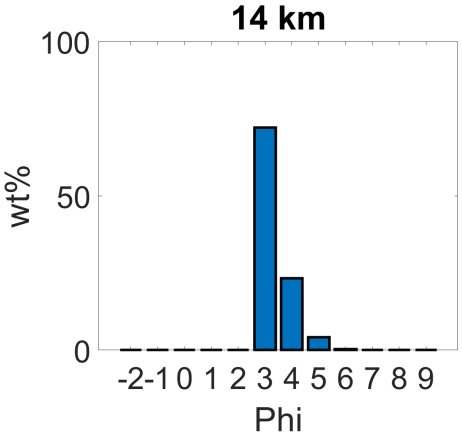
14 km
100
50
0
wt%
-2-1 0 1 2 3 4 5 6 7 8 9
Phi

(n)

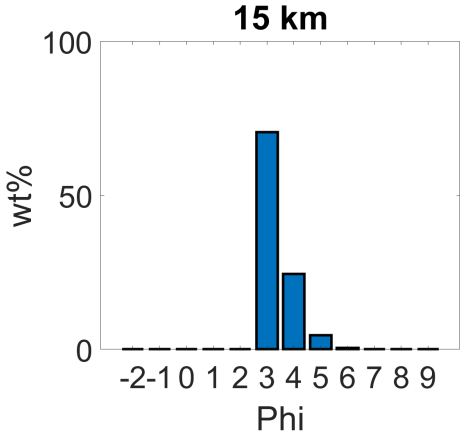
15 km
100
50
0
wt%
-2-1 0 1 2 3 4 5 6 7 8 9
Phi

(o)

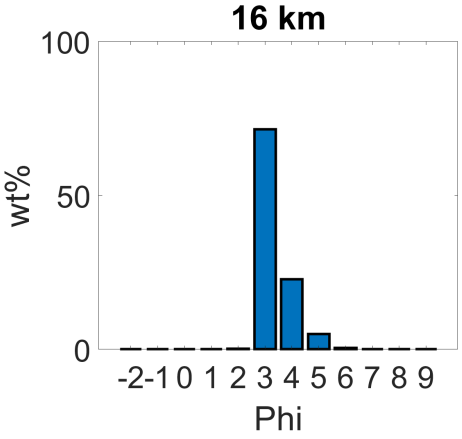
16 km
100
50
0
wt%
-2-1 0 1 2 3 4 5 6 7 8 9
Phi

(p)

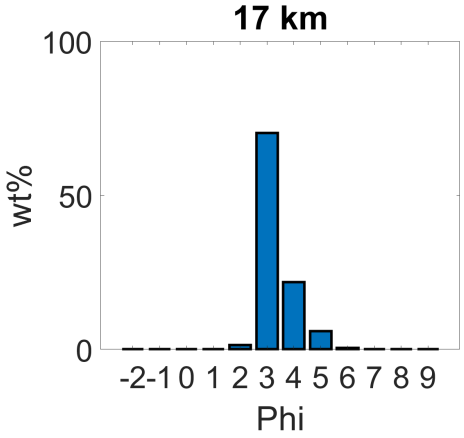
17 km
100
50
0
wt%
-2-1 0 1 2 3 4 5 6 7 8 9
Phi

(q)

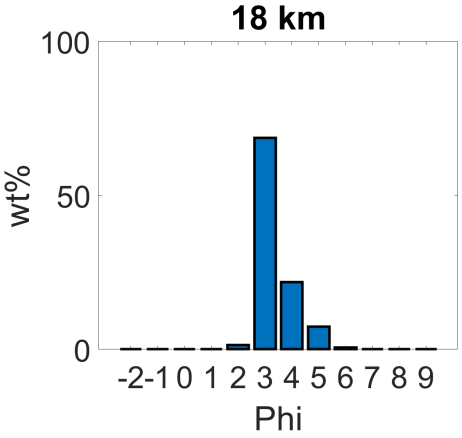
18 km
100
50
0
wt%
-2-1 0 1 2 3 4 5 6 7 8 9
Phi

(r)

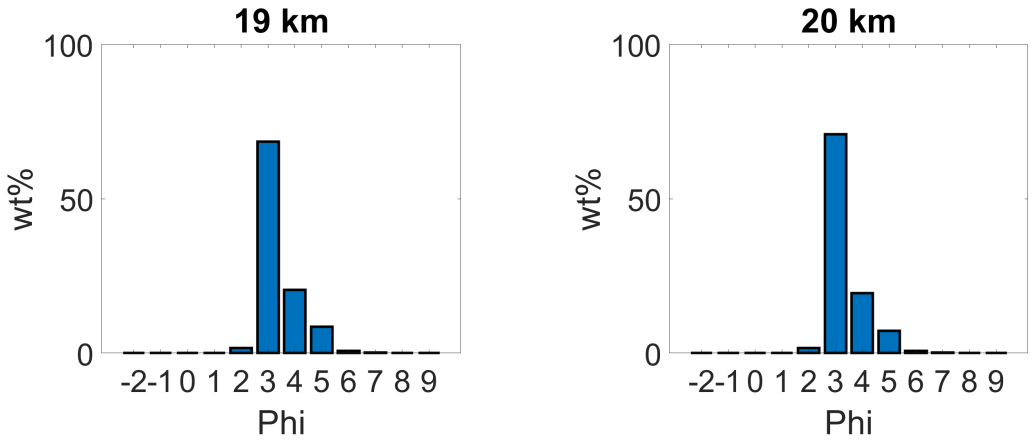

(s) **(t)**

Figure 3B.3: Size distribution in the deposit from 1 to 20 km in the simulations using $\Phi_{tot} = 2 \times 10^{-5}$.

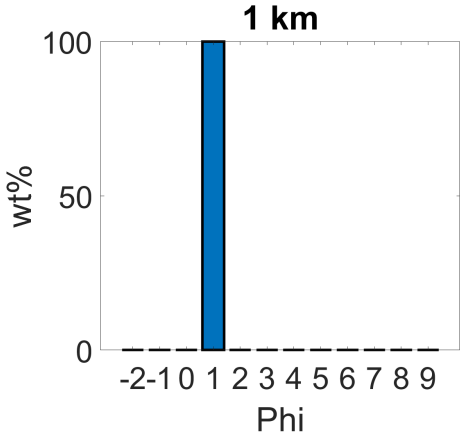
1 km
100
50
0
wt%
-2-1 0 1 2 3 4 5 6 7 8 9
Phi

(a)

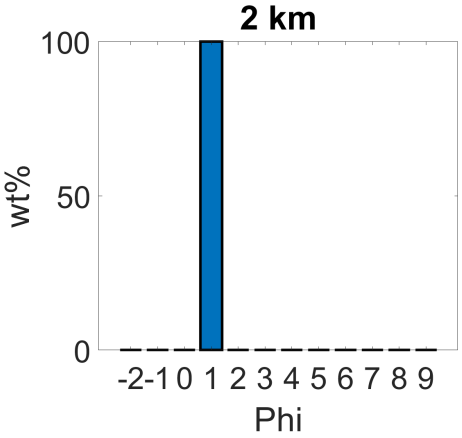
2 km
100
50
0
wt%
-2-1 0 1 2 3 4 5 6 7 8 9
Phi

(b)

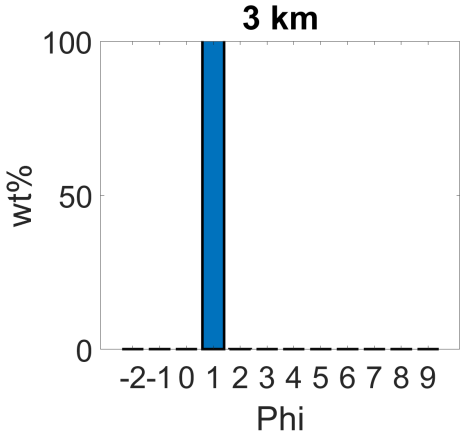
3 km
100
50
0
wt%
-2-1 0 1 2 3 4 5 6 7 8 9
Phi

(c)

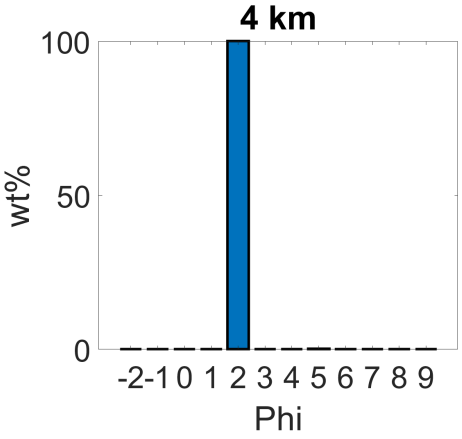
4 km
100
50
0
wt%
-2-1 0 1 2 3 4 5 6 7 8 9
Phi

(d)

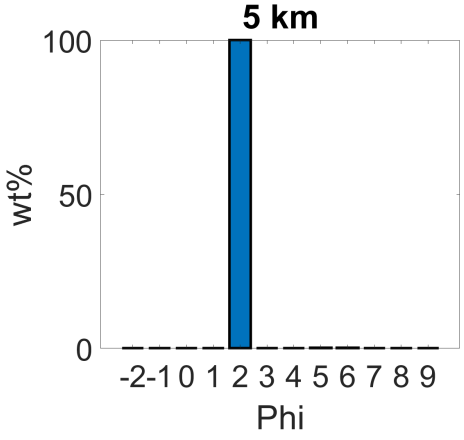
5 km
100
50
0
wt%
-2-1 0 1 2 3 4 5 6 7 8 9
Phi

(e)

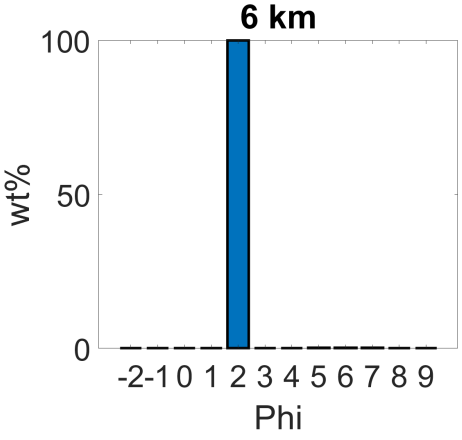
6 km
100
50
0
wt%
-2-1 0 1 2 3 4 5 6 7 8 9
Phi

(f)

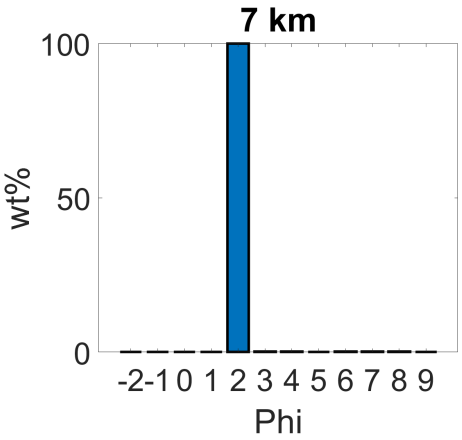
7 km
100
50
0
wt%
-2-1 0 1 2 3 4 5 6 7 8 9
Phi

(g)

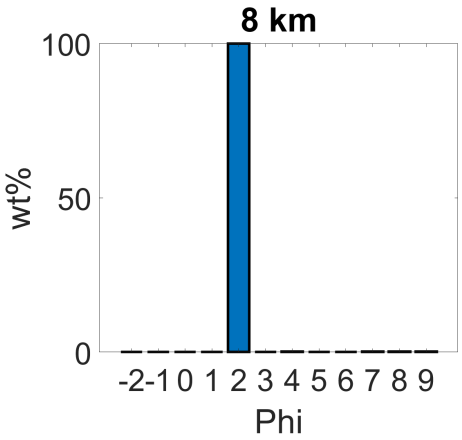
8 km
100
50
0
wt%
-2-1 0 1 2 3 4 5 6 7 8 9
Phi

(h)

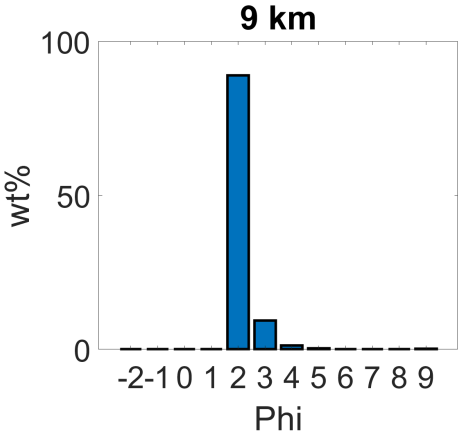
9 km
100
50
0
wt%
-2-1 0 1 2 3 4 5 6 7 8 9
Phi

(i)

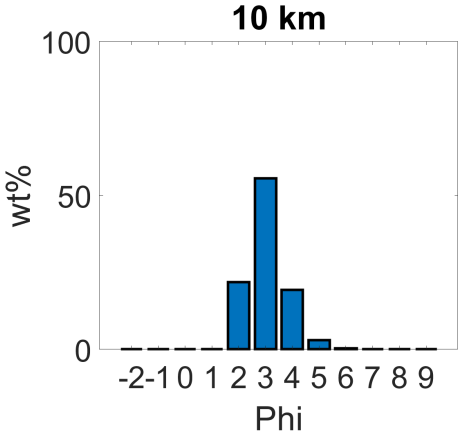
10 km
100
50
0
wt%
-2-1 0 1 2 3 4 5 6 7 8 9
Phi

(j)

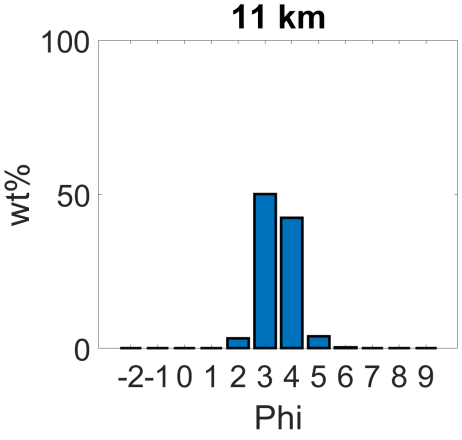
11 km
100
50
0
wt%
-2-1 0 1 2 3 4 5 6 7 8 9
Phi

(k)

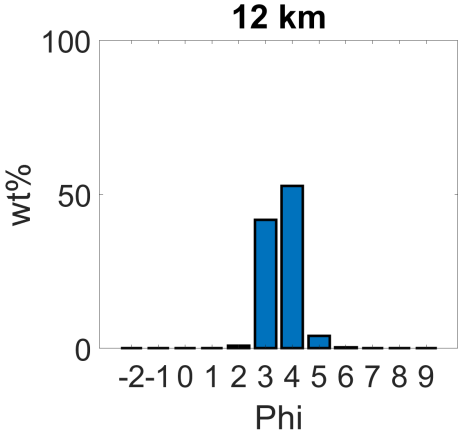
12 km
100
50
0
wt%
-2-1 0 1 2 3 4 5 6 7 8 9
Phi

(l)

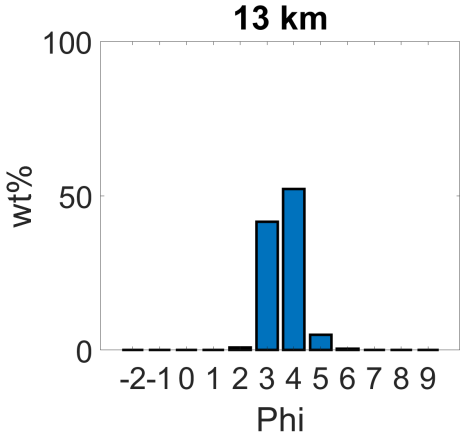
13 km
100
50
0
wt%
-2-1 0 1 2 3 4 5 6 7 8 9
Phi

(m)

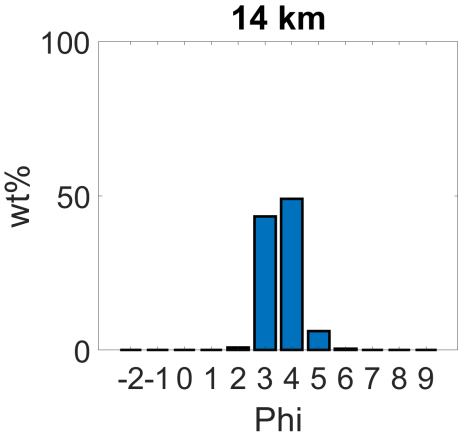
14 km
100
50
0
wt%
-2-1 0 1 2 3 4 5 6 7 8 9
Phi

(n)

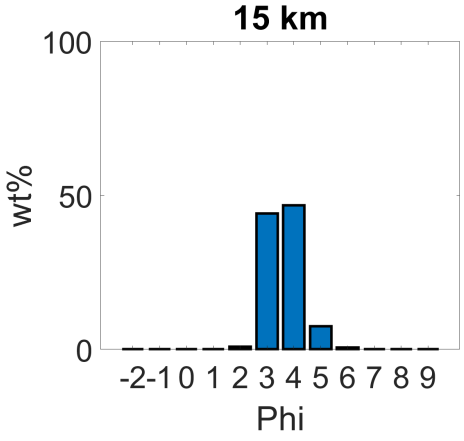
15 km
100
50
0
wt%
-2-1 0 1 2 3 4 5 6 7 8 9
Phi

(o)

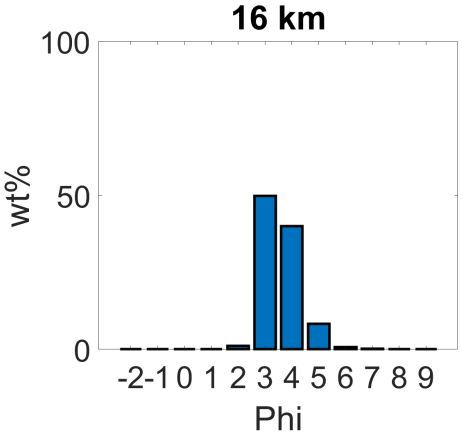
16 km
100
50
0
wt%
-2-1 0 1 2 3 4 5 6 7 8 9
Phi

(p)

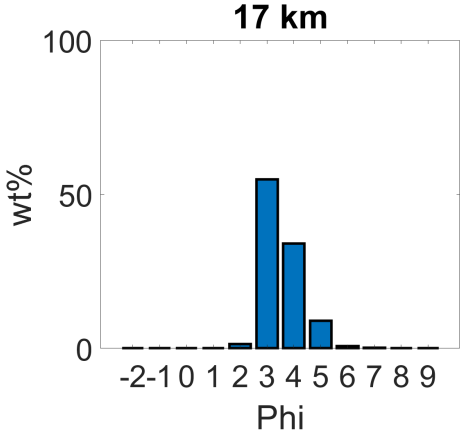
17 km
100
50
0
wt%
-2-1 0 1 2 3 4 5 6 7 8 9
Phi

(q)

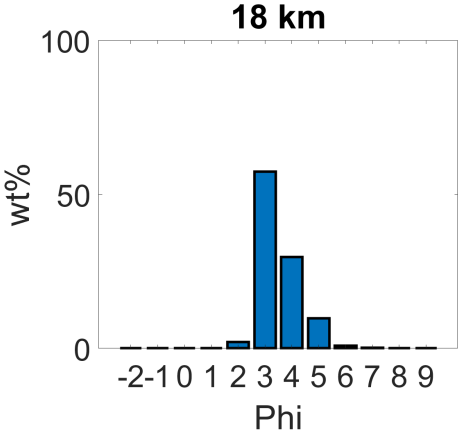
18 km
100
50
0
wt%
-2-1 0 1 2 3 4 5 6 7 8 9
Phi

(r)

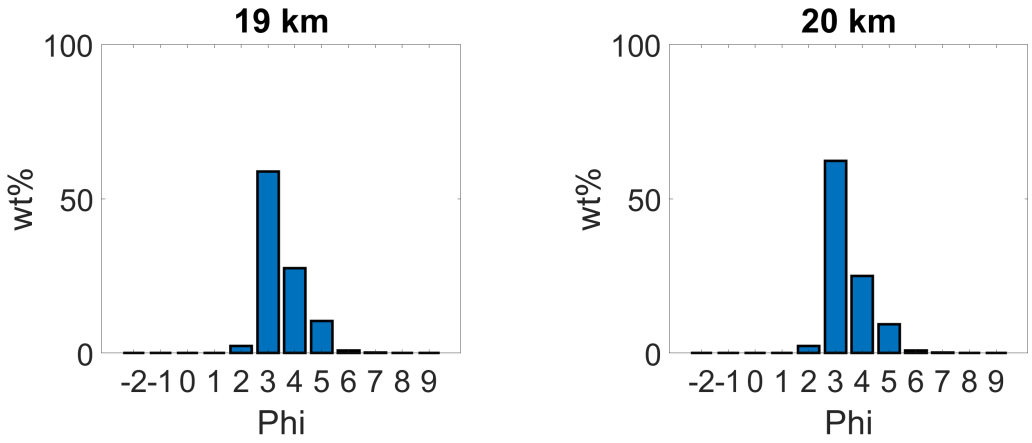

(s) **(t)**

Figure 3B.4: Size distribution in the deposit from 1 to 20 km in the simulations using $\Phi_{tot} = 3 \times 10^{-5}$.

3.C Simulation of SDGIs in air for a static configuration

Here we show some simulation results in air for a static configuration. The configuration is strongly similar to the one presented in the first chapter (i.e. two superposed layers). The numerical domain is a box of dimension $75 \times 303 \times 385$ m. The initial fluid density is 1.225 kg/m^3 in the upper layer and 1.235 kg/m^3 in the lower layer. The particle size is 40 μm and the particle density is 2519.24 kg/m^3. We clearly observe on Figure 3C.1 that fingers are triggered for an initial particle volume fraction of 4×10^{-6}.

Figure 3C.1: Simulation snapshot using an initial volume fraction of 4×10^{-6}.

Chapter 4

Numerical investigations of the interaction between particle aggregation and settling-driven gravitational instabilities

4.1 Introduction

Particle aggregation is a phenomenon that occurs at various scales and in numerous fields such as astrophysics [Wurm and Blum, 2000; Brisset et al., 2013; Bracco et al., 1999], medical sciences [Rahim et al., 2020; Piederriere et al., 2004] or chemistry [Kepkay, 1994; Nakouzi et al., 2018]. In volcanology, ash aggregation is a reversible or irreversible process which has also the potential to increase the vertical terminal velocity of fine particles by clustering them into bigger structures [Lane et al., 1993; Brown et al., 2012]. Consequently, given the numerous underlying implications, the dynamics associated with particle aggregation have been widely investigated in order to improve our understanding [Gilbert and Lane, 1994; James et al., 2002, 2003; Durant et al., 2009; Rose and Durant, 2011; Brown et al., 2012; Van Eaton et al., 2012; Van Eaton and Wilson, 2013; Burns et al., 2017; Vogel et al., 2019; Rossi et al., 2021]. Evidences of airborne volcanic ash aggregation have been observed in the field during several explosive eruptions such as the 1980 eruption at Mount Saint Helens (US) [Sorem, 1982; Hobbs et al., 1981], the 2010 eruption of Eyjafjallajökull (Iceland) [Bonadonna et al., 2011; Taddeucci et al., 2011] and eruptions of Sakurajima volcano (Japan) [Bagheri et al., 2016; Gabellini et al., 2020; Vecino et al.,

2022; Gilbert et al., 1991]. Moreover, the most recent events have provided opportunities to use sophisticated measurement techniques (e.g. high-speed cameras, sticky papers, etc.) to study the characteristics of aggregates before their breakup when they reach the ground [Vecino et al., 2022; Pollastri et al., 2021; Gabellini et al., 2020; Bagheri et al., 2016; Taddeucci et al., 2011]. In parallel, some laboratory investigations have been performed in order to constrain the different processes that may come into play during aggregation. Indeed, ash aggregation has been associated with the action of several processes such as electrostatic forces [Gilbert et al., 1991; Schumacher, 1994; James et al., 2002, 2003] as well as humidity [Telling and Dufek, 2012; Van Eaton et al., 2012]. The different insights provided by these field and laboratory investigations have certainly improved the models describing aggregation.

4.1.1 Modelling ash aggregation

Modelling ash aggregation is a key challenge for the improvement of Volcanic Ash Transport and Dispersal Models (VATDMs) [Folch, 2012]. Several models have been developed in order to describe the aggregation process, i.e., how the initial grain-size distribution is modified as a result of the aggregation of individual particles into larger clusters. Some models are based on observations [Biass et al., 2014; Bonadonna and Phillips, 2003; Bonadonna et al., 2002; Mastin et al., 2013; Cornell et al., 1983] while others are built from theoretical studies [Costa et al., 2010; Textor et al., 2006; Veitch and Woods, 2001]. Despite previous theoretical and experimental works [Lu et al., 1998; Pumir and Wilkinson, 2016, and references therein], the description of particle aggregation, especially the particle collisional interaction in a highly turbulent environment, remains partly unconstrained. Some numerical investigations have focused on the hydrodynamic properties of fractal aggregates [Nguyen, 2007] and on the link between turbulence and the aggregation process [Wang et al., 2019; Pesmazoglou et al., 2017]. Wang et al. [2019] used a multi-phase model involving the Lattice Boltzmann Method (LBM) to solve for the fluid phase motion, coupled with suspended spherical and mono-sized particles. An isotropic turbulence is applied to the fluid in order to enhance the collision of particles and investigate

the role of the particle volume fraction. However, it has been found that the presence of particles tends to affect the fluid turbulent kinetic energy differently at large and small scales. Since each particle collision is treated individually, this kind of microscopic model can rapidly become critically computationally-expensive with an increasing number of particles. Indeed, the high particle concentration within a volcanic cloud (typically in the range $[10^7; 10^{11}]$ particles/m^3 [Rossi, 2018]) clearly demonstrates the need for other approaches. A macroscopic approach involving stochastic modelling for aggregation [Pesmazoglou et al., 2016] is used in Pesmazoglou et al. [2017] in order to study the coagulation of particles in turbulent jets. The main results showed that the residence time of particles is a key parameter to form aggregates, as well as the need for an accurate formulation of the different aggregation kernels affected by the turbulence. Indeed, many macroscopic approaches for aggregation result from the Population Balance Equation (PBE) [Kumar and Ramkrishna, 1996; Kumar et al., 2006; Pesmazoglou et al., 2016; Rossi, 2018]. The PBE is often referred to as the coalescent coagulation [Mitchell and Frenklach, 2003] theoretically formulated by Smoluchowski [1917]. This theory is summarised by the so-called Smoluchowski Coagulation Equation (SCE) which describes the evolution of the particle number density $n(m,t)$ (which is a function of the particle mass m and the time t) and has been applied to various fields involving liquid aerosols [Koch and Friedlander, 1990; Beeckmans, 1965] as well as solid particle aggregates [Zidar et al., 2018; Higuchi et al., 1963]. Considering two particles respectively of masses m and m', the SCE is obtained using the conservation equation and we have

$$\begin{aligned}\frac{dn(m,t)}{dt} = \frac{1}{2}\int_0^m K(m-m',m')\,n(m-m',t)\,dm' \\ - \int_0^\infty K(m,m')\,n(m,t)\,n(m',t)\,dm',\end{aligned} \tag{4.1}$$

where $K(m,m')$ is an operator called the coalescence kernel which represents the probability of a collision creating a particle of mass $m+m'$. The kernel $K(m,m')$ is an operator which includes all the governing physical processes describing the interaction between particles. The discrete equivalent of equation 4.1 (i.e., for a discretised particle size spectrum) is given by the equation describing the evolution

of n_k, the number density of particles with size class k, obtained by collision of particles of size classes i and j

$$\frac{dn_k}{dt} = \frac{1}{2}\sum_{i+j=k} K\left(m_i, m_j\right) n_i n_j - n_k \sum_{i=1}^{\infty} K\left(m_i, m_k\right) n_i. \tag{4.2}$$

The factor of 1/2 in front of the first term (i.e., the rate of formation of particles of size k) is important as it corrects the fact that collision are accounted for twice within the summation. An analytical solution can be derived for an ideal case which involves constant coagulation kernels and an initial monodisperse distribution of particles of the same mass [Friedlander, 2000]. For instance, this situation may be associated with the isothermal brownian coagulation for particles of size ≤ 1 μm and ultimately the coagulation kernel remains constant. Then, assuming the total number of particles $N_{tot} = \sum_{i=1}^{\infty} n_i$, the solution of equation 4.2 for the isothermal brownian coagulation case is given by [Friedlander, 2000]

$$N_{tot}\left(t\right) = \frac{N_{tot}\left(0\right)}{1 + \left(K N_{tot}\left(0\right) t/2\right)}. \tag{4.3}$$

Several discretisation strategies have been used in order to improve the accuracy of models based on the SCE, especially the discretisation of the particle size distribution [Kumar and Ramkrishna, 1996; Kumar et al., 2006]. Indeed, an unequally-discretised particle size distribution allows the exploration of a wide range of sizes but leads to a fundamental problem of the mass conservation to deal with. The so-called fixed pivot technique [Kumar and Ramkrishna, 1996] allows the development of a numerical scheme for aggregation with a relatively coarse discretisation of the particle size range, conserving the mass and the moments of the distribution.

The discrete method described above, coupled with the work of Costa et al. [2010], represents a simplified framework to model the aggregation of volcanic ash, taking in account different aspects (differential sedimentation, turbulent shear, etc...). Usually, the aggregation kernels are a function of the sticking efficiency between particles and the collision rates due to Brownian motion, turbulence caused by inertial effects, differential sedimentation or turbulent and laminar shear. Then, the modification of the TGSD caused by ash aggregation is generally simulated using a sim-

plified framework by including source and sink terms within Eulerian [Folch et al., 2020; Textor et al., 2006] and Lagrangian [Jones et al., 2007; Beckett et al., 2022] dispersal models for volcanic ash. Interestingly, alternative methods are also used in numerical plume models such as *PLUME-MoM* [de'Michieli Vitturi and Pardini, 2021] where the SCE is solved using a hybrid method combining both the discrete method and the method of moments [Marchisio et al., 2003; Nguyen et al., 2016]. The method of moments (especially the Quadrature Method of Moments (QMOM)) is a very efficient CFD scheme to simulate polydisperse systems. The strategy is based on the tracking of some lower-order moments of the particle size distribution (i.e., we solve the transport equation for each moment). Furthermore, the similarity of the method of moments with the theory behind the LBM has allowed the development of aggregation schemes by integrating source terms in collision models such as the Bhatnagar-Gross-Krook (BGK) model [Majumder et al., 2012]. We make the choice of the simplified framework given by the discrete method. Its simplicity allows us to easily implement it within our hybrid 3D LB-Finite difference model.

4.1.2 Objectives and structure of the chapter

The first objective of this chapter is the implementation of particle aggregation within the 3D numerical model described in Lemus et al. [2021] (Chapter 2), with the ultimate goal of studying the interaction between aggregation and SDGIs. After a description of the governing equation used to simulate aggregation, we explain how we integrate the different source/sink terms into the particle transport equation using the simplified framework provided by the discrete SCE. Then, the model is validated through comparisons with analytical solutions obtained for simple cases. Once the model is validated, we propose to explore the sedimentation of particles when both aggregation and SDGIs occur. As both processes enhance the premature deposition of fine ash, the goal here is to study if aggregation has a significant effect on the collective settling induced by SDGIs and/or the opposite. Those investigations are particularly focused on the ground deposit signature in order to characterise quantitatively the possible impact on tephra deposits.

4.2 Methods

4.2.1 Governing equations

In order to include the aggregation process within our continuum phase model, we consider the polydisperse formulation, i.e., we discretise the particle size distribution with several classes and solve the advection-diffusion-settling equation for each particle size class. Thus, the buoyant force term in the fluid momentum equation becomes

$$\vec{F} = \left[\left(\frac{\rho_p - \rho_0}{\rho_0} \right) \phi_{tot} + \left(\frac{\rho}{\rho_0} - 1 \right) (1 - \phi_{tot}) \right] \vec{g} \tag{4.4}$$

where ρ_p is the particle density, ρ_0 the ambient density, $\vec{g}$ the gravitational acceleration and ϕ_{tot} the total particle volume fraction given by

$$\phi_{tot} = \sum_{i=1}^{N_c} \phi_i. \tag{4.5}$$

ϕ_i being the volume fraction of the i^{th} size class.

The continuous particle size spectrum is discretised into N_c classes and the i^{th} class is described by the quantities (ϕ_i, m_i, D_{pi}), the particle volume fraction, mass and diameter respectively. Then the integration of the aggregation process is made possible by the inclusion of source/sink terms in the transport equation. The evolution of the number of particles per unit volume N_i (belonging to the i^{th} size class) is described by the fixed-pivot equation [Kumar et al., 2006; Rossi, 2018]

$$\frac{dN_i}{dt} = B_i - D_i, \tag{4.6}$$

where B_i and D_i are respectively the birth and death terms (units: $\mathrm{m}^{-3}.\mathrm{s}^{-1}$). Knowing that the particle volume fraction is given by $\phi_i = N_i V_{pi}$, with the volume of a single particle (assuming spherical particles) $V_{pi} = \pi D_{pi}^3/6$, equation 4.6 becomes

$$\frac{d\phi_i}{dt} = \frac{\pi D_{pi}^3}{6} \left[B_i - D_i \right], \tag{4.7}$$

Finally, combining the general advection-diffusion-settling law describing the transport of particles (equation 2.6) with the source terms given above, we can

write a complete relation including aggregation:

$$\frac{\partial \phi_i}{\partial t} + (\vec{u_f} - V_{si}\vec{e_z}) . \vec{\nabla}\phi_i = D_{ci}\nabla^2\phi_i + \frac{\pi D_{pi}^3}{6}\left[B_i - D_i\right]. \tag{4.8}$$

The birth and death terms depend on different kernels describing the particle sticking efficiency and the collision rate. In order to ensure mass conservation, these kernels are weighted by coefficients that are functions of the particle masses. Then, the birth and death terms for a specific size class i capture the interaction with other classes and are given by:

$$\begin{aligned} B_i = & \sum_{m_i \leq (m_k + m_j) < m_{i+1}}^{j \geq k} \left(1 - \frac{1}{2}\delta_{kj}\right)\left(\frac{m_{i+1} - m}{m_{i+1} - m_i}\right) K_{kj} N_k N_j \\ & + \sum_{m_{i-1} \leq (m_k + m_j) < m_i}^{j \geq k} \left(1 - \frac{1}{2}\delta_{kj}\right)\left(\frac{m - m_{i-1}}{m_i - m_{i-1}}\right) K_{kj} N_k N_j \end{aligned} \tag{4.9}$$

$$D_i = \sum_{j=1}^{N_c} K_{ij} N_i N_j \tag{4.10}$$

with δ_{kj} the Kronecker delta which takes the value 1 when $i = j$ and 0 otherwise. Also, note that here, $m = m_k + m_j$. The birth term Bi in equation 4.9 represents the portion of mass added to the size class i due to aggregration of smaller particles. Similarly, the death term Di (equation 4.10) corresponds to the removal of mass from size class i due to agggregation forming larger particles. K_{ij} is the aggregation kernel which describes the interaction between particles in the i^{th} and j^{th} classes. K_{ij} can be written as the combination of two operators as $K_{ij} = \alpha_{ij}.\beta_{ij}$, where α_{ij} is related to the sticking efficiency and β_{ij} to the collision rate between particles. Note that α_{ij} is a dimensionless parameter while β_{ij} has the units of [$m^3.s^{-1}$]. Splitting the kernel like this allows us to consider several properties of the flow individually. Here we will focus on some specific collision rates commonly found in volcanology [Costa et al., 2010] such as those due to the turbulent shear β_{ij}^{TS} and the differential settling β_{ij}^{DS}. Thus, in that case, the total collision rate is given by $\beta_{ij} = \beta_{ij}^{TS} + \beta_{ij}^{DS}$

and these collision rates are given by the following relations

$$\beta_{ij}^{TS} = \left(\frac{\pi\epsilon}{15\nu}\right)^{\frac{1}{2}} (D_{pi} + D_{pj})^3 , \tag{4.11}$$

where ϵ is the fluid dissipation rate of turbulent kinetic energy and ν the fluid kinematic viscosity, and

$$\beta_{ij}^{DS} = \frac{\pi}{4} (D_{pi} + D_{pj})^2 |V_{si} - V_{sj}|. \tag{4.12}$$

The sticking efficiency is a complex quantity which depends on several parameters inherent in each collision, such as the presence of any liquid layer around particles, the electric charge or even chemical interactions [Pollastri et al., 2021]. Here we assume an average sticking efficiency defined for each particle size class and given by the relation (cf. the original work on wet aggregation in Costa et al. [2010])

$$\alpha_{ij} = \frac{c_1}{(St_{ij}/St_{cr})^q + 1}, \tag{4.13}$$

where St_{ij} is a Stokes number given by

$$St_{ij} = \frac{8\rho_p |Vs_i - Vs_j|}{9\mu_f} \left(\frac{D_{pi} D_{pj}}{D_{pi} + D_{pj}}\right), \tag{4.14}$$

with μ_f the fluid dynamic viscosity. This formulation depends on parameters empirically fitted (i.e., q, St_{cr} and c_1) with experiments and controls the interactions between particles. According to fittings with experimental data, Costa et al. [2010] proposed that $c_1 = 1$, $St_{cr} = 1.3$ and $q = 0.8$. However, it is interesting to estimate the sensitivity of the sticking efficiency to these parameters, in particular q. This exponent controls the sticking efficiency and, as q increases, the efficiency to form aggregates of larger sizes decays to zero (see Figure 4.2.1)

4.2.2 Numerical implementation

The different source/sink terms mentioned above are implemented in the finite difference scheme used to solve for the particle transport. We observe in equation 4.11 that the information about the turbulence in the fluid is given by ϵ. This

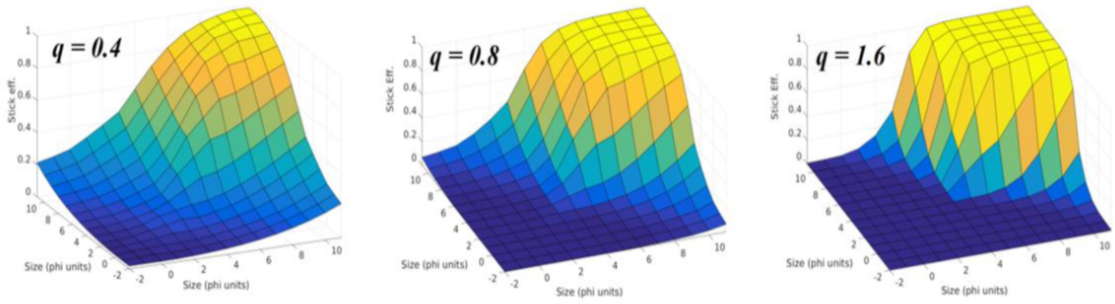

Figure 4.2.1: Effect of the q parameter on the sticking efficiency for collisions between differently sized particles. (From [Rossi, 2018])

rate expresses how the Turbulent Kinetic Energy (TKE) is dissipated by viscous forces and can be considered as a sink term in the transport equation of the TKE. In order to compute ϵ in our 3D hybrid model, we use the capability of *Palabos* to perform Large Eddy Simulations (LES) thanks to the Smagorinsky model [Latt et al., 2020]. This sub-grid model assumes the Reynolds number is high enough that small scales eddies are the only cause of energy dissipation and, thus, we can mimic this dissipation with an equivalent eddy viscosity given by the relation [Katopodes, 2019]

$$\nu_t = (C_s \delta x)^2 \sqrt{\bar{S}_{ij} \bar{S}_{ij}}, \tag{4.15}$$

where C_s is the so-called Smagorinsky constant, which usually varies from 0.1 and 0.2 [Davidson, 2015], and is fixed at 0.12 in our simulations. $\bar{S}$ is the strain rate tensor. One way to integrate this subgrid viscosity in the LBM-BGK model is to correct the shear viscosity contribution in the relaxation time formulation which becomes:

$$\tau^* = \frac{\delta t}{2} + \frac{\nu + \nu_t}{c_s^2}. \tag{4.16}$$

Ultimately, ϵ is function of the eddy viscosity and the strain rate tensor, which gives us

$$\epsilon = 2\nu_t \bar{S}_{ij}^2 = (C_s \delta x)^2 \bar{S}^3. \tag{4.17}$$

Finally, we observe here that in order to calculate the TKE dissipation rate we only

need to compute the strain rate tensor. In *Palabos*, we can easily estimate the shear stress tensor which is function of the off-equilibrium populations. Then, we can simply deduce the strain rate which is simply proportional.

4.3 Results

4.3.1 Model validation

We first validate the numerical implementation of aggregation process within the 3D numerical model. For all validation simulations, we start with a monodisperse particle distribution and observe the evolution of the total particle number per unit volume. Indeed, as soon as aggregates form, we expect a decrease in the total number of particles per unit volume which is, assuming spherical particles, estimated using

$$N_{tot} = \sum_{i=1}^{N_c} N_i = \sum_{i=1}^{N_c} \frac{6\phi_i}{\pi D_{pi}^3}. \tag{4.18}$$

Through the validation process, we apply constant aggregation kernels in order to compare with the analytical formulation derived for the isothermal Brownian coagulation (equation 4.3). Additionally, no feedback force (i.e., buoyant force on the fluid by the particle phase) is assumed in order to focus only on the particle phase. The arbitrary domain is a column of air with dimensions (in km) $0.075 \times 0.030 \times 0.385$. The domain is discretised in cells of size $\delta x = 0.002$ km (when the resolution is 500 nodes/km) and $\delta x = 0.004$ km (when then resolution is 250 nodes/km). The upper part of the domain (with a thickness of 0.135 km) is uniformly filled with particles in order to have an initial particle volume fraction $\phi_{tot} = 2 \times 10^{-6}$. First, we set the particle settling velocity to zero and we study the evolution of the total particle number density at a single node in the numerical mesh. Figure 4.3.1 shows the temporal evolution of the particle density number, normalised by its initial value, for four different values of the coagulation kernel. As expected, we clearly observe that the rate of decrease in the particle number (which commences instantaneously) increases as the kernel amplitude increases. Moreover, we also notice an extremely good agreement between our simulations and the analytical

prediction. This suggests that our numerical model is accurately able to produce aggregates at the rate predicted by theory.

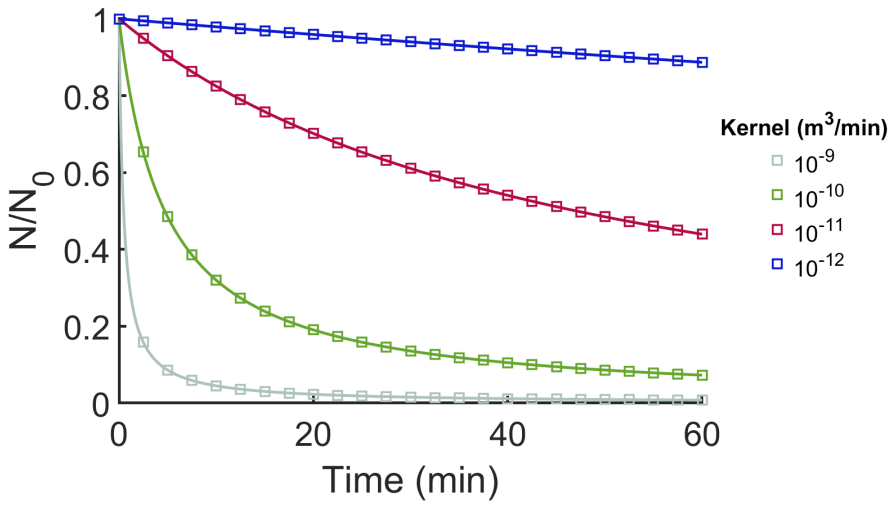

Figure 4.3.1: Temporal evolution of the normalised particle number density for different coagulation kernel values. The squares are the simulation results while the solid line is the analytical prediction given by equation 4.3.

Next, we add further complexity by allowing a non-zero settling velocity for the particle phases in order to characterise the effect of settling. The coagulation kernel is fixed at 10^{-9} m^3/min and we assign the same settling velocity V_s (in that case $V_s = 0.0075$ m/s) to each particle size class regardless of their size. Figure 4.3.2a shows the simulation results for two different grid resolutions, namely, 250 and 500 nodes/km (recall that the grid spacing is the reciprocal of the resolution). For a grid resolution of 125 nodes/km, the agreement with the theoretical formulation is still very good even though a slight discrepancy is apparent. This difference is due to the numerical diffusion introduced by the advection by settling. However, we observe that the discrepancy vanishes at higher resolution (500 nodes/km), which is coherent with the fact that the numerical diffusion is a function of the grid spacing. As the results are very good using a grid resolution of 500 nodes/km, we keep this value and now apply the correct settling associated with each size class. Then, Figure 4.3.2b shows a very good agreement between the results of this simulation and the analytical solution despite the fact that the size classes are advected at different settling velocities.

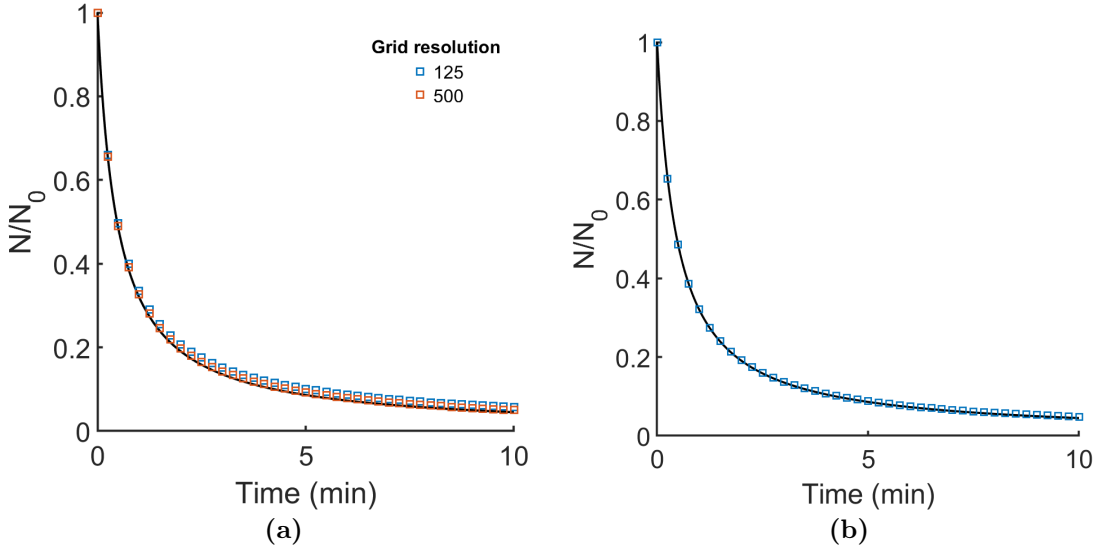

Figure 4.3.2: Temporal evolution of the normalised particle density number using (a) a fixed settling velocity for all size classes and different grid resolutions and (b) the physical settling velocity associated with each particle size. The grid resolution used is 500 nodes/km. The black solid lines are the analytical prediction.

4.3.2 Interaction between particle aggregation and settling-driven gravitational instabilities

The goal of this section is to explore the sedimentation of particles when both aggregation and SDGIs occur. The numerical domain consists of a static configuration similar to the one used in the first chapter [Lemus et al., 2021]. It is a large box of air with dimensions (in km) $0.075 \times 0.303 \times 0.385$ involving two layers: a particle laden upper layer of thickness 0.135 km placed above a denser lower layer of thickness 0.250 km. We used no slip boundary conditions for the fluid LB solver and no-flux boundary conditions for the finite difference schemes solving for the transport of particles and density-altering quantities. We performed two different sets of simulations involving two different synthetic initial particle size distributions as shown in Figures 4.3.4a and 4.3.6a. We made the choice of implementing two specific collision rates involving the particle sedimentation (β^{DS}) and the turbulence (β^{TS}). Our simulations start with a quiescent configuration, so initially without turbulence (i.e. only β^{DS} is non-zero as the dissipation rate is zero), but as soon as SDGIs form, turbulence is created as shown in Figure 4.3.3. Indeed, Figures 4.3.3a and 4.3.3c show snapshots of the particle volume fraction respectively at 6.5 s and

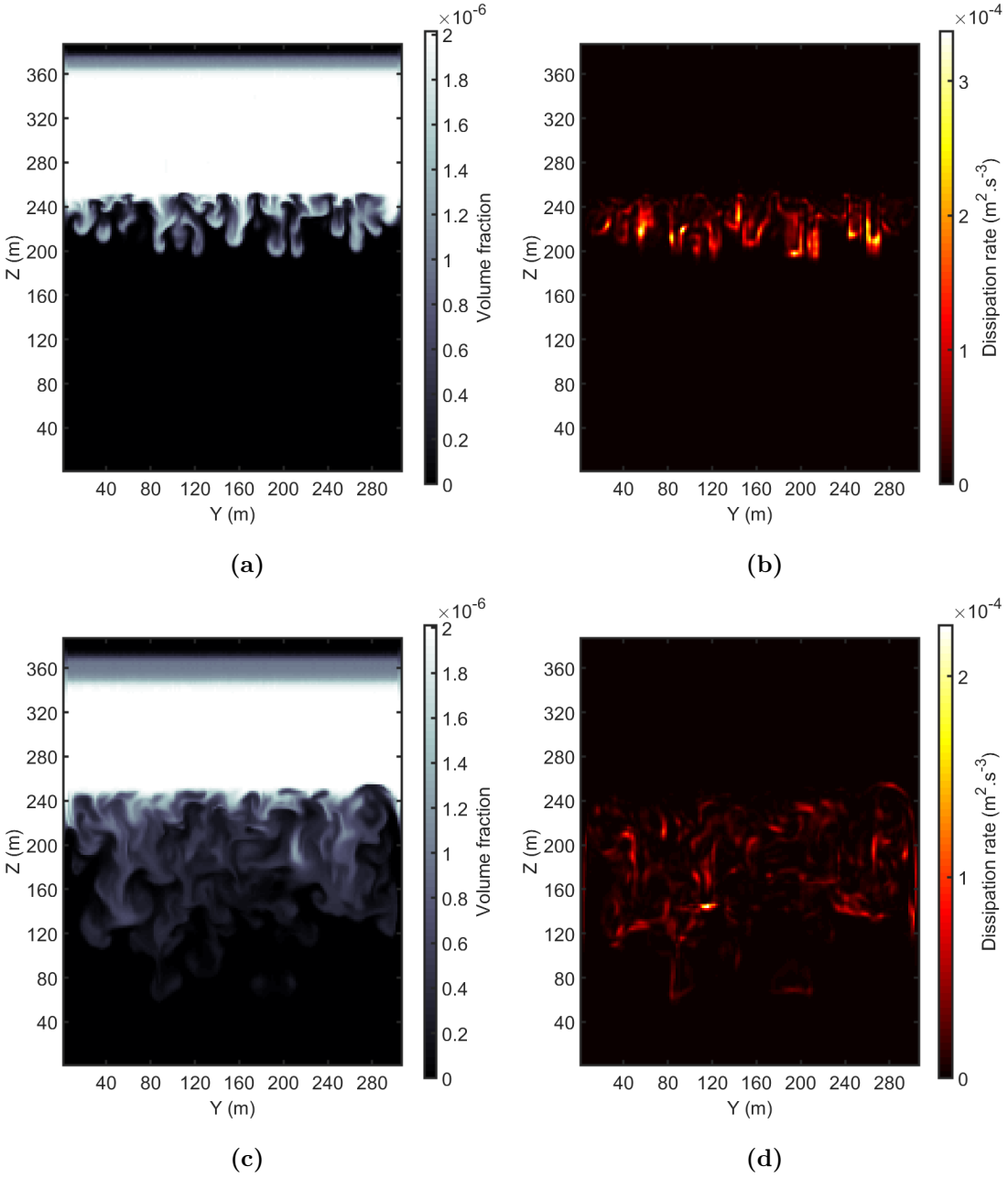

Figure 4.3.3: (a), (c) Snapshots of a simulation respectively at 6.5 and 12 min. The shown quantity is the total particle volume fraction. (b), (d) Maps of the associated dissipation rate of turbulent kinetic energy ϵ. For those simulations, no aggregation is considered yet in order to focus only on the turbulence generated by SDGIs.

12 s for simulations without aggregation (actually slices in the (y, z) plane of the 3D domain) and Figures 4.3.3b and 4.3.3d show the associated dissipation rate. We effectively observe that the dissipation rate is zero in the upper layer while it is of the order of 10^{-4} m^2.s^{-3} in the lower layer. This is expected as initially the upper layer is quiescent and the turbulence is created once the convection induced by the

fingers' propagation starts.

Simulations with a coarse grainsize distribution as input

In the first set of simulations, almost all sizes in the particle size distribution are initially present with different weights (Figure 4.3.4a). In that case, the coarse particles initially present settle individually such that it would be possible to highlight how the creation of more coarse particles would affect the individual settling process. For a reference case, we simulated the sedimentation of particles without any aggregation. Then, we included the aggregation varying the sticking efficiency, i.e., using two different values of q in equation 4.13. Figures 4.3.4b and 4.3.4c shows the grainsize distribution in the whole domain after 10 minutes for $q = 1.6$ and $q = 0.8$, respectively. We observe that aggregation seems to be more efficient for the smallest value of q. In all simulations, SDGIs are observed so the effect of the addition of aggregation is investigated through parameters such as the mass deposited on the ground and the associated accumulation rate (AR). Figure 4.3.5a shows the total particle mass deposited on the ground for the three performed simulations. First, we see that for $q = 0.8$, the aggregation process reduces the initial time that particles take to reach the bottom of the domain. Secondly, we observe a small change in the curve slope after around 16 minutes which suggests a change in the sedimentation process. This change is even more pronounced when we compute the instantaneous AR as seen in Figure 4.3.5b. For all cases, we observed a constant AR in a time interval $[T_1; T_2]$, suggesting individual settling, where T_1 is the time when the first particles reach the floor (obviously by individual settling) while we observe that T_2 is the time when the first fingers reach on the ground. Interestingly, after T_2 the AR does not remain constant but increases in time, revealing the presence of SDGIs as described in Lemus et al. [2021]. Furthermore, the effect of aggregation is clear, with non-zero values of q leading to greater ARs throughout.

Simulations with a fine grainsize distribution as input

The second set of simulations involves a wider synthetic distribution of particle sizes and the simulations are initialised with a fine size distribution (Figure 4.3.6a). This

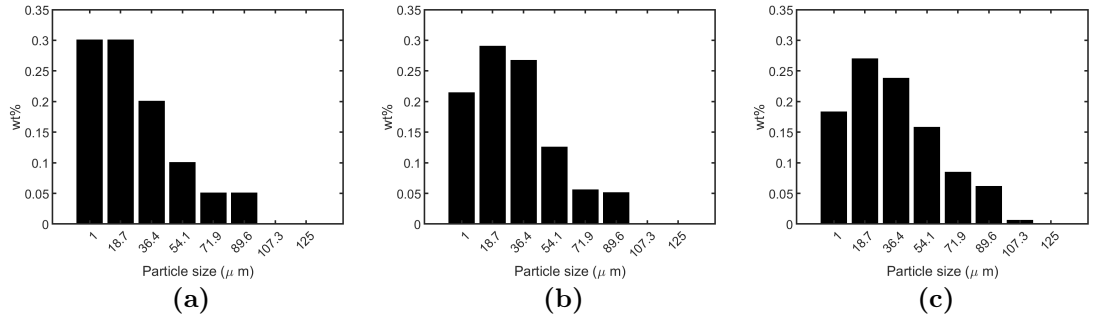

Figure 4.3.4: TGSD for the first set of simulations. (a) is the initial distribution which initially contains almost all size bins, (b) the distribution after 10 min using $q = 1.6$ and (c) $q = 0.8$.

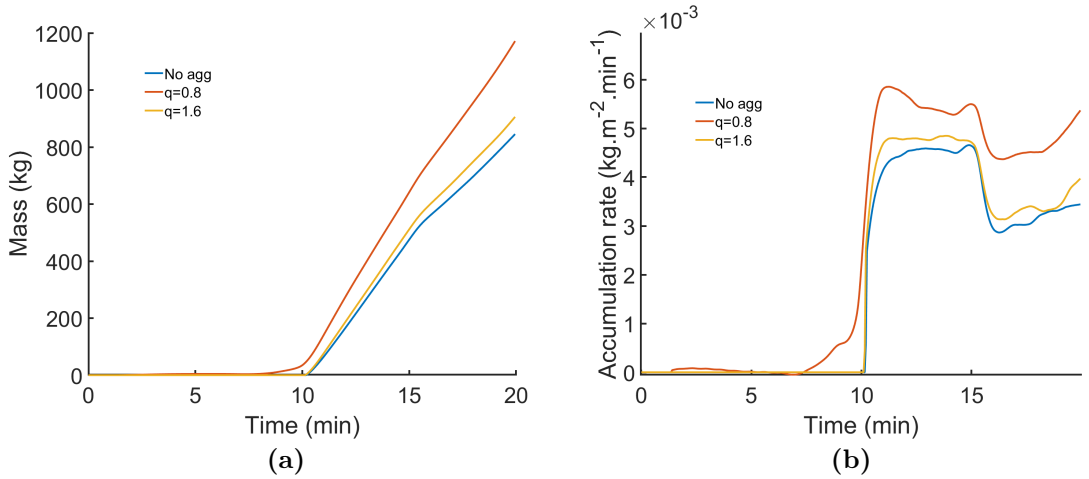

Figure 4.3.5: (a) Total mass of particle deposited at the bottom of the numerical domain as a function of time. (b) The associated instantaneous accumulation rate.

TGSD has been chosen arbitrarily in order to avoid the individual settling of coarse particle initially present. When the aggregation process is enabled, it is obviously more efficient for $q = 0.8$ than for $q = 1.6$, as there are more coarse particles after 10 minutes (see Figures 4.3.6b and 4.3.6c). We then follow the same strategy as before by interrogating the deposited mass and the AR. Here, we observed the presence of fingers but almost no individual settling. Figure 4.3.7a confirms the premature deposition enhanced by the aggregation as the deposited mass for $q = 0.8$ starts increasing before the other situations. Additionally, the mass seems to accumulate at a greater rate as soon as there is aggregation. This is indeed observable on the AR plotted on Figure 4.3.7b. For all cases, the AR increases as expected in the presence of SDGIs. However, the slope is clearly steeper for $q = 0.8$ suggesting that the creation of coarser particles by aggregation further enhance the rate of

sedimentation. An interesting observation is also that, around 25 min, the AR for the case $q = 0.8$ becomes constant, implying that the sedimentation regime switches from collective to individual settling (i.e. end of convection).

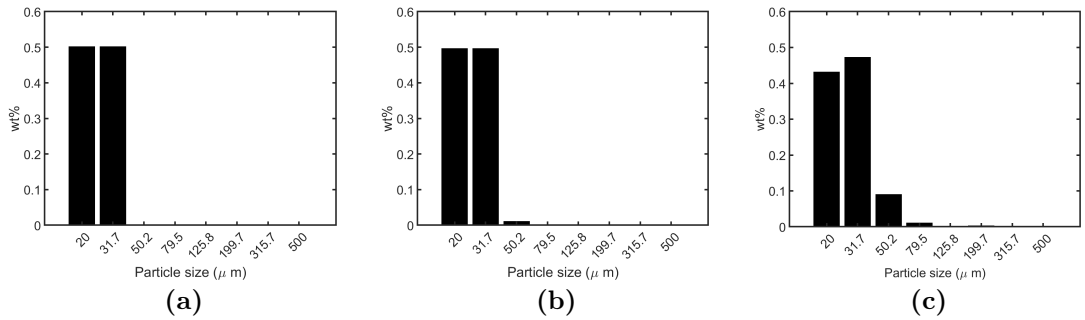

Figure 4.3.6: Particle size distribution for the second set of simulations. (a) is the initial distribution which contains relatively fine fractions, (b) the distribution after 10 min using $q = 1.6$ and (c) $q = 0.8$.

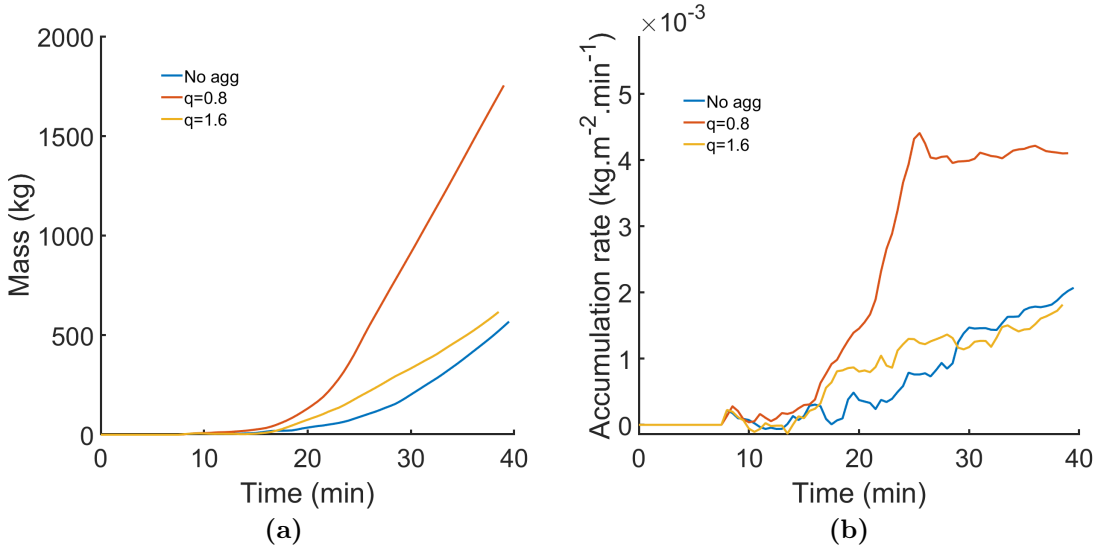

Figure 4.3.7: (a) Total mass of particle deposited at the bottom of the numerical domain. (b) The associated instantaneous accumulation rate.

4.4 Discussion

4.4.1 Caveats

The integration of this coagulation scheme within *Palabos* allowed us to perform simulations on fine grids ($\delta x = 0.002$ km over a domain extent of 0.385 km). Then,

for the biggest domain used and thanks to the capability of *Palabos* to perform calculations on massively parallel computers, we could simulate 20 minutes of physical time in ≈ 8 *hours* on 288 cores. However, our implementation could be significantly improved in order to reduce the calculation time by changing the way we solve simultaneously the transport of each size class. Indeed, for each size class, we set up a scalar field in order to solve the transport equation. This surely requires an certain amount of memory and of communication. Thus, everything might be gathered in a single tensor field of dimension equal to the number of size classes in order to improve the communication and the memory management.

The discrete formulation of the aggregation scheme within our numerical model has been successfully validated by comparison with an analytical solution of the Smoluchowski equation. Whilst this ensures some numerical stability, there are some caveats to consider. Indeed, the discrete method implemented for the aggregation involves a finite number of bins representing samples of the continuous particle size spectrum. Obviously, the greater the number of bins, the more accurate the evolution of the TGSD will be. However, for evident reasons related with numerical costs, the number of bins needs to be limited. In our case, we solve simultaneously the advection-diffusion-settling (with aggregation) equation for each particle size class which definitely increases the calculation time. Then, the discretisation of the size spectrum has to be accurate to cover a relevant range of sizes and the use of a logarithmic sampling is well suited [Rossi, 2018].

Regarding the model itself, it is critical to define accurately the sticking efficiency which depends on several parameters. We used the formulation given in equation 4.13 [Costa et al., 2010] in order to define an average value for each size pair. However, this formulation depends on empirical parameters (i.e. c_1, q and St_{cr}) which have been scaled using experimental fittings [Costa et al., 2010; Gilbert and Lane, 1994]. Whilst sensitivity analyses have been performed in order to constrain those parameters [Rossi, 2018; Beckett et al., 2022], the sticking efficiency during volcanic ash collisions remains difficult to characterise. A resulting interesting question is: is there a difference between the sticking efficiency in clouds and in fingers? A way to investigate this aspect is to study specific parameters which affect the sticking

efficiency in both the cloud and fingers (humidity, electrification...).

Additionally, there is no denying that the same interrogation is relevant regarding the collision rates. In the model, the collision rate is given by the operator β and describes specific dynamics such as the effect of sedimentation and turbulence. Indeed, we used two kernels describing the aforementioned processes i.e. the differential sedimentation β^{DS} and the turbulent shear β^{TS} in our simulations. Of course, other kernels exist in order to include different processes in volcanology, but we neglected them in our study. There are for instance the Brownian motion β^{BM} which is negligible given the particle sizes involved or else the laminar shear β^{LS}, not relevant in our configuration as there is no shear. There is also the turbulent-inertial kernel β^{TI} which is a function of the velocity provided by the fluid on each particle size inside eddies. However, one important assumption of our single-phase model is that particles have no inertia, thus this kernel is also neglected.

β^{DS} is a function of the terminal velocities of particles which are the Stokes velocities in our simulations, given the fact that we start with a quiescent configuration. However, as soon as SDGIs appear, the induced turbulence and mixing by eddies on the edges of fingers for instance, make particles move at a different velocity than their respective Stokes velocities. This suggests a need for a more accurate formulation of the terminal velocities inside fingers. The effect of turbulence on the formation of aggregates is described by β^{TS} which is a function of the dissipation rate of turbulent kinetic energy ϵ. In our simulations, we showed that ϵ is in the order of 10^{-4} $\mathrm{m}^2.\mathrm{s}^{-3}$ in the presence of fingers. This value is several orders of magnitude lower than the plausible range [0.1 - 100] $\mathrm{m}^2.\mathrm{s}^{-3}$ suggested by Rossi [2018] for a volcanic cloud. In order to investigate if the turbulence within fingers enhances aggregation, there is need to evaluate if the value of ϵ in fingers is higher than in the cloud. However, our configuration, which starts with a quiescent ambient, is not representative of the atmospheric turbulence and thus, the gradient of ϵ is not relevant to compare with nature. This highlights the need for a more complete model which simulates accurately the turbulence.

4.4.2 Combination of aggregation with settling-driven gravitational instabilities

We performed two different sets of simulations involving different synthetic initial size distributions chosen arbitrary in order to study different sedimentation processes in the presence of aggregation. We showed that aggregation affects both individual and collective settling, contributing to different ground signatures, i.e. the AR and the bimodal grainsize distribution. Indeed, the simulations already initially involving a fraction of coarse particles showed that even the individual settling is enhanced because the constant AR is higher than the case without aggregation. As the AR for individual settling is proportional to the particle settling velocity [Lemus et al., 2021], this is coherent as the settling velocity increases with the size of aggregates. In addition, besides the enhanced AR as a signature, there is also the bimodal grainsize distribution if we assume that aggregates break on the ground, revealing the fine particle fractions. With the simulations starting with a fine particle fraction, we were able to characterise the effect of aggregation on SDGIs. Indeed, Lemus et al. [2021] showed that in the absence of shear, there is a characteristic ground signature of SDGIs which is a temporally increasing AR. The present study has shown that aggregation has the potential to enhance this signature, which is coherent given the fact that the sedimentation rate increases with the particle size [Lemus et al., 2021].

Regarding the effect of SDGIs on the aggregation process, we showed that the turbulence inside fingers ensures some conditions to produce aggregates. Whilst the need for more studies in order to compare those turbulent conditions with the ones inside the cloud, fingers are good channels to keep aggregation processes active until the final deposition of aggregates on the ground. Indeed, let's imagine that when aggregation occurs in the cloud, aggregates leave the cloud and settle in their final form and size on the ground. Interestingly, in the presence of SDGIs, aggregates that leave the cloud and sediment within fingers are able to continue their growth until the final deposition on the ground.

Finally, we can imagine extreme situations where aggregation may dampen the formation of SDGIs. Indeed, the formation of aggregates with different settling velocities may get the cloud interface more diffuse, causing the buoyancy gradient

inefficient to trigger instabilities. Therefore, this can be investigated using a finer discretisation of the particle size spectrum (i.e. a greater number of bins). Another situation is when aggregation is enough efficient to build particles of size beyond the size limit where no fingers are formed [Lemus et al., 2021].

4.5 Conclusions

Both particle aggregation and settling-driven gravitational instabilities have the potential to enhance the premature sedimentation of volcanic fine ash. However, the interaction between these two processes has never been investigated. This work has shown a successful integration of the aggregation process within the 3D LBM model described in Lemus et al. [2021] (Chapter 2). The use of the simplified framework provided by the discrete method in order to solve the Smoluchowski equation have shown very good agreement with an analytical solution for a simple problem. Then, the updated model has been used to investigate on how the presence of aggregation affects the collective settling by SDGIs. Interesting outcomes include:

- First, we observed that aggregation affects all sedimentation modes (i.e. individual and SDGIs) by increasing the AR. In the case of individual settling (constant AR), the production of aggregates increase the settling velocity and ultimately the AR. For SDGIs, the characteristic ground signature (higher AR than individual settling) is enhanced by aggregation.

- Second, there is also an effect of SDGIs on aggregation as the turbulence generated within fingers contribute to the creation of aggregates. This aspect is interesting as fingers can be seen as a tunnel between the cloud and the ground, within which aggregation continues to occurs.

- Third, we implemented the aggregation scheme in a numerical framework which allows to perform calculation on massively parallel computers. Whilst our code remains numerically stable, some other technical improvements could be done in order to reduce the numerical cost (i.e. number of cores, simulation time, memory...)

Finally, further investigations are still needed in order to constrain crucial parameters between the cloud and fingers, such as the sticking efficiency, the turbulence etc...This highlight once again the need for a more complete model taking in account the turbulence inside a volcanic cloud.

Author Contributions

Jonathan Lemus integrated the aggregation model in the model, conducted the simulations, data analysis and drafted the manuscript. Eduardo Rossi provided the aggregation model and helped for the implementation and validation. Jonas Lätt and Bastien Chopard supervised the use of the Palabos code. All authors have contributed to data interpretation as well as the editing and finalising of the paper.

Acknowledgments

All the simulations presented in this paper have been performed using the High Performance Computing (HPC) facilities *Baobab* and *Yggdrasil* of the University of Geneva.

Chapter 5

Two-phase model using the Lattice Boltzmann Method for the simulation of particle suspensions

5.1 Introduction

The single-phase model described in the second chapter [Lemus et al., 2021] has been used to investigate the dynamics of settling-driven gravitational instabilities (SDGIs) at various scales. The main assumptions underlying the use of a single-phase (or continuum) approach is that particles are small enough and in sufficiently large number that they remain fully coupled with the fluid, also implying that particles have no inertia [Chou and Shao, 2016; Yamamoto et al., 2015; Harada et al., 2013]. Whilst grid-based numerical methods, such as our single-phase model, suffer some intrinsic numerical diffusion [Ferziger and Peric, 2002], we managed to reduce this limitation by implementing a specific finite difference scheme. Indeed, the Weighted Essentially Non-Oscillatory (WENO) finite-difference scheme implemented ensures a low-diffusive [Liu et al., 1994; Jiang and Shu, 1996] and non-dispersive method despite the high-order accuracy (see [Godunov, 1954, 1959] for details on dispersion of high order schemes). Additionally, the ease of implementation offered by a finite difference scheme allows easy coupling with Lattice Boltzmann methods (LBM) on uniform grids [Lemus et al., 2021].

Various Euler, continuum-phase methods [Ferziger and Peric, 2002; Chou and

Shao, 2016; Jacobs et al., 2013; Burns and Meiburg, 2014; Yu et al., 2014; Liu et al., 1994; Jiang and Shu, 1996] can be applied in order to simulate multi-phase systems by solving the transport equation for each phase. However, numerical diffusion, even reduced, may remain a critical problem when tracking the interface between immiscible phases [Mansour et al., 2021; Zhao et al., 2011; Zhang et al., 2006, 2014]. Among the so-called interface-tracking methods used to handle such problems [Chen and Hagen, 2011, and references therein], one efficient technique is the particle-based method. This method can be seen as a hybrid between Lagrangian and Eulerian solvers. The domain is still discretised with a grid with the advantages of the Lagrangian tracking of passive tracers that follow a specific phase in order to precisely define the interface. Given the fact that point particles are used in large number, we drastically decrease the diffusion usually introduced by fully grid-based methods because the interface between the particle suspension and the underlying denser layer is directly related to the presence of particles or not in one cell. Also, any grid-based method can be improved with passive tracers as has been the case with the Lattice Boltzmann Method (LBM) [Lätt et al., 2013]. Finally, whilst grid-based methods provide an efficient means of solving multi-phase flows at relatively low numerical cost, particle-based methods allow improved accuracy but at increased numerical cost, since the position of a large number of Lagrangian particles need to be tracked, even though their velocities are given by the fluid [Santos et al., 2012]. However, for some types of multi-phase problems, especially involving solid phases, the motion of each individual particle has to be solved explicitly because, due to their inertia, they are no longer fully coupled with the fluid. Then, the numerical cost becomes even greater than the aforementioned particle-based methods because of the need for solving the equation of motion for each particle as well as the feedback on the fluid [Chou and Shao, 2016; Yamamoto et al., 2015; Harada et al., 2013]. Thus, this allows the inclusion of some fundamental aspects, such as drag effects. Of course, in the same way that there is a limit separating the use of a single-phase model (particles fully coupled with the fluid) and the use of a two-phase model (with inertial point particles) [Harada et al., 2013; Yamamoto et al., 2015; Maxey and Riley, 1983], there is also a limit in the use of point particles. Indeed, increasing

the size of particles increases the effect of each particle on the flow, reducing the accuracy of Lagrangian methods and, thus, leading to the use of immersed bodies [Ferry and Balachandar, 2001].

This chapter describes a two-phase model developed to complement the single-phase model presented in the first chapter [Lemus et al., 2021]. The main motivation of a two-phase model is the capability to simulate flows when the single-phase assumptions are no longer valid i.e., when the particle inertia is not negligible anymore. Given the high numerical cost underlying the simulation of a large number of individual particles, this model is intended to be used in order to study problems at small spatial and temporal scales, such as the entrainment induced by SDGIs for instance [Chou and Shao, 2016]. Also, in converse to the single-phase model, particles can now have inertia, which enables the study of the coupling with the fluid within fingers. However, since we use point particles, the model needs to be used in conditions when the implicit Lagrangian formulation is still valid, i.e., when the fluid flow is not affected by boundary effects at the fluid-particle interface (Basset force) and when the added mass effect is negligible [Ferry and Balachandar, 2001]. In the rest of this chapter, we first present the governing equations of the model. Secondly, we describe the numerical approach taken in order to solve the equations. Finally, we present a qualitative comparison to results obtained with the single-phase model in a reduced domain.

5.2 Methods

5.2.1 Governing equations

The two-phase model explicitly solves the equations of motion for point particles in a fluid flow. The mathematical formulation associated with the two-phase model is similar to that used for the single-phase model. In the single-phase model, the coupling between the fluid and the particle phase is mutual. Indeed, the fluid velocity is needed in order to define the convective term of the particle phase while the solution of the transport equation is required for the buoyant force term in the fluid momentum equation. We recall the Navier-Stokes momentum equation for an

incompressible fluid

$$\frac{\partial \vec{u}_f}{\partial t} + (\vec{u}_f.\vec{\nabla})\vec{u}_f = -\frac{1}{\rho_0}\vec{\nabla}p_f + \nu\nabla^2\vec{u}_f + \vec{F}, \tag{5.1}$$

where $\vec{u}_f\,(\vec{x},t)$ is the fluid velocity, t the time, p_f the pressure, ρ_0 a reference density of the carrier fluid, ν the kinematic viscosity, $\vec{F}$ the body force term and $\vec{x}$ the position vector. Now considering the two-phase model, the body force term in a control volume is the feedback force of particles on the fluid which, under the Boussinesq approximation, is given by [Chou and Shao, 2016]

$$\vec{F} = -\frac{\rho_p}{\rho_0}\sum_{i=1}^{N_p}\phi_p\frac{\vec{u_{f,i}} - \vec{v_i}}{\tau_i}, \tag{5.2}$$

where ρ_p is the particle fluid density, N_p the number of particles in the control volume, ϕ_p the volume fraction of a single particle, $\vec{u_{f,i}}$ the fluid velocity estimated at the location of the i^{th} particle, $\vec{v_i}$ and τ_i respectively the velocity and relaxation time, respectively, of the i^{th} particle. Note that this force term is the contribution of each particle within the control volume. We also observe that the particle relaxation time is needed and there are several ways to define it, depending on the fluid-particle interaction. Here, we use the Schiller [1933] relaxation time, as is commonly suggested, also providing an accurate contribution of the drag effects [Chou and Shao, 2016; Cerminara et al., 2016]

$$\tau_i = \frac{\rho_p D_{p,i}^2}{\rho_0 18\nu\left(1 + 0.15Re_{p,i}^{0.687}\right)}, \tag{5.3}$$

where $D_{p,i}$ is the particle diameter and $Re_{p,i}$ the particle Reynolds number given by

$$Re_{p,i} = \frac{|\vec{u_{f,i}} - \vec{v_i}|D_{p,i}}{\nu}. \tag{5.4}$$

Finally, the remaining quantity is the particle velocity which is the solution to the equation of motion given by Newton's second law. Thus, assuming that the forces acting on a single particle are the gravitational force, the buoyancy force and the drag force, we have

$$\rho_p \frac{d\vec{v_i}}{dt} = \rho_p \frac{\vec{u_{f,i}} - \vec{v_i}}{\tau_i} + (\rho_p - \rho_0)\,\vec{g}. \tag{5.5}$$

Note that the drag force derives from Stokes law and because $\rho_p \gg \rho_0$ we neglect other effects such as the added mass, the pressure gradient, the Basset history and the Saffman terms [Ferry and Balachandar, 2001].

5.2.2 Numerical implementation

The model is implemented within the *Palabos* framework which provides a built-in library to simulate particles [Latt et al., 2020]. Thus, our model benefits from the capability of *Palabos* to perform calculations on massively parallel computers. Here, we will describe how particle positions are numerically calculated and how we estimate the fluid velocity at the particle locations. The fluid motion is classically simulated using the LBM-BGK model, allowing for an external force as it is described in the first chapter [Lemus et al., 2021].

In order to calculate the position of a particle at a time $t + \Delta t$ (Δt being the time step), we need to solve its equation of motion. Several methods, such as the Euler method, Verlet integration or even Runge-Kutta methods [Hairer et al., 1993; Verlet, 1967], are available in order to numerically solve such ordinary differential equations (ODEs). Verlet integration is the strategy chosen in *Palabos* in order to calculate the particle position because it presents non negligible advantages, as we go onto explain. The method is based on the combination of the two Taylor expansions of $\vec{x}(t+\Delta t)$ and $\vec{x}(t-\Delta t)$. Indeed, by summing those two functions and rearranging, we obtain a relation which provides the position of the particle in the next time step

$$\vec{x}(t + \Delta t) = 2\vec{x}(t) - \vec{x}(t - \Delta t) + \frac{d^2x(t)}{dt^2}\Delta t^2 + O(\Delta t^4). \tag{5.6}$$

We observe that the summation deleted the contribution of the velocity, making the next particle position a function of it's previous position, the current position and it's acceleration only. This represents a gain in terms of computational time compared to other methods as there is no need to compute the velocity in order

to update the position of the particle. Further advantages can be highlighted by comparing different ODE-solving methods when applied to the simple case of a harmonic oscillator. This problem is described by the following equation

$$\frac{d^2x(t)}{dt^2} + kx(t) = 0 \tag{5.7}$$

where $x(t)$ is the position of the particle and k a positive spring constant. Assuming the initial conditions $x(0) = 1$ and $x'(0) = 0$ (in dimensionless units), a solution for this equation is $x(t) = cos(\sqrt{k}t)$. Figure 5.2.1 shows a comparison between the solutions given by the classical Euler method, Verlet integration and the 4^{th} order Runge-Kutta (RK4) method. We clearly see in Figure 5.2.1a that, for a coarse time discretisation, the Euler method is unstable while the Verlet integration and the RK4 method accurately reproduce the analytical solution. Reducing the time step partially stabilises the solution obtained by the Euler method (Figure 5.2.1b) but, still, small divergence occurs after some time. The accuracy for both the Verlet and RK4 is conserved whilst the simulation times are:

- 0.00137 s for the Verlet integration
- 0.00135 s for the Euler method
- 0.003484 s for the RK4 method.

Thus, the time taken to apply the RK4 method is more than twice the time required by the Verlet method. To conlcude, the Verlet integration is more stable than the Euler method and provides a reduced execution time compared to RK4 for an equivalent accuracy. This final aspect is crucial in order to reduce the total computational time when dealing with a large number of particles.

Now that we have a procedure to update the position of each particle, we need to estimate the fluid velocity at the particular location of that particle. Indeed, this parameter is needed in order to compute the body force term, the relaxation time and the drag force. Grid-based models calculate macroscopic or mesoscopic (in the case of the LBM) quantities at each node of the grid (i.e., the discretised domain). In our two-phase model, the positions of particles are not confined to the grid nodes

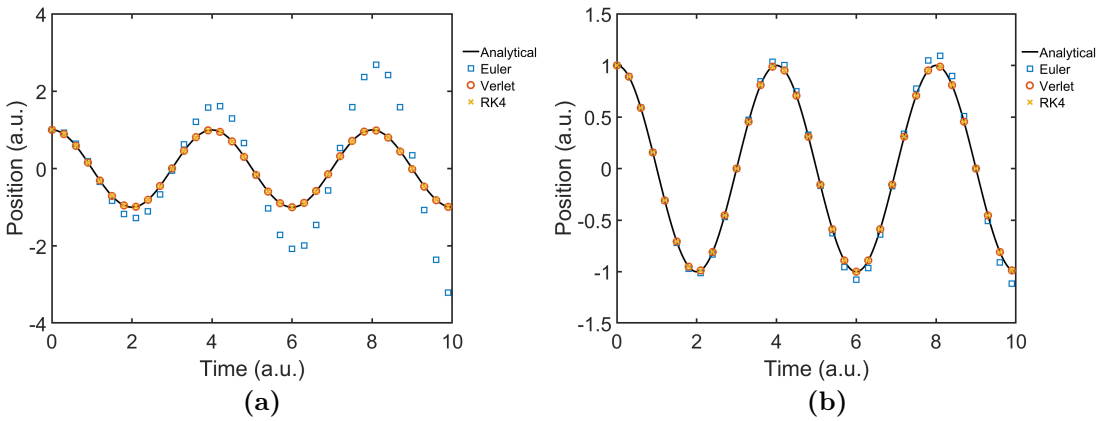

Figure 5.2.1: Comparison between solutions for a harmonic oscillator obtained using the Euler method, Verlet integration and the 4^{th} order Runge-Kutta method for a harmonic oscillator using time steps of (a) 0.1 and (b) 0.01 (dimensionless units).

and particles can move *continuously* between the grid nodes (the limit being the precision of the data type used for the particle position). When a particle is located between nodes, the fluid velocity is not available as it is calculated only on the grid nodes. In a 1-dimensional domain we can apply a simple linear interpolation. However, since our model is 3D, we estimate the velocity at the particle location using a trilinear interpolation [Bourke, 1999].

5.3 Results

The developed 3D two-phase model has not yet been used for investigations of settling-driven gravitational instabilities (SDGIs). However, we have performed some simulations in order make some qualitative comparisons with the single phase model. We consider the same conditions as those used in Chapter 2 (in water, grid spacing $\delta x = 0.001$ m, particle-laden upper layer, sugar solution in the lower layer and particle size of 40 μm) except that we use here a domain half the size of that previously considered (i.e. $0.0375 \times 0.151 \times 0.193$ in m). Figure 5.3.1 shows a comparison between initial results from the single-phase and the two-phase models for equivalent conditions. Both simulations have been performed on 256 cores, which allowed us to simulate 20 s of physical time in ≈ 4 hours for the single-phase model and ≈ 80 hours for the two-phase (≈ 6 million particles simulated).

In order to visualise the two-phase model results in the same way as those from

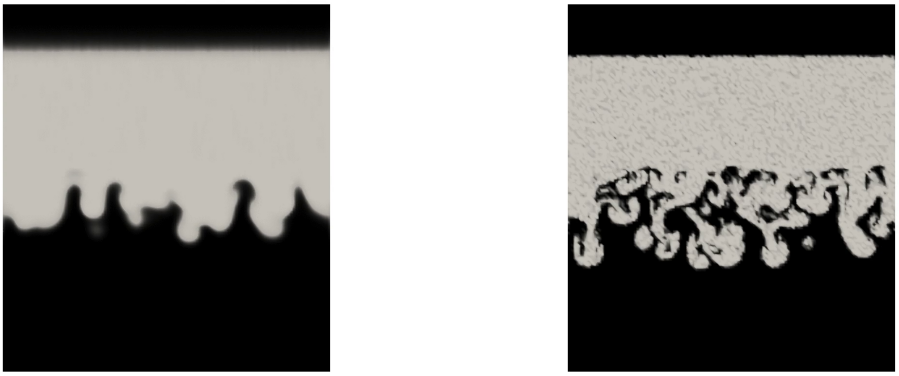

(a) (b)

Figure 5.3.1: Snapshots of simulations 15 s after barrier removal for (a) the single-phase model and (b) the two-phase model. For both cases the initial particle volume fraction is 3.97×10^{-4}.

the single-phase model, we computed the particle volume fraction in every cell as

$$\phi = \frac{N_p V_p}{\delta x} \tag{5.8}$$

with N_p the number of particles in a cell of size δx and V_p the volume of a single particle (assumed to be spherical).

We observe that both models produce fingers. However, the SDGIs in the two-phase model appear to be more resolved and better developed. A fundamental reason for this is that the numerical diffusion is zero when simulating particles individually, avoiding the smoothing of the interface and allowing the development of fine structures.

5.4 Discussion

The two-phase model using the LBM to solve for the continuous phase and discrete point particles has strong potential for the study of fine structures, such as turbulent eddies at the edges of fingers, or the effect of drag on particle sedimentation. Whilst there is some possibility for further optimisation, computational cost remains a critical factor, limiting application of such methods when dealing with a large number of particles. Here, we presented an example of a simulation with a dilute configuration (equivalent to a particle concentration of 1 g/l). The qualitative results

have shown that there are slight differences between the single-phase and the two-phase model. Indeed, fingers seem to be better developed in the two-phase case, suggested they are triggered earlier than the single-phase case. A explanation to that might be the absence of numerical diffusion in the two-phase model, implying a less diffuse interface between the particle suspension and the lower layer. However, another reason might be the neglected forces in the particle-fluid interaction such as the added mass, the Basset force, the pressure-gradient and the Saffman terms. In volcanic clouds, the condition $\rho_p \gg \rho_0$ is certainly valid to neglect the previously mentioned effects while it is not the case when considering glass beads in water (i.e., in the experiments and the associated simulations). In that case, further simulations including the neglected forces are definitely required to infer if they can remain neglected in our configuration. Additionally, the computational time may increase unsustainably just by multiplying the initial concentration by 10, as was done in Fries et al. [2021] and Lemus et al. [2021] in order to extend the range of particle concentrations. Ultimately, it is a matter of size ratio (between the size of particle and the flow characteristic length) and concentration. Current computational capabilities mean that the use of this model for the transport of micron-sized particles within a full volcanic cloud is impractical as the density number is usually in the range $[10^7; 10^{11}]$ particles/m^3 [Rossi, 2018]. Additionally, the use of a two-phase model suffers from several limitations. When the particle concentration and ratio of particle size and flow characteristic length allow a reasonable number of particle, the use of this two-phase model is practical and potentially useful. However, it is necessary to make sure that the flow around each particle is not affected by any drag effects such that the Lagrangian formulation is still valid [Ferry and Balachandar, 2001].

5.5 Conclusions

We have developed a two-phase model simulating the individual motion of particles within a particle suspension. This model has been qualitatively compared with our 3D single-phase model (Chapter 2) and showed that it is possible to trigger

SDGIs. Interestingly, this model enables the study of fine structures since there is no numerical diffusion of the particle field. Essentially, we have highlighted:

- The high accuracy of the Verlet integration for calculating particle positions
- The model allows the inclusion of further effects such as the drag, providing insights into the decoupling of particles with the fluid inside fingers. The entrainment of ambient fluid at the edges of fingers is also a parameter that can be investigated.
- Given the numerical cost of this discrete model, its use is limited to problems involving a reasonable number of particles, despite the possible improvement and optimisation that can be done.

Author Contributions

Jonathan Lemus developed the two-phase model program within the Palabos framework. Jonas Lätt and Bastien Chopard supervised the use of the Palabos code. All authors have contributed to data interpretation as well as the editing and finalising of the paper.

Acknowledgments

All the simulations presented in this paper have been performed using the High Performance Computing (HPC) facilities *Baobab* and *Yggdrasil* of the University of Geneva.

Chapter 6

Conclusions and future perspectives

This thesis presents insights into the dynamics of SDGIs thanks to the development of a 3D hybrid numerical model. First, the novel combination between a Lattice Boltzmann method and the low-diffusive WENO scheme has been validated with experimental and theoretical results. Additionally, further investigations allowed me to constrain critical parameters such as the Grashof number, but also to extract a characteristic ground signature for SDGIs (Chapter 2). Second, the addition of shear due to the horizontal motion of fluid showed that the sedimentation of particles affects the geometry of the cloud. Interestingly, a case study has highlighted that SDGIs can produce a bimodal signature in the deposit despite the absence of aggregation (Chapter 3). This has a very important implication for the genreal understanding of volcanic clouds as SDGIs are now identified to be non negligible processes that enhance the premature deposition of fine ash. Third, the successful integration of the Smoluchowski coagulation equation with our 3D numerical model supported the possibility to investigate the interaction between aggregation and SDGIs. Indeed, it has been shown that aggregation enhances both individual and collective settling while the turbulence inside fingers may trigger the formation of aggregates (Chapter 4). It also implies that the interpretations of tephra deposits, especially in the case of bimodal grainsize distribution, should take in account both the contributions of aggregation and SDGIs. Finally, a second model has been developed in order to investigate the small scale dynamics related to fingers propagation. The presented two-phase model solves the motion equation of individual particles which can be critical when the number of particles drastically increases (Chapter 5).

6.1 Application of the 3D single-phase model to a static configuration

The 3D numerical model has been developed by combining the efficiency of the Lattice Boltzmann method to model complex flows, with the low diffusive WENO finite difference scheme. The main assumption underlying the validity of such a model is that particles remain fully coupled with the fluid, with no inertia and are in large number. Besides the possibility to perform calculations of massively parallel computers, the model as been validated in several ways. In the very early stage of the instability growth (which can be seen as linear), the model has shown very good agreements with the results provided by linear stability analysis. Moreover, the transition to the nonlinear regime has also been validated comparing results such as the vertical finger velocity with experiments. Finally, besides the validation, we extended the analytical formulations provided by Hoyal et al. [1999] to describe the evolution of the particle concentration in the lower layer, as well as the accumulation rate. Through the validation process, the model has confirmed that the value of 10^3 previously suggested by Hoyal et al. [1999] and coming from the thermal analogy, is an order of magnitude less than the value measured in both simulations and experiments (see also [Barnard, 2021]). This suggests that the analogy with the thermal case is not relevant or that the Grashof number is not suitable to scale the PBL thickness. So, there is a need to perform further investigations in order to derive an accurate scaling of the PBL and the numerical model may certainly help as it accurately simulates SDGIs from the early linear stages to the later non-linear regime. Admittedly, the critical Grashof number may be a criterion for triggering the formation of fingers, but there is also an additional condition. Indeed, as soon as the particle individual settling velocity becomes greater than the instability growth rate, no SDGIs are susceptible to form. Thus, there is a size threshold for the formation of fingers, which depends on the density of particles, the viscosity of the medium and also the bulk density difference between the two fluid layers.

Furthermore, as the sedimentation of particle is strongly affected by SDGIs, evidence of their presence is found in the particle accumulation rate. Indeed, particles

that settle individually cause a constant accumulation rate while the convection induced by collective settling provides a temporally increasing accumulation rate. In addition, the associated spatial distribution is heterogeneous given that fingers do not reach the ground at the same time. These interesting outcomes show that in the absence of shear, the accumulation rate is an accurate ground signature of SDGIs.

6.2 Effect of shear on the dynamics of settling-driven gravitational instabilities

In chapter 3, the lateral motion inducing shear at the particle interface has been studied. The lateral motion is created by both gravitational spreading and the wind advection. Once again, the model has been validated with theoretical and experimental results regarding the spreading of particle-free gravity currents. The model is able to reproduce the energy loss caused by internal dissipative effects, affecting the current thickness. Another important fact is that the spreading velocity of the gravity current is directly related to the reduced gravity g'. This parameter describes the change in the gravitational acceleration due to buoyancy forces and increases when the density difference between the current and the ambient also increases. The addition of particles in such free-surface gravity currents, is interesting in the sense that the current shape is affected by the sedimentation. More precisely, in the presence of collective settling which enhances the sedimentation, the current deformation is significant. Naturally, the sedimentation of particles during spreading also entrains fluid, removing material from the current, causing the thinning of its head. However, this happens when the current spreading is low enough to allow the sedimentation (i.e. with low g'). Otherwise, a rapid spreading tends to dampen particle sedimentation because of the current inertia.

Regarding the ground signature of SDGIs, the evolution of the accumulation rate seems to be similar to the static case, but not necessarily due to collective settling. However, the heterogeneous deposit in the presence of collective settling remains an indicative ground signature. Therefore, a more relevant ground signature, especially in the presence of shear, can be extracted within the grainsize distribution. The

application to an ash cloud from the 2010 eruption of the Eyjafjallajökull volcano using input data from field observations [Manzella et al., 2015; Bonadonna et al., 2011], showed that SDGIs have the potential to produce a bimodal grainsize distribution in the deposit. This result is extremely important as the bimodality in the deposit grainsize cannot only be attributed to ash aggregation.

6.3 Combination of particle aggregation with settling-driven gravitational instabilities

Particle aggregation and SDGIs are candidates to explain the premature sedimentation of fine ash from volcanic clouds. They both contribute to the associated ground signature which is a bimodal grainsize distribution. The chapter 4 combines the two processes in order to investigate their interaction. The implementation of the discrete Smoluchowski coagulation equation (SCE) allows to define source/sink terms for the particle transport equation. Thanks to the application of the fixed-pivot technique, the source/sink terms provide the mass transfer between particle size classes due to aggregation, ensuring mass conservation. Some validation steps using the analytical solution of the SCE for the isothermal brownian coagulation have been performed and showed that the model is numerically stable. Then, in order to study the interaction between aggregation and SDGIs in a volcanic context, relevant aggregation kernels have to be used. Among the different kernels considered in volcanology, some are neglected (such as the brownian motion, the laminar shear or else the turbulent-inertial) given the assumption underlying our numerical model. However, the most important kernels associated with the differential sedimentation and turbulent shear are conserved. An interesting way to highlight to effect of aggregation is to vary the sticking efficiency in order to modulate the rate at which aggregates are formed. We highlighted that aggregation affects all sedimentation modes (i.e. individual and collective) by increasing the accumulation rate. In the case of individual settling for which the accumulation rate is constant, the production of aggregates increases the settling velocity and ultimately the accumulation rate. For collective settling, the characteristic ground signature (i.e. increasing

accumulation rate) is conserved but also enhanced by aggregation. Moreover, the turbulence generated within fingers certainly contribute to the creation of aggregates. This aspect is interesting as it shows that aggregation occurs not only inside the volcanic plume and cloud but also within fingers.

6.4 Development of a two-phase model

A second model has been developed and described in Chapter 5. This two-phase model solves the fluid motion with the Lattice Boltzmann method while the motion equation is explicitly solved for each individual particle. Each particle position is updated using the Verlet integration [Verlet, 1967] which provides an accurate and fast algorithm. The model allows the inclusion of the particle drag effect which proves to be useful to investigate how the particle coupling affects the dynamics of SDGIs. The main outcome is that, given the numerical effort involved in the simulation of a large number of individual particles, the use of such a model is limited, despite the actual resources available.

6.5 Future perspectives

Our numerical investigations provide interesting insights into the dynamics of SDGIs and their interaction with particle aggregation. The developed single-phase and two-phase models nicely complement the field and experimental studies and expand the spectrum of analysed physical parameters. However, additional work is needed to improve our understanding of collective settling.

From a theoretical point of view, the scaling of the PBL thickness is critical as it defines the characteristic length of the problem [Hoyal et al., 1999; Carazzo and Jellinek, 2012]. So far, this parameter was expressed as a function of the critical Grashof number taken from the thermal analogy. Our investigations, strengthened by previous studies [Yu et al., 2014; Burns and Meiburg, 2014] have revealed that the instability development depends on the particle settling velocity V_s as well as on the volume fraction ϕ and that the thermal Grashof number is not accurate to describe SDGIs. Indeed, in the analytical formulation $\delta_{PBL} = (Gr_c \nu^2/g')^{1/3}$ [Hoyal

et al., 1999], there is no clear dependence on V_s and ϕ, which suggests the need for another scaling taking those parameters into account, in order to better describe the triggering conditions of SDGIs.

Some improvements of the numerical models developed so far are strongly recommended in relation to both the implemented physics and to the performances.

- Volcanic clouds in the atmosphere are characterised by highly turbulent flows given the high range of Reynolds numbers [Fries et al., 2021]. The turbulence plays an important role for instance in the mixing inside the cloud or else the collision rates between particles. Thus, the parameters controlling the triggering of SDGIs such as the particle concentration or the particle size (indirectly by aggregation), are doubtlessly dependent. We constrained the various parameters controlling the initial conditions for the development of ash fingers. However, the different single-phase simulations performed for this thesis did not take into account the turbulence having the potential to influence those initial conditions. Defining an accurate estimation of the turbulence profile within a volcanic cloud is not trivial as it depends on the volcanic plume dynamics and the atmospheric conditions. This aspect suggests the need for the coupling with existing plume models or the development of a more complete model of volcanic plume/cloud. The latter would effectively help to constrain the eruption source parameters (ESP) and the atmospheric conditions promoting the cloud requirements to trigger SDGIs.

- Concerning the technical improvements for the performances of the 3D single phase model, a minor aspect can be the increase of the order for the WENO scheme accuracy (i.e. from 3^{rd} to 5^{th} order). Thus, the mixing resulting from the fingers propagation should be better resolved. Therefore, a major improvement would be about the numerical strategy to model polydisperse size distribution. Indeed, as we solve the transport equation for each size class, the adopted strategy can be significantly improved in terms of memory handling and execution time (i.e. the use of a single $TensorField$ instead of several $ScalarFields$ [Latt et al., 2020]). Finally, for both the single-phase and

two-phase models, the performance can be strongly improved thanks to the use of GPUs (Graphical Processing Units) [Latt et al., 2020; Kotsalos et al., 2021].

A final important aspect that still needs to be developed is the development of a comprehensive parametrisation of SDGIs to be integrated in ash dispersal models. While aggregation modifies the total grainsize distribution during the volcanic cloud dispersal [Rossi et al., 2021; Rossi, 2018; Folch et al., 2020; Beckett et al., 2022], SDGIs reduces the residence time of fine ash locally through a different mechanism. However, given the fact that to explicitly model fingers is challenging, there is a need to introduce a parameter representing the amount of fine ash removed from the cloud. In a Eulerian model such as FALL3D for instance [Folch et al., 2020], this parameter can be included as a sink term in the particle transport equation. In lagrangian models such as NAME [Jones et al., 2007; Beckett et al., 2022], the fine fraction can be removed from the cloud using "ghost" particles with a terminal velocity equivalent to the average finger vertical velocity.

A final word concerns the importance of the collaborations between various fields in order to concentrate efforts on a research topic. The model validation would not be possible without the experimental investigations while the numerical investigations suggested to measure specific parameters on the field in order to highlight SDGIs. Everything starts with the contemplation of a phenomenon such as a volcanic eruption, and ends with the motivation to improve dispersal models in order to preserve an economic system and save lives. This perfectly express the beauty of science.

Bibliography

Alsinan, A., Meiburg, E., Garaud, P., 2017. A settling-driven instability in two-component, stably stratified fluids. Journal of Fluid Mechanics 816, 243–267. doi:10.1017/jfm.2017.94.

Andronico, D., Scollo, S., Cristaldi, A., 2015. Unexpected hazards from tephra fallouts at mt etna: The 23 november 2013 lava fountain. Journal of Volcanology and Geothermal Research 304, 118–125.

Bagheri, G., Bonadonna, C., Manzella, I., Vonlanthen, P., 2015. On the characterization of size and shape of irregular particles. Powder Technology 270, 141–153.

Bagheri, G., Rossi, E., Biass, S., Bonadonna, C., 2016. Timing and nature of volcanic particle clusters based on field and numerical investigations. Journal of Volcanology and Geothermal Research 327, 520–530.

Bagnato, E., Aiuppa, A., Bertagnini, A., Bonadonna, C., Cioni, R., Pistolesi, M., Pedone, M., Hoskuldsson, A., 2013. Scavenging of sulphur, halogens and trace metals by volcanic ash: The 2010 Eyjafjallajökull eruption. Geochimica et Cosmochimica Acta 103, 138–160. doi:10.1016/j.gca.2012.10.048.

Balasubramanian, S., Zhong, Q., 2018. Entrainment and mixing in lock-exchange gravity currents using simultaneous velocity-density measurements. Physics of Fluids 30, 056601.

Baltensperger, R., Berrut, J.p., 2001. The linear rational collocation method 134, 243–258.

Barnard, J.M., 2021. On the dynamics of stratified particle-laden plumes. Journal of Fluid Mechanics 925.

Barsotti, S., Neri, A., 2008. The vol-calpuff model for atmospheric ash dispersal: 2. application to the weak mount etna plume of july 2001. Journal of Geophysical Research: Solid Earth 113.

Beckett, F., Rossi, E., Devenish, B., Witham, C., Bonadonna, C., 2022. Modelling the size distribution of aggregated volcanic ash and implications for operational atmospheric dispersion modelling. Atmospheric Chemistry and Physics 22, 3409–3431. doi:10.5194/acp-22-3409-2022.

Beeckmans, J., 1965. Numerical solutions of smoluchowski's equations for the coagulation of uncharged aerosols. Canadian Journal of Chemistry 43, 2312–2318.

Benjamin, T.B., 1968. Gravity currents and related phenomena. Journal of Fluid Mechanics 31, 209–248. doi:10.1017/S0022112068000133.

Berrut, J.P., Mittelmann, H.D., 2004. Adaptive point shifts in rational approximation with optimized denominator. Journal of Computational and Applied Mathematics 164-165, 81–92. doi:10.1016/S0377-0427(03)00485-0.

Bhatnagar, P., Gross, E., Krook, M., 1954. A model for collision processes in gases. Physical Review 94, 515–525.

Biass, S., Bonadonna, C., Connor, L., Connor, C., 2016. Tephraprob: a matlab package for probabilistic hazard assessments of tephra fallout. Journal of Applied Volcanology 5, 1–16.

Biass, S., Scaini, C., Bonadonna, C., Folch, A., Smith, K., Höskuldsson, A., 2014. A multi-scale risk assessment for tephra fallout and airborne concentration from multiple icelandic volcanoes–part 1: Hazard assessment. Natural hazards and earth system sciences 14, 2265–2287.

Blong, R., 2000. Volcanic hazards and risk management, in: Encyclopedia of volcanoes. Academic Press, pp. 1215–1227.

Bonadonna, C., Biass, S., Menoni, S., Gregg, C.E., 2021. Assessment of risk associated with tephra-related hazards. doi:10.1016/b978-0-12-818082-2.00008-1.

Bonadonna, C., Costa, A., 2013. Modeling of tephra sedimentation from volcanic plumes. Modeling volcanic processes: The physics and mathematics of volcanism , 173–202.

Bonadonna, C., Costa, A., Folch, A., Koyaguchi, T., 2015a. Tephra dispersal and sedimentation, in: The Encyclopedia of Volcanoes. Elsevier, pp. 587–597.

Bonadonna, C., Folch, A., Loughlin, S., Puempel, H., 2012. Future developments in modelling and monitoring of volcanic ash clouds: Outcomes from the first IAVCEI-WMO workshop on Ash Dispersal Forecast and Civil Aviation. Bulletin of Volcanology 74, 1–10. doi:10.1007/s00445-011-0508-6.

Bonadonna, C., Genco, R., Gouhier, M., Pistolesi, M., Cioni, R., Alfano, F., Hoskuldsson, A., Ripepe, M., 2011. Tephra sedimentation during the 2010 Eyjafjallajkull eruption (Iceland) from deposit, radar, and satellite observations. Journal of Geophysical Research: Solid Earth 116. doi:10.1029/2011JB008462.

Bonadonna, C., Mayberry, G.C., Calder, E.S., Sparks, R.S., Choux, C., Jackson, P., Lejeune, A.M., Loughlin, S.C., Norton, G.E., Rose, W.I., Ryan, G., Young, S.R., 2002. Tephra fallout in the eruption of Soufrière Hills Volcano, Montserrat. Geological Society Memoir 21, 483–516. doi:10.1144/GSL.MEM.2002.021.01.22.

Bonadonna, C., Phillips, J.C., 2003. Sedimentation from strong volcanic plumes. Journal of Geophysical Research: Solid Earth 108, 1–28. doi:10.1029/2002jb002034.

Bonadonna, C., Phillips, J.C., Houghton, B.F., 2005. Modeling tephra sedimentation from a Ruapehu weak plume eruption. Journal of Geophysical Research: Solid Earth 110, 1–22. doi:10.1029/2004JB003515.

Bonadonna, C., Pistolesi, M., Cioni, R., Degruyter, W., Elissondo., 2015b. Dynamics of wind-affected volcanic plumes: The exampleof the 2011 Cordón Caulle eruption, Chile. Journal of Geophysical Research: Solid Earth , 3782–3803doi:10.1002/2015JB012608.Received.

Borisova, A.Y., Toutain, J.P., Stefansson, A., Gouy, S., de Parseval, P., 2012. Processes controlling the 2010 eyjafjallajökull explosive eruption. Journal of Geophysical Research: Solid Earth 117.

Bosse, T., Kleiser, L., Härtel, C., Meiburg, E., 2005. Numerical simulation of finite reynolds number suspension drops settling under gravity. Physics of Fluids 17, 037101.

Bourke, P., 1999. Interpolation methods. Miscellaneous: projection, modelling, rendering 1.

Bracco, A., Chavanis, P.H., Provenzale, A., Spiegel, E.A., 1999. Particle aggregation in a turbulent keplerian flow. Phys. Fluids 11, 2280. doi:10.1063/1.870090, arXiv:astro-ph/9810336.

Brisset, J., Heißelmann, D., Kothe, S., Weidling, R., Blum, J., 2013. The suborbital particle aggregation and collision experiment (space): Studying the collision behavior of submillimeter-sized dust aggregates on the suborbital rocket flight rexus 12. Review of Scientific Instruments 84, 094501. doi:10.1063/1.4819443.

Brown, R.J., Bonadonna, C., Durant, A.J., 2012. A review of volcanic ash aggregation. Physics and Chemistry of the Earth 45-46, 65–78. doi:10.1016/j.pce.2011.11.001.

Burgisser, A., W. Bergantz, G., E. Breidenthal, R., 2005. Addressing Complexity in Laboratory Experiments: The Scaling of Dilute Multiphase Flows in Magmatic Systems. Journal of Volcanology and Geothermal Research 141, N{\textdegree} 3–4, 245–265. doi:10.1016/j.jvolgeores.2004.11.001.

Burns, F.A., Bonadonna, C., Pioli, L., Cole, P., Stinton, A., 2017. Ash aggregation during the 11 february 2010 partial dome collapse of the soufriere hills volcano, montserrat. Journal of Volcanology and Geothermal Research 335, 92–112.

Burns, P., Meiburg, E., 2012. Sediment-laden fresh water above salt water: Linear stability analysis. Journal of Fluid Mechanics 691, 279–314. doi:10.1017/jfm.2011.474.

Burns, P., Meiburg, E., 2014. Sediment-laden fresh water above salt water: Nonlinear simulations. Journal of Fluid Mechanics 762, 156–195. doi:10.1017/jfm.2014.645.

Bursik, M., Yang, Q., Bear-Crozier, A., Pavolonis, M., Tupper, A., 2021. The development of volcanic ash cloud layers over hours to days due to atmospheric turbulence layering. Atmosphere 12, 1–19. doi:10.3390/atmos12020285.

Bursik, M.I., Sparks, R.S., Gilbert, J.S., Carey, S.N., 1992. Sedimentation of tephra by volcanic plumes: I. Theory and its comparison with a study of the Fogo A plinian deposit, Sao Miguel (Azores). Bulletin of Volcanology 54, 329–344. doi:10.1007/BF00301486.

Cantero, M.I., Lee, J.R., Balachandar, S., Garcia, M.H., 2007. On the front velocity of gravity currents. Journal of Fluid Mechanics 586, 1–39.

Carazzo, G., Jellinek, A.M., 2012. A new view of the dynamics, stability and longevity of volcanic clouds. Earth and Planetary Science Letters 325-326, 39–51. doi:10.1016/j.epsl.2012.01.025.

Carazzo, G., Jellinek, A.M., 2013. Particle sedimentation and diffusive convection in volcanic ash-clouds. Journal of Geophysical Research: Solid Earth 118, 1420–1437. doi:10.1002/jgrb.50155.

Cardoso, S.S.S., Zarrebini, M., 2001. Convection driven by particle settling surrounding a turbulent plume. Chemical Engineering Science 56, 3365–3375. doi:10.1016/S0009-2509(01)00028-8.

Carey, S., 1997. Influence of convective sedimentation on the formation of widespread tephra fall layers in the deep sea. Geology 25, 839–842. doi:10.1130/0091-7613(1997)025<0839:IOCSOT>2.3.CO;2.

Carey, S., Sparks, R., 1986. Quantitative models of the fallout and dispersal of tephra from volcanic eruption columns. Bulletin of volcanology 48, 109–125.

Cartwright, J.H., Feudel, U., Károlyi, G., De Moura, A., Piro, O., Tél, T., 2010. Dynamics of Finite-Size Particles in Chaotic Fluid Flows. volume 2010. doi:10.1007/978-3-642-04629-2_4.

Castruccio, A., Rust, A., Sparks, R., 2010. Rheology and flow of crystal-bearing lavas: Insights from analogue gravity currents. Earth and Planetary Science Letters 297, 471–480.

Cavus, H., Kazkapan, D., 2013. Magnetic kelvin–helmholtz instability in the solar atmosphere. New Astronomy 25, 89–94. doi:https://doi.org/10.1016/j.newast.2013.04.001.

Cerminara, M., Esposti Ongaro, T., Berselli, L.C., 2016. Ashee-1.0: a compressible, equilibrium–eulerian model for volcanic ash plumes. Geoscientific Model Development 9, 697–730.

Chandrasekhar, S., 1961. Hydrodynamic and hydromagnetic stability. Oxford ed.

Chapman, D., Browning, K.A., 1997. Radar observations of wind-shear splitting within evolving atmospheric kelvin-helmholtz billows. Quarterly Journal of the Royal Meteorological Society 123, 1433–1439. doi:https://doi.org/10.1002/qj.49712354114.

Chen, F., Hagen, H., 2011. A survey of interface tracking methods in multiphase fluid visualization, in: Visualization of Large and Unstructured Data Sets-Applications in Geospatial Planning, Modeling and Engineering (IRTG 1131 Workshop), Schloss Dagstuhl-Leibniz-Zentrum fuer Informatik.

Chen, S., Doolen, G.D., 2010. Lattice Boltzmann Method for fluid flows. Scholarpedia 5, 9507. doi:10.4249/scholarpedia.9507.

Chou, Y.J., Gu, S.H., Shao, Y.C., 2015. An euler–lagrange model for simulating fine particle suspension in liquid flows. Journal of Computational Physics 299, 955–973.

Chou, Y.J., Shao, Y.C., 2016. Numerical study of particle-induced Rayleigh-Taylor instability: Effects of particle settling and entrainment. Physics of Fluids 28. doi:10.1063/1.4945652.

Christodoulou, G.C., 1985. Interfacial mixing in stratified flows. J. Hydraul. Res. 24, 77–92.

Cioni, R., Pistolesi, M., Bertagnini, A., Bonadonna, C., Hoskuldsson, A., Scateni, B., 2014. Insights into the dynamics and evolution of the 2010 eyjafjallajökull summit eruption (iceland) provided by volcanic ash textures. Earth and Planetary Science Letters 394, 111–123.

Constantinescu, R., Hopulele-Gligor, A., Connor, C.B., Bonadonna, C., Connor, L.J., Lindsay, J.M., Charbonnier, S., Volentik, A.C.M., 2021. The radius of the umbrella cloud helps characterize large explosive volcanic eruptions. Communications Earth & Environment 2, 1–8. doi:10.1038/s43247-020-00078-3.

Cornell, W., Carey, S., Sigurdsson, H., 1983. Computer simulation of transport and deposition of the campanian y-5 ash. Journal of Volcanology and Geothermal Research 17, 89–109.

Cortese, T.A., Balachandar, S., 1995. High performance spectral simulation of turbulent flows in massively parallel machines with distributed memory. The International journal of supercomputer applications and high performance computing 9, 187–204.

Costa, A., Folch, A., Macedonio, G., 2010. A model for wet aggregation of ash particles in volcanic plumes and clouds: 1. Theoretical formulation. Journal of Geophysical Research: Solid Earth 115, 1–14. doi:10.1029/2009JB007175.

Costa, A., Folch, A., Macedonio, G., 2013. Density-driven transport in the umbrella region of volcanic clouds: Implications for tephra dispersion models. Geophysical Research Letters 40, 4823–4827. doi:10.1002/grl.50942.

Courant, R., Friedrichs, K., Lewy, H., 1928. Über die partiellen Differenzengleichungen der mathematischen Physik. Mathematische Annalen 100, 32–74. doi:10.1007/BF01448839.

Crimaldi, J.P., 2008. Planar laser induced fluorescence in aqueous flows. Experiments in Fluids 44, 851–863. doi:10.1007/s00348-008-0496-2.

Davarpanah Jazi, S., Wells, M.G., 2016. Enhanced sedimentation beneath particle-laden flows in lakes and the ocean due to double-diffusive convection. Geophysical Research Letters 43, 10,883–10,890. doi:10.1002/2016GL069547.

Davarpanah Jazi, S., Wells, M.G., 2020. Dynamics of settling-driven convection beneath a sediment-laden buoyant overflow: Implications for the length-scale of deposition in lakes and the coastal ocean. Sedimentology 67, 699–720.

Davidson, P.A., 2015. Turbulence: an introduction for scientists and engineers. Oxford university press.

Degruyter, W., Bonadonna, C., 2012. Improving on mass flow rate estimates of volcanic eruptions. Geophysical Research Letters 39, 1–6. doi:10.1029/2012GL052566.

Del Bello, E., Taddeucci, J., Scarlato, P., Andronico, D., Scollo, S., Kueppers, U., Ricci, T., et al., 2017. Effect of particle volume fraction on the settling velocity of volcanic ash particles: insights from joint experimental and numerical simulations. Scientific reports 7, 1–11.

Dellino, P., Gudmundsson, M., Larsen, G., Mele, D., Stevenson, J., Thordarson, T., Zimanowski, B., 2012. Ash from the eyjafjallajökull eruption (iceland): Fragmentation processes and aerodynamic behavior. Journal of Geophysical Research: Solid Earth 117.

Dioguardi, F., Mele, D., Dellino, P., 2018. A new one-equation model of fluid drag for irregularly shaped particles valid over a wide range of reynolds number. Journal of Geophysical Research: Solid Earth 123, 144–156.

Drazin, P.G., 1958. The stability of a shear layer in an unbounded heterogeneous inviscid fluid. Journal of Fluid Mechanics 4, 214–224. doi:10.1017/S0022112058000409.

Durant, A.J., 2015. RESEARCH FOCUS: Toward a realistic formulation of fine-ash lifetime in volcanic clouds. Geology 43, 271–272. doi:10.1130/focus032015.1.

Durant, A.J., Rose, W.I., Sarna-Wojcicki, A.M., Carey, S., Volentik, A.C.M., 2009. Hydrometeor-enhanced tephra sedimentation: Constraints from the 18 May 1980 eruption of Mount St. Helens. Journal of Geophysical Research 114, B03204. doi:10.1029/2008JB005756.

Ellison, T.H., Turner, J.S., 1959. Turbulent entrainment in stratified flows. J. Fluid Mech. 6, 423–448.

Ernst, G., Davis, J., Sparks, S., 1994. Bifurcation of volcanic plumes in a crosswind. Bulletin of Volcanology 56, 159–169. doi:10.1007/BF00279601.

Farenzena, B.A., Silvestri, J.H., 2017. Linear stability analysis of particle-laden hypopycnal plumes. Phys. Fluids 29, 124102.

Farenzena, B.A., Silvestrini, J.H., 2017. Linear stability analysis of particle-laden hypopycnal plumes. Physics of Fluids 29. doi:10.1063/1.4999343.

Ferry, J., Balachandar, S., 2001. A fast eulerian method for disperse two-phase flow. International journal of multiphase flow 27, 1199–1226.

Ferziger, J.H., Peric, M., 2002. Computational Methods for Fluid Dynamics.

Folch, A., 2012. A review of tephra transport and dispersal models : Evolution , current status , and future perspectives. Journal of Volcanology and Geothermal Research 235-236, 96–115. doi:10.1016/j.jvolgeores.2012.05.020.

Folch, A., Mingari, L., Gutierrez, N., Hanzich, M., Macedonio, G., Costa, A., 2020. FALL3D-8.0: A computational model for atmospheric transport and deposition of particles, aerosols and radionuclides - Part 1: Model physics and numerics. Geoscientific Model Development 13, 1431–1458. doi:10.5194/gmd-13-1431-2020.

Friedlander, S.K., 2000. Smoke, dust and haze: Fundamentals of aerosol dynamics.

Fries, A., Lemus, J., Jarvis, P.A., Clarke, A.B., Phillips, J.C., Manzella, I., Bonadonna, C., 2021. The Influence of Particle Concentration on the Formation of Settling-Driven Gravitational Instabilities at the Base of Volcanic Clouds. Frontiers Earth Sciences doi:doi:10.3389/feart.2021.640090.

Gabellini, P., Rossi, E., Bonadonna, C., Pistolesi, M., Bagheri, G., Cioni, R., 2020. Physical and aerodynamic characterization of particle clusters at sakurajima volcano (japan). Frontiers in Earth Science , 420.

Ganser, G.H., 1993. A rational approach to drag prediction of spherical and nonspherical particles. Powder Technology 77, 143–152. doi:10.1016/0032-5910(93)80051-B.

Gilbert, J., Lane, S., 1994. The origin of accretionary lapilli. Bulletin of Volcanology 56, 398–411. doi:10.1007/BF00326465.

Gilbert, J., Lane, S., Sparks, R., Koyaguchi, T., 1991. Charge measurements on particle fallout from a volcanic plume. Nature 349, 598–600.

Gislason, S.R., Hassenkam, T., Nedel, S., Bovet, N., Eiriksdottir, E.S., Alfredsson, H.A., Hem, C.P., Balogh, Z.I., Dideriksen, K., Oskarsson, N., et al., 2011. Characterization of eyjafjallajökull volcanic ash particles and a protocol for rapid risk assessment. Proceedings of the National Academy of Sciences 108, 7307–7312.

Gladstone, C., Ritchie, L., Sparks, R., Woods, A., 2004. An experimental investigation of density-stratified inertial gravity currents. Sedimentology 51, 767–789.

Godunov, 1954. Different methods for shock waves. Moscow State University .

Godunov, 1959. A difference scheme for numerical solution of discontinuous solution of hydrodynamic equations. Math. Sbornik 47, 271–306.

Goldstein, S., 1931. On the stability of superposed streams of fluids of different densities. Proceedings of the Royal Society of London. Series A, Containing Papers of a Mathematical and Physical Character 132, 524–548.

Gouhier, M., Eychenne, J., Azzaoui, N., Guillin, A., Deslandes, M., Poret, M., Costa, A., Husson, P., 2019. Low efficiency of large volcanic eruptions in transporting very fine ash into the atmosphere. Scientific Reports 9, 1–12. doi:10.1038/s41598-019-42489-z.

Gudmundsson, G., 2011. Respiratory health effects of volcanic ash with special reference to Iceland. A review. Clinical Respiratory Journal 5, 2–9. doi:10.1111/j.1752-699X.2010.00231.x.

Gudmundsson, M.T., Thordarson, T., Höskuldsson, Á., Larsen, G., Björnsson, H., Prata, F.J., Oddsson, B., Magnússon, E., Högnadóttir, T., Petersen, G.N., et al., 2012. Ash generation and distribution from the april-may 2010 eruption of eyjafjallajökull, iceland. Scientific reports 2, 1–12.

Guffanti, M., Mayberry, G., Casadevall, T., Wunderman, R., 2008. Volcanic hazards to airports. Natural Hazards 51, 287–302. doi:10.1007/s11069-008-9254-2.

Guo, Z., Zheng, C., Shi, B., 2002. Discrete lattice effects on the forcing term in the lattice Boltzmann method 65, 1–6. doi:10.1103/PhysRevE.65.046308.

Guzdar, P.N., Satyanarayana, P., Huba, J.D., Ossakow, S.L., 1982. Influence of velocity shear on the Rayleigh-Taylor instability. Geophysical Research Letters 9, 547–550. doi:https://doi.org/10.1029/GL009i005p00547.

Hairer, E., Syvert P., N., Wanner, G., 1993. Solving ordinary differential equations I. Springer.

Hallworth, M.A., Phillips, J.C., Huppert, H.E., Sparks, R.S.J., 1993. Entrainment in turbulent gravity currents. Nature 362, 829–831.

Harada, S., Kondo, M., Watanabe, K., Shiotani, T., Sato, K., 2013. Collective settling of fine particles in a narrow channel with arbitrary cross-section. Chemical Engineering Science 93, 307–312. doi:10.1016/j.ces.2013.01.054.

van Haren, H., Gostiaux, L., 2010. A deep-ocean kelvin-helmholtz billow train. Geophysical Research Letters 37. doi:https://doi.org/10.1029/2009GL041890, arXiv:https://agupubs.onlinelibrary.wiley.com/doi/pdf/10.1029/2009GL041890.

Härtel, C., Meiburg, E., Necker, F., 2000. Analysis and direct numerical simulation of the flow at a gravity-current head. Part 1. Flow topology and front speed for slip and no-slip boundaries. Journal of Fluid Mechanics 418, 189–212. doi:10.1017/S0022112000001221.

Harten, A., 1983. High resolution schemes for hyperbolic conservation laws. Journal of Computational Physics 49, 357–393. doi:https://doi.org/10.1016/0021-9991(83)90136-5.

He, X., Luo, L.s., 1997. Lattice Boltzmann Model for the Incompressible Navier-Stokes Equation 88, 927–944.

von Helmholtz, H., 1886. Über discontinuierliche Flüssigkeits-Bewegungen. Ber. Akad. Wiss. Berlin 23, 215–228.

Henniger, R., Kleiser, L., 2012. Temporal evolution, morphology, and settling of the sediment plume in a model estuary. Physics of Fluids 24, 086601.

Higuchi, W., Okad, R., Stelter, G., Lemberger, A., 1963. Kinetics of rapid aggregation in suspensions. comparison of experiments with the smoluchowski theory. Journal of Pharmaceutical Sciences 52, 49–54.

Hobbs, P.V., Radke, L.F., Eltgroth, M.W., Hegg, D.A., 1981. Airborne studies of the emissions from the volcanic eruptions of mount st. helens. Science 211, 816–818.

Hosseini, S.A., Darabiha, N., Thévenin, D., Eshghinejadfard, A., 2017. Stability limits of the single relaxation-time advection-diffusion lattice Boltzmann scheme. International Journal of Modern Physics C 28, 1–31. doi:10.1142/S0129183117501418.

Hoyal, D.C.J.D., Bursik, M.I., Atkinson, J.F., 1999. The influence of diffusive convection on sedimentation from buoyant plumes , 205–220.

Huppert, H.E., Simpson, J.E., 1980. The slumping of gravity currents. Journal of Fluid Mechanics 99, 785–799.

Jacobs, C.T., Collins, G.S., Piggott, M.D., Kramer, S.C., Wilson, C.R., 2013. Multiphase flow modelling of volcanic ash particle settling in water using adaptive unstructured meshes. Geophysical Journal International 192, 647–665. doi:10.1093/gji/ggs059.

James, M.R., Gilbert, J.S., Lane, S.J., 2002. Experimental investigation of volcanic particle aggregation in the absence of a liquid phase. Journal of Geophysical Research: Solid Earth 107, ECV–4.

James, M.R., Lane, S.J., Gilbert, J.S., 2003. Density, construction, and drag coefficient of electrostatic volcanic ash aggregates. Journal of Geophysical Research: Solid Earth 108.

Jarvis, P.A., Fries, A., Lemus, J., Clark, A., Manzella, I., Phillips, J., in prep. Kelvin-Helmholtz instabilities and mixing in surface-propagating gravity currents , 1–38.

Jenkins, S.F., Wilson, T., Magill, C., Miller, V., Stewart, C., Blong, R., Marzocchi, W., Boulton, M., Bonadonna, C., Costa, A., 2015. Volcanic ash fall hazard and risk. 2015. doi:10.1017/CBO9781316276273.005.

Jiang, G.S., Shu, C.W., 1996. Efficient Implementation of Weighted ENO Schemes. Journal of Computational Physics 228, 202–228.

Johnson, C.G., Hogg, A.J., Huppert, H.E., Sparks, R.S.J., Phillips, J.C., Slim, A.C., Woodhouse, M.J., 2015. Modelling intrusions through quiescent and moving ambients. Journal of Fluid Mechanics 771, 370–406. doi:10.1017/jfm.2015.180.

Jones, A., Thomson, D., Hort, M., Devenish, B., 2007. The U.K. Met Office's Next-Generation Atmospheric Dispersion Model, NAME III. Air Pollution Modeling and Its Application XVII , 580–589doi:10.1007/978-0-387-68854-1_62.

Kaminski, E., Tait, S., Ferrucci, F., Martet, M., Hirn, B., Husson, P., 2011. Estimation of ash injection in the atmosphere by basaltic volcanic plumes: The case of the eyjafjallajökull 2010 eruption. Journal of Geophysical Research: Solid Earth 116.

Katopodes, N.D., 2019. Chapter 8 - turbulent flow, in: Katopodes, N.D. (Ed.), Free-Surface Flow. Butterworth-Heinemann, pp. 566–650. doi:https://doi.org/10.1016/B978-0-12-815489-2.00008-3.

Keck, J.B., Cottet, G.H., Meiburg, E., Mortazavi, I., Picard, C., 2021. Double-diffusive sedimentation at high Schmidt numbers: Semi-Lagrangian simulations. Physical Review Fluids 6, 1–10. doi:10.1103/PhysRevFluids.6.L022301.

Kelvin, W.T., 1871. Hydrokinetic solutions and observations. Philos. Mag 42, 362–377.

Kepkay, P.E., 1994. Particle aggregation and the biological reactivity of colloids. Marine Ecology-Progress Series 109, 293–293.

Kimura, S., Smyth, W., 2007. Direct numerical simulation of salt sheets and turbulence in a double-diffusive shear layer. Geophysical Research Letters 34.

Koch, W., Friedlander, S., 1990. The effect of particle coalescence on the surface area of a coagulating aerosol. Journal of Colloid and Interface Science 140, 419–427.

Konopliv, N., Lesshafft, L., Meiburg, E., 2018. The influence of shear on double-diffusive and settling-driven instabilities. J. Fluid Mech. 849, 902–926.

Koochesfahani, M.M., 1984. Experiments on turbulent mixing and chemical reactions in a liquid mixing layer. Ph.D. thesis. California Institute of Technology. doi:10.7907/Y7BR-C556.

Kotsalos, C., Latt, J., Beny, J., Chopard, B., 2021. Digital blood in massively parallel cpu/gpu systems for the study of platelet transport. Interface focus 11, 20190116.

Kruger, T., Kusumaatmaja, H., Kuzmin, A., Shardt, O., Goncalo, S., Viggen, E.M., 2017. The lattice boltzmann method, principles and practice. 207. doi:10.1191/0265532206lt326oa.

Kumar, J., Peglow, M., Warnecke, G., Heinrich, S., Mörl, L., 2006. Improved accuracy and convergence of discretized population balance for aggregation: The cell average technique. Chemical Engineering Science - CHEM ENG SCI 61, 3327–3342. doi:10.1016/j.ces.2005.12.014.

Kumar, S., Ramkrishna, D., 1996. On the solution of population balance equations by discretization—i. a fixed pivot technique. Chemical Engineering Science 51, 1311–1332.

Laibe, G., Price, D.J., 2014. Dusty gas with one fluid. Monthly Notices of the Royal Astronomical Society 440, 2136–2146. doi:10.1093/mnras/stu355, arXiv:1402.5248.

Lane, S., Gilbert, J., Hilton, M., 1993. The aerodynamic behaviour of volcanic aggregates. Bulletin of Volcanology 55, 481–488.

Latt, J., Malaspinas, O., Kontaxakis, D., Parmigiani, A., Lagrava, D., Brogi, F., Belgacem, M.B., Thorimbert, Y., Leclaire, S., Li, S., Marson, F., Lemus, J., Kotsalos, C., Conradin, R., Coreixas, C., Petkantchin, R., Raynaud, F., Beny, J., Chopard, B., 2020. Palabos: Parallel Lattice Boltzmann Solver. Computers and Mathematics with Applications doi:10.1016/j.camwa.2020.03.022.

Leclaire, S., Parmigiani, A., Malaspinas, O., Chopard, B., Latt, J., 2017. Generalized three-dimensional lattice Boltzmann color-gradient method for immiscible two-phase pore-scale imbibition and drainage in porous media. Physical Review E 95, 33306. doi:10.1103/PhysRevE.95.033306.

Lemus, J., Fries, A., Jarvis, P.A., Bonadonna, C., Chopard, B., Lätt, J., 2021. Modelling Settling-Driven Gravitational Instabilities at the Base of Volcanic Clouds Using the Lattice Boltzmann Method. Frontiers in Earth Science 9. doi:10.3389/feart.2021.713175, arXiv:2106.07694.

Lewis, D.J., 1950. The instability of liquid surfaces when accelerated in a direction perpendicular to their planes. II. Proceedings of the Royal Society of London. Series A. Mathematical and Physical Sciences 202, 81–96. doi:10.1098/rspa.1950.0086.

Linden, P., 1974. Salt fingers in a steady shear flow. Geophysical and Astrophysical Fluid Dynamics 6, 1–27.

Liu, E., Cashman, K., Rust, A., 2015. Optimising shape analysis to quantify volcanic ash morphology. GeoResJ 8, 14–30.

Liu, X.D., Osher, S., Chan, T., 1994. Weighted Essentially Non-Oscillatory Schemes. Journal of Computational Physics , 1–32.

Lowe, R.J., Linden, P., Rottman, J.W., 2002. A laboratory study of the velocity structure in an intrusive gravity current. Journal of Fluid Mechanics 456, 33–48.

Lu, S., Ding, Y., Guo, J., 1998. Kinetics of fine particle aggregation in turbulence. Advances in Colloid and Interface Science 78, 197–235.

Lund, K.A., Benediktsson, K., 2011. Inhabiting a risky earth: The eyjafjallajökull eruption in 2010 and its impacts (respond to this article at http://www. therai. org. uk/at/debate). Anthropology Today 27, 6–9.

Lätt, J., Kontaxakis, D., Chatagny, L., Muggli, F., Chopard, B., 2013. Hybrid Lattice Boltzmann Method for the Simulation of Blending Process in Static Mixers. International Journal of Modern Physics C 24, 1340009. doi:10.1142/S0129183113400093.

Majumder, A., Kariwala, V., Ansumali, S., Rajendran, A., 2012. Lattice boltzmann method for population balance equations with simultaneous growth, nucleation, aggregation and breakage. Chemical Engineering Science 69, 316–328. doi:https://doi.org/10.1016/j.ces.2011.10.051.

Mansour, M., Kasetti, S., Thévenin, D., Nigam, K.D., Zähringer, K., 2021. Numerical study of the separation of two immiscible liquids in helical and straight pipes. Chemical Engineering and Processing-Process Intensification , 108654.

Manville, V., Wilson, C.J., 2004. Vertical density currents: A review of their potential role in the deposition and interpretation of deep-sea ash layers. Journal of the Geological Society 161, 947–958. doi:10.1144/0016-764903-067.

Manzella, I., Bonadonna, C., Phillips, J.C., Monnard, H., 2015. The role of gravitational instabilities in deposition of volcanic ash. Geology 43, 211–214. doi:10.1130/G36252.1.

Marchisio, D.L., Vigil, R.D., Fox, R.O., 2003. Quadrature method of moments for aggregation–breakage processes. Journal of colloid and interface science 258, 322–334.

Marino, B.M., Thomas, L.P., Linden, P.F., 2005. The front condition for gravity currents. Journal of Fluid Mechanics 536, 49–78. doi:10.1017/S0022112005004933.

Marzano, F.S., Picciotti, E., Di Fabio, S., Montopoli, M., Mereu, L., Degruyter, W., Bonadonna, C., Ripepe, M., 2016. Near-Real-Time Detection of Tephra Eruption Onset and Mass Flow Rate Using Microwave Weather Radar and Infrasonic Arrays. IEEE Transactions on Geoscience and Remote Sensing 54, 6292–6306. doi:10.1109/TGRS.2016.2578282.

Mastin, L.G., Schwaiger, H., Schneider, D.J., Wallace, K.L., Schaefer, J., Denlinger, R.P., 2013. Injection, transport, and deposition of tephra during event 5 at redoubt volcano, 23 march, 2009. Journal of volcanology and geothermal research 259, 201–213.

Maters, E.C., Cimarelli, C., Casas, A.S., Dingwell, D.B., Murray, B.J., 2020. Volcanic ash ice-nucleating activity can be enhanced or depressed by ash-gas interaction in the eruption plume. Earth and Planetary Science Letters 551, 116587.

Maxey, M.R., Riley, J.J., 1983. Equation of motion for a small rigid sphere in a nonuniform flow. Physics of Fluids 26, 883–889. doi:10.1063/1.864230.

Maxworthy, T., 1999. The dynamics of sedimenting surface gravity currents. Journal of Fluid Mechanics 392, 27–44.

McCool, W.W., Parsons, J.D., 2004. Sedimentation from buoyant fine-grained suspensions. Continental Shelf Research 24, 1129–1142.

Mereu, L., Marzano, F.S., Montopoli, M., Bonadonna, C., 2015. Retrieval of Tephra Size Spectra and Mass Flow Rate from C-Band Radar during the 2010 Eyjafjallajökull Eruption, Iceland. IEEE Transactions on Geoscience and Remote Sensing 53, 5644–5660. doi:10.1109/TGRS.2015.2427032.

Miles, J.W., 1961. On the stability of heterogeneous shear flows. Journal of Fluid Mechanics 10, 496–508. doi:10.1017/S0022112061000305.

Mitchell, P., Frenklach, M., 2003. Particle aggregation with simultaneous surface growth. Phys. Rev. E 67, 061407. doi:10.1103/PhysRevE.67.061407.

Mukherjee, P., Balasubramanian, S., 2020. Energetics and mixing efficiency of lock-exchange gravity currents using simultaneous velocity and density fields. Physical Review Fluids 5, 063802.

Nakouzi, E., Soltis, J.A., Legg, B.A., Schenter, G.K., Zhang, X., Graham, T.R., Rosso, K.M., Anovitz, L.M., De Yoreo, J.J., Chun, J., 2018. Impact of solution chemistry and particle anisotropy on the collective dynamics of oriented aggregation. ACS nano 12, 10114–10122.

Nguyen, P., 2007. Numerical simulations of the lattice boltzmann method for determination of hydrodynamic properties of fractal aggregates.

Nguyen, T.T., Laurent, F., Fox, R.O., Massot, M., 2016. Solution of population balance equations in applications with fine particles: mathematical modeling and numerical schemes. Journal of Computational Physics 325, 129–156.

Niemeier, U., Timmreck, C., Kinne, S., Rast, S., Self, S., Place, D., Keynes, M., 2009. Initial fate of fine ash and sulfur from large volcanic eruptions. Atmos. Chem. Phys., 9 , 9043–9057doi:https://doi.org/10.5194/acp-9-9043-2009.

Noriega, H., Reggio, M., Vasseur, P., 2013. Natural convection of nanofluids in a square cavity heated from below. Computational Thermal Sciences: An International Journal vol. 5, no.

Olson, B.J., Larsson, J., Lele, S.K., Cook, A.W., 2011. Nonlinear effects in the combined Rayleigh-Taylor/Kelvin-Helmholtz instability. Physics of Fluids 23, 114107. doi:10.1063/1.3660723.

Ottolenghi, L., Prestininzi, P., Montessori, A., Adduce, C., La Rocca, M., 2018. Lattice boltzmann simulations of gravity currents. European Journal of Mechanics-B/Fluids 67, 125–136.

Parmigiani, A., Huber, C., Chopard, B., Latt, J., Bachmann, O., 2009. Application of the multi distribution function lattice Boltzmann approach to thermal flows. The European Physical Journal Special Topics 171, 37–43. doi:10.1140/epjst/e2009-01009-7.

Parsons, J.D., Bush, J.W., Syvitski, J.P., 2001. Hyperpycnal plume formation from riverine outflows with small sediment concentrations. Sedimentology 48, 465–478.

Patočka, V., Calzavarini, E., Tosi, N., 2020. Settling of inertial particles in turbulent Rayleigh-Bénard convection. Physical Review Fluids 5, 1–36. doi:10.1103/PhysRevFluids.5.114304, arXiv:2005.05448.

Patterson, M.D., Caulfield, C., McElwaine, J., Dalziel, S., 2006. Time-dependent mixing in stratified kelvin-helmholtz billows: Experimental observations. Geophysical research letters 33.

Pesmazoglou, I., Kempf, A., Navarro-Martinez, S., 2016. Stochastic modelling of particle aggregation. International Journal of Multiphase Flow 80, 118–130.

Pesmazoglou, I., Kempf, A., Navarro-Martinez, S., 2017. Large eddy simulation of particle aggregation in turbulent jets. Journal of Aerosol Science 111, 1–17.

Piederriere, Y., Meur, J.L., Cariou, J., Abgrall, J., Blouch, M., 2004. Particle aggregation monitoring by speckle size measurement; application to blood platelets aggregation. Opt. Express 12, 4596–4601. doi:10.1364/OPEX.12.004596.

Pollastri, S., Rossi, E., Bonadonna, C., Merrison, J.P., 2021. Modelling the effect of electrification on volcanic ash aggregation. Frontiers in Earth Science 8. doi:10.3389/feart.2020.574106.

Prata, A., Prata, A., 2012. Eyjafjallajökull volcanic ash concentrations determined using spin enhanced visible and infrared imager measurements. Journal of Geophysical Research: Atmospheres 117.

Prata, A.T., Mingari, L., Folch, A., Macedonio, G., Costa, A., 2021. FALL3D-8.0: A computational model for atmospheric transport and deposition of particles, aerosols and radionuclides - Part 2: Model validation. Geoscientific Model Development 14, 409–436. doi:10.5194/gmd-14-409-2021.

Prata, F., Rose, B., 2015. Volcanic Ash Hazards to Aviation, Academic Press, Amsterdam, pp. 911–934. doi:https://doi.org/10.1016/B978-0-12-385938-9.00052-3.

Pumir, A., Wilkinson, M., 2016. Collisional aggregation due to turbulence. Annual Review of Condensed Matter Physics 7, 141–170.

Rahim, S., Jan Iftikhar, F., Malik, M.I., 2020. Chapter 16 - biomedical applications of magnetic nanoparticles, in: Shah, M.R., Imran, M., Ullah, S. (Eds.), Metal Nanoparticles for Drug Delivery and Diagnostic Applications. Elsevier. Micro and Nano Technologies, pp. 301–328. doi:https://doi.org/10.1016/B978-0-12-816960-5.00016-1.

Ray, T.P., 1981. Kelvin–Helmholtz instabilities in radio jets. Monthly Notices of the Royal Astronomical Society 196, 195–207. doi:10.1093/mnras/196.2.195.

Reiss, N.M., Corona, T.J., 1977. An Investigation of a Kelvin-Helmholtz Billow Cloud. Bulletin of the American Meteorological Society 58, 159–162. doi:10.1175/1520-0477(1977)058<0159:aioakh>2.0.co;2.

Riley, C.M., Rose, W.I., Bluth, G.J., 2003. Quantitative shape measurements of distal volcanic ash. Journal of Geophysical Research: Solid Earth 108.

Roche, O., Carazzo, G., 2019. The contribution of experimental volcanology to the study of the physics of eruptive processes, and related scaling issues: A review. Journal of Volcanology and Geothermal Research 384, 103–150. doi:https://doi.org/10.1016/j.jvolgeores.2019.07.011.

Rose, W.I., Durant, A.J., 2011. Fate of volcanic ash: Aggregation and fallout. Geology 39, 895–896.

Rossi, E., 2018. A new perspective on volcanic particle sedimentation and aggregation. Ph.D. Thesis , 1–194.

Rossi, E., Bagheri, G., Beckett, F., Bonadonna, C., 2021. The fate of volcanic ash: premature or delayed sedimentation? Nature communications 12, 1–9.

Sammonds, P., McGuire, B., Edwards, S., 2010. Volcanic hazard from iceland: analysis and implications of the eyjafjallajökull eruption. UCL Institute for risk and disaster reduction, London .

Santos, F., Ferreira, V., Tomé, M., Castelo, A., Mangiavacchi, N., McKee, S., 2012. A marker-and-cell approach to free surface 2-d multiphase flows. International journal for numerical methods in fluids 70, 1543–1557.

Saxby, J., Beckett, F., Cashman, K., Rust, A., Tennant, E., 2018. The impact of particle shape on fall velocity: Implications for volcanic ash dispersion modelling. Journal of Volcanology and Geothermal Research 362, 32–48.

Schiller, L., 1933. A drag coefficient correlation. Zeit. Ver. Deutsch. Ing. 77, 318–320.

Schumacher, R., 1994. A reappraisal of mount st. helens' ash clusters-depositional model from experimental observation. Journal of volcanology and geothermal research 59, 253–260.

Scollo, S., Bonadonna, C., Manzella, I., 2017. Settling-driven gravitational instabilities associated with volcanic clouds: new insights from experimental investigations. Bulletin of Volcanology 79, 1–14. doi:10.1007/s00445-017-1124-x.

Scollo, S., Folch, A., Coltelli, M., Realmuto, V.J., 2010. Three-dimensional volcanic aerosol dispersal: A comparison between Multiangle Imaging Spectroradiometer (MISR) data and numerical simulations. Journal of Geophysical Research Atmospheres 115, 1–14. doi:10.1029/2009JD013162.

Scollo, S., Tarantola, S., Bonadonna, C., Coltelli, M., Saltelli, A., 2008. Sensitivity analysis and uncertainty estimation for tephra dispersal models. Journal of Geophysical Research: Solid Earth 113, 1–17. doi:10.1029/2007JB004864.

Searcy, C., Dean, K., Stringer, W., 1998. Puff: A high-resolution volcanic ash tracking model. Journal of Volcanology and Geothermal Research 80, 1–16.

Sharp, D.H., 1984. An overview of Rayleigh-Taylor instability. Physica D: Nonlinear Phenomena 12, 3–18. doi:10.1016/0167-2789(84)90510-4.

Shin, J.O., Dalziel, S.B., Linden, P.F., 2004. Gravity currents produced by lock exchange. Journal of Fluid Mechanics 521, 1–34. doi:10.1017/S002211200400165X.

Shumlak, U., Roderick, N.F., 1998. Mitigation of the Rayleigh–Taylor instability by sheared axial flows. Physics of Plasmas 5, 2384–2389. doi:10.1063/1.872913.

Simpson, J.S., 1997. Gravity currents in the environment and the laboratory. Cambridge Univ. Press.

Smoluchowski, M., 1917. Mathematical theory of the kinetics of the coagulation of colloidal solutions. Z. Phys. Chem 92, 129–68.

Smyth, W.D., Kimura, S., 2007. Instability and diapycnal momentum transport in a double-diffusive, stratified shear layer. Journal of physical oceanography 37, 1551–1565.

Smyth, W.D., Moum, J.N., 2012. Ocean mixing by kelvin-helmholtz instability. Oceanography 25, 140–149.

Sorem, R.K., 1982. Volcanic ash clusters: Tephra rafts and scavengers. Journal of Volcanology and Geothermal Research 13, 63–71. doi:https://doi.org/10.1016/0377-0273(82)90019-1.

Sparks, R., Carey, S., Sigurdsson, H., 1991. Sedimentation from gravity currents generated by turbulent plumes. Sedimentology 38, 839–856.

Spence, R.J.S., Kelman, I., Baxter, P.J., Zuccaro, G., Petrazzuoli, S., 2005. Natural Hazards and Earth System Sciences Residential building and occupant vulnerability to tephra fall. Natural Hazards and Earth System Sciences 5, 477–494.

Stein, A., Draxler, R.R., Rolph, G.D., Stunder, B.J., Cohen, M., Ngan, F., 2015. Noaa's hysplit atmospheric transport and dispersion modeling system. Bulletin of the American Meteorological Society 96, 2059–2077.

Stenchikov, G., Ukhov, A., Osipov, S., Ahmadov, R., Grell, G., Cady-Pereira, K., Mlawer, E., Iacono, M., 2021. How Does a Pinatubo-Size Volcanic Cloud Reach the Middle Stratosphere? Journal of Geophysical Research: Atmospheres 126. doi:10.1029/2020JD033829.

Stokes, G.G., 1851. On the Theories of the Internal Friction of Fluids in Motion, and of the Equilibrium and Motion of Elastic Solids. Mathematical and Physical Papers vol.1 9, 75–129. doi:10.1017/CBO9780511702242.005.

Strang, E.J., Fernando, H.J.S., 2001. Entrainment and mixing in stratified flows. J. Fluid Mech. 428, 349–386.

Sutherland, B.R., Gingras, M.K., Knudson, C., Steverango, L., Surma, C., 2018. Particle-bearing currents in uniform density and two-layer fluids. Physical Review Fluids 3, 023801.

Sutherland, B.R., Mueller, B., Sjerve, B., Deepwell, D., 2021. Particle settling from constant-flux surface gravity currents and a near-stationary particle-bearing layer. Physical Review Fluids 6, 063802.

Taddeucci, J., Scarlato, P., Montanaro, C., Cimarelli, C., Del Bello, E., Freda, C., Andronico, D., Gudmundsson, M., Dingwell, D., 2011. Aggregation-dominated ash settling from the eyjafjallajökull volcanic cloud illuminated by field and laboratory high-speed imaging. Geology 39, 891–894.

Telling, J., Dufek, J., 2012. An experimental evaluation of ash aggregation in explosive volcanic eruptions. Journal of Volcanology and Geothermal Research 209, 1–8.

Textor, C., Graf, H.F., Herzog, M., Oberhuber, J.M., Rose, W.I., Ernst, G.G., 2006. Volcanic particle aggregation in explosive eruption columns. part i: Parameterization of the microphysics of hydrometeors and ash. Journal of volcanology and geothermal research 150, 359–377.

Thomas, L., Dalziel, S., Marino, B., 2003. The structure of the head of an inertial gravity current determined by particle-tracking velocimetry. Experiments in fluids 34, 708–716.

Thorpe, S.A., 1973. Experiments on instability and turbulence in a stratified shear flow. Journal of Fluid Mechanics 61, 731–751. doi:10.1017/S0022112073000911.

Turner, J.S., 1973. Buoyancy Effects in Fluids. Cambridge University Press, Cambridge. doi:DOI:10.1017/CBO9780511608827.

Van Eaton, A.R., Muirhead, J.D., Wilson, C.J., Cimarelli, C., 2012. Growth of volcanic ash aggregates in the presence of liquid water and ice: an experimental approach. Bulletin of volcanology 74, 1963–1984.

Van Eaton, A.R., Wilson, C.J., 2013. The nature, origins and distribution of ash aggregates in a large-scale wet eruption deposit: Oruanui, new zealand. Journal of Volcanology and Geothermal Research 250, 129–154.

Vecino, M., Rossi, E., Freret-Lorgeril, V., Fries, A., Gabellini, P., Lemus, J., Pollastri, S., Poulidis, A.P., Iguchi, M., Bonadonna, C., 2022. Aerodynamic characteristics and genesis of aggregates at sakurajima volcano, japan. Scientific reports 12, 1–13.

Veitch, G., Woods, A.W., 2001. Particle aggregation in volcanic eruption columns. Journal of Geophysical Research: Solid Earth 106, 26425–26441.

Verlet, L., 1967. Computer "experiments" on classical fluids. i. thermodynamical properties of lennard-jones molecules. Phys. Rev. 159, 98–103. doi:10.1103/PhysRev.159.98.

de'Michieli Vitturi, M., Pardini, F., 2021. Plume-mom-tsm 1.0. 0: a volcanic column and umbrella cloud spreading model. Geoscientific Model Development 14, 1345–1377.

Vogel, A., Durant, A.J., Cassiani, M., Clarkson, R.J., Slaby, M., Diplas, S., Krüger, K., Stohl, A., 2019. Simulation of volcanic ash ingestion into a large aero engine: particle–fan interactions. Journal of Turbomachinery 141.

Völtz, C., Pesch, W., Rehberg, I., 2001. Rayleigh-Taylor instability in a sedimenting suspension. Physical Review E 65, 011404. doi:10.1103/PhysRevE.65.011404.

Wang, G., Wan, D., Peng, C., Liu, K., Wang, L.P., 2019. Lbm study of aggregation of monosized spherical particles in homogeneous isotropic turbulence. Chemical Engineering Science 201, 201–211.

Watt, S.F., Gilbert, J.S., Folch, A., Phillips, J.C., Cai, X.M., 2015. An example of enhanced tephra deposition driven by topographically induced atmospheric turbulence. Bulletin of Volcanology 77. doi:10.1007/s00445-015-0927-x.

Webster, H.N., Devenish, B.J., Mastin, L.G., Thomson, D.J., Van Eaton, A.R., 2020. Operational modelling of umbrella cloud growth in a Lagrangian volcanic ash transport and dispersion model. Atmosphere 11, 1–22. doi:10.3390/atmos11020200.

Wilson, T.M., Cole, J.W., Stewart, C., Cronin, S.J., Johnston, D.M., 2011. Ash storms: Impacts of wind-remobilised volcanic ash on rural communities and agriculture following the 1991 Hudson eruption, southern Patagonia, Chile. Bulletin of Volcanology 73, 223–239. doi:10.1007/s00445-010-0396-1.

Wurm, Blum, 2000. An experimental study on the structure of cosmic dust aggregates and their alignment by motion relative to gas. The Astrophysical journal 529 1, L57–L60.

Yamamoto, Y., Hisataka, F., Harada, S., 2015. Numerical simulation of concentration interface in stratified suspension: Continuum-particle transition. International Journal of Multiphase Flow 73, 71–79. doi:10.1016/j.ijmultiphaseflow.2015.03.007.

Yu, X., Hsu, T.J., Balachandar, S., 2013. Convective instability in sedimentation: Linear stability analysis. Journal of Geophysical Research: Oceans 118, 256–272. doi:10.1029/2012JC008255.

Yu, X., Hsu, T.J., Balachandar, S., 2014. Convective instability in sedimentation: 3-D numerical study. Journal of Geophysical Research: Oceans , 3868–3882doi:10.1002/2014JC010089.Received.

Zhang, J., Guo, J., Gong, D.t., Wang, L.y., Tang, C., Zheng, Z.c., 2006. An investigation on oil/water separation mechanism inside helical pipes. Journal of Hydrodynamics 18, 336–340.

Zhang, W., Wu, Z., Li, D., 2005. Effect of shear flow and magnetic field on the Rayleigh-Taylor instability. Physics of Plasmas 12, 1–5. doi:10.1063/1.1872892.

Zhang, Y., Guo, C., Hou, H., Xue, G., 2014. Experimental research and numerical simulation on gas-liquid separation performance at high gas void fraction of helically coiled tube separator. International Journal of Chemical Engineering 2014.

Zhao, Y., Li, X., Cheng, J., Yang, C., Mao, Z.S., 2011. Experimental study on liquid–liquid macromixing in a stirred tank. Industrial & engineering chemistry research 50, 5952–5958.

Zhu, Y., Toon, O.B., Jensen, E.J., Bardeen, C.G., Mills, M.J., Tolbert, M.A., Yu, P., Woods, S., 2020. Persisting volcanic ash particles impact stratospheric SO2 lifetime and aerosol optical properties. Nature Communications 11, 1–11. doi:10.1038/s41467-020-18352-5.

Zidar, M., Kuzman, D., Ravnik, M., 2018. Characterisation of protein aggregation with the smoluchowski coagulation approach for use in biopharmaceuticals. Soft matter 14, 6001–6012.